Brown Dwarfs and UKIDSS

David Edwin Alexander Baker

Supervisor:

Richard Jameson

A thesis submitted for the degree of
Doctor of Philosophy
at the University of Leicester

X-ray & Observational Astronomy Group
Department of Physics & Astronomy
University of Leicester

December 2010

Declaration

I hereby declare that no part of this thesis has been previously submitted to this or any other University as part of the requirement for a higher degree. The work described herein was conducted by the undersigned, except for contributions from colleagues as acknowledged in the text.

David Edwin Alexander Baker
December 15, 2010

Brown Dwarfs and UKIDSS

David Edwin Alexander Baker

ABSTRACT

In this thesis I present the work of two studies into the population of low-mass stars and brown dwarfs within the open galactic clusters of Praesepe and Blanco 1 using optical and infrared photometry. Observing these objects within clusters is of great importance as their known ages and distances allow for comparisons to be made between the observed results and those predicted from theoretical formation and evolutionary models, whilst expanding our understanding of the initial mass function. Following an introduction to the formation, evolution and observational history of brown dwarfs in Chapter 2 an overview of the principle data reduction processes and instruments used in this thesis is given in Chapter 3.

Chapter 4 presents the result of the survey carried out in Praesepe using archival 2MASS, SDSS and UKIDSS data in a range of filters. Proper motion information is combined with colour magnitude cuts to select out and classify objects that are considered to be cluster members. Over 280 members have been identified with a cluster mass function that is consistent with the values presented for other clusters found. This mass function is in disagreement with previous values found for Praesepe.

Chapter 5 presents the results of a follow up J band survey using WFCAM to the CFHT12k I and z survey of Moraux et al. (2007). The data reduction and membership selection procedure are discussed with 27 low-mass objects found to be members.

Chapter 6 in contrast to the previous chapters presents a study not of brown dwarfs but of a suspected main-sequence, magnetic white-dwarf binary system found during an archival search of the UKIDSS DR3 database for objects with unusual Y band colours. The evidence for this system being a Polar is presented along with a discussion as to the assumed system properties. Follow up observations using the IAC-80 telescope, UKIRT and the SWIFT satellite are also presented.

Finally in Chapter 7 I summarise the results from each chapter and identify areas of future work.

Publications

A significant amount of work contained in this thesis has been published in the following paper:

Baker, D. E. A., Jameson, R. F., Casewell, S. L., Deacon, N., Lodieu, N., Hambly, N., "Low-mass stars and brown dwarfs in Praesepe", MNRAS, 2010, 408, 2457-2475

Acknowledgements

To my supervisor Richard Jameson I wish to offer my greatest thanks, for not only agreeing to take me on as his student but for the countless hours he has spent patiently explaining and guiding me through my work. I wish to also thank Sarah Casewell who has not only been a source of constant help and advice through out these last three years but for also provided me with the chance of observing in Hawaii - a trip I'll never forget. I would never of got this far however had it not been for Matt Burleigh who as my undergraduate tutor was the person who suggested that I apply for a PhD. His subsequent teachings in observational astronomy whilst at the INT, in dealing with Iberia and how to negotiate the Munich U-Bahn whilst always finding to best places to eat and more importantly drink have been gratefully received.

Next I wish to thank the many students of the XROA and TA groups who I have had the pleasure of knowing whilst working towards their own PhDs. In particular I wish to thank Nathan Dickinson, Paul Steele, James Duke, Chris Cottis, David Boyce, Richard Owen, Amy Scott, Katherine Lawrie, Vicky Heard, Chris Nixon, Peter Cossins and Owen Littlejohns. A special thanks goes to Lucy Heil - we started, stressed, finished and survived!

To Charly Feldman and Richard Hampson, not only do I wish you all the best for your future together but I wish to express my gratitude for helping to keep me sane whilst writing this thesis and providing me with plenty of good company during all those trips to 'Dos' over these last few years, particularly when going for the breakfasts!

To the many members of the ULSC and ULSU Surf Club who I have been fortunate enough to call friends over the years, you've provided me with fantastic memories and experiences and although there are far far too many of you to thank individually I would like to especially thank Dan Howard, Elliott Collins, Ben Start, Samantha Mears, Matt Allsop, Tim Jones, James Rathbone, Lisa Hayward, Ryan Bennett and Matthew Davis.

I would also thank to Samantha Hill, Claire Wilkinson, Samantha Phillips (née Bird), Hazel Robbins, Matthew Tonkin, Sarah Brooks, Timo Carr, Ben Rozitis, Diane Robbins, James Geraghty, Ben Holmes, Mark Andrews, Katie Barber (née Howard), Ben Pollard and Natalie Clegg.

Finally, I dedicate this thesis to my family. Without their love and support none of this would have been possible. Mum, Dad, Anna, I am and will be forever grateful.

Contents

List of Figures

List of Tables

Chapter 1

Introduction

1.1 Preface

Large scale surveys such as the UK Infrared Deep Sky Survey (UKIDSS) are ideally suited to studying and statistically characterising both large populations of objects and for finding rare or new types of objects. The focus of this thesis is primarily on locating candidate low-mass star/brown dwarf members in the two open galactic clusters of Praesepe and Blanco 1 utilising wide area deep multi-epoch data. The theory and observations of brown dwarfs are also discussed. Finally from the Large Area Survey (LAS) of UKIDSS a suspected Polar is discussed.

1.2 Thesis Structure

Chapter 2 of this thesis gives an overview of brown dwarf formation, structure and evolution as well as detailing their observational history and how this has lead to the definition of new spectral types. A brief discussion on the atmospheric models used, is also presented, along with recent results concerning the initial mass function (IMF) of the low-mass star/brown dwarf population in open clusters.

Chapter 3 describes the methodology and instruments that have been used within this thesis. A short discussion on the basics of photometry and general image data reduction is presented along with an overview of the pattern matching techniques and astrometric procedures that have been used to calculate proper motions for the candidate objects. The chapter ends with a short description of the surveys that have been used to provide some of the data for this thesis.

Chapter 4 presents the results of a deep, wide field photometric and proper motion survey of the Praesepe open star cluster. The data acquisition and analysis is discussed. Colour magnitude diagrams, proper motion diagrams, luminosity functions and mass function results are also presented.

Chapter 5 describes the study of the southern hemisphere Blanco 1 cluster using a combination of CFHT12k archival optical data and follow up J band imaging to try and constrain the initial candidate members of the cluster. Again the data calibration, analysis and results are discussed.

Chapter 6 details the study of a suspected polar found during an archival search of the UKIDSS database for objects with unusual Y band colours. Only two objects were found with 1 being identified as the Polar, GG Leo. Follow up imaging and spectroscopic data of the second unknown object are presented along with an overview of assumed system properties.

Chapter 7 summarises the conclusions from the previous 3 science chapters and ends with suggestions on ways in which the work presented could be followed up.

Chapter 2

Brown Dwarf Theory and Observations

2.1 Introduction

Stars, objects common to the unaided eye in the night sky are the source of most of the Universe's light. The processes governing the production of the energy that is needed to power them were reported by Bethe (1939), who found that for stars similar in type to our Sun, the source of this power lay in the proton-proton chain (p-p chain) of reactions. For the more massive stars, it was likely the carbon-nitrogen-oxygen cycle that supplied their energy. While these stars are converting hydrogen into helium via their respective energy generation processes they exist in hydrostatic equilibrium, balancing the force of gravitational collapse. Changes to the internal chemistry of these stars lead them, depending on their initial masses, on very different evolutionary paths. For the highest mass stars that rapidly exhaust their supplies of hydrogen and go on to fuse the higher mass elements (up to the fusion of iron) the end remnant will be a black hole. For stars of slightly smaller masses ($<25\mathrm{M}_{\odot}$) a neutron star is the end point of evolution, whilst for stars similar to our Sun ($<8\mathrm{M}_\odot$) the end result will be a white dwarf. For the lowest mass stars (ones that are just able to sustain nuclear fusion) their evolution is far less dramatic. By virtue of being just on the hydrogen burning limit they very slowly convert their stores of hydrogen into helium and essentially stay in equilibrium for times longer than the age of the Universe. There is, however, another class of star-like object, one that was never massive enough to generate the internal pressures needed to increase the core temperature high enough to begin the p-p chain and drive the process of hydrostatic equilibrium. These “failed stars” simply cool from the time they were formed, evolving throughout their life to later spectral types. Theorised by Kumar (1963) and Hayashi & Nakano (1963) these objects were initially termed “black dwarfs” due to their low luminosities, however it was Tarter (1975) who gave them their now more common name of brown dwarfs (BDs). This term in itself is slightly misleading as the colour of a BD is not actually brown but rather a magenta colour. This is due to the combination of red from the blackbody component, BD emission peaks in the infrared (IR) and an absence of green due to the presence of the sodium (Na D) lines which are prominent in the spectra of these objects. This colour can also be affected by the presence of other alkali metals and clouds that form within their atmosphere (Burrows et al., 2001). The boundary between the stars able to support themselves on the main sequence and the BDs below the hydrogen burning limit was calculated by Kumar (1963) as between 0.07 and $0.09\mathrm{M}_\odot$ for population I and II stars respectively, with Hayashi & Nakano (1963) predicting $\sim 0.08\mathrm{M}_\odot$. More recent work by Chabrier et al. (2000) and Saumon & Marley (2008) has shown the metallicity dependent nature of this boundary value, with the minimum value of $\sim 73\mathrm{M}_\mathrm{J}$ rising to $\sim 80\mathrm{M}_\mathrm{J}$ for an object with a metallicity ratio of [M/H]=-2.0. There is therefore a relatively clear distinction that can be made between BDs and stars based on their mass and source of energy (nuclear processes vs gravitational contraction). However, as the masses decrease towards those of the giant planets (a limit of $\leq 13\mathrm{M_J}$ was proposed by Basri 2000) another division will have to be considered. One way of possibly separating BDs from planets is via their method of formation. There are several theories of brown dwarf formation and it is possible that more than one of these actually takes place. Among the more favoured explanations are that they form in a very similar way to stars, from the collapse and fragmentation of a molecular cloud or that during the protostellar stage the accretion of material from the disk is interrupted either by photo-evaporation or dynamical ejection. Finally they may form in a way not too dissimilar to planets via accretion of gas via a rocky core in an accretion disk.

2.2 Formation

In 1902 Sir James Jeans investigated how small perturbations from hydrostatic equilibrium in a molecular cloud could lead to the clumping and collapse of material (which begins the formation of a protostar). The characteristic mass which triggers this collapse of material bears his name and can be derived following a simplified situation in which effects such as rotation and magnetic fields are neglected.

For a spherical cloud of material the virial theorem can be used to balance the kinetic (K) and gravitational energies (U) associated with the material thus,

$$2K + U = 0. \tag{2.1}$$

If the force of the gas pressure is dominant (2K > |U|), then the cloud will expand. If the reverse is true then the gravitational potential dominates the kinetic term and the cloud will contract. This gravitational potential can be expressed as,

$$U = -\frac{3\mathrm{G}{M_c}^2}{5R_c}, \tag{2.2}$$

where G is the gravitational constant and M_c and R_c are the mass and radius of the cloud respectively. The cloud's thermal energy can also be expressed as,

$$K = \frac{3}{2}N\mathrm{k}T = \frac{3M_c\mathrm{k}T}{2\mu m_H}, \tag{2.3}$$

where N is the number of particles, k the Boltzmann constant, T the temperature of the contracting cloud, μ is the mean molecular weight and m_H the molecular mass of hydrogen. By arranging for the condition of collapse and replacing R_c with the assumption that the mass density (ρ_0) is constant throughout the cloud,

$$R_c = \left(\frac{3M_c}{4\pi\rho_0}\right)^{\frac{1}{3}}, \tag{2.4}$$

the mass limit of collapse ($M_c > M_J$) can be found to be,

$$M_J \simeq \left(\frac{5kT}{G\mu m_H}\right)^{\frac{3}{2}} \left(\frac{3}{4\pi\rho_0}\right)^{\frac{1}{2}}. \tag{2.5}$$

The criterion of collapsing the cloud of density ρ_0 can also be expressed in terms of a minimum radius, the Jeans length (R_J),

$$R_J \simeq \left(\frac{15kT}{4\pi G\mu m_H \rho_0}\right)^{\frac{1}{2}}. \tag{2.6}$$

This assumes that the collapsing section of the molecular cloud is surrounded by an infinite and constant density background medium. Assuming that even after the simplifications have been made the Jeans Mass gives the lower limit of mass for the formed object, it is still of the order of several solar masses (Larson 1992; Elmegreen 1999) and so it seems that BDs forming in exactly the same way as stars can be ruled out. Nevertheless BDs have been found in the presence of disks (Luhman et al. 2007a) as well as with similar kinematics and spatial densities to those of stars (Joergens 2006; Luhman 2006). These three observations can be interpreted as BDs having similar properties to stars (Luhman et al. 2007b) and so although the formation process may not be identical it may share many similarities.

2.2.1 Formation by turbulent fragmentation

The first proposed method of BD formation is that of turbulent fragmentation of the molecular cloud, which has been explored in simulations by Padoan & Nordlund (2002). In the simulations the interstellar turbulence creates a wide range of dense structures, with those designated as prestellar cores having a mass spectrum similar to the observed stellar initial mass function. The process of formation is thought to be hierarchical in nature following the arguments of Hoyle (1953). Thus, after one part of the molecular cloud has collapsed it will fragment into smaller subclouds which upon contraction will also again fragment into smaller clouds dubbed “sub-subclouds” by Whitworth et al. (2007). This process can continue until these small fragmented clouds reach the opacity limit, the point determining the minimum formation mass. The opacity limit occurs when the small fragmented subclouds enter the optically thick regime or are collapsing at a sufficiently large rate such that the PdV work done on them is unable to be radiated away efficiently causing the subcloud to heat up (Rees 1976; Low & Lynden-Bell 1976). The opacity limit has traditionally been determined based upon a process of three dimensional hierarchical fragmentation, there is however no evidence for this occurring in nature. This is because at every stage of collapse the fragments that form do so slower than the overall collapse of the cloud due to them being less Jeans unstable. The result is that any fragments that do form are likely to become merged with each other. There is evidence to suggest however, that star formation proceeds quickly (“in a crossing time”) once a molecular cloud has been formed, Elmegreen (2000). Here the three dimensional hierarchical fragmentation prescription is replaced by one of two dimensional one-shot fragmentation of a shocked layer. Boyd & Whitworth (2005) find that under specific circumstances BDs as low as 2.6$\mathrm{M_J}$ can be created, with masses $\lesssim$5$\mathrm{M_J}$ being created under more relaxed conditions.

2.2.2 Formation by disk fragmentation

The second possible mechanism through which BDs can form is via fragmentation of a large circumstellar disk surrounding an already formed central object (see Figure 2.1). Here the BDs that form as companions to the central object form within the spiral arms of the disk. Some of the initial numerical simulations predicted that the mechanism would not work, but after the models were updated to include prescriptions for improved radiative transfer to correctly model the cooling (Stamatellos et al. 2007; Stamatellos & Whitworth 2009; Walch et al. 2009; Walch et al. 2010) the method was proved viable. Whilst objects can be shown to form in such a manner, the efficiency with which they form is far from well constrained. The simulations have also predicted that after formation, the BDs are dynamically ejected with a significant proportion of this population consisting of BD-BD binaries. Burgasser et al. (2005) provide some observational evidence for this scenario in their discovery of the close (11 AU) system Gl 337CD. Evidence is also presented by the simulations that suggests that the BDs that do form within the disk and are still associated with the system tend to evolve to wide binary orbits ($\sim$200 AU), thus reproducing the "brown dwarf desert" effect. The term "brown dwarf desert" refers to the result that very few sub-solar/BD companions have been found at small separations ($\leq$5 AU) from main sequence solar type stars (Marcy & Butler 2000; Grether & Lineweaver

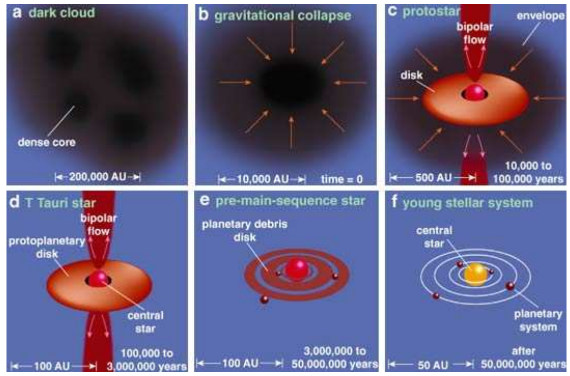

FIGURE 2.1. Pictorial representation of star formation illustrating the disc formation process and the subsequent formation of a planetary system. Of the planetary system objects that form brown dwarfs are a possible outcome. Image courtesy of Greene (2001).

2006). As with the other methods proposed there are circumstances that can mitigate against the formation scenario. One such factor is the introduction of turbulence. Turbulent motions that are introduced into the disk can provide support for it against collapse, thus preventing fragmentation. As such a measurement of disk turbulence becomes an important factor of determining the stability of the disk, in effect it is analogous to the cooling timescale (Bertin & Lodato 1999; Cossins 2010).

2.2.3 Formation via ejection from the accretion disk

Another method of forming BDs is via ejection from the accretion disk, as proposed by Reipurth (2000) and Reipurth & Clarke (2001). Here the protostellar cores which have formed from the gravitational collapse of the gas are still embedded in their parental circumstellar disc. However, unlike in the stellar formation scenario the accretion of matter which causes the core to heat up and begin fusion of hydrogen is interrupted.

One cause of interruption could be due to encounters with other protostellar cores which could either halt the accretion process by cutting off the gas supply or cause the object to be ejected from the disc. The need to model the disc in these situations has lead many to conduct numerical simulations of such interacting systems (Watkins et al. 1998; Bate et al. 2003; Goodwin et al. 2004a; Goodwin et al. 2004b). These simulations have shown that objects as low as $0.005\mathrm{M}_{\odot}$ can be produced given the right situations. The ejection of the BDs from the disk does however raise the issue of the kinematics. In a cluster of stars one would expect to see a distinct difference between the stellar and BD populations, since the BDs would have higher velocities than the more massive stars. It has been suggested though that for clusters with intrinsically high velocity dispersions, such as the Pleiades, that this effect would be hard to discern. Another failing of this formation scenario is that it cannot explain the large number of close BD binaries that have been found (Pinfield et al. 2003; Lodieu et al. 2008).

2.2.4 Formation by photo-erosion

The fourth proposed method of BD formation starts with an already formed core ($\gtrsim 1\mathrm{M}_{\odot}$) that is then overrun by an HII region propagating outwardly from an already formed high mass star (Hester et al., 1996). When this initial core encounters the HII region the resulting compression wave caused by the increase in external pressure triggers the collapse process. This process occurs from the outside in and begins the formation of a protostar. The formation also causes an expansion wave to be reflected away from the core, which results in an inward velocity field aiding accretion onto the protostar. The expansion wave soon encounters the ionisation front which begins to photo-erode the material that is in the circum-protostar environment. This erosion of material stops when the ionisation front has penetrated so close to the protostar that the kinetic energy the ionised gas possesses is not enough to break the gravitational attraction of the core. All the material inside the ionisation front at this point is accreted onto the protostar. On the basis of a semi-analytic analysis of this method, Whitworth & Zinnecker (2004) showed that the final mass is given by,

$$M \approx 0.01\mathrm{M}_{\odot} \left(\frac{a_I}{0.3kms^{-1}}\right)^6 \left(\frac{\dot{\mathcal{N}}_{LyC}}{10^{50}s^{-1}}\right)^{-1/3} \times \left(\frac{n_0}{10^3cm^{-3}}\right)^{-1/3}, \qquad (2.7)$$

where a_I is the isothermal sound speed of the neutral gas in the core, $\dot{\mathcal{N}}_{LyC}$ is the rate at which the star(s) exciting the HII region emit hydrogen-ionising photons, and n_0 is the density in the ambient HII region. Although this formation scenario is capable of producing low-mass stars and BDs it is unlikely to be the dominant means of BD creation as it is very inefficient. This inefficiency arises from the need to have an already massive pre-existing core in order to form one single low-mass star or BD. It also requires the nearby presence of an OB star and so cannot account for the formation of all BDs but could account for some BD-BD binaries as their creation is possible via this process.

2.2.5 Brown Dwarf Binaries

For any of the afore mentioned formation theories to be successful they have to not only be able to form single BD systems with the correct properties but also multiple systems, the most common of which is a binary system. Binary systems are commonplace throughout the galaxy and provide key test beds for studies into dynamical and co-evolutionary processes. High-resolution ground based imaging (with and without adaptive optics) and space based imaging have been used to look for these binary systems in the field (Reid et al. 2001; Burgasser et al. 2003; Gizis et al. 2003) and in nearby clusters and associations (Martín et al. 2003; Pinfield et al. 2003; Kraus et al. 2005). Some other observations using high-resolution spectroscopy have also been conducted in order to look for binaries that cannot be visually separated due to their smaller orbital separation (Reid et al. 2002, Joergens 2006). The results of these surveys have presented a binary fraction in the field of typically 10-30%, with the systems possessing close orbital separations (93% having $\Delta < 20$ AU) and predominantly near equal mass configurations (Burgasser et al. 2007). The imaging surveys of Pinfield et al. (2003) and Chappelle et al. (2005) attempted to measure the unresolved binary fraction of these low mass systems in clusters via their over-luminosity (an equal mass binary will have an over-luminosity of 0.75 mag). The result from Pinfield et al. (2003) of a 50% binary fraction is in disagreement with the field population result. It is however complicated by the lack of a membership assignment on the systems presented, thus raising the possibility that some contamination may have occurred (Burgasser et al. 2007). As the binary fraction is a result of formation scenarios and can be observationally determined it provides a key way of discriminating between them. The fragmentation scenarios favour a higher binary fraction with often wide orbits, whilst the ejection scenarios favour the close in binary systems although the binary fraction is substantially reduced. The presence of binary systems provides further complications to the studies of the initial mass function but unless it can be determined accurately any correction to the system mass function only serves to add ambiguity.

2.3 The Initial Mass Function and the Mass-Luminosity Relationship

The initial mass function (IMF) describes the number of stars within a given sample as a function of their mass. As such, it is dependent upon the formation process, which as shown in Section 2.2 is not yet fully understood. Because the process of stellar and substellar formation may be influenced by the local environment, a lot of work has been undertaken to find evidence for this occurring within the IMF. The IMF was first introduced in Salpeter (1955) and provided a useful way of reporting stellar numbers as a function of mass. Work that followed showed evidence that the single power law reported by Salpeter (1955), equation 2.8 below, was probably not representative across the whole mass range and a multi-segment power law (Kroupa et al. 1993) or log-normal form (Miller & Scalo 1979; Adams & Fatuzzo 1996 and Chabrier 2003) could also represent the observed data. The mathematical prescriptions for each form of the IMF mentioned above are shown below, first is the Salpeter formalism followed by the description offered for the Chabrier log-normal form.

$$\xi\left(\log m\right) = \frac{dN/dV}{d\log m} = \frac{dn}{d\log m}. \tag{2.8}$$

Here in Salpeter form, the IMF, $\xi\left(\log m\right)$, is defined as the number of stars (N) in a volume of space (V) per logarithmic mass interval $d\log m$. Scalo (1986) also use a Salpeter like representation in defining what he terms the mass spectrum, $\xi\left(m\right)$, which can be related to equation 2.8 thus,

$$\xi\left(m\right) = \frac{dn}{dM} = \frac{1}{m\ln 10}\xi\left(\log m\right). \tag{2.9}$$

Both functions can be related to the stellar/BD mass as

$$\xi\left(\log m\right) \propto m^{-x} \tag{2.10}$$

and

$$\xi\left(m\right) \propto m^{-\alpha}. \tag{2.11}$$

The indices x and α are related by $x = \alpha - 1$[1]. It is therefore important to ensure that when quoting the numerical results of the slope that the specific functional form being used is identified, failure to do so can lead to misinterpretation of results. In this thesis I have used the Scalo (1986) α representation for my data.

[1]An initial mass function that can be described as "flat" or "falling" in logarithmic units can still be rising in linear units (Bastian et al., 2010).

An alternative commonly used is the Chabrier (2003) log-normal formalism for the IMF which by definition has a characteristic mass of M_c and a width of σ as is shown by equation 2.12

$$\xi\left(m\right) = \frac{dN}{d\log M} = A\exp\left[\frac{-\left(\log M - \log M_c\right)^2}{2\sigma^2}\right]. \tag{2.12}$$

Alongside these two common representations of the mass function it should be noted that what is actually observed is the luminosity function of the sample. This requires the use of some mass-luminosity relationship to transform the observational properties (fluxes, colours) into physical parameters of the star/BD (mass, effective temperature). Two of the ways in which the luminosity function is transformed into a mass function are by a) placing objects onto an Hertzsprung-Russell diagram via the use of colour, spectroscopy and proper motion information in order to estimate their mass or b) calculating the luminosity function for a certain bandpass and using theoretical mass-luminosity relationships to transform it into a mass function. I have used the second approach, however neither method is without its flaws. The first method is very telescope time intensive and may suffer in the immediate future as sensitive, deep surveys are inadequately supported by spectroscopic instruments, whilst the second method is subject to our current understanding of the structure and atmospheric models which currently lack prescriptions to deal with magnetic activity and rotation (Allard 2010). The mass function is expressed using the luminosity function and mass-luminosity relationship thus,

$$\frac{dn}{dM}(m)_{\tau} = \left(\frac{dn}{dM_{\lambda}(m)}\right)\left(\frac{dM_{\lambda}(m)}{dm}\right)_{\tau}. \tag{2.13}$$

With, $\frac{dn}{dM_{\lambda}(m)}$ giving the luminosity function, $\frac{dM_{\lambda}(m)}{dm}$ the mass-luminosity relationship, τ the age, $M_{\lambda}(m)$ the absolute magnitude and λ the filter wavelength. By changing the functional form of the IMF and/or claiming evidence of varying IMFs, certain astrophysical problems can be solved/described differently. For example, certain variations in the IMF could result in very different star-formation histories of the Universe. It becomes important therefore to ask, is the initial mass function universal or does its shape vary? Bastian et al. (2010) provide a good review on studies of the IMF.

It is partly for this reason that the United Kingdom Infrared Deep Sky Survey (UKIDSS; Lawrence et al. 2007) Galactic Clusters Survey (GCS) program was initiated. During the course of its science observation lifetime it aims to measure the substellar mass function in a number of Galactic clusters and star forming associations, encompassing a range of ages and galactic environments. The benefit of using open clusters and star forming regions is that each individual one should possess only minor age and metallicity spreads as the objects should be coeval and from the same formation site. These facts coupled with a common distance make studies of the IMF considerably easier in clusters than for the field population. Large clusters are not fully representative of all star and BD formation as these objects can form is much smaller associations and even in isolation. A caveat therefore to studying the IMF in clusters is that they evolve over time, resulting in a depletion of their low-mass members through dynamical interactions that cause objects to be ejected from the cluster and into the field (see Section 2.3). Further corrections[2] also need introducing to account for the fact that the measured mass function may contain unseen binaries (Kroupa 2001) and that this binary population also will evolve over time (Kroupa 2002). In this thesis corrections have not been made for binarity and so the mass functions reported should be more formally termed as the system mass functions. Table 2.1 shows a compilation of values for various cluster mass functions retrieved from the literature (original table from Lodieu 2004) with Table 2.2 showing a small compilation for those fitted with a Chabrier type log-normal function.

[2]If these corrections are not applied then it is again important that the fact be noted. The functional form of the mass function should also be explicitly stated to avoid inadvertently comparing the indices of x and α with one another.

Table 2.1. Compilation of various IMF results for a range of clusters in the literature.

Cluster	Age (Myr)	Distance (parsecs)	Mass Range ($M_\odot$)	Mass function slope (α)	References
Praesepe	600	180	1.00 - 0.08	1.40$\pm$0.2	Kraus & Hillenbrand (2007)
			0.50 - 0.10	1.80$\pm$0.1	Boudreault et al. (2010)
Coma Berenices	400	90	1.00 - 0.2	0.60$\pm$0.3	Kraus & Hillenbrand (2007)
Blanco 1	$\sim$125	260	0.60 - 0.03	0.69$\pm$0.15	Moraux et al. (2007)
Pleiades	125$\pm$8	130	0.25 - 0.40	1.00$\pm$0.50	Martin et al. (1998)
			0.40 - 0.040	0.60$\pm$0.15	Bouvier et al. (1998)
			0.50 - 0.055	0.50$\pm$0.20	Tej et al. (2002)
			0.60 - 0.030	0.80	Dobbie et al. (2002)
			0.48 - 0.030	0.60$\pm$0.11	Moraux et al. (2003)
α Per	90$\pm$10	182	0.30 - 0.035	0.59$\pm$0.05	Barrado y Navascués et al. (2002)
			1.00 - 0.20	0.86	Deacon & Hambly (2004)
Upper Sco	5	145	0.30 - 0.01	0.60$\pm$0.1	Lodieu et al. (2007b)
σ Ori	3-8	352	0.20 - 0.013	0.80$\pm$0.4	Béjar et al. (2001)
			0.11 - 0.006	0.60$\pm$0.2	Caballero et al. (2007)
			0.072 - 0.007	0.60	González-García et al. (2006)
			0.49 - 0.01	0.50$\pm$0.2	Lodieu et al. (2009)
λ Ori	5	400	0.70 - 0.02	0.73$\pm$0.05	Barrado y Navascués et al. (2004)
Taurus	1-2	140	0.30 - 0.0035		Briceño et al. (2002)
					Luhman (2004)

Table 2.2. Small compilation of some of the Chabrier type log-normal mass function results found in the literature.

Cluster	Age (Myr)	Distance (parsecs)	Mass Range ($M_\odot$)	Log-Normal Mass Function (M_c and σ)	References
Hyades	625±50	46.3	3.00 - 0.050	0.60, 0.39	Bouvier et al. (2008)
Praesepe	600	180	0.70 - 0.06	0.22, 0.57	Boudreault et al. (2010)
Blanco 1	∼125	260	3.00 - 0.03	0.36, 0.58	Moraux et al. (2007)
Pleiades	125±8	130	0.56 - 0.035	0.24, 0.34	Lodieu et al. (2007a)

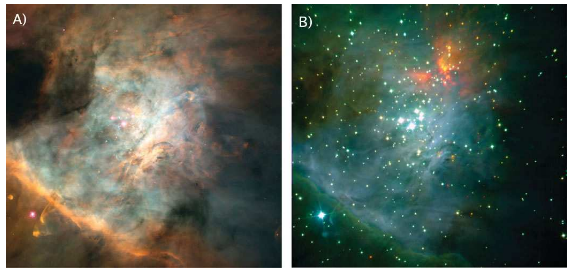

FIGURE 2.2. (a) Optical and (b) infrared views of an embedded Trapezium cluster associated with the Great Orion Nebula. North is on the left, and west at the top. Figure and caption from Lada (2010)

2.3.1 Open cluster formation and evolution

Recent N-body simulations of cluster formation carried out by Kroupa (2001) have provided evidence that open galactic clusters may have formed from regions similar to the Orion Nebula Cluster. The groups of stars that are formed are at first highly embedded within their parental molecular clouds and are obscured heavily by the interstellar dust (See Figure 2.2). Work by Miller & Scalo (1978), Adams & Myers (2001) and Kroupa (2001) has shown that once the dust has been cleared due to the presence of strong stellar winds emanating from the OB stars around 10% of the stars remaining are then left bound together forming an open cluster. The significant loss of mass due to the expulsion of the gas allows for young coeval stars and systems that formed with a higher velocity dispersion to become unbound from the open cluster creating the moving group populations. Through accurate measurements of their space motions these moving group systems can be traced back to their associated open cluster (Pinfield et al. 2006, Jameson et al. 2008) thereby providing a key diagnostic in their study - age.

The objects that are formed in an open cluster can generally be assumed to be an homogeneous population, yet as the cluster ages the population of objects created from the collapse of the molecular cloud will undergo a process of dynamical evolution. This dynamical evolution can be brought about via interactions between intra-cluster members, inter-cluster forces and molecular gas regions each of which affect the kinematics of the system resulting in spatial disruptions that manifest themselves as dynamical mass segregation and evaporation of the low-mass members. The segregation process describes the migration of objects with higher masses towards the gravitational potential well of the association, whilst those objects of lower mass find themselves moving outward to higher energy orbits as they receive an increase to their kinetic energy. Calculating mass functions for the inner and outer halo regions of the cluster can reveal this effect, with Schilbach et al. (2006) reporting evidence of mass segregation for the majority of the 600 clusters in their sample. Pinfield et al. (1998) and Jameson et al. (2002) use the technique of fitting King profiles to a set of Pleiades candidates in different mass bins in order to determine the core radius. The core radius increases for the lower mass stars such that $r_c \propto < \sigma^2 >^{1/2} \propto 1/\sqrt{m}$. This indicates mass segregation and that the cluster is relaxed (i.e has achieved equipartition of energy). In contrast Holland et al. (2000) find evidence to suggest that the low mass cluster stars of Praesepe appear to have an excess of energy as there is a deviation from the $< \sigma^2 >^{1/2} \propto 1/\sqrt{m}$ relation. This is reconciled by suggesting that there may have been a recent collision between Praesepe and a smaller subcluster.

The segregation of objects has also been suggested by Bonnell et al. (2001b) to be a natural consequence of stellar formation. Here, the protostars find themselves in a competitive accretion environment: stars forming within higher density gas at the centre are able to accrete more material. Bonnell et al. (2001a) provide theoretical simulations that show a preference for higher mass stars forming in the central regions, whilst those of lower mass being more evenly distributed. This primordial mass segregation has been observed by Sirianni et al. (2002) who prefer this as an explanation for the segregation seen in NGC 330 as opposed to that offered by dynamical evolution. As the lower mass members gain kinetic energy and move onto more energetic orbits and migrate outwards they can potentially reach a point at which their velocity becomes higher than the escape velocity of the cluster, thus beginning a period of evaporation of the lower mass objects (Adams et al. 2002b; de La Fuente Marcos & de La Fuente Marcos 2000). This loss of low-mass stars and BDs has been reported by Bouvier et al. (2008) and has been suggested as an explanation for the difference between the mass functions of the older Hyades (Bouvier et al. 2008) and the younger Pleaides (Lodieu et al. 2007a) clusters. Numerical simulations carried out by Adams et al. (2002b) show that for the Hyades between 70% and 90% of the original BD population may have succumbed to evaporation/ejection, whilst 88% of the BD population remains in the Pleiades. For the Praesepe cluster the fraction varies between 56% remaining and 2% remaining of the original population.

2.4 Evolution of a brown dwarf

As discussed already the force of gravitational collapse in stars is balanced by the energy generated via nuclear fusion, resulting in a state of hydrostatic equilibrium.This pressure does not however support BDs against gravitational collapse and thus they will cool off inexorably as they age. From birth until $\approx 10^6$ years in age, the BD evolves along the "Hayashi track" (Hayashi 1961). This is a period of contraction of radius and decreasing luminosity for which the effective temperature of the BD remains about constant. If the BD had a sufficiently high initial temperature, any deuterium contained within the atmosphere would be subject to depletion via deuterium burning. If deuterium burning is occurring, this can temporarily halt the gravitational collapse thus ensuring a brief period (from 10^6 until 3×10^6 yrs) of constant radius, effective temperature and luminosity, after which, the BD continues to cool throughout its lifetime. As they age BDs will eventually contract to a limiting radius. This occurs when the collapse is halted by a sufficient rise in the electron degeneracy pressure[3]. As the mass and radius have a dependency upon age and are critical for determining such properties as the temperature, luminosity and gravity of the BD, a large amount of effort has been invested in determining how these parameters evolve over time.

[3]This is an application of the Pauli exclusion principle that states that no two electrons in a single atom can have the same four quantum numbers (n, l, m_l and m_s)

2.4.1 The evolution of luminosity

Figure 2.3 shows the luminosity evolution for isolated low-mass stars red dwarf stars (blue), BDs above $13\mathrm{M_J}$ (red) and those below (green). At ages of approximately 1 Gyr the splitting of the stellar and BD populations begins to become evident as the stars stabilise their luminosity, equating their thermonuclear energy production with that of photon luminosity loss from the surface (they now exist on the main sequence). A phase of deuterium burning is also evident for BDs of mass $13\mathrm{M_J}$ at young ages. Following the model calculations of Burrows et al. (2001), the luminosity evolution for a BD/substellar object can be given by equation 2.14

$$L \sim 4 \times 10^{-5}\mathrm{L_\odot} \left(\frac{10^9 yr}{t}\right)^{1.3} \left(\frac{M}{0.05\mathrm{M_\odot}}\right)^{2.64} \left(\frac{\kappa_R}{10^{-2} cm^2 g^{-1}}\right)^{0.35}, \tag{2.14}$$

where g is the surface gravity (cm s^{-2}), κ_R is an average atmospheric Rosseland mean opacity (cm g^{-1}), t is the age in years and M the object mass in terms of the Sun. Burrows et al. (2001) note that for different atmospheric and equation of state prescriptions, as well as differing metalicities, that the numbers will be altered but argue that the basic systematics for evolution of late time objects are fully described by the above equation. One result that can be drawn from equation 2.14 is that for a low-mass BD ($0.02\mathrm{M_\odot}$) its luminosity at a very young age (1Myr) would be of the order $7{\times}10^{-3}\mathrm{L_\odot}$, whilst the same BD at the age of the Hyades cluster would have a luminosity of the order $1.6{\times}10^{-6}\mathrm{L_\odot}$. It is for this reason that BDs located in evolved open clusters have only recently been found, thanks to the increased sensitivity that modern day instruments can provide. For the low-mass main sequence stars where luminosity becomes independent of age a power-law relationship can be shown that links luminosity and mass (Burrows & Liebert 1993),

$$L_{star} \sim 10^{-3}\mathrm{L}_{\odot} \left(\frac{M}{0.1\mathrm{M}_{\odot}}\right)^{2.2}. \tag{2.15}$$

This shows that the dependence on mass of the luminosity is weaker for those stars on the main sequence than for the BDs below it.

2.4.2 The evolution of temperature

As well as evolutionary sequences for luminosity, Burrows et al. (2001) show for the same mass tracks the evolution of temperature. Figure 2.4 shows again the clear distinction between those stars that are powered via thermonuclear fusion and those objects below the hydrogen burning limit. For the objects whose core does not reach the sufficiently high temperature ($\sim 3\times 10^6$K) to trigger the onset of fusion, their temperature profiles show a rise, peak and then decline as age increases. A similar equation to that of equation 2.14 can also be defined to describe the effective temperature of these objects, again from Burrows et al. (2001) and shown in Figure 2.5,

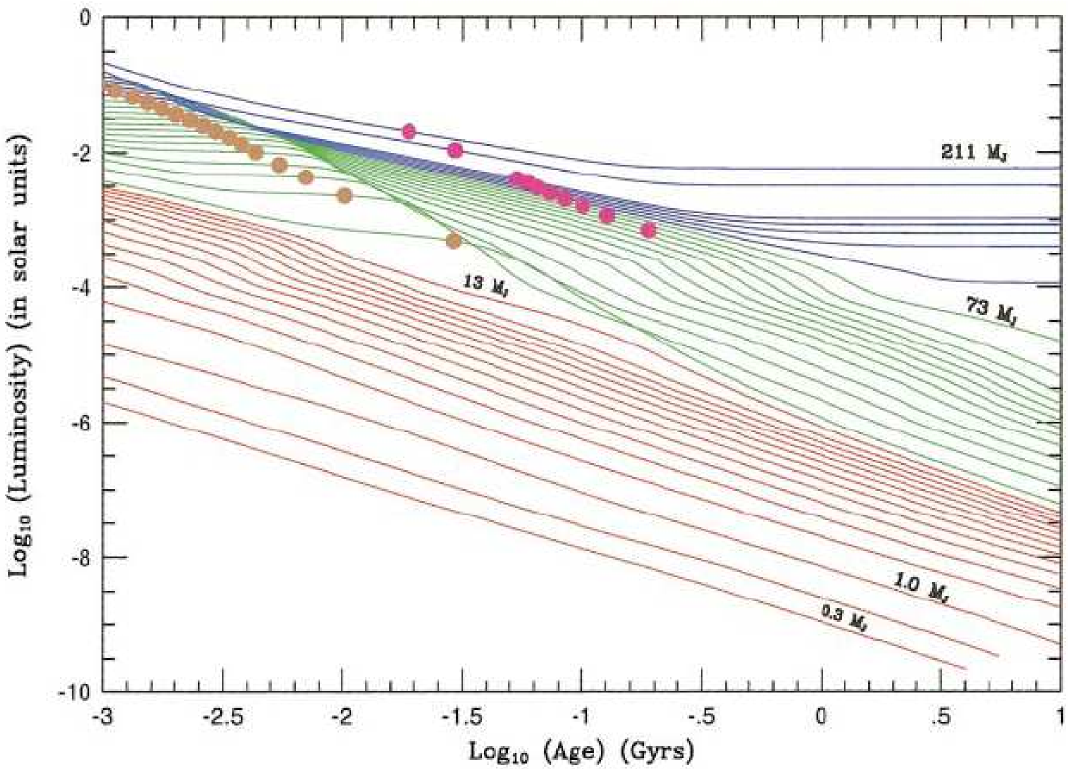

FIGURE 2.3. Evolution of the luminosity (in $L_\odot$) of isolated solar-metallicity red dwarf stars and substellar-mass objects versus age (in years). The stars are shown in blue, those brown dwarfs about $13M_J$ are shown in green, and brown dwarf/giant planets equal to or below $13M_J$ are shown in red. Though the colour categories are based on deuterium or light hydrogen burning, they should be considered arbitrary *vis á vis* whether the object in question is a brown dwarf or a planet, sensibly distinguished on the basis of origin. The masses of the substellar objects/stars portrayed are 0.3, 0.5, 1.0, 2.0, 3.0, 4.0, 5.0, 6.0, 7.0, 8.0, 9.0, 10.0, 11.0, 12.0, 13.0 and $15.0M_J$ and 0.02, 0.025, ,0.03, 0.035, 0.04, 0.045, 0.05, 0.055, 0.06, 0.065, 0.07, 0.075, 0.08, 0.085, 0.09, 0.095, 0.1, 0.15, $0.2M_\odot$ ($\equiv 211M_J$). For a given object, the gold dots mark when 50% of the deuterium has burned and the magenta dots mark when 50% of the lithium has burned. Note that the lithium sequence penetrates into the brown dwarf regime near $0.065M_\odot$, below the hydrogen burning main sequence edge mass. Figure and caption from Burrows et al. (2001).

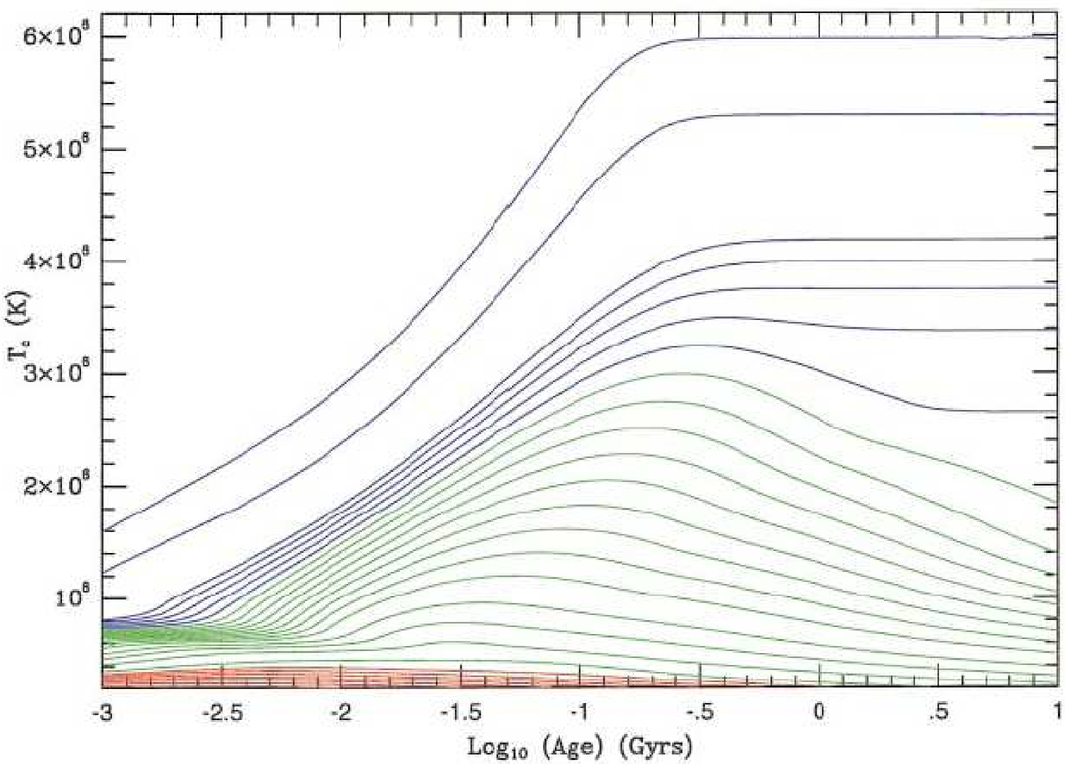

FIGURE 2.4. The central temperature (T_c) in K vs the logarithm (base ten) of the age (in Gyr) for the same mass set of substellar objects presented in Figure 2.3, the red lines are for models with masses equal to or below $13\mathrm{M_J}$, the green lines are for objects above $13\mathrm{M_J}$ and below the edge of the main sequence, and the blue are for stars (red dwarfs) up to $0.2\mathrm{M_\odot}$. Figure and caption from Burrows et al. (2001).

$$T_{eff} \sim 1550K \left(\frac{10^9 yr}{t}\right)^{0.32} \left(\frac{M}{0.05\mathrm{M_\odot}}\right)^{0.83} \left(\frac{\kappa_R}{10^{-2}cm^2g^{-1}}\right)^{0.088}. \tag{2.16}$$

2.4.3 The evolution of radius

Burrows et al. (2001) also provide calculations to show how the radius of the same objects evolves over time. This can be seen in Figure 2.6. Here, there is again a decrease with age before a steady radius is reached. For the older substellar objects the radius

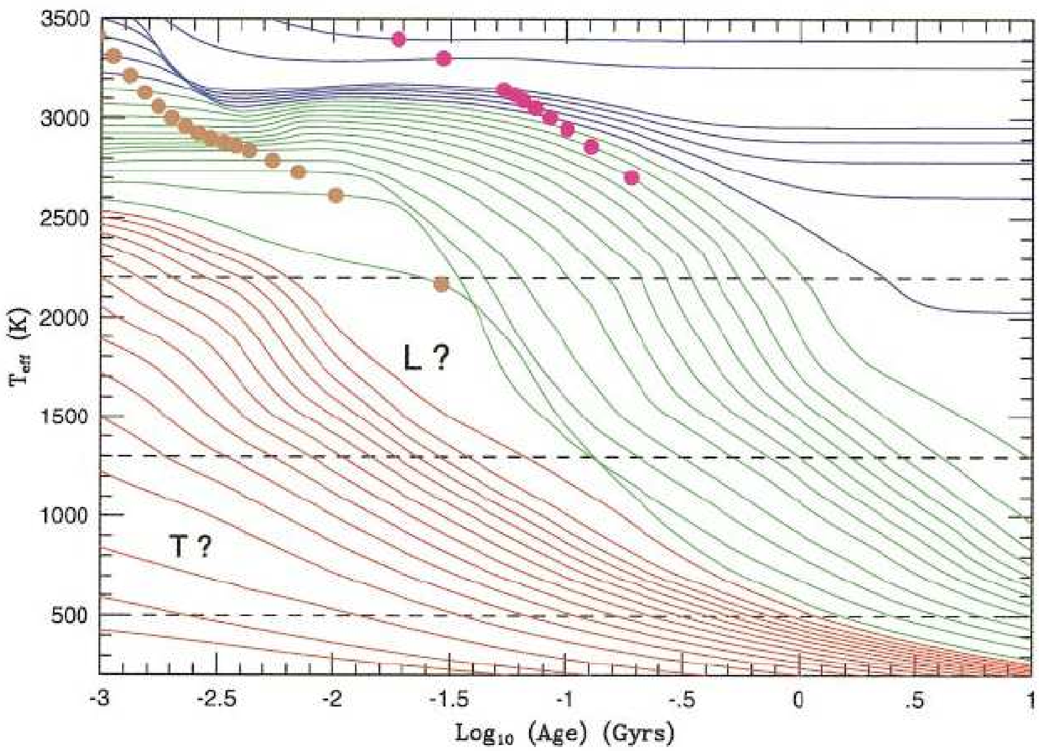

FIGURE 2.5. This figure depicts the evolution of T_{eff} (in K) with age for the mass set used in Figure 2.3 and with the same colour scheme. Superposed are dots which mark the ages for a given mass at which 50% of the deuterium (gold) and lithium (magenta) are burned. Though the L and T dwarf regions are as yet poorly determined and are no doubt functions not only of T_{eff}, but of gravity and composition, approximate realms for the L and T dwarfs are indicated with the dashed horizontal lines. The spectral type M borders spectral type L on the high-temperature side. Note that the edge of the hydrogen-burning main sequence is an L dwarf and that almost all brown dwarfs evolve from M to L to T spectral types. Figure and caption from Burrows et al. (2001).

is independent of the object's mass[4] (to within 30%), and is brought about by competition in the equation of state between the Coloumb and electron degeneracy pressures. Chabrier & Baraffe (2000) show that this mass-radius relation is given by R$\propto$M$^{-1/8}$ when there is partial degeneracy and a non-negligible contribution from the Coulomb pressure. For full degeneracy as in white dwarfs, the relation is R$\propto$M$^{-1/3}$. Again Burrows et al. (2001) provide an approximation for the radius of old substellar objects as shown by equation 2.17,

$$R \sim 6.7 \times 10^4 km \left(\frac{10^5}{g}\right)^{0.18} \left(\frac{T_{eff}}{1000K}\right)^{0.11,.} \quad (2.17)$$

where, g is the surface gravity.

2.5 Discovery of Brown dwarfs

Twenty two years after the initial work of Kumar (1963), the first dedicated BD conference took place (Kafatos et al. 1986). Despite this landmark occasion no BD discoveries were reported, though this can be attributed to the lack of sensitivity afforded to the instruments at the time. Probst (1983) for instance had used a single pixel IR photometer to look for companions within 15 arc-seconds of nearby white dwarfs as indicated by an IR excess[5]. This was followed up by McCarthy et al. (1985) who improved upon the

[4]The least massive have the larger radii.

[5]Companions to white dwarfs are easier to find than companions to main sequence stars due to the contrast ratio being vastly reduced

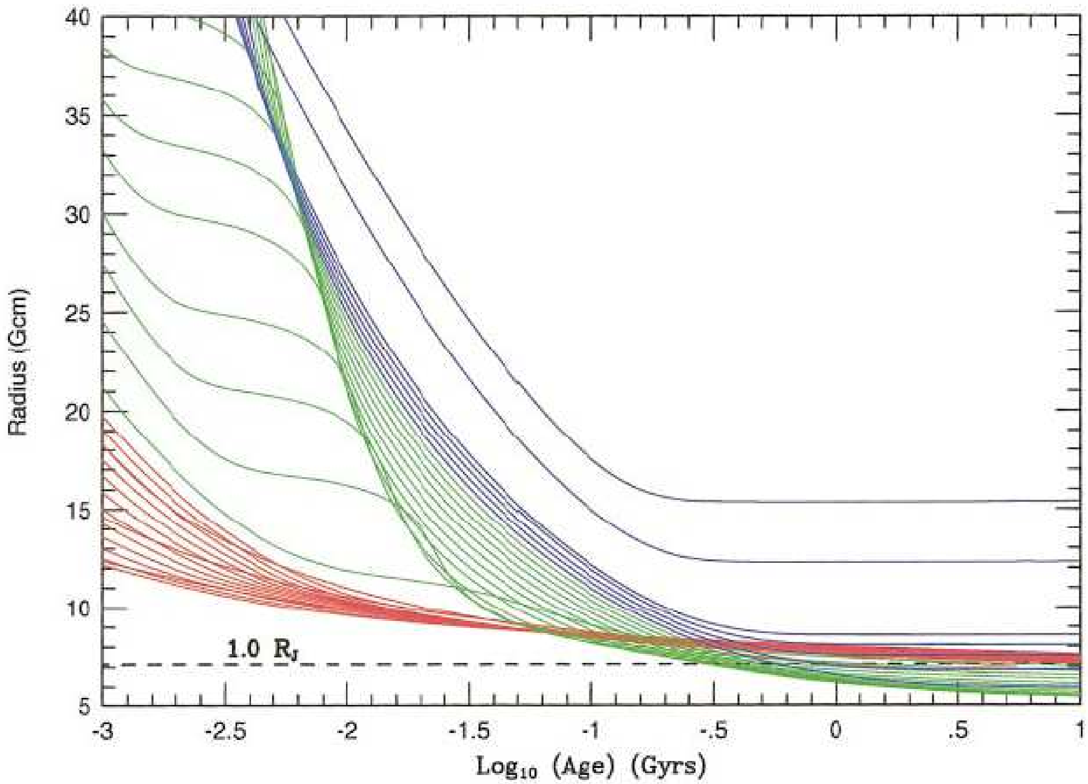

FIGURE 2.6. The radius (in units of 10^9cm) of substellar-mass objects with the masses given in Figure 2.3 vs the $\log_{10}$ of the age (in Gyr). The same colour scheme that was used in Figure 2.3 is used here. Red is for the low-mass substellar objects, green is for the intermediate mass substellar objects, and blue is for the stars. Also shown is the radius of Jupiter. Note that the radii are not monotonic with mass and that they cluster near the radius of Jupiter at late times, despite the wide range of masses from $0.3M_J$ to $0.2M_\odot$ represented. Figure and caption from Burrows et al. (2001).

method of Probst (1983) by using the same instrument but in conjunction with speckle interferometry. By reducing the distorting effects of the atmosphere via taking rapid exposures, the sensitivity of the survey could be increased allowing for fainter and closer companions to be found. Their detection of a faint red dwarf was not however reproduced by subsequent observations and was heavily discussed at the 1986 meeting. Following these first surveys Forrest et al. (1988) replaced the single pixel detector with a 32×32 Indium antimonide (InSb) detector and whilst this produced several faint object discoveries none were again regarded as being BDs. Whilst these ground based surveys at NASA's Infrared Telescope Facility were occurring, the Infrared Astronomical Satellite (IRAS) was launched. After completing its far infrared all sky survey, the results again concluded zero BD detections (Beichman 1987). A very red cool companion to the white dwarf GD 165 was however found in 1988 by Becklin & Zuckerman (1988), with a distance of 32 parsecs and a temperature of 1800 K it remained one of the best BD candidates for 7 years. After a spectroscopic analysis by Kirkpatrick et al. (1999a) showed a depletion of lithium GD 165B could no longer be considered to be a BD. It was however also lacking in titanium oxide, one of the defining features of M-dwarf spectra (Kirkpatrick et al. 1993), a fact that eventually lead to the subsequent creation of the L-dwarf spectral type by Kirkpatrick et al. (1999b). By the time of the 1994 European Southern Observatory meeting "The Bottom of the Main Sequence" held in Garching, Germany (Tinney 1995), not a single confirmed BD detection had been reported. This came without too much surprise as the mass function results at the time indicated that they should indeed be rare. The fact of the matter was that the surveys were simply still not sensitive enough, a point made by D'Antona (1995).

2.5.1 GL 229B

It was at the Ninth Cambridge Cool Stars Workshop held in Florence in 1995 that the discovery of a faint companion to an M-dwarf (GL 229) was announced following a coronographic survey of nearby low mass stars carried out at the Palomar 60-inch telescope. The companion had first been detected in 1994 but any announcement of it was delayed whilst proper motion data was gathered (Nakajima et al. 1995) to ensure it was associated with the primary, as well as spectral data (Oppenheimer et al. 1995), to confirm its remarkably low temperature ($T_{eff}\leq$1200K), well below that required for hydrogen burning to occur. The companion GL 229B (see Figure 2.7) was the first incontrovertible BD found. Its spectrum also showed a remarkable similarity to that of the planet Jupiter, with striking features due to the presence of water and methane in the K and H bands (see Figure 2.8). In contrast to the L-dwarfs spectral type proposed by Kirkpatrick et al. (1999b) the photometric results of Matthews et al. (1996) for GL 229B could only be reproduced when the model spectra calculated by Tsuji et al. (1996) used a prescription containing zero contributions from silicate dust. This was confirmed by results from Oppenheimer et al. (1998) with a high signal-to-noise near-infrared (NIR) spectrum along with an optical spectrum that was almost featureless. GL 229B like GD 165B necessitated the introduction of an additional spectral class, the T-dwarfs, following on from the L-dwarfs defined by Kirkpatrick et al. (1999b). It should be noted for completion's sake that the BD of Tiede 1 located in the Pleiades was also announced at the Florence workshop. As an M-dwarf though, its discovery although unprecedented, did not create as much of an impact as that of GL 229B.

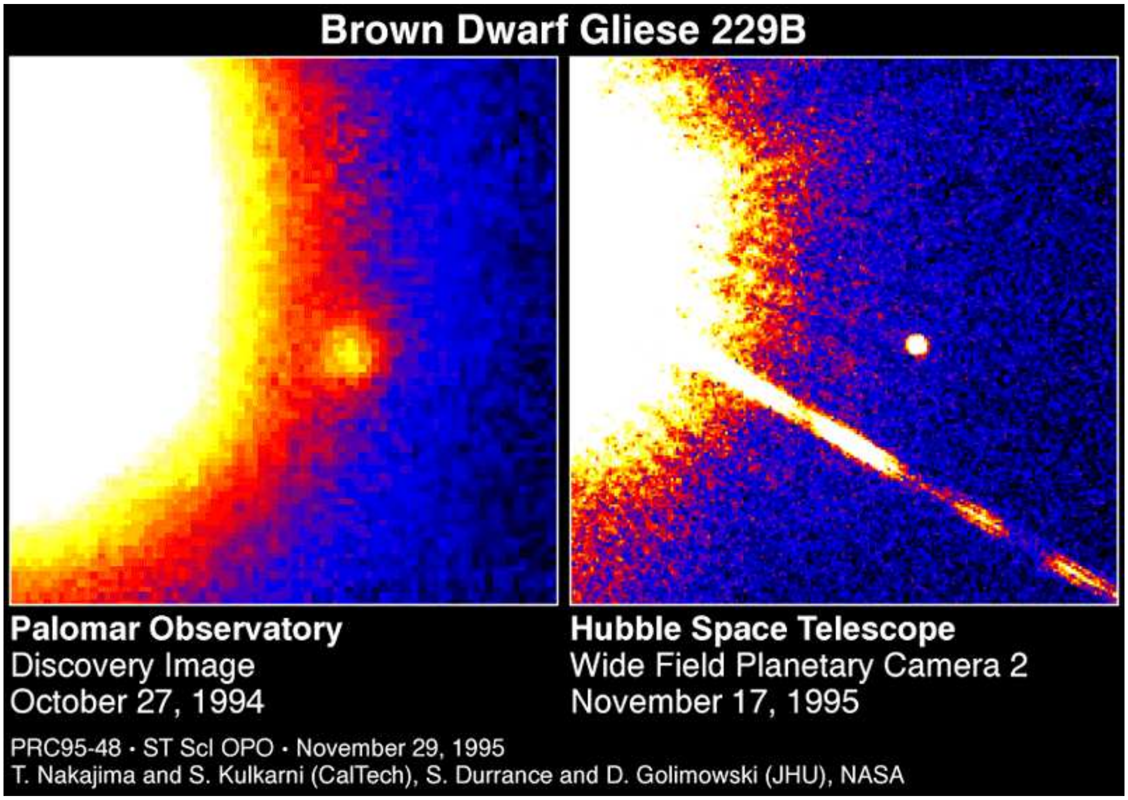

FIGURE 2.7. [left] - The BD (centre) was first observed in far red light October 27, 1994 using the adaptive optics device and a 60-inch reflecting telescope on Palomar Mountain in California. Another year was required to confirm that the object was actually gravitationally bound to the companion star. GL 229B is at least four billion miles from its companion star, roughly the separation between the planet Pluto and our Sun. Even though a chronograph on the detector masked most of the light from the star, which is off the left edge of the image, it is so bright relative to the brown dwarf the glare floods the detector.[right] - This image of the GL 229B (centre) was taken with Hubble Space Telescope's Wide Field Planetary Camera-2, infrared light, on November 17, 1995. The Hubble observations will be used to accurately measure the BD's distance from Earth, and yield preliminary data on its orbital period, which may eventually offer clues to the dwarf's origin. Though the star Gliese 229 is off the edge of the image, it is so bright it floods Hubble detector. The diagonal line is a diffraction spike produced by the telescope's optical system. Credit: S. Kulkarni (Caltech), D.Golimowski (JHU) and NASA.

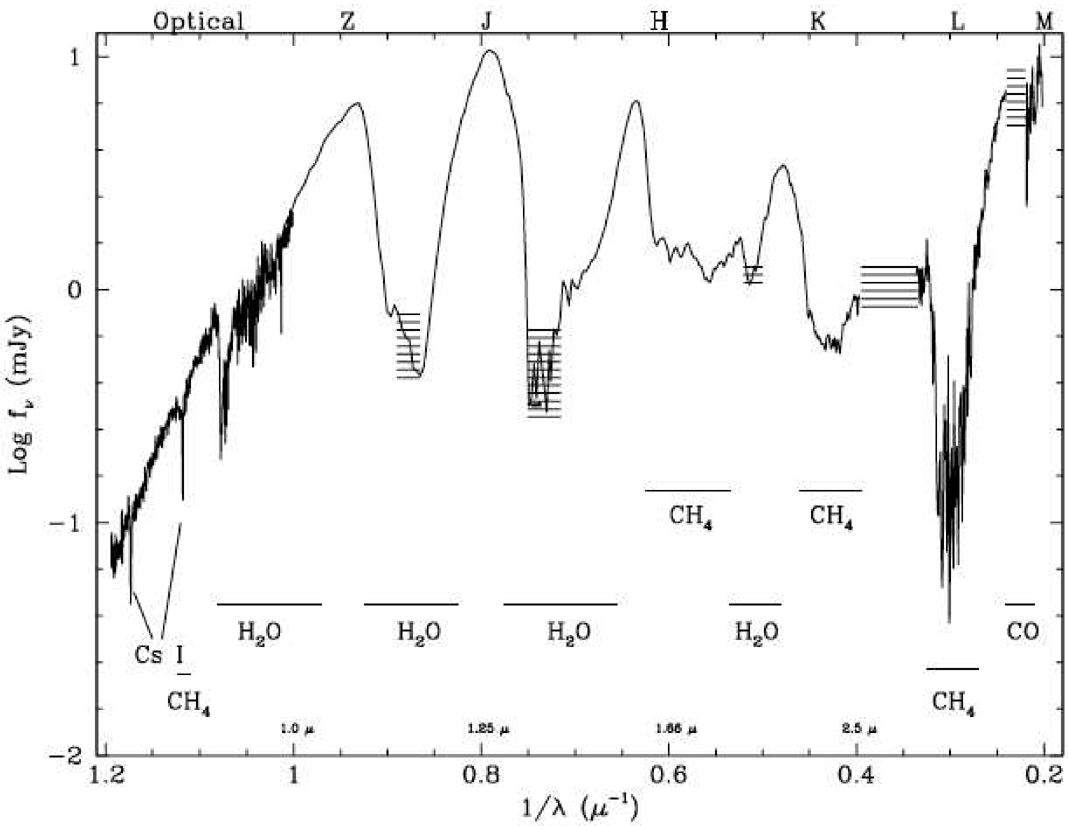

FIGURE 2.8. Spectrum of GL 229B from 0.84 to 5μm. Major opacity sources are indicated. Regions with horizontal bars correspond to wavelengths where the atmosphere is too opaque to permit collection of useful data from the ground. Along the top of the plot are indicated the filters corresponding to the various wavelength bands. Figure and caption from Oppenheimer et al. (1998)

2.6 Lithium

As the difference between stars and BDs lies in the nuclear behaviour of their cores, testing for the behaviour can allow for discrimination between these two populations of objects. Whilst the fusion of hydrogen into helium does not occur, objects greater than $13\mathrm{M_J}$ will be able to burn deuterium and those greater than about $60\mathrm{M_J}$ capable of burning lithium (Li). The temperature required for this is about 2.4×10^6K and is achieved via the following reaction,

$$Li^6 + H^1 \rightarrow He^3 + He^4, \tag{2.18}$$

$$Li^7 + H^1 \rightarrow 2He^4. \tag{2.19}$$

These reactions lie behind a technique known as the "lithium test" (Rebolo et al. 1992). For stars with ages $\geq$100 Myr the Li is quickly and efficiently depleted from the stellar atmosphere. BDs (of mass $<60\mathrm{M_J}$) on the other hand are fully convective and aren't able to reach the required central temperatures needed to ignite the lithium burning process. Therefore if Li is observed in the spectra then the object can be considered as a BD candidate. Pavlenko et al. (1995) found that for temperatures between 1500-3000K the Li line strength should be strong, a fact confirmed by observations[6]. The strength of the Li resonance line (Li I doublet at 6708Å) is found not to show signs of decreasing until over 90$\%$ of the Li has been depleted. The timescale for depletion of the Li can

[6]Along with Stuik et al. (1997) they consider the effects of non-local thermodynamic equilibrium and chromosphere activity to be of "secondary" importance.

also allow for estimation of the object's age as well as determining its sub-stellar nature. The process of "lithium dating" is not however without its caveats. It is possible for a false positive to be given if observing a very young star that has not had sufficient time to deplete its Li ($<$10 Myr). Likewise a false negative can be produced for high mass old BDs as the highest mass BDs will over a sufficiently long period of time begin to show signs of Li depletion. It was these caveats that lead Basri et al. (1996) to conclude that the Pleiades cluster was older than had been previously thought, see Figure 2.9, with Stauffer et al. (1998) confirming the assumption with a measured age of 125Myrs. Basri (1998) extended the "lithium dating" technique beyond that for calculating the age of clusters in an attempt to also age field objects. Figure 2.10 shows that if Li is observed an upper boundary is given to the mass and age of the object, whilst a non-detection would provide a lower boundary. For an object to be automatically classified as substellar it must lie below the temperature for which the Li has just been depleted (marked by the horizontal line) and contain Li in its observed spectra. Jeffries (2000) and Basri (2000) provide reviews on the principles, usage and results of the "lithium test" and "lithium dating".

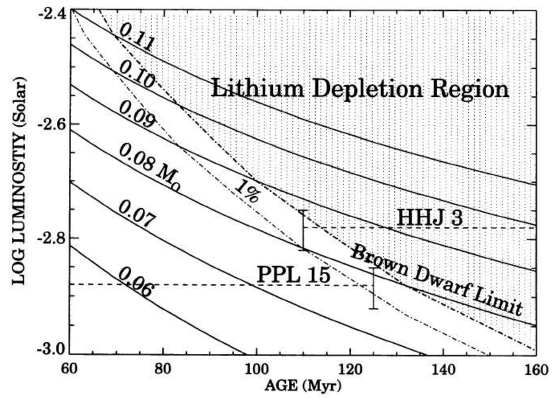

FIGURE 2.9. The diagram used to calculate the age of the Pleiades cluster based upon the partial detection of lithium in object HHJ3 and the absence of Li in object PPL15. The luminosity for objects 0.11-0.06$\mathrm{M}_\odot$ as a function of age from the models of Nelson et al. (1993) are shown as the solid curves. Figure from Basri et al. (1996).

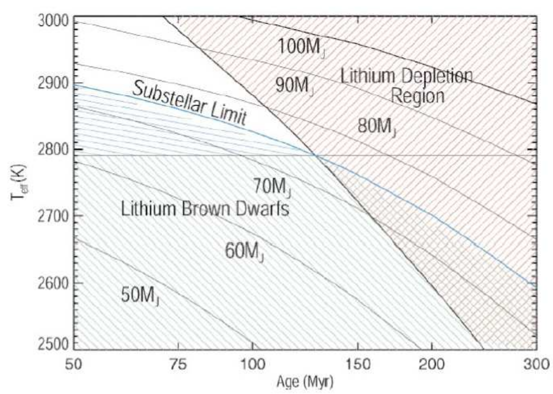

FIGURE 2.10. The lithium test. The effective temperature vs. age of low mass objects, from models by Baraffe and Chabrier. The solid lines labelled with mass are cooling tracks in the relevant age range. The substellar limit at 75 Jupiter's is noted in blue. The region beyond which lithium depletion has proceeded to 99% (where it could be easily noted spectroscopically) is marked with red hatching. The horizontal line marks the temperature at which the substellar boundary crosses the depletion region. Below this line, in the green hatched region, an observation of Li in an object guarantees that it is substellar. In the red/green region the lithium test for substellarity will give a false negative, while in the blue hatched region it does not distinguish between stars and BDs (unless the age is known). Figure and caption from Basri (2000).

2.7 Spectral Types

After the discoveries of GD 165B (Becklin & Zuckerman 1988) and GL 229B (Nakajima et al. 1995) along with others such as Teide 1 (Rebolo et al. 1996), Kelu 1 (Ruiz et al. 1997) and a whole host of objects from the DENIS and Two Micron All Sky Survey (2MASS; Skrutskie et al. 2006) surveys it became apparent that additions to the Harvard MK classification system of Morgan et al. (1943)[7] were needed. The first of the additions proposed was the "L" spectral type for objects similar to GD 165B, followed by the "T" spectral type[8] for those with similarities to GL 229B (Kirkpatrick et al. 1999b). If there is to be a subsequent need for a new spectral class with so few letters remaining, the letter "Y" has been chosen.

2.7.1 M-dwarfs

The M-dwarf spectral sequence was extended beyond its original ending of M2 (Morgan et al. 1943) first by Johnson & Morgan (1953) with later additions made by Boeshaar (1976) before a well formed sequence was established by Kirkpatrick et al. (1991). The M-dwarfs are characterised by strong titanium oxide bands (TiO), atomic potassium (K) I and sodium (Na) I doublet lines in the optical with strong water (H_2O), carbon monoxide (CO), iron hydride (FeH), K I and Na I features appearing in the IR. Hawley et al. (1996)

[7] prior to the additions the classification system was constructed with letters OBAFGKM determining a "spectral type" where O stars had the hottest temperatures and M stars the coolest. In addition to the "spectral type" a luminosity class is often added, with the distinction 0, I, II ,III ,IV, V, VI and VII being used to separate main sequence stars (V) from the super-giants (I).

[8] Also sometimes called "methane" dwarfs.

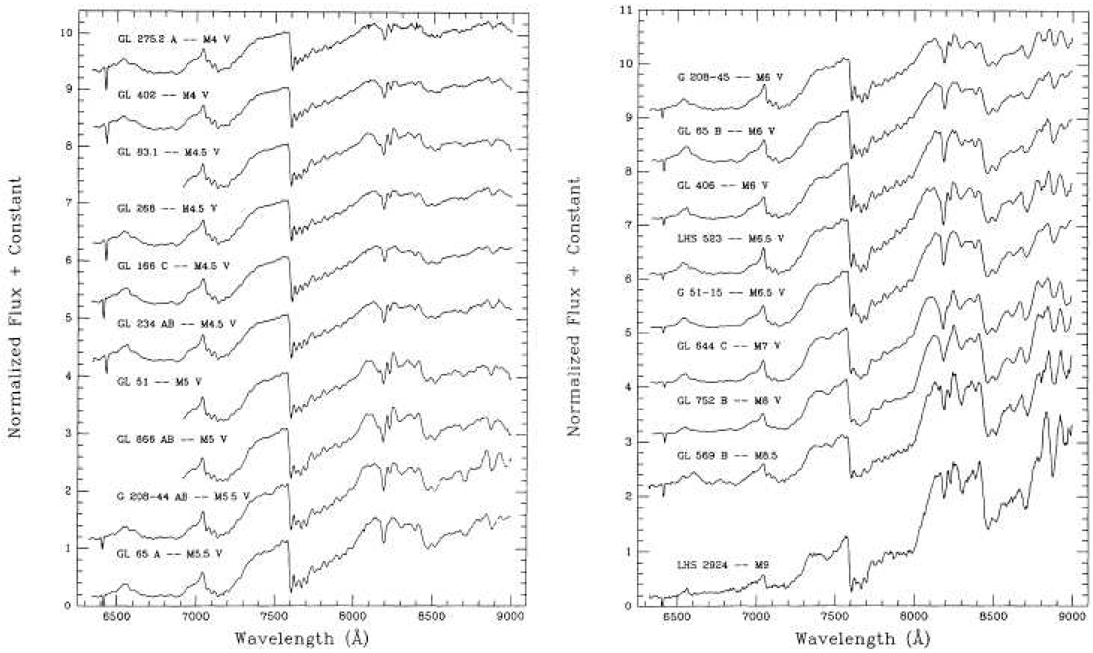

FIGURE 2.11. Example M dwarf spectra from M4 to M9 from Kirkpatrick et al. (1991). Each spectra have been normalised to 7500Å with a vertical offset added for clarity. Absorption features due to telluric O_2 and H_2O have not been removed.

also find an increase in Hα emission which peaks about midway through the group (M6-M7) before declining strongly for the later types. The Hα line strength is a key indicator of the chromospheric activity level of the M-dwarf. As per the discussion in Section 2.6 Li may also be present in an M-dwarf spectra providing it has a sufficiently low mass. Example M-dwarf spectra can be seen in Figure 2.11 .

2.7.2 L-dwarfs

The L-dwarfs are noted for their redder optical, optical-NIR and NIR colours when compared with M-dwarfs[9]. The optical spectra of the L-dwarfs show a mixture of atomic and

[9] $R - I \geq 2.2$, $I - J \geq 3.0$ and $J - K \geq 1.2$, $0.7 \leq J - H \leq 1.5$, $0.4 \leq H - K \leq 1.0$.

molecular bands such as the neutral alkali lines of Na I, K I, Rubidium (Rb) I, Caesium (Cs) I and occasionally Li I. The metal oxide bands of TiO and vandium oxide (VO) which are present in the earliest of the L-dwarfs (although vastly suppressed in strength compared to those seen in the M-dwarf spectra) give way to the metal hydrides of CrH, FeH and CaOH with water bands beginning to appear at the very latest L-types. This weakening of the TiO and the strengthening of the dust should be noted as occuring all within a relative sense. The classification of L-dwarf spectra is based upon an extension of the MK system by Kirkpatrick et al. (1999a) through the use of far optical spectra (ideally between 6500Å -10000Å , with the smaller 7000Å -9000Å range being adequate). The wavelengths at which some of these prominent features can be seen is given in Table 2.3 with Figure 2.13 showing a comparison of selected L-dwarf spectra. The Kirkpatrick et al. (1999b) scheme uses several spectral ratios to represent the strength of the aforementioned bands and lines. These ratios are then used in conjunction with "standard" object spectra such as those shown in Table 2.5 in order to specify the spectral subtype. A separate scheme proposed by Martín et al. (1999) uses the PC3 spectral index. The PC3 index is a measure of the pseudo continuum ratio, 8230-8270Å to 7540-7580Å . A second PC6 ratio was also used but found to be far less reliable. For objects suspected of being of type M2.5 to L1 the PC3 index can be used in equation 2.20 to find the spectral subtype, whilst for those thought to be between L1 and L6 equation 2.21 should be used.

$$SpT = -6.685 + 11.715 \times (PC3) - 2.024 \times (PC3)^2 , \tag{2.20}$$

$$SpT = 8.557 + 1.181 \times (PC3) - 0.047 \times (PC3)^2 . \tag{2.21}$$

A plot of the spectral type subclass versus the PC3 index can be seen in Figure 2.12. The NIR (0.95-2.3μm) can also be used to help classify objects as it contains strong H_2O, FeH and CO bands alongside the neutral atomic Na, Fe, K, Al and Ca lines. There is not yet however an agreed classification scheme that has been derived for the IR, as most schemes, such as the one proposed by Geballe et al. (2002)[10] rely on a mapping to the optical sequences above. As noted by Kirkpatrick (2005) it should not be assumed that objects classified with optical spectroscopy alone would follow the same ordering given measurements undertaken in the NIR. This is because the wavelengths involved probe different regions of the object's atmosphere. Studies by Reid et al. (2001), Testi et al. (2001) and McLean et al. (2003) have shown however that for the L-dwarfs the spectral sequence is usually robust.

2.7.3 L/T Transition Dwarfs

The L/T transition BDs comprise a mixture of the two spectral types, those of the latest L-type and earliest T-type. Lacking the strong molecular absorption that helps define the T-dwarfs ($0 \leq$ J-K ≤ 2.0) yet being red enough to escape detection in the relatively shallow optical/NIR surveys such as DENIS they were hard to find. Leggett et al. (2000) were the first to identify such objects during a search of the SDSS EDR data. The L/T transition BDs are an interesting grouping as they show at near constant effect temperature the

[10]The Geballe et al. (2002) scheme uses a series of H_2O and CH_4 bands to provide their classification indices.

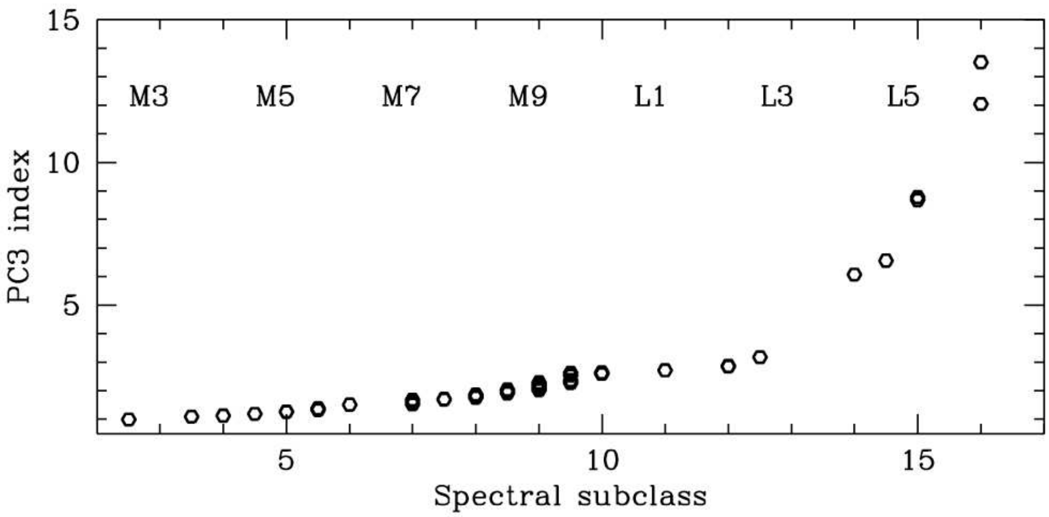

FIGURE 2.12. Plot of the PC3 indices for given spectral subclasses. X-axis values larger than 9.5 correspond to the L spectral type, i.e., x=10=L0. The uncertainties in the PC3 indices are smaller than the size of the points. Figure and caption from Martín et al. (1999).

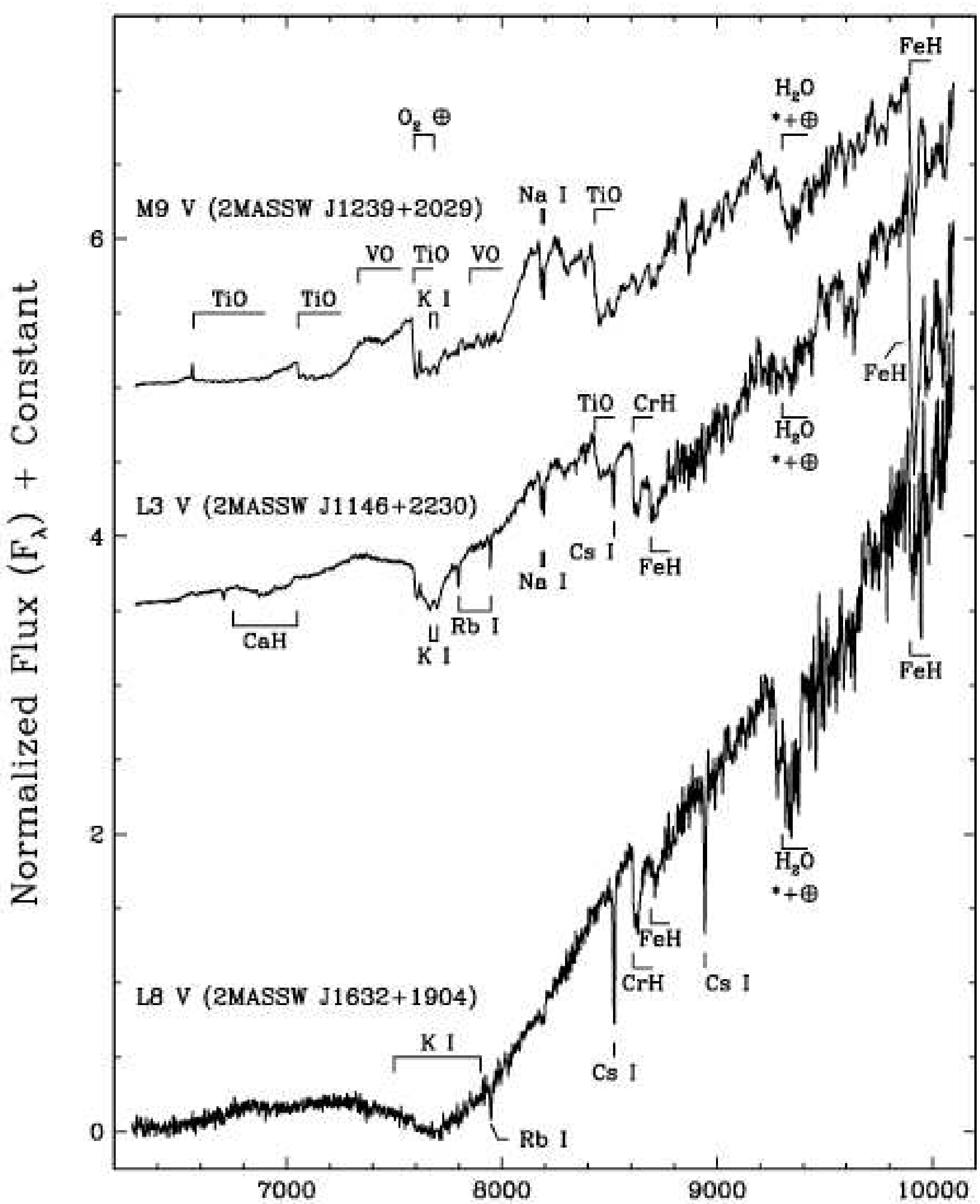

FIGURE 2.13. Enlarged spectra of a late-M, early-to mid-L, and late-L dwarf. Prominent features are marked. Note the absence of oxide absorption in the L dwarfs along with the dominance of alkali lines and hydride bands. Names for the 2MASS objects have been abbreviated. Figure and caption from Kirkpatrick et al. (1999b).

Table 2.3. Line list of features typically seen in the atmospheres of L-dwarfs. Table courtesy of Kirkpatrick et al. (1999a).

Atom/Molecule	Location (Å)	Transition
Hα^a	6563	$3d\ ^2D_{5/2}$-$2p\ ^2P_{3/2}$
Li I^a	6708	$2s\ ^2S_{1/2}$-$2p\ ^2P_{3/2,1/2}$
CaH^{a,b}	Broad trough ∼6750-7050	0-0 band of $A\ ^2\Pi$-$X\ ^2\Sigma$
TiO^a	7053 head, degraded to red	0-0 band of $A\ ^2\Phi$-$X\ ^3\Delta$
VO^a	Broad trough ∼7334-7534	1-0 band of $B\ ^4\Pi$-$X\ ^4\Sigma^-$
TiO^a	7589 head, degraded to red	0-1 band of $A\ ^3\Phi$-$X\ ^3\Delta$
K I^b	7665	$4s\ ^2S_{1/2}$-$4p\ ^2P_{3/2}$
K I	7699	$4s\ ^2S_{1/2}$-$4p\ ^2P_{1/2}$
Rb I	7800	$5s\ ^2S_{1/2}$-$5p\ ^2P_{3/2}$
VO^a	Broad trough ∼7851-7973	0-0 band of $B\ ^4\Pi$-$X\ ^4\Sigma^-$
Rb I	7948	$5s\ ^2S_{1/2}$-$5p\ ^2\mathrm{P}_{1/2}$
Na I	8183	$3p\ ^2P_{1/2}$-$3d\ ^2\mathrm{D}_{3/2}$
Na I	8195	$3p\ ^2P_{3/2}$-$3d\ ^2\mathrm{D}_{5/2,3/2}$
TiO^a	8206 head, degraded to red	0-2 band of $A\ ^3\Phi$-$X\ ^3\Delta$
TiO^a	8432 head, degraded to red	0-0 band of $E\ ^3\Pi$-$X\ ^3\Delta$
Cs I	8521	$6s\ ^2S_{1/2}$-$6p\ ^2P_{3/2}$
CrH	8611 head, degraded to red	0-0 band of $A\ ^6\Sigma^+$-$X\ ^6\Sigma^+$
FeH	8692 head, degraded to red	1-0 band of $A\ ^4\Delta$-$X\ ^4\Delta$
Cs I	8943	$6s\ ^2S_{1/2}$-$6p\ ^2P_{1/2}$
H_2O^b	Broad trough around ∼9300	ν_1+ν_3 = 3
VO^{a,b}	Broad trough ∼9540-9630	1-0 band of $A\ ^4\Pi$-$X\ ^4\Sigma^-$
FeH	9896 head, degraded to red	0-0 band of $A\ ^4\Delta$-$X\ ^4\Delta$
CrH	9969 head, degraded to red	0-1 band of $A\ ^6\Sigma^+$-$X\ ^6\Sigma^+$

^{a}Feature not seen in all L dwarfs. ^{b}Contaminated by telluric absorption bands.

quick transition from the dusty L-dwarf atmospheres to the dust free/depleted T-dwarfs. Ideas suggesting cloud fragmentation and weather-like behaviour have been proposed but not clearly identified (Burgasser et al. 2002b; Goldman et al. 2008). Another interesting result of the search for L/T transition dwarfs has however revealed that they have a higher occurance rate of binarity than compared to other BD-BD systems (Burgasser et al. 2006; Liu et al. 2006). The binary fraction is a parameter with which formation scenarios can be constrained whilst the systems themselves can provide useful test-beds of evolutionary models.

2.7.4 T-dwarfs

The T-dwarfs or "methane" dwarfs are cooler than the L-dwarfs that precede them. With temperatures lower than 1300K and extending down to ∼600-500K for objects such as SDSS1416+13B (Burningham et al. 2010a), Wolf 940B (Burningham et al. 2009; Leggett et al. 2010) and UGPS 0722-05 (Lucas et al. 2010), the latter being the coolest currently known BD[11] the dust layers of L-dwarfs condense to lay below the observable photosphere. Many of the T-dwarf discoveries have come from the Sloan Digital Sky Survey (SDSS; York et al. 2000), 2MASS and UKIDSS surveys, for example Chiu et al. (2006), Burgasser et al. (2004), Pinfield et al. (2008) and Burningham et al. (2010b). The T-dwarfs have extremely red optical/optical-NIR colours that move them in some cases beyond the detection limits of the optical R and I filters. Due to their intrinsic faintness in the optical there doesn't exist an optical classification scheme as there does for the

[11] It has been suggested that UGPS 0722-05 could tentatively be considered as a Y0 object given its current T10 typing by Lucas et al. (2010).

L-dwarfs. Instead the T-dwarf spectral sequence is derived from NIR spectral indices and is then tagged onto the optical MK sequence (Burgasser et al. 2002a; Geballe et al. 2002). The red-ward progression of colour is not however mirrored in the IR, here the colours of the T-dwarfs reverse and begin increasing blue-ward for later types. This is brought about due to an increase in CH_4 absorption in the H and K filters with water vapour bands also suppressing the K band flux. Strong K I doublets are also present in IR with CO appearing in earlier types and disappearing for the later ones. Table 2.4 shows the features that are expected to be visible in the T-dwarf spectra, whilst Table 2.5 shows an updated version of the table presented by Kirkpatrick (2005) listing the objects that have been chosen to be the so called anchor points in the spectral sequence for both the L and the T-dwarfs. The updates to this come from the combined effort of revising the Burgasser et al. (2002a) and Geballe et al. (2002) schemes by Burgasser et al. (2006), the latter work now providing the means by which all further T-dwarfs are classified. Figure 2.14 shows a T5 dwarf spectrum from Burgasser et al. (2006) with some of the spectral regions marked, whilst Figure 2.15 shows the whole IR T dwarf spectral sequence, again from Burgasser et al. (2006).

2.8 Atmospheric Models

The structure models of Burrows et al. (2001) and others deal in intrinsic properties of the BDs, mass, luminosity and effective temperature. These are not directly observable quantities. The observables are the magnitudes, colours and spectra from the BD atmospheres. Therefore we need and use atmospheric models to try and derive these intinsic

Table 2.4. 0.9-2.5μm features in T dwarf Spectra. Table and caption from Burgasser (2001).

Atom/Molecule	Location (μm)	Transition	Ref.
K I	0.7665^b	$4s\ ^2S_{1/2}$-$4p\ ^2P_{3/2,1/2}$	1,2,3
K I	0.7699^b	$4s\ ^2S_{1/2}$-$4p\ ^2P_{3/2,1/2}$	1,2,3
H_2O	0.925-0.940	$3(\nu_1,\nu_3)$	4
H_2O	0.945-0.980	$2(\nu_1,\nu_3) + 2\nu_2$	4
CH_4^{c}	0.960-1.02	$3(\nu_1,\nu_3) + 1(\nu_2,\nu_4)$	5
FeH	0.9896 bandhead	0-0 band of$A\ ^4\Delta$-$X\ \Delta$	6
H_2O	1.07-1.11	$3(\nu_1,\nu_3)$-ν_2	4
CH_4	1.10-1.24	$3(\nu_1,\nu_3)$	7,8
H_2O	1.11-1.16	$2(\nu_1,\nu_3)+\nu_2$	4
H_2O	1.16-1.23	$1(\nu_1,\nu_3)+3\nu_2$	4
K I	1.1690	$4p\ ^2P_0$-$3d\ ^2D$	1
K I	1.1773	$4p\ ^2P_0$-$3d\ ^2D$	1
H_2^{c}	centered at 1.20	2-0 Quadrupole (CIA)	9
K I	1.2432	$4p\ ^2P_0$-$5s\ ^2S$	1
K I	1.2522	$4p\ ^2P_0$-$5s\ ^2S$	1
CH_4	1.30-1.50	$2(\nu_1,\nu_3)+1(\nu_2,\nu_4)$	7,8
H_2O	1.33-1.43	$2(\nu_1,\nu_3)$	4
H_2O	1.43-1.52	$1(\nu_1,\nu_3)+2\nu_2$	4
CH_4	1.60-1.80	$2(\nu_1,\nu_3)$	7,8
H_2O	1.71-1.80	$2(\nu_1,\nu_3)$-ν_2	4
H_2O	1.80-2.08	$1(\nu_1,\nu_3)+\nu_2$	4
CH_4	2.20-2.60	$1(\nu_1,\nu_3)+1(\nu_2,\nu_4)$	7,8
CO	2.294 bandhead	2-0 $X^1\Sigma^+$-$X^1\Sigma^+$	10
CO^c	2.323 bandhead	3-1 $X^1\Sigma^+$-$X^1\Sigma^+$	10
H_2	centered at 2.35	1-0 Quadrupole (CIA)	9

[a]Nomenclature for H_2O and CH_4 bands are X(ν_i,ν_j) where bands are formed from the set of X ν_i and ν_j transitions. For example, $2(\nu_1,\nu_2)$ covers the transitions $\delta\nu=2\nu_1$, $\nu_1+\nu_3$, and $2\nu_3$. [b]Pressure-broadened out to 1μm Burrows et al. (2000). [c]Not yet detected but suspected to exist. REFS - (1) Wiese et al. (1966); (2) Tsuji et al. (1999); (3) Burrows et al. (2000); (4) Auman (1967); (5) Dick & Fink (1977); (6) Phillips et al. (1987); (7) Danielson (1966); (8) Fink & Larson (1979); (9) Lenzuni et al. (1991); (10) Krotov et al. (1980).

Table 2.5. Original table from Kirkpatrick (2005) showing anchors for the optical classification of L-dwarfs taken from Kirkpatrick et al. (1999b) with T-dwarf anchors from Burgasser et al. (2003) for the optical and IR. An update has been made to the T-dwarf anchors based upon the revised NIR spectral type sequence given by Burgasser et al. (2006).

Spectral Type	Optical Anchor	Near-IR Anchor
L0	2MASP J0345432 + 254023	...
L1	2MASSW J1439284 + 192915	...
L2	Kelu-1 (at J13054019 - 2541059)	...
L3	2MASSW J1146345 + 223053	...
L4	2MASSW J1155009 + 230706	...
L5	DENIS-P J1228.2 - 1547	...
L6	2MASSs J0850359 + 105716	...
L7	DENIS-P J0205.4 - 1159	...
L8	2MASSW J1632291 + 190441	...
T0	...	SDSS J120747.17 + 024424.8
T1	...	SDSS J083717.21-000018.0
T2	SDSS J125453.90 - 012247.4	SDSS J125453.90 - 012247.4
T3	...	2MASS J12095613 - 1004008
T4	...	2MASSI J22541892 + 3123498
T5	...	2MASS J15031961 + 2525196
T6	SDSS J162414.37 + 002915.6	SDSS J162414.37 + 002915.6
T7	...	2MASS J07271824 + 1710012
T8	2MASS J04151954 - 093506	2MASS J04151954 - 093506

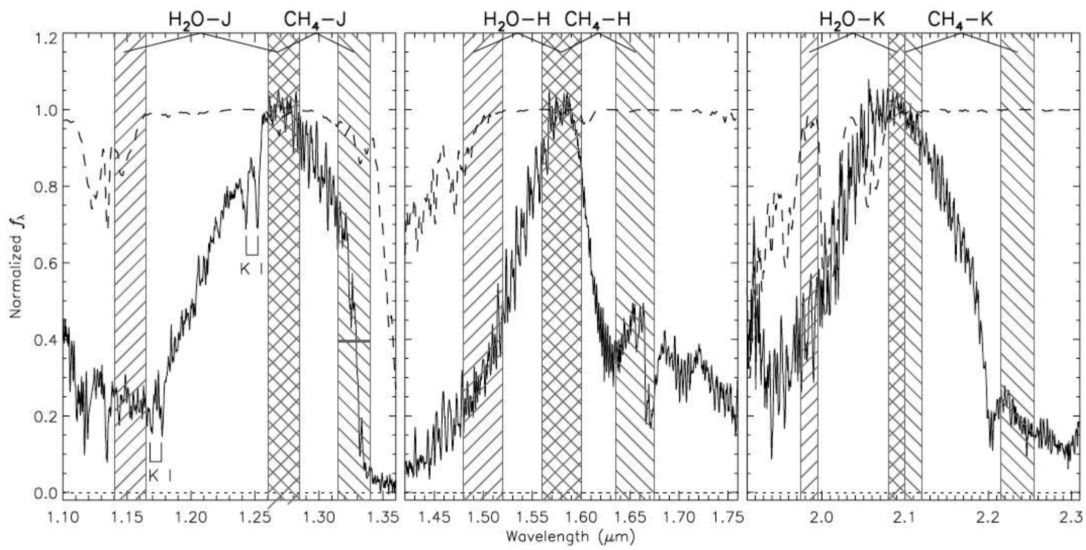

FIGURE 2.14. Spectral regions sampled by the six H_2O and CH_4 indices defined in Table 3 of Burgasser et al. (2006). The spectrum is of the T5 standard 2MASS 1503+2525 Burgasser et al. (2004). The dashed line present in the plot is a telluric transmission spectrum typical for Mauna Kea.

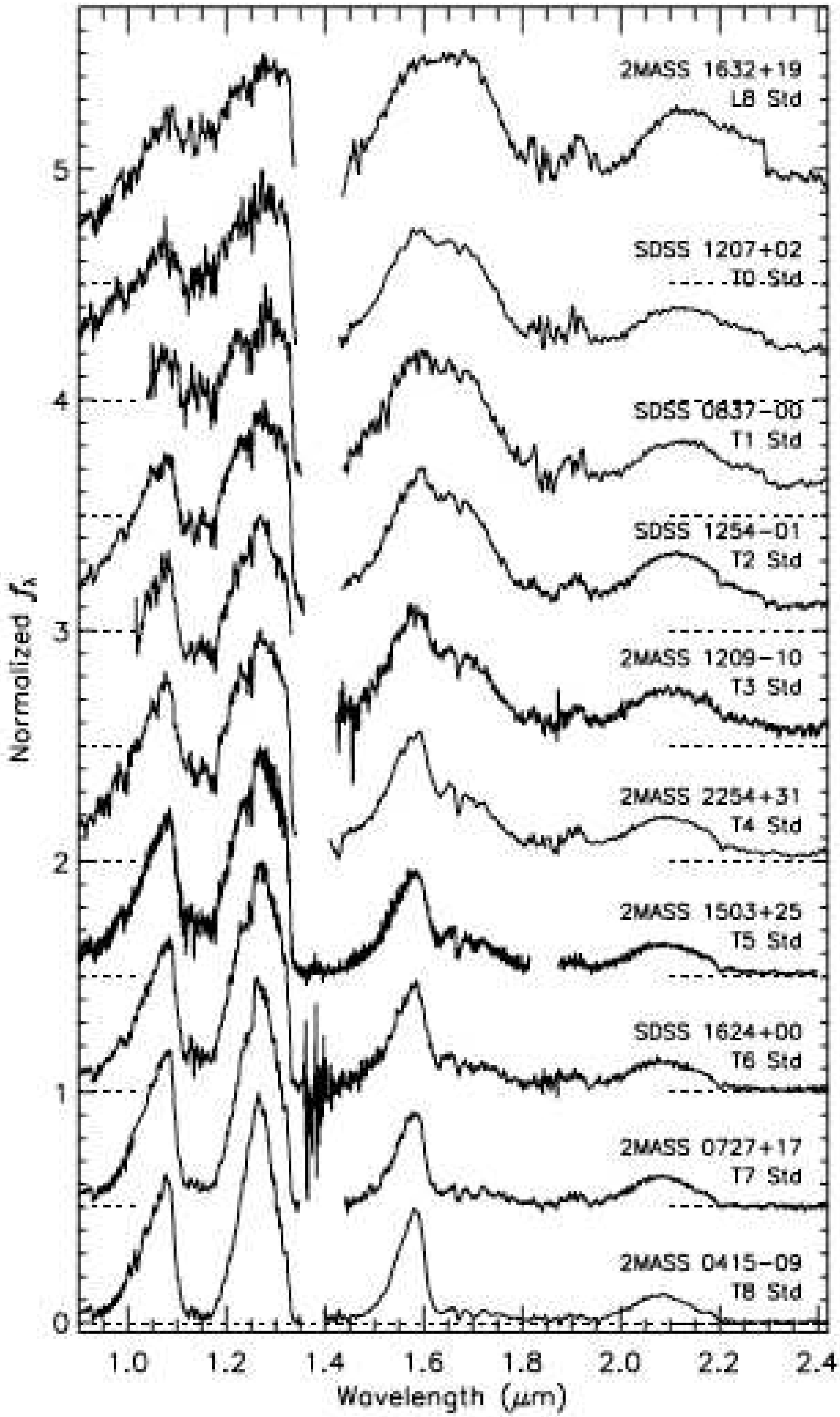

FIGURE 2.15. Shown above is the NIR spectral sequence given by the T-dwarf anchor points of Burgasser et al. (2006). An optically defined L8 standard from Kirkpatrick et al. (1999b) is shown for comparison.

properties. Some of the more commonly used models are described below.

2.8.1 Lyon/Phoenix Models

The models from the Lyon group aim to reproduce the properties of low-mass stars and BDs in three distinct regimes. First come the NextGen models (Baraffe et al. 1998), these are generally used to describe objects that are relatively warm ($T_{eff} \geq 1700$K) and do not take into account any forms of dust, dealing only with the gas phase. Sources of opacity are considered and as atomic and molecular line lists have been improved upon so to have the models. The current version of the NextGen models being used are called BT-NextGen. As the objects cool they begin to form dust clouds in their atmospheres, prompting the reddening that one sees in the optical and NIR to occur. Objects with these "dusty" atmospheres are modelled this time by the DUSTY models (Chabrier et al. 2000; Baraffe et al. 2002). For the even cooler objects with dust free atmospheres the COND models of Allard et al. (2001) and Baraffe et al. (2003) are more appropriate. The models use the state-of-the-art stellar atmosphere and non-local-thermodynamic-equilibrium radiative transfer code PHOENIX[12]. Again with updated opacity lists the current models are designated as BT-DUSTY and BT-COND. The DUSTY models describe reasonably well the observed NIR colours and spectra of the early L-dwarfs but the optical colours aren't reproduced with the same accuracy. The COND models with their dust-free representation of an atmosphere (modelling T-dwarfs) again reproduce the observed results rather well, yet they fail in reproducing the transition between the L and T-dwarfs and

[12]PHOENIX is now currently on version 15 as of 30th November, 2009.

hence the join between the DUSTY and COND models still remains their biggest problem. Work by Helling et al. (2008) also used the PHOENIX code, however instead of the DUSTY and COND prescriptions for treating dust within the atmosphere the authors used their own prescription called DRIFT. DRIFT deals with seed formation, growth, evaporation, gravitational settling and element conservation in order to better describe the actual cloud formation processes that are occurring within these atmospheres.

2.8.2 AMES Models

The theoretical atmospheric models of Marley et al. (2002) and Saumon et al. (2003) used a self-consistent treatment of cloud formation, a first for the time. They noted that the optical i-z' colour was extremely sensitive to the chemical equilibrium assumptions made and showed that the i-z' vs J-K two colour diagram was also useful due to different chemical processes being responsible for individual colours. In order to model the observed colours of solar metallicity dwarfs the authors used a radiative-convective equilibrium atmosphere model from Marley et al. (1996) with newer alkali opacities and a precipitating cloud model from Ackerman & Marley (2001). The cloud model assumes that the clouds are horizontally homogeneous and in a steady state by which the gas being transported upwards by turbulent mixing is balanced by the downward transport of condensate by sedimentation. Complexities surrounding the efficiency of the sedimentation process are consolidated into an adjustable parameter, F_{rain}, larger values of which mean greater precipitation and thus thinner clouds[13]. The condensates the authors con-

[13]The ammonia cloud decks of Jupiter are best modelled by $F_{rain} = 3$.

sider are Fe, $MgSiO_3$ and H_2O deciding that other species such as Al_2O_3 are relatively insignificant sources of opacity. By using a self-consistent approach to the cloud formation and sedimentation Marley et al. (2002) find that the J-K colours they achieve are far less red than those given by models with no sedimentation, such as the DUSTY models. In fact the peak of the J-K colour is too blue and the transition blue-ward for the T-dwarfs occurs at a much slower rate than is observed.

2.8.3 Tsuji Models

Tsuji et al. (1996) attempted to model cool dwarf spectra by assuming that dust forms everywhere providing that the thermodynamical condition of condensation was met. These models were successful in reproducing M and early L-dwarf spectra but failed for the cooler later L and T dwarfs. To rectify this the work of Tsuji (2001) created the unified cloudy model. For the warmer dwarfs where T_{eff} is greater than the critical temperature of condensation (T_{cr}) the dust remains in the photosphere whilst if T_{eff} is less than T_{cr} then the dust grains precipitate out leaving a dust free atmosphere more representative of the T dwarfs. The authors noted that these models are however best described as "no means a self-consistent theoretical model at present, but rather a kind of semiemprical model...thus the aims of our UCMs is not to provide exact quantitative fits to observed data at present. It is hoped that our semiemprical approach will be of some help as a guide to interpreting and analyzing the observed data of ultracool dwarfs.", Tsuji et al. (2004).

2.8.4 Tucson Models

The models proposed by Burrows et al. (2006) used the most recent gas-phase molecular opacities coupled with a model for refractory clouds to produce a series of theoretical spectra covering a T_{eff} range of 2200 to 700K. Alongside the change in T_{eff} the authors also vary metallicity and gravity, the later they conclude is the "second parameter" that helps govern the L-T sequence. Despite varying the parameters they find that there is not a single combination of cloud particle size and gravity that can account for the observed spectra in the L-T transition. This, as in the other models shows that the physics involved in the cloud meteorology is incredibly complex and poorly understood. Despite this, for decreasing T_{eff} the Burrows et al. (2006) model does capture the transition from CO to CH_4 in the K band, the FeH and CrH features and the emergence of the neutral alkali features along with the disappearance of the TiO and VO in the L-dwarfs, however the "brightening" seen in the J band and the overall dimness of the latest L-dwarfs is not reproduced.

2.9 Conclusions

This chapter has provided a brief introduction to the history, theory and observations associated with low-mass stars and BDs. An overview of the different formation theories has been presented along with short discussions on how BDs are expected to evolve and the concept of the IMF. A compilation of some of the recent IMF results for various clusters has been presented in Tables 2.1 and 2.2. In addition an overview of the spectral types and features associated with BDs has been shown alongside a discussion on the atmospheric models currently being employed to model these objects.

Chapter 3

Observational Techniques

3.1 Introduction

This chapter serves to describe the instruments and techniques used in acquiring and analysing the data presented within this thesis. The acquisition of data from on-line catalogues and the photometric and spectroscopic reduction of the relevant data is also detailed.

3.1.1 Photometry, Magnitudes and Colours.

The quantification of light (photometry) is a measurement of the energetic output of a celestial object. For astronomers this flux[1] can be subdivided into separate narrow ranges of wavelength via the use of various filters on a telescope. Combining the information received from a set of filters, properties such as the effective temperature can be deter-

[1]Flux is defined as the amount of light energy per unit area per unit time in a given bandpass.

mined. The division of astronomical objects based upon their brightness was first devised by Hipparchus in 120 BC. The celestial objects were divided into six groups based upon the time it took them to be observable after sunset and before the end of astronomical twilight. Those that were first to appear were designated as first magnitude, whilst those that were last to appear were designated as sixth magnitude. As telescopes and instruments developed it was noted that some classes of stars actually contained a rather broad range of brightnesses and that the ratios of brightness between successive classes was approximately 2.5[2]. In 1856 N. R. Pogson proposed that the current system be formalised so that a magnitude difference of 5 should equal a brightness ratio of 100 to 1. The Pogson magnitude scale can thus be written as,

$$\frac{F_1}{F_2} \equiv \left(\sqrt[5]{100}\right)^{m_2-m1} \simeq 2.5119^{m_2-m_1}. \tag{3.1}$$

Here, F_1 and F_2 are the fluxes that are measured for the stars with magnitudes m_1 and m_2 respectively. A more common form of the expression is found by taking logarithms to give,

$$m_2 - m_1 = -2.5 \log\left(\frac{F_2}{F_1}\right). \tag{3.2}$$

The above equations do not take into account any zero point for the system, neither do they allow the calculation of a magnitude for a star by itself. This inter dependence has

[2]This incidentally shows that the human eye operates on a logarithmic basis.

lead to the need to find and define subtable stars and systems for which to perform photometric calibration. The equations also by definition still maintain the relationship that brighter objects have numerically smaller magnitudes when compared to fainter ones. The brightest star in the night sky outside of our solar system (Sirius) has an apparent visual magnitude of -1.46, whilst the Moon by contrast appears much brighter and has a visual magnitude of -12.5. Stars over 1×10^{12} fainter than Sirius (magnitude 30) have been observed with the aid of the Hubble Space Telescope. The visual magnitude mention above relates to the fact that these measures of flux have come from observing the star through a particular filter, which therefore denotes a certain wavelength dependency. In this case equation 3.2 can be more appropriately expressed as,

$$m_{2_\lambda} - m_{1_\lambda} = -2.5 \log \left(\frac{F_{2_\lambda}}{F_{1_\lambda}} \right). \tag{3.3}$$

As well as being wavelength dependent these magnitudes are also distance dependent, hence the term apparent magnitude. A bright star located at a sufficiently large distance away from an observer can appear fainter when compared to a star that is in reality intrinsically faint. This makes comparing luminosities of stars difficult. To correct for this the absolute magnitude of a star can instead be calculated. This is the magnitude the star would have if it were placed at a distance of 10 parsecs (pc) from the observer. The relationship between apparent magnitude (m) and absolute magnitude (M) is shown in equation 3.4

$$m_\lambda - M_\lambda = 5\log\left(\frac{d}{10}\right) = 5\log d - 5. \tag{3.4}$$

Here, d is the distance to the object in pc. If the distance is more than a few pc then the effects of interstellar absorption (if present) must be taken into account. This can be achieved thus,

$$(m - M)_\lambda = (m - M)_0 + A_\lambda, \tag{3.5}$$

where A_λ is a measure of the extinction in the direction of the star in the particular filter passband in question. Correcting the apparent magnitudes to a standard distance (absolute magnitude) and observing in the same filter still does not account for the behaviour of the individual instrument. For this reason the detections still need an additional correction applied to place them onto a calibrated magnitude system. The two main systems that exist are one based on the A0 star α Lyr (Vega) or the AB magnitude system. For the system based on Vega the calibrating or A0 star is defined as having a magnitude of zero in all filters and can be used as the second star in Pogons's equations thus giving

$$m = -2.5\log F + C_{zero}. \tag{3.6}$$

Where C_{zero} is 2.5log the offset in $ergs/sec/cm^2$ for a zero magnitude star. For the AB system the magnitude is based upon the flux per unit frequency i.e. $Watts/m^2/Hz$.

This is constant for a zero colour object and is defined as,

$$m_\nu(\lambda) \equiv -2.5 \log F_\nu(\lambda) - 48.60. \tag{3.7}$$

The two IR surveys of 2MASS and UKIDSS use the Vega calibration system (UKIDSS is calibrated against 2MASS; Hodgkin et al. 2009), whilst the optical SDSS uses the AB system (Fukugita et al., 1996).

Measuring an object in more than one photometric filter allows a property called the colour index to be defined (C_{index}). This is the difference between the magnitudes in the two different band-passes and is independent of distance.

$$C_{index} = m(\lambda_1) - m(\lambda_2) \tag{3.8}$$

The rules of convention use the magnitude of the bluer wavelength for λ_1 and the redder wavelength for λ_2. Thus as objects become cooler and their energy peaks at longer and longer wavelengths they become redder and move to the right on a colour-magnitude plot. A notable exception to this are the T-dwarfs whose infrared colours reverse from very red towards bluer colours as they cool. This is due to the presence of CH_4 absorption in the H and K bands and strong water vapour bands which also suppress the K band flux. Colours in the IR can also be used as a test for dust disks around objects such as brown and white dwarfs. Here the scattering of light into the IR by the dust disk causes

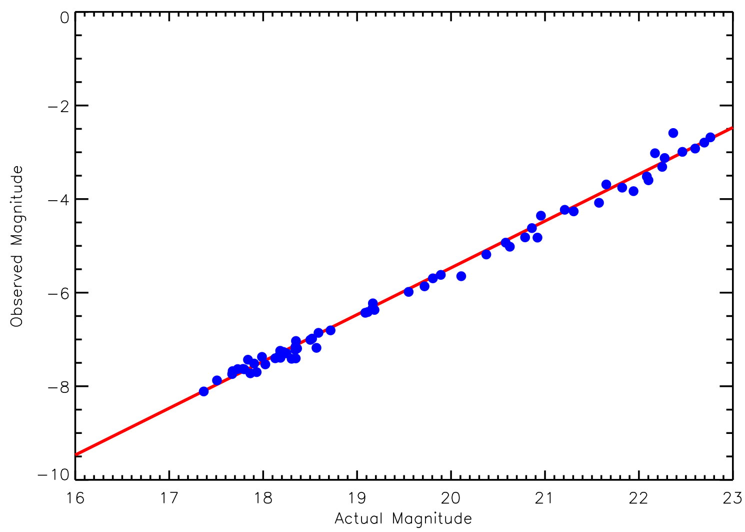

FIGURE 3.1. Example of a plot used to determine the zero-point for using CFHT12k data obtained for analysis in Chapter 5 via linear regression.

an excess amount of flux to be observed. (Conversely if one is observing through regions of interstellar dust the colour must be appropriately corrected).

3.1.2 Instrumental Zero-points

The flux measured by an instrument can be turned into a magnitude by using equation 3.9,

$$m = -2.5 \log F + C_{inst}. \tag{3.9}$$

The constant value C_{inst} is referred to as the zero-point offset and it is used to transform the instrumental magnitude onto a properly established reference frame. This is done using stars of known magnitude, such as those located in the Landolt fields (Landolt 1992; Landolt 2009) or those from the 2MASS catalogues (Hodgkin et al. 2009). In order for the zero-point constant to be determined the measured instrumental magnitudes of the stars are plotted against their known magnitude. This yields a linear relationship for regions where the detector is well behaved. The gradient of the line is fixed at 1 and thus the y-intercept yields the zero-point[3], C_{inst}. For instruments that use multiple chips to cover a large field of view, such as WFCAM, the zero-point must be calibrated for each individual chip. This is often done in the pipeline processing stage of data reduction. A typical graph used to determine a zero-point can be see in Figure 3.1

3.1.3 Atmospheric Corrections

The Earth's atmosphere prevents the majority of the electro-magnetic radiation that arrives from space from reaching the ground. This opaqueness of the atmosphere only allows observations in the optical/NIR and the radio to be carried out from the ground. Even then, the atmosphere is not totally transparent as dust particulates, water vapour and various volatile organic compounds/aerosols all absorb and scatter the incoming photons of light. This is the process that causes the sky to be blue and sunsets to be red. The amount of scattering is dependent on the wavelength of the radiation and the direction that it is being viewed from (the amount of atmosphere it is having to pass through). For shorter wavelengths the Rayleigh scattering off of molecules in the atmosphere is proportional to λ^{-4}, whereas the absorption process dominates over the Rayleigh scattering at

[3]If the zero-point of the detector is said to be stable then the observational conditions can be described as being photometric.

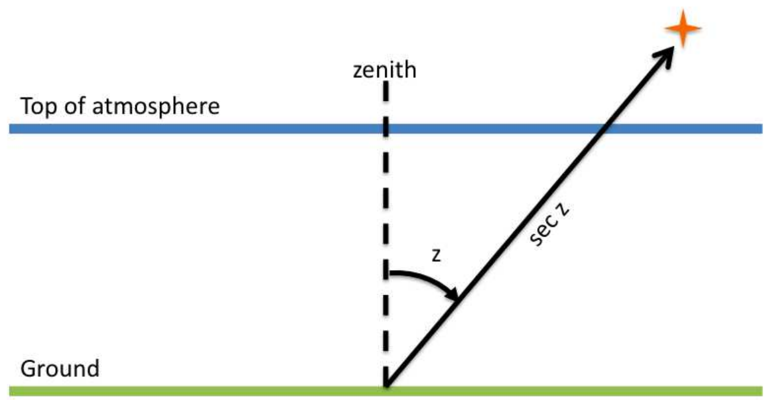

FIGURE 3.2. A schematic diagram illustrating the concept of airmass.

longer wavelengths. This effect is termed atmospheric extinction. Correcting for this allows the star's photometric properties to be determined as if the telescope and instrument were space based. A schematic showing the amount of atmosphere that the photons must pass through is shown by Figure 3.2 with equation 3.10 defining the quantity referred to as the airmass (X).

$$X = \sec\zeta\left[1 - 0.0012\left(\sec^2\zeta - 1\right)\right], \tag{3.10}$$

where ζ is the angular distance from zenith. The above expression is more suitable when larger values of ζ are used but for values less than 60° the equation can be simplified to just

$$X = \sec\zeta. \tag{3.11}$$

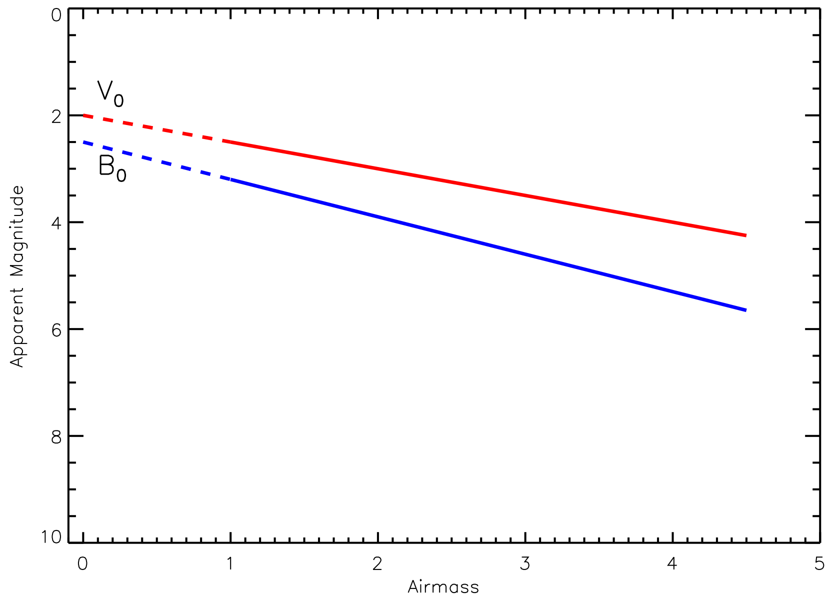

FIGURE 3.3. Figure showing the linear regression process used to determine the extinction coefficient. The two lines indicate the dependence that this extinction factor has on wavelength.

Observing a standard star throughout the night as it moves towards and away from the zenith means a curve of apparent magnitude versus airmass can be plotted. As the extinction is wavelength dependent the extinction correction value k_λ must be calculated for each filter used, and must be done so every night that science observations are carried out. A typical extinction correction plot for which k_λ is determined via linear regression can be seen in Figure 3.3

Applying the extinction correction, the magnitude of the star as seen from above the Earth's atmosphere would then be,

$$m_{\lambda 0} = m_\lambda - k_\lambda X. \tag{3.12}$$

As the work in this thesis is conducted at the red-ward end of the visual spectrum and into the IR and is not concerned with milli-magnitude precision second order extinction corrections are not considered. It is however worth noting that for certain types of astronomy it may become important. Taking the colour of an object, the true colour above the atmosphere can be shown to be,

$$C_{index} = m_{\lambda_1} - m_{\lambda_2} - (k_{\lambda_1} - k_{\lambda_2})\, X, \tag{3.13}$$

which can be simplified to allow computation of the colour extinction term k_c as,

$$C_{index} = C - k_c X. \tag{3.14}$$

Now the distribution of energy transmitted through a filter to the detector is a combination of the transmissivity of a filter (which is dependent upon the wavelength of the light incident upon it) and the spectral energy distribution of the observed object. If two differently coloured stars are thus observed through the same two filters as the objects again move toward and away from zenith, two different values of k_c will be determined. One for each differently coloured star (see Figure 3.3). An expression that combines the first and second order extinction corrections (k' and k'' respectively) can be constructed thus,

$$k = k' + k''C. \tag{3.15}$$

Substituting this back into the expressions given in equations 3.12 and 3.14 yields the relationships

$$m_{\lambda 0} = m_{\lambda} - k'_{\lambda}X - k''_{c}CX \tag{3.16}$$

and

$$C_{index} = C - k'_{c}X - k''_{c}CX. \tag{3.17}$$

3.1.4 Differential Refraction

When dealing with observations of different colour another factor that can be important (particularly for the optical but less so for the IR) is that of differential chromatic refraction (DCR). Here the position of the object as seen by the detector is altered from its true position due to the light being refracted by different amounts depending upon wavelength. Thus if a star is observed at one epoch in a very blue filter and another epoch in a red filter an additional offset will be present, lifting the object towards the zenith. As the amount of refraction is dependent upon the amount of atmosphere that the light is traversing it is thus dependent upon the airmass, and, the angle from the zenith. The corrections that should be added to the proper motions to account for the atmospheric dispersion are taken from Evans & Irwin (1995) and shown below,

$$\Delta\mu_\alpha \cos\delta = \frac{\{[R_s\,(C_{ref}) - R_s\,(C_{target})] \sin B_s \tan\zeta_s - [R_p\,(C_{ref}) - R_p\,(C_{target})] \sin B_p \tan\zeta_p\}}{\Delta t} \tag{3.18}$$

and

$$\Delta\mu_\delta = \frac{\{[R_s\,(C_{ref}) - R_s\,(C_{target})] \cos B_s \tan\zeta_s - [R_p\,(C_{ref}) - R_p\,(C_{target})] \cos B_p \tan\zeta_p\}}{\Delta t}, \tag{3.19}$$

where R is the constant of refraction for the colour term C, B the parallactic angle[4] and Δt is the epoch difference. The subscripts of s and p refer to the secondary and primary epoch and C_{ref} and C_{target} refer to the average colour of the stars or galaxies used in the reference frame and the colour of the target object. Figure 3.4 taken from Hambly et al. (2001) shows the calculated values of the coefficient R as a function of B_J and R filters used in the SuperCOSMOS survey. Here over the range of colour the coefficient of refraction in the red passband varies by only a small amount, corresponding to about 10 mas. This will be considerably less for the redder CFHT I and z, SDSS z' and UKIDSS $ZYJHK$ pass-bands that have been used in this thesis and so will likely not contribute a large source of error on proper motions.

[4]This is the direction angle to the zenith measured from north and is positive in the direction of increasing right ascension

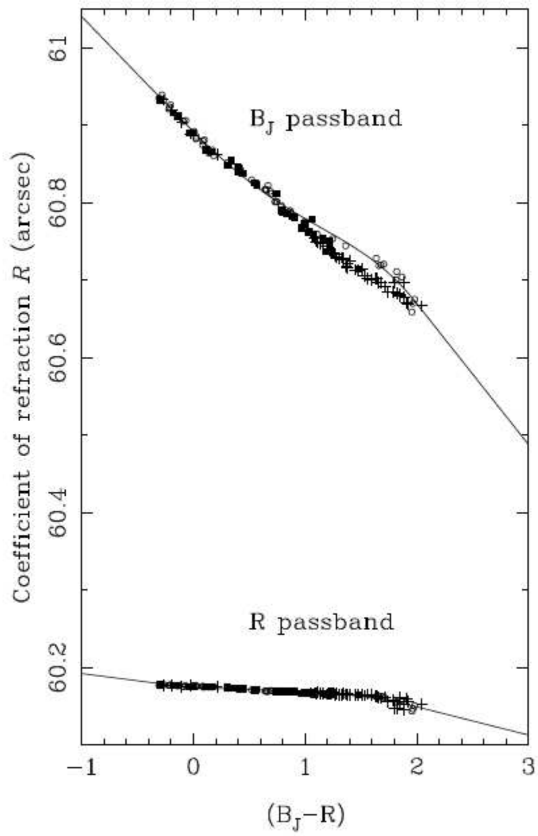

FIGURE 3.4. Computational models of R, the coefficient of refraction, as a function of (B_J-R) colour. The symbol types are + for giants, filled squares for sub-giants, and open circles for dwarfs. The solid lines are least-squares polynomial fits to the dwarf data, along with linear extrapolations to provide an estimate of R for any colour (cf. Evans & Irwin 1995, fits 11 and 12). Figure and caption from Hambly et al. (2001).

3.2 Detectors

Historically photographic plates and photomultipliers were used in the optical and single element detectors in the IR. For some years now CCDs have become the detectors of choice for work in the optical and IR arrays for the IR due to their high quantum efficiencies ($\sim$95%), large dynamic range and linear response to the incoming light.

3.2.1 CCDs

The charged coupled device or CCD combines the best qualities of the previous generations of optical detectors into that of a single device. The CCD itself is a two dimensional silicon (Si) grid array consisting of individually separate photosensitive capacitors called pixels (picture elements). The creation of the CCD by Bell Laboratories in 1970 has culminated in it being used for many aspects of astronomy (astrometry, photometry and spectroscopy). Each pixel in the CCD can store an associated charge until it is read out from the detector. The creation of the charge in the pixel is attributed to an electron being promoted from the valence band to the conduction band. This occurs either via the photoelectric effect as an incoming photon passes through the elements of the telescope before interacting with the CCD surface or via thermal excitation of the crystal lattice. The creation of the electron-hole pair and the subsequent creation of a depletion region is shown schematically in Figure 3.5.

Here a positive voltage is applied to the gate of the pixel, causing the depletion region

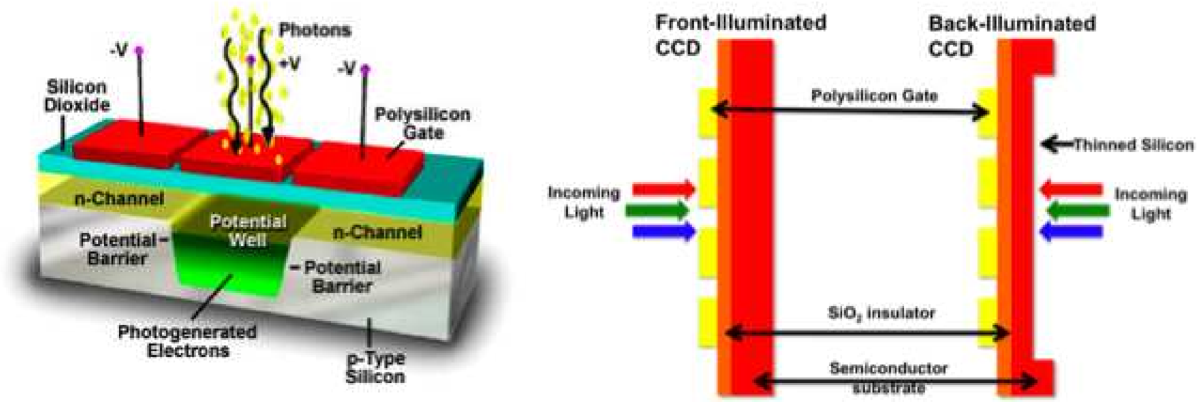

FIGURE 3.5. The left hand image shows an illustration of a CCD pixel, with the incoming photons passing through a gate held at positive voltage causing a potential well to develop as the photogenerate electrons accumulate after the positively formed holes migrate away. The right hand image shows a simple cartoon illustrating the difference between the layouts of a front-side-illuminated CCD and that of a thinned back-side-illuminated CCD.

to form as the positive hole migrates away leaving behind the electron. As the electrons accumulate they begin to shield the newly forming holes from this positive bias. This limits the amount of charge that can be stored in a single pixel element. Any pixel approaching this limit is said to be saturated and the detector begins to perform in a non-linear manner. Before this point the charge accumulated is proportional to the amount of light received. After the required exposure time, the voltages across the CCD gates are varied in such a manner as to move the charge down each column one row at a time, with the final row (the readout register) being varied in such a way as to move the charge perpendicularly across the array into an amplifier, before finally being passed to an analogue-to-digital converter. The gain of the detector is defined as the number of electrons that are required to register as one analogue-to-digital unit. An additional value is often added and this is called the bias offset. Modern CCD devices often have analogue to digital converters that have between 12 and 16 bits, this allows for resolutions of up to 65,536 counts.

There are two main designs of CCD those that are front-side-illuminated and those that are said to be back-side-illuminated. For a front-side-illuminated CCD as shown in Figure 3.5 the incoming photons must pass through the gates located on the surface of the CCD. This reduces the sensitivity of the detector particularly for the shorter, bluer wavelengths. As an alternative the CCD maybe placed "upside down" with the incoming photons now having to pass through the silicon substrate. The substrate has to be thinned to allow for a sufficient amount of transmission of the incoming light and as a result the back-side-illuminated CCDs are often more complicated and expensive to manufacture.

The first CCDs contained relatively few pixel elements in arrays about 256×256 pixels in size. These have now been surpassed with arrays over 2040×2040 now commonplace. The individual arrays have themselves been tiled together in ever increasing numbers to offer astronomers detectors that are capable of observing large fields of view in a single exposure - ideal for large survey programs to be conducted. Combining this large field of view with high sensitivity due to large quantum efficiencies has allowed CCDs to revolutionise astronomical detections of faint objects such as BDs and transiting extrasolar planets. The work presented in this thesis has made use of data taken from three sets of cameras; Those in the SDSS photometric camera, The CFHT12k mosaic camera on the Canada-France-Hawaii-Telescope (CFHT) and CAMELOT (acronym of 'Teide Observatory Light Improved Camera' in Spanish) on the Instituto de Astrofísica de Canarias telescope with its 82cm diameter primary mirror (IAC-80).

3.2.2 The SDSS photometric camera

The SDSS photometric camera (Gunn et al. 1998) is a large-format mosaic CCD camera that consists of two arrays. The first is a photometric array using 30 2048×2048 CCDs with pixel sizes of 24 μm giving a pixel scale of 0.4 arc seconds per pixel. The effective imaging area of 720cm^2 allows for a 3°field of view. The second array uses 24 400 × 2048 CCDs with the same pixel size and is used for astrometric accuracy. The photometric detectors are arranged in six columns of five chips (Figure 3.6), one chip for each filter colour ($ugriz'$) allowing for simultaneous photometry to be carried out on the observed field. The SDSS telescope is also unique in its operation in that it scans continuously

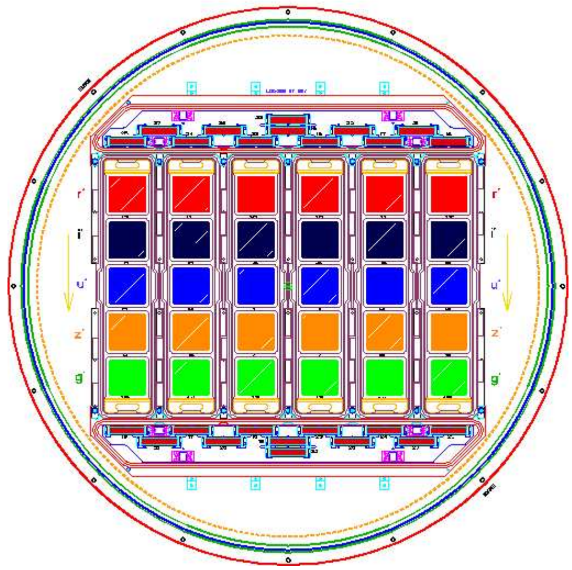

FIGURE 3.6. Focal plane of the SDSS camera showing the location of the 30 CCDs, each colour coded to show the filter to which they have been assigned.

throughout the night across the sky. The readout process for the CCDs compensates for this movement of the telescope thus helping to drastically reduce the amount of time it takes to conduct a large area survey.

3.2.3 CFHT12k

The CFHT's CFHT12k camera (Cuillandre et al. 2001) was one of the largest CCD mosaic cameras used in astronomy covering 42×28 arc minutes. Before being succeeded by its replacement MegaCam in 2003, CFHT12k was placed at the prime focus and consisted of 12 2048×4096 pixel back-side illuminated CCDs with a pixel scale of 0.206 pixels per arc second. The arrangement of its focal plane can be seen in Figure 3.7. Alongside the usual $BVRI$ filters the CFHT12k camera also had access to the z filter which became particularly useful for detecting BDs.

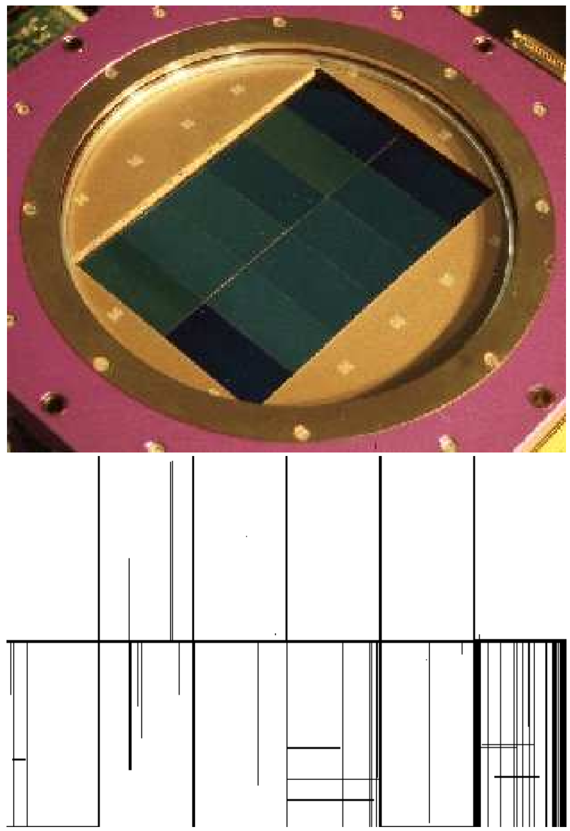

FIGURE 3.7. Top: Photograph of the CFHT12k focal plane showing the layout of the 12 CCDs. Bottom: An image showing the cosmetic quality of the CCD mosaic. CCD05 is particularly affected with a large concentration of bad columns (lower right chip).

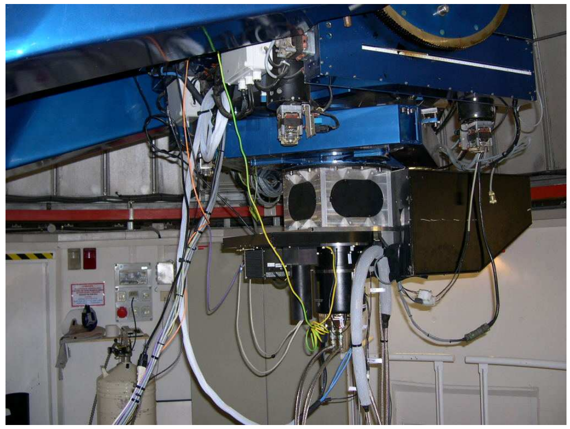

FIGURE 3.8. Image showing the CAMELOT CCD mounted on the IAC-80 telescope.

3.2.4 CAMELOT

The CAMELOT camera is the CCD detector for the IAC-80 telescope that is operated by the IAC on La Palma. It contains a single E2V 2048×2048 back-side illuminated CCD with a 10.4 arc minute field of view and a 0.304 arc seconds per pixel resolution. An image of CAMELOT mounted to the telescope is shown in Figure 3.8.

3.2.5 Infrared arrays

IR arrays operate on very similar principles to those governing CCDs (the photoelectric effect). However unlike the CCDs designed for use with optical wavelengths they must interact with IR photons. These photons have a much lower energy due to their longer wavelength and thus require the detectors to have slightly different designs. The first IR sensitive detectors were small in size, typically 32×32 pixels and were made of Indium antimonide (InSb). For a detector at a temperature of 77 K this corresponded to a band gap energy of ≈0.22 eV (λ_{cutoff} ≈5.6 μm). The dominance of the surroundings emitting in the IR and small band gap energy causes large amounts of thermal excitation to occur within the detector leading to a thermal current being generated. For this reason it was imperative that the detectors be cooled to very low temperatures that remain stable over long periods of time and that noise introduced by the thermal current is removed in the data processing. Unlike the optical CCDs, IR arrays are unable to transfer charge from pixel to pixel and so are usually paired to a CCD for the transfer of the electrons that describe the exposed image. They also operate without a shutter, this can cause complications when imaging bright objects as the array must be read out to avoid a ghost image being left behind from any residual photons. As with the progression of CCDs to ever larger sizes, IR arrays have also developed, the largest of which include the Wide Field CAMera (WFCAM; Casali et al. 2007) mounted on UKIRT and the VISTA-IR camera (Dalton et al. 2006) on the VISTA telescope at Paranal (see Figures 3.9 and 3.10 respectively for their focal plane layouts). One of the other main differences between CCDs and IR arrays is that images taken with an IR array must be dithered. The movement caused by the dithering allows for a median filtered background image to be constructed. This can effectively remove the bright sky background caused by water and atmospheric air-glow OH lines. This in turn allows long exposure time images to be developed from many shorter observations. The majority of the work in this thesis has used WFCAM at some point. A useful review on astronomical IR arrays is provided by Rieke (2007).

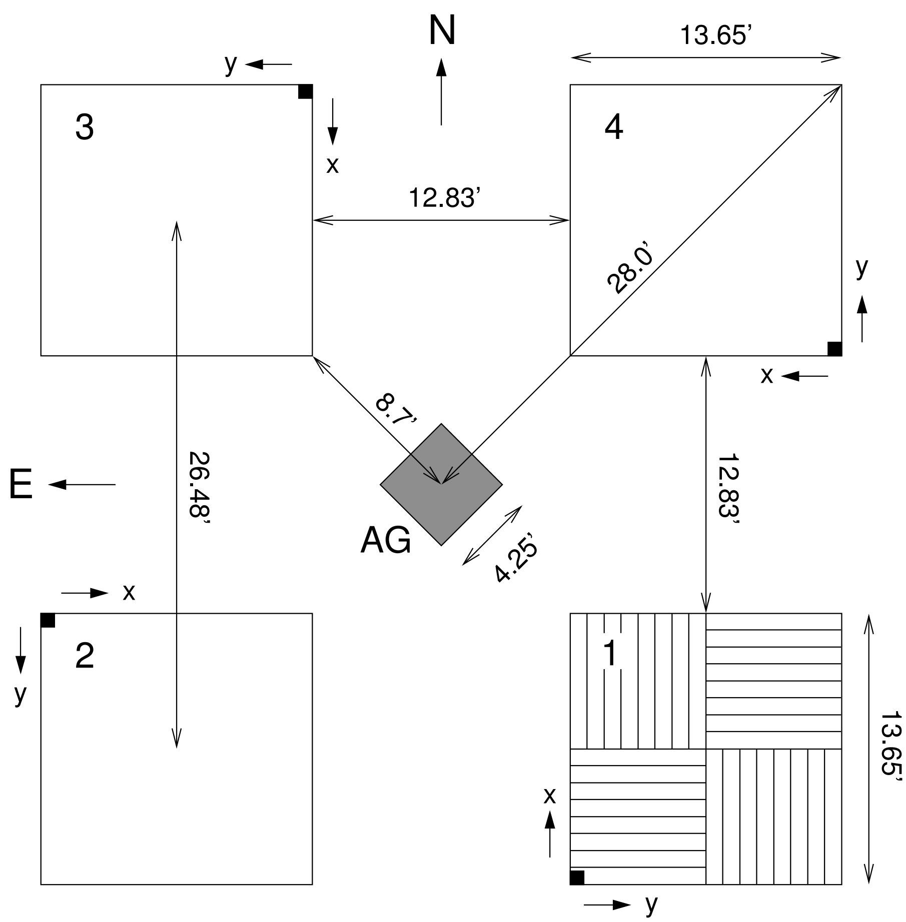

FIGURE 3.9. Figure showing the layout and orientation of the four WFCAM IR arrays along with the autoguider located at the centre.

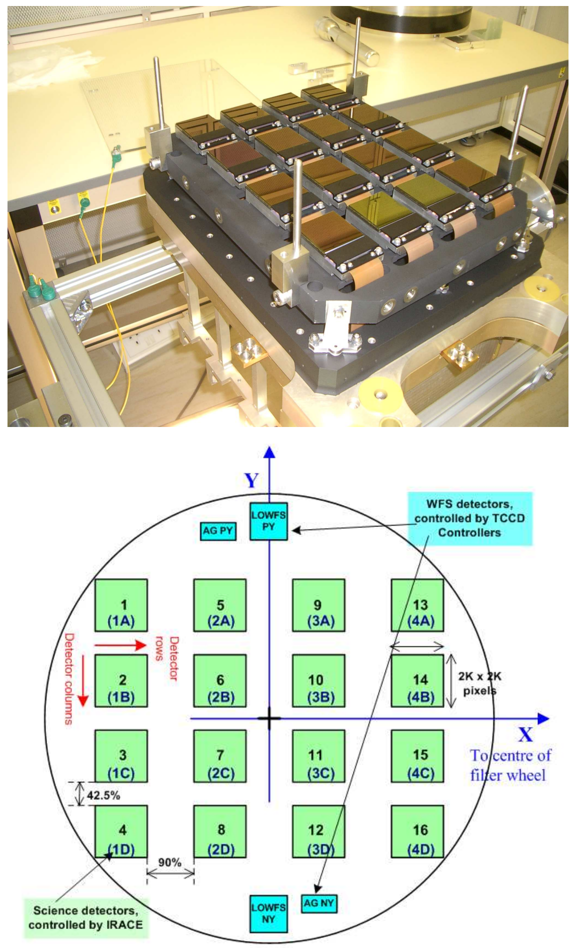

FIGURE 3.10. Top: Photograph showing the VISTA-IR camera mosaic. Bottom: Focal plane layout of the VISTA-IR camera showing the relative layout and inter-array spacing.

3.2.6 WFCAM

WFCAM mounted on UKIRT is currently its only instrument in operation following a programmatic review by the Science and Technology Facilities Council. The camera itself consists of 4 2048 $\times$ 2048 Rockwell Hawaii-2 type (HgCdTe) detectors deposited on a sapphire crystal substrate, Casali et al. (2007). The four infrared arrays are supplemented with Z, Y, J, H, and K filters. By moving the telescope/detector to one side, up or down and then back to the other side the four infrared arrays can create from the four paw-prints a single tile that covers some $\approx$0.8 deg^2. The pixel scale of WFCAM is 0.4 arc seconds per pixel.

3.2.7 Spectrographs

A spectrograph works to disperse the incoming photons to allow for investigations of how the intensity varies with wavelength. In producing a spectrum of an astronomical object its elemental and molecular makeup can be identified, allowing insight into a range of physical properties and processes, such as the temperature of stars or the complex atmospheric physics that govern the transition between the L and T-dwarfs. Modern spectrographic systems combine a slit, a diffraction grating and a detector. The slit(s) are aligned so as to separate the target object from other nearby astronomical sources whilst the grating is used to disperse the light which is then incident upon the detector. The use of gratings to perform the dispersal of light is different to that offered by a classical prism in a number of ways. Of notable importance is the fact that they disperse red light more than blue light, whilst also allowing for the formation of several other orders of spectra to be formed either side of the central image. These are referred to as the first, second and higher orders. To minimise the formation of these higher orders the gratings are often blazed. The blazing of a grating consists of forming the grating with a series of non-symmetrical grooves, a consequence of which is that the light becomes highly focused causing it to produce only certain orders. Spectrographs can be highly configurable with regard to their gratings and optics, examples of which include the echelle spectrographs such as HARPS (High Accuracy Radial velocity Planet Searcher; Mayor et al. 2003), that employ two diffraction gratings to produce a cross dispersed spectrum. The spectra produced in this thesis have been obtained by the William Herschel Telescope's (WHT) Intermediate dispersion Spectrograph and Imaging System (ISIS).

ISIS is a double-armed spectrograph mounted at the cassegrain focus of the WHT that is capable of moderate resolution work (8-120Å mm^{-1}). Its double-armed nature, permitted by the use of dichroic slides, allows for observations in each arm (termed red and blue) to be carried out simultaneously. Each arm is augmented by the use of different CCDs. The blue arm employs a 4096×2048 blue-sensitive thinned EEV12 CCD, whilst the opposing red arm uses a red sensitive 4096×2048 RED+ array[5].

[5]Additional details on the Blue arm, Red arm and the Dichroic can be found at http://www.ing.iac.es/Astronomy/instruments/isis/index.html.

3.3 Image data reduction

This section describes some of the common processes involved in reducing photometric or spectroscopic data taken in either the optical or the IR.

3.3.1 Bias removal

There are fundamentally two types of detector calibration, those that correct for additive systematic noise in the data and those that correct for multiplicative noise. Bias removal and Dark Current correction (see next sub-section) deal with the additive noise whilst Flat Fielding (Section 3.3.3) deals with a multiplicative case. Additive corrections are put in place to correct the counts received from the detector so that a pixel count of zero is returned when no light is incident upon it. The Bias image is the most basic detector calibration image. It is taken with the shutter closed with a zero second exposure. In reality this means that the detector is first reset and then immediately read out. Manufacturers of CCDs purposefully introduce an electronic offset in the amplifier. This is done to ensure that a positive signal is received by the Analog-to-Digital converter and that the read noise is properly sampled. As well as taking bias images as described above a second method used to determine the introduced offset is to use an area of the image called the overscan region. This region is not a physical part of the CCD but rather a virtual extension of it. It is produced by and contains a record of the noise introduced through the physical act of reading out the CCD. The mean value from the overscan is subtracted from the image. At this point the image is said be “overscan corrected”[6]. The overscan gives only the mean value of the bias offset in each line, it does not contain information about the structure along the CCD line itself. To correct for this one takes not one bias image but several bias images over a very short time span. They are then combined into one image called the “master bias” in order to increase the signal to noise ratio. This master bias contains information on the pixel-to-pixel structure of the detector’s read noise. It is subsequently subtracted from all further science frames so as to ensure an accurate measure of the counts recorded per pixel is obtained.

3.3.2 Dark Current Correction

The output from a pixel may in some cases have another component that adds to the pixel’s response. This addition has no relation to the light incident upon it but is instead a thermal component or “dark current”. This dark current is due to electrons being thermally excited thus causing the electron-hole pair creation rather that it being due to an incoming photon. This is of particular importance for IR arrays as by design they are tuned to respond to photons of similar wavelength (energy) to that of the local thermal environment making them susceptable to large dark current generation. To compensate for this fact many astronomical CCDs and IR arrays are cooled to very low temperatures (often with liquid nitrogen) in order to help reduce the thermal exitcation by the local surroundings. In order to remove the dark current, as with the bias frame, an image must be acquired where the only signal is that of the dark current. This is achieved by taking

[6]As well as overscan correcting the image, the overscan region of the image is also clipped away leaving only an image with pixels that correspond to real light gathering pixels on the CCD.

an exposure of the same length as the science frame but with the zero incident light upon the detector. The reason for ensuring the exposure is of the same length as the science frame is that the dark current is a time dependent phenomena, with more charge building up as the exposure time increases. These dark current frames are usually taken as near to the science exposure in time as is possible so that they are done under similar thermal conditions.

3.3.3 Flat Fielding

Finally the case of multiplicative noise is considered. This scaling arises from variations in the pixel to pixel quantum efficiency and non-uniform illumination of the CCD and is corrected via the process of flat fielding. Flat fields are filter dependent and must be taken for each filter set used. There are three ways of producing the flat fields. The first uses the twilight sky, as this provides any easily accessible source of uniform illumination. As the sky rapidly changes is brightness during this time care must be taken to not over saturate or under expose the detector and to obtain a sufficiently high number of images in the various filter sets needed[7]. The second method relies on observing a uniformly illuminated screen or part of the telescopes dome, these are often referred to as dome flats. Unlike the twilight flats these can be observed at any time and so it is easy to obtain a large number in each filter for better signal-to-noise. Another advantage is that the lighting conditions can be carefully controlled to help avoid any colour differences which could lead to errors in the photometry, a notable problem for broad band filters.

[7] After sunset one would take sky flats in increasingly red filters whilst a blue-ward progression would be used as the sky brightens.

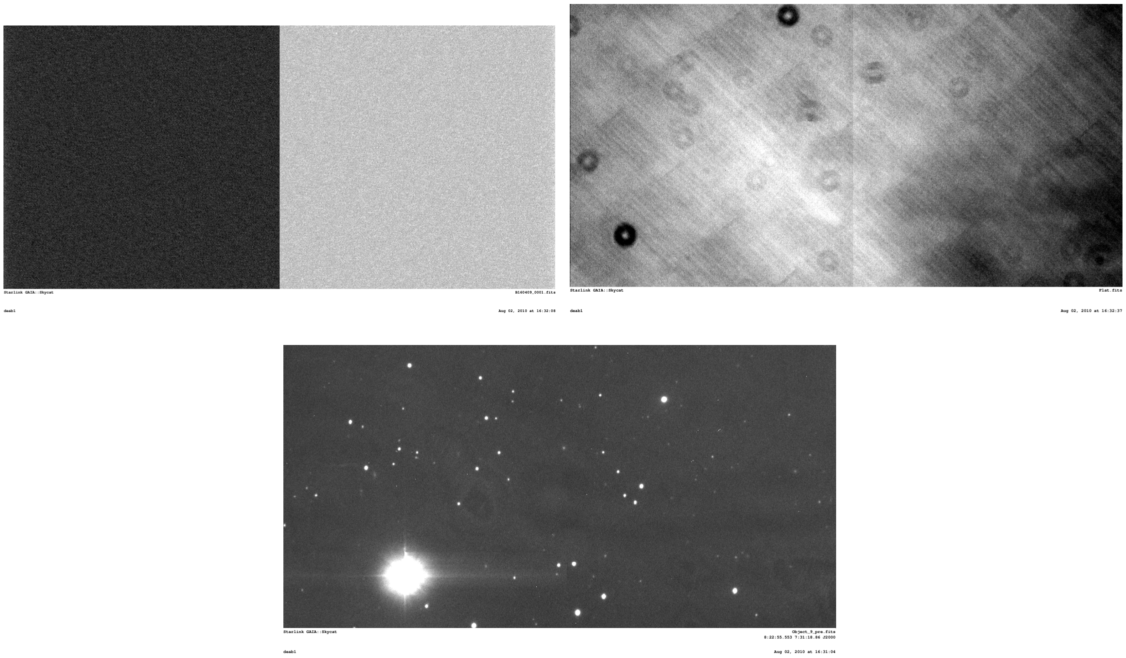

FIGURE 3.11. Three images showing top left: A bias image, top right: A flat field image and centre bottom: A final reduced science frame.

The illumination of the screen is however not quite as uniform as that of the twilight sky. If one is fortunate enough to be in a position to take advantage of both methods then the flats for each filter type can be combined. This combines the high spatial information of the dome flat with the low spatial information of the twilight flat to provide a superior master flat frame. The final type of flat field used is a night sky flat. Here the aim is to observe a patch of sky that is devoid of as many stars as possible. Whilst allowing the flats to be constructed from images taken during the science run (same illumination, focus and colour) they typically have much lower signal to noise and so should be considered a last resort for optical data but are more suitable for use in the IR. Figure 3.11 shows an image after having bias and flat fielding applied.

The method of reducing science ready images can be considered to be expressed by the following equations;

$$F_{\lambda}^{n}[x,y] = \frac{F_{\lambda}[x,y] - B[x,y]}{MODE\left(F_{\lambda}[x,y] - B[x,y]\right)}, \tag{3.20}$$

$$S_{\lambda}^{*}[x,y] = \frac{S_{\lambda}[x,y] - \left(\frac{t_s}{t_d}\right) D[x,y] - B[x,y]}{F_{\lambda}^{n}[x,y]}, \tag{3.21}$$

with $B[x,y]$, $D[x,y]$, $F_{\lambda}[x,y]$ and $S_{\lambda}[x,y]$ representing the Bias, Dark, Flat and Science images. t_s and t_d are the respective exposure times.

3.3.4 Source Detection

Some of the data in this thesis has come from independent telescope observations, that is to say ones that have been not been conducted as part of a large survey such as UKIDSS or SDSS, which have extensive pipelines for data reduction and photometric calibration. As such these observations do not have files containing information on the objects present in the image. All that is presented is a 2d CCD image with the pixel responses. In this case source detection programs have been used to detect and classify objects present within the image. I have used $SExtractor$ (Bertin & Arnouts, 1996) both from within the STARLINK $GAIA$ program and as an separate command line utility and the Cambridge Astronomy Survey Unit's $imcore$ routine. $SExtractor$ and $imcore$ like many object detection programs run a series of routines to calculate the background level of the image and determine if pixels belong to the background or not (amongst other options such as an object's ellipticity). Typically for a series of pixels to be classified as an object they must share common borders and have flux above some defined threshold limit (specified by the user). The parameters must be chosen carefully to ensure that faint objects are retrieved yet the number of false detections is minimised.

3.3.5 Aperture photometry

After the source detection has been completed, the next step is often to calculate the photometry of the object. One of the most important quantities for achieving good quality photometric data is the Signal-to-Noise ratio (SNR) from the object to the noise inherent in the data. A simplified version of the equation used to calculate the SNR is given below.

$$SNR = \frac{gN_{star}^{net}}{\sqrt{gN_{star}^{net} + ngN_{sky} + nN_R^2}} \tag{3.22}$$

where g is the gain, n the pixels within the aperture, N_{sky} the number of sky counts, N_R the read noise and N_{star}^{net} the net counts for the target object. To maximise the signal-to-noise a balance is needed between the size of the apertures used. Too small a size will inadequately measure the photometry of the object as flux outside the aperture is ignored whilst too large an aperture will introduce many pixels containing unneeded read and sky background noise. Aperture photometry is a relatively easy method for calculating the flux of a target object as it relies on few assumptions. Two (or more) software based apertures of differing radii are placed over the star's central position (as determined by the source detection routines), the larger of the two apertures is defined so as to encompass the object and a portion of the surrounding background, whilst the smaller aperture just encompasses the object. The resultant annulus then provides the flux from the background only. This in turn provides the object's flux by subtracting it from the larger aperture. Using equation 3.6, the flux from the object can be converted into an exposure corrected instrumental magnitude (m) as seen below,

$$m = -2.5 \log_{10} \left(\frac{f_{obj}}{t_{exp}} \right). \tag{3.23}$$

Here, f_{obj} is the object's flux from the aperture that has been used on the integrated image with t_{exp} giving the exposure time of the image. This is not the final magnitude as it still has to be corrected for the photometric zero-point of the instrument, the extinction coefficient (Sections 3.1.2 and 3.1.3) and the aperture correction. The aperture correction is needed as the aperture size used will not be totally perfect for the whole image. For example a relatively small aperture may be used in a case where the majority of objects in the image are faint point sources. If there exists a bright source however, the flux from that object will extend into the annulus that is used to estimate the background and thus not all of it will be counted by the smaller, object focused aperture. The aperture correction accounts for this missed flux. The photometry reported by the UKIDSS, SDSS and 2MASS catalogues have had their photometry calculated and corrected by their respective processing pipelines. For the UKIDSS-SDSS candidate members in Chapter 4 it was necessary to calculate the magnitudes from their original FITS files (which only contained flux information). The equations used to calculate the magnitudes (correcting for extinction and aperture) will be detailed in the relevant section. The CASU pipeline that processed the CFHT12k data calculated fluxes for a range of aperture sizes. The core radius was set at 3.5 pixels and it was this value that was used for the aperture size and fluxes in this work (the aperture correction value for this aperture size is listed as APCOR in the respective FITS headers).

3.4 Optical spectroscopic data reduction

The optical spectra of the suspected polar ULAS0822+0730 presented in Chapter 6 were reduced using routines from the Image Reduction and Analysis Facility (IRAF). The routines used were $ccdproc$, $zerocombine$, $crcombine$, $response$, $apall$, $identify$, $dispcor$, $standard$, $sensfunc$ and $calibrate$[8]. As with normal CCD imaging data, a series of bias and flat field images are taken alongside the science image. Supplementary to these are additional images of an arc-lamp frame which, provides a reference frame for wavelength calibration and a standard star spectrum that is used for flux calibration of the target. Firstly, the bias frames are combined into a master bias frame before being subtracted. Each frame is then divided through by a combined master flat field. Next, a region a few pixels in size bracketing the spectrum is selected out from the image. This is used to provide an estimate of the background and remove any possible sky lines from the spectrum. Ideally the spectrum should be (near) perpendicular to the slit direction. Once an estimate of the background has been made, it too is subtracted from the spectra frames. The observed arc-lamp spectra (CuNe+CuAr for the WHT ISIS data in this thesis) is then compared to an emission spectrum of the elements in the lamp which allows for a mapping of pixels into wavelength units, providing a wavelength calibration

[8]For full details of their use refer to the IRAF website: http://iraf.noao.edu

for the target and standard spectra. An example of the arc-lamp spectrum used can be seen in Figure 3.12. After extracting a wavelength calibrated spectrum of the target and standard star the next step is to load a wavelength extinction map for the observatory's location[9]. After doing so, the $standard$ routine is run. This compares and computes the ratio of the observed fluxes of the standard star against those tabulated for it in the IRAF database over the bandpass being used. These ratios are then fit by a "sensitivity" function generated by the $sensfunc$ routine. The final step is then to apply the air mass extinction correction and "sensitivity" function generated with the standard star to produce a wavelength and flux calibrated spectrum of the science target. This is done using the "calibrate" routine. Because the WHT ISIS contains both a blue and a red arm the whole process had to be carried out twice, once for each individual arm.

3.5 Filter systems

Astronomical filters are designed so as to allow the transmission of selected wavelength ranges through to the detector. As such, they can be divided into three discrete groupings each one being better suited to certain tasks. Firstly there are the broad band filters, these typically have a spectral widths of $\approx$1000Å and thus allow for a comparatively large amount of flux to be gathered over the same time period when compared to the other two filter groupings. However, they suffer in that the flux they receive can be influenced by the many spectral lines that they cover. The intermediate filters cover a smaller range typically of the order 100-500Å , whilst the smallest range covered is that

[9]The file from http://www.ing.iac.es/Astronomy/observing/conditions/wlext.html was used as the wavelength extinction map for the WHT ISIS spectra.

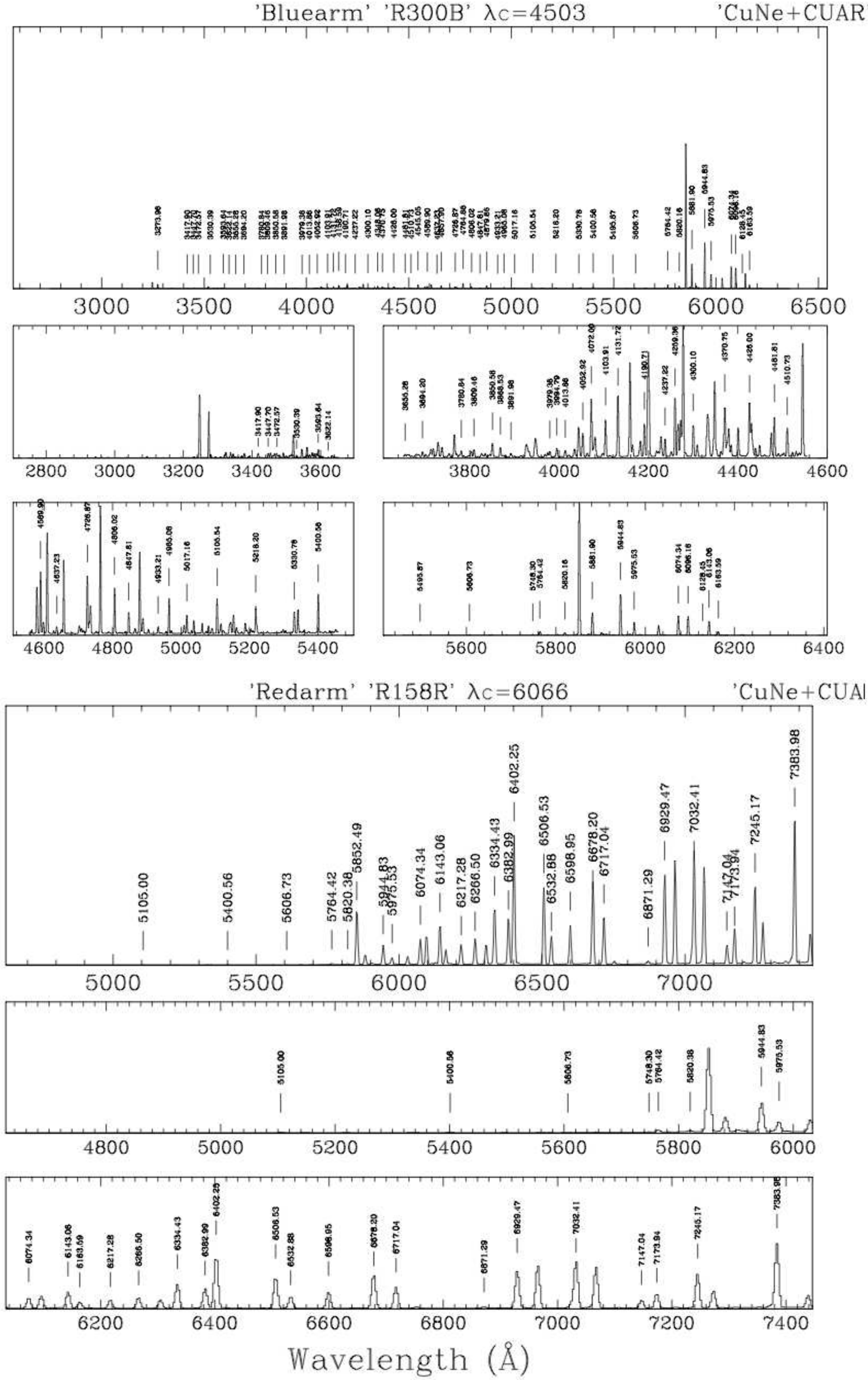

FIGURE 3.12. CuNe+CuAr arc-lamp spectra provided by the Isaac Newton Group of telescopes for use in wavelength calibrating the red and blue arms of the ISIS instrument.

of the narrow band filters (5-100Å). The narrow band filters are constructed so that their limited spectral windows are centred on specific wavelengths such as the Hα (6563Å).

3.5.1 Far optical filters

This thesis has made use of the far optical SDSS i and z' filters alongside the CFHT12k I and z filters, transmission curves for which can be seen in Figure 3.13 alongside the other Sloan optical filters. These are the reddest optical filters that can be used with a CCD before an IR array must be employed as the detector element of the telescope. The SDSS z' and CFHT12k z filters unlike the others described are open ended, as there is no cut off in their transmission profile as they extend into the IR. The cut off is infact applied by the decrease in the quantum efficiency of the CCD as the photons move from the optical into the IR (note the WFCAM Z filter is not open ended).

3.5.2 Infrared Filters

As the wavelength of light received by the telescope transitions into the spectral region known as the NIR the effects of the Earth's atmosphere become important as it is no longer completely transparent, suffering from the effects of the various water vapour bands, as shown by the grey curve in Figure 3.14. The IR filters have subsequently been designed to operate in the regions where the transmission peaks. The most commonly used IR filters are the J, H and K filters centred on $\approx$1.2μm, $\approx$1.6 μm and $\approx$2.2 μm. The photometric measurements obtained with these filters are often referred to as being on

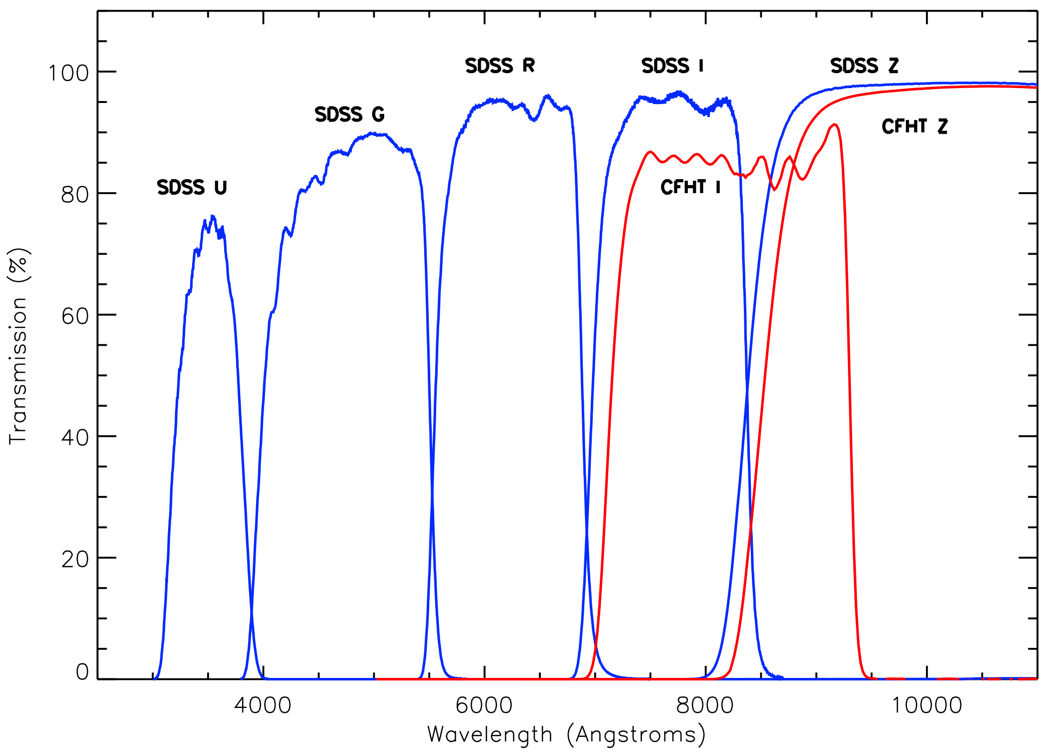

FIGURE 3.13. Transmission profiles for the optical SDSS $ugriz'$ filters alongside those of the CFHT12k I and z filters.

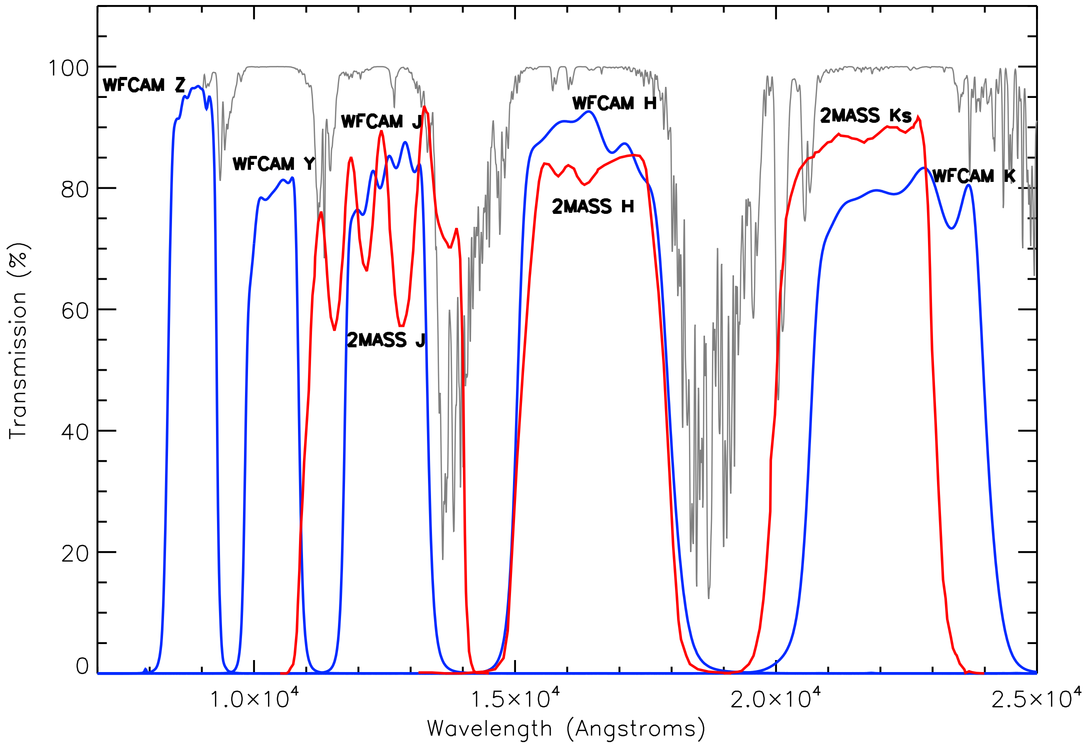

FIGURE 3.14. Transmission profiles for the IR WFCAM and 2MASS filters. The grey curve shows the Earth's atmospheric transmission as a function of wavelength, courtesy of the IRTRANS4 program and provided by the UKIRT web pages.

the MKO system in honour of the Maua Kea Observatory where the filters were initially developed. The WFCAM J, H and K filters are also on the MKO system. The 2MASS survey alternatively employs a modified version of these filters with K being replaced by the Ks (K short filter) as shown by the red curves in Figure3.14. The WFCAM filter set is also supplemented by the Z and Y band filters, with the relatively narrow Y band sitting in the blue-ward window of 1.1 microns. UKIDSS is the first survey to extensively use the Y band (Warren et al. 2007) which was selected to distinguish T-dwarfs from quasars and could also potentially lead to the identification of new sources with interesting spectral features appearing at $\approx 1\mu$m.

3.6 Astrometry

The final step in reducing the imaging data is the attachment of an astrometic solution to allow the pixel coordinates to be transformed into those that represent a world coordinate system (Right Ascension and declination). The methods used to derive the astrometric solution can also be used to calculate an object's proper motion and are discussed below.

3.6.1 Pattern Matching, Astrometric solutions and Proper motion determination

A large proportion of this work has relied on detecting objects in multiple epochs and/or in different filters. Observing at different times, with different telescopes and filter sets has lead to the challenge of matching these objects together. To solve this problem I have written and implemented a set of IDL routines. To begin with, two input lists (A and B) need to be created[10] These two lists consist of at minimum the positions of the objects, additionally the flux or magnitude (instrumental or calibrated) of each object can be taken into account. The positions can be supplied as either Right Ascension (RA) and declination (dec) in radians or degrees or as x and y pixel positions, or a combination of the two. In crowded fields one may wish to use the x and y pixel coordinates as opposed to the RA and dec, as these are likely to be far more accurate in determining the position of the object (slight truncation of coordinates can often occur when creating object catalogues). Alternatively to avoid changing between units if a suitably reliable world coordinate sys-

[10]Each list corresponds to sources detected in a particular image.

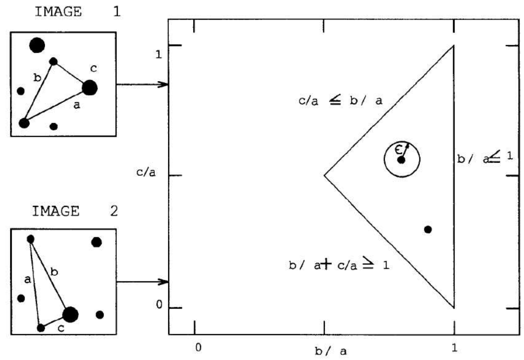

FIGURE 3.15. Example of how two triangles are formed between a set of stars and then compared in triangle space to determine if the triplet is a potential match. Figure from Valdes et al. (1995).

tem (WCS) has been attached to the image, the pixel locations / RA and dec information can be transformed via the astrometry matrix information contained within the respective FITS headers. As a note, care should be taken when matching objects solely on x and y pixel coordinates that the observed fields do contain some area of overlap as objects of completely different RA and dec may have similar pixel coordinates (If care were not taken, or a mistake was made this should be detected upon examining the results of the pattern matching fit). If any magnitude/flux information has been supplied alongside the positions then the two lists are sorted in order of decreasing brightness. Depending upon the user's choice either the whole list of objects or a smaller subset are then taken to be pattern matched. The reason for sorting by brightness (if available/wanted) is that unless the exposure times are significantly different, it is likely the case that bright objects in one image will correspond to bright objects in another, making it easier and more likely to find matching objects (Valdes et al. 1995). Each object in a list is then made to form a triangle with the other available objects (see Figure 3.15). The number of triangles that a list of N objects (N_{obj}) can form is,

$$N_{triangles} = \frac{N_{obj}\left(N_{obj}-1\right)\left(N_{obj}-2\right)}{6}. \tag{3.24}$$

The triangles formed can then be represented in triangle space as points (xt, yt) thus,

$$x_t = \frac{b}{a}, \tag{3.25}$$

$$y_t = \frac{c}{a}. \tag{3.26}$$

The values of a, b and c are the lengths of the triangle sides in decreasing order. This transformation to triangle space is independent of the image scales, orientation or any offsets. Any matching triplets in the two lists will have points that lie close to each other in this triangle space (see Figure 3.15). An N_{obj_A} x N_{obj_B} matrix is then setup and whenever a triplet match is encountered respective elements in the matrix are incremented by 1. An illustration of this can be seen in Figure 3.15. There is of course the potential for mismatches but cumulatively it is easy to see from the "voting matrix" which the most likely matches are. A selected portion of the objects with the highest total votes are then used to derive a suitable coordinate transformation going from list A to list B. This transformation can be either a linear 6 parameter transformation, a quadratic 12 parameter transformation or a cubic 16 parameter transformation. Higher order fits require a higher selected number of objects. For this thesis both the linear and quadratic transformations have been used. These are shown below,

	1	2	3	4	5	6	7	8	9	10	11	12	13	14	15	16	17	18	19	20
1	4	**29**	2	0	0	2	1	3	3	2	1	0	0	1	0	0	2	0	0	1
2	**42**	*8*	1	2	1	1	1	2	2	1	1	1	1	0	4	0	0	1	0	7
3	2	3	**21**	0	1	0	0	1	0	0	3	0	0	2	2	0	2	1	0	2
4	3	0	2	0	**53**	0	1	1	2	1	0	2	2	2	1	0	2	3	2	0
5	3	1	0	**24**	2	0	1	0	4	2	2	0	0	1	2	0	1	0	0	0
6	0	1	3	2	1	2	0	1	0	2	*9*	3	0	0	2	2	3	1	1	0
7	0	2	1	1	0	**29**	1	1	1	0	0	0	2	0	0	0	0	2	0	0
8	1	1	1	2	1	1	1	2	0	1	3	2	1	0	3	1	1	0	1	1
9	2	0	0	0	0	4	1	**21**	1	0	2	0	0	0	2	1	1	2	1	1
10	3	1	0	1	1	1	**20**	2	1	*5*	3	1	1	0	1	1	1	0	0	0
11	2	2	1	1	2	*5*	2	3	**46**	1	0	0	3	2	2	1	2	2	2	0
12	1	0	0	1	0	1	1	1	1	1	2	2	0	0	1	1	1	0	2	*6*
13	2	0	1	2	1	0	1	0	0	2	1	3	0	1	0	0	0	0	1	0
14	0	2	3	0	0	0	0	2	0	1	3	3	0	1	**31**	2	2	3	1	0
15	0	0	*5*	1	4	0	0	1	1	0	4	0	1	1	0	2	0	0	0	0
16	1	1	2	3	2	1	2	0	1	0	1	**18**	0	0	2	2	1	2	0	0
17	0	1	2	2	1	1	0	0	2	**23**	1	0	1	0	0	1	1	0	0	0
18	0	3	0	1	1	0	2	1	1	3	0	0	2	1	1	0	1	1	1	0
19	0	0	0	0	0	0	1	3	1	1	0	4	2	0	2	2	0	**28**	3	1
20	*6*	4	0	4	0	4	1	1	1	1	1	0	1	0	2	0	1	0	0	0

FIGURE 3.16. Example of a voting matrix. Figure from Valdes et al. (1995).

$$x' = A + Bx + Cy, \tag{3.27}$$

$$y' = D + Ex + Fy, \tag{3.28}$$

$$x' = A + Bx + Cy + Dx^2 + Exy + Fy^2, \tag{3.29}$$

$$y' = G + Hx + Iy + Jx^2 + Kxy + Ly^2. \tag{3.30}$$

These equations are solved via the process of Gaussian elimination (with partial pivoting) and back substitution (Chapra & Canale 2005). Next the transformation is applied to all the objects that made up the voting matrix, taking them from the coordinates in list A to that of list B. The absolute difference between positions in the frame of list B is then found. The mean of these values is then multiplied by 1.48 to convert from the median absolute deviation (MAD) to a root mean squared (RMS) value, this is the initial RMS value. Objects whose movement is greater than 3 times the initial RMS are then removed and the transformation recalculated (with the original x and y values from list A, be they pixel or celestial coordinates). Again the RMS is calculated and objects removed if necessary. The process is iterated until either no more objects are rejected or there are not enough objects (fewer than 3 for the linear case) to enable a transformation at which point the routines exit with an associated error message. Assuming the first case is true and a successful transformation has been created there now exists two lists that contain no fast moving objects, cosmic rays or other artifacts, just matched objects. These two lists however have been created from those objects that were passed from the original list A and B to the voting matrix (either a random selection or magnitude sorted list). For cases where the number used in the voting matrix is smaller than either of the lists the refined transformation is then applied to the whole of the original list A and the slow process of selecting the nearest object in list B is begun, in order to produce the matched lists.

The determination of the transformation matrix can be used not only to find pairs of matched objects but also to calculate an object's proper motion or an astrometric solution for an uncalibrated image. To calculate a proper motion one has their target object (the one for which a proper motion value is desired) and a list of reference objects. These again should appear in two epochs. Here the reference objects have ideally already been matched but they are still checked and subjected to the RMS rejection to ensure they exhibit as close to zero motion as possible. The resulting transformation in this case is then applied to the target object. This places it in the second epoch's reference frame. The proper motion is the difference in the coordinates reported from the transformation and the values found in the second epoch divided by the epoch difference. Whilst it is possible to calculate this with RA and dec, my preferred method is to use the x and y pixel coordinates often/usually supplied by the FITS catalogues to calculate the transformation. The transformed and reported pixel locations in the second epoch image are then transformed through the IDL procedure[11] $xyad$. This uses the FITS header astrometry of the second epoch image to transform the coordinates into RA and dec. Thus the difference in RA and dec now gives the total motion of the object in degrees. This is easy to convert into milliarcseconds per year following equations 3.31 and 3.32.

$$\mu_\alpha cos\delta = \frac{\delta RA \times 3600 \times 1000}{epochdifference} \times cos(dec) \tag{3.31}$$

and

$$\mu_\delta = \frac{\delta dec \times 3600 \times 1000}{epochdifference}. \tag{3.32}$$

To create, update or correct an astrometric solution one again relies on the identification of objects between two images. In this case one image has a reliable WCS and the resulting list of matched objects allows for a mapping of x and y pixels into RA and dec. For the work in this thesis I have written a series of scripts that will perform object detection on my uncalibrated images and then either use the catalogue of positions for a known image or, using the telescope's pointing as an approximate guide, carry out a query to obtain the RA and dec from one of the many astronomical catalogues (2MASS for example). Once a transformation from x and y pixels into RA and dec has been established a

[11] $xyad$, $starast$ and their companion routines used for reading in and manipulating FITS files from within IDL are provided by the IDL Astronomy Users Library hosted by Goddard Space Flight Centre.

series of coordinates needs to be defined, the first is that of the pixels at the centre of the image. These are the $CRPIX1$ and $CRPIX2$ values found in the FITS header with the quantities $CRVAL1$ and $CRVAL2$ representing the pixel values in RA and dec. Next two other pixel coordinates are randomly specified with the appropriate transformation equations 3.27- 3.30 being used to obtain their Ra and dec. These three pixel and celestial coordinate groupings are supplied to the $starast$ IDL procedure which, using the equations described in Calabretta & Greisen (2002) constructs an appropriate coordinate description matrix (CD Matrix). Using the 3 reference positions allows for a determination of the orientation of the coordinate system. By default a gnomonic TAN zenithal perspective projection is assumed (The UKIDSS WFCAM data use the ZPN projection, details of which can be found in section 5.1.7 of Calabretta & Greisen 2002). Figure 3.17 shows two images of part of the Blanco 1 cluster analysed in Chapter 5. The top image is the original image that has an approximate WCS solution supplied as part of the data reduction pipeline, the values for which are given in Table 3.1. Sources from the 2MASS catalogue are overlaid on the image with a clear disagreement being shown. Using the process described above the bottom image was produced with an updated WCS solution, again the same 2MASS sources are overlaid in the image with each source now being properly identified in the image. Specifically the process for calculating a gnomonic TAN world coordinate system solution is as follows.

Firstly for the gnomonic TAN projection, (α_0,δ_0) = (α_p,δ_p), the celestial longitude and latitude of the fiducial point equals the celestial longitude and latitude of the native pole (the values given to $CRVAL1$ and $CRVAL2$, the origin in the native system). The

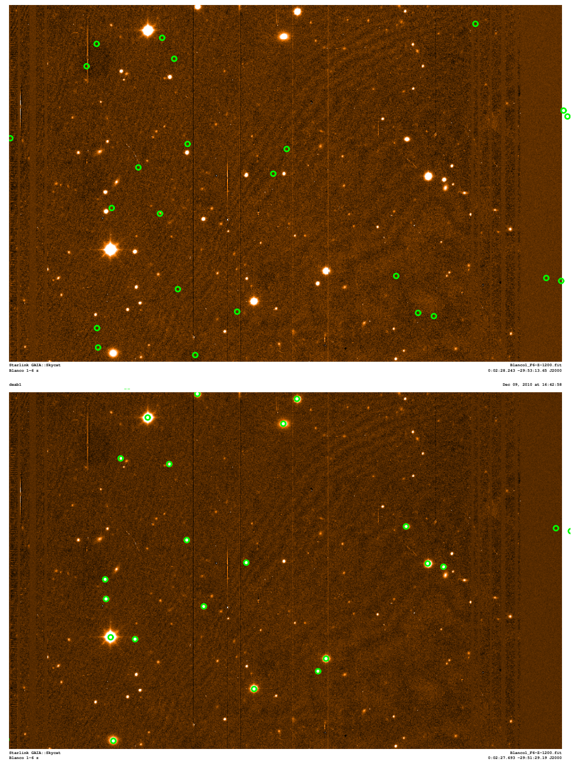

FIGURE 3.17. Top: Image of the Blanco 1 field with the initial WCS supplied by the CFHT Elixir data reduction pipeline (Magnier & Cuillandre, 2004), the values of which can be seen in Table 3.1, overlaid with the 2MASS catalogue. Bottom: The same image as above but with an updated WCS after parsing through the pattern matching and WCS generating scripts.

	Poor WCS structure	Good WCS structure
CRVAL 1	0.27785	0.61538
CRVAL 2	-29.981	-29.858
CRPIX 1	-4136	1040
CRPIX 2	3725	2064
CD 11	5.735×10^{-5}	5.623×10^{-5}
CD 12	3.134×10^{-7}	2.660×10^{-7}
CD 21	-1.538×10^{-7}	-3.465×10^{-8}
CD 22	-5.735×10^{-5}	-5.666×10^{-5}

Table 3.1. WCS information for the Blanco 1 images shown in Figure 3.17 before and after astrometrically calibrating against the 2MASS catalogue.

native coordinates ϕ and θ are those derived from the x and y pixel coordinates before they themselves are converted into the celestial coordinates of Ra and dec. A work-flow of the process can be seen in Figure 1 of Calabretta & Greisen (2002). A rotation matrix designed to handle the spherical coordinate rotation used to describe the transformation to and from celestial and native coordinates is then defined as the following;

$$\begin{pmatrix} l \\ m \\ n \end{pmatrix} = \begin{pmatrix} r_{11} r_{12} r_{13} \\ r_{21} r_{22} r_{23} \\ r_{31} r_{32} r_{33} \end{pmatrix} \begin{pmatrix} l' \\ m' \\ n' \end{pmatrix} \tag{3.33}$$

Note, the above format describes the transformation from celestial into native coordinates (the inverse/transpose performs the native into celestial coordinate calculation). $r_{11}, r_{21}, r_{31}, r_{12}, r_{22}, r_{32}, r_{13}, r_{23}$ and r_{33} are defined as;

$$r_{11} = -\sin\alpha_p \sin\phi_p - \cos\alpha_p \cos\phi_p \sin\delta_p, \tag{3.34}$$

$$r_{12} = \cos\alpha_p \sin\phi_p - \sin\alpha_p \cos\phi_p \sin\delta_p, \tag{3.35}$$

$$r_{13} = \cos\phi_p \cos\delta_p, \tag{3.36}$$

$$r_{21} = \sin\alpha_p \cos\phi_p - \cos\alpha_p \sin\phi_p \sin\delta_p, \tag{3.37}$$

$$r_{22} = -\cos\alpha_p \cos\phi_p - \sin\alpha_p \sin\phi_p \sin\delta_p, \tag{3.38}$$

$$r_{23} = \sin\phi_p \cos\delta_p, \tag{3.39}$$

$$r_{31} = \cos\alpha_p \cos\delta_p, \tag{3.40}$$

$$r_{32} = \sin\alpha_p \cos\delta_p, \tag{3.41}$$

$$r_{33} = \sin\alpha_p, \tag{3.42}$$

with ϕ_p equal to $180°$ and l', m' and n' being defined as;

$$l' = \cos\delta\cos\alpha, \tag{3.43}$$

$$m' = \cos\delta\sin\alpha, \tag{3.44}$$

$$n' = \sin\delta. \tag{3.45}$$

Solving the matrix for the values of l, m and n allows the native latitude and longitude to be found (in radians),

$$\theta = \arcsin\left(r_{31} \times l' + r_{32} \times m' + r_{33} \times n'\right), \tag{3.46}$$

and

$$\phi = \arctan\left(\frac{r_{11} \times l' + r_{12} \times m' + r_{13} \times n'}{r_{21} \times l' + r_{22} \times m' + r_{23} \times n'}\right). \tag{3.47}$$

Having found θ and ϕ the Cartesian projected plane coordinates can then simply be expressed as;

$$\xi = R_\theta \sin\phi \tag{3.48}$$

and

$$\eta = R_\theta \cos\phi. \tag{3.49}$$

Note, I have used ξ and η for my projected plane coordinates rather than x and y as in Calabretta & Greisen (2002) to avoid confusion with x and y representing the pixel coordinates. For the gnomonic TAN case R_θ is given by

$$R_\theta = \frac{180^\circ}{\pi} \cot\theta. \tag{3.50}$$

Finally the coordinate description matrix is expressed for the 3 points as

$$CD = \begin{pmatrix} A, B, 0, 0 \\ 0, 0, A, B \\ C, D, 0, 0 \\ 0, 0, C, D \end{pmatrix}^{-1} \begin{pmatrix} \xi_1 \\ \eta_1 \\ \xi_2 \\ \eta_2 \end{pmatrix}, \tag{3.51}$$

$$CD = \begin{pmatrix} a, 0, c, 0 \\ b, 0, d, 0 \\ 0, a, 0, c \\ 0, b, 0, d \end{pmatrix} \begin{pmatrix} \xi_1 \\ \eta_1 \\ \xi_2 \\ \eta 2 \end{pmatrix}. \tag{3.52}$$

With

$$A = x1 - CRPIX1, \tag{3.53}$$

$$B = y1 - CRPIX2, \tag{3.54}$$

$$C = x2 - CRPIX1, \tag{3.55}$$

$$D = y2 - CRPIX2, \tag{3.56}$$

Finally the elements of the coordinate description matrix are then given as

$$CD_{11} = a \times \xi_1 + c \times \xi_2, \tag{3.57}$$

$$CD_{12} = b \times \xi_1 + d \times \xi_2, \tag{3.58}$$

$$CD_{21} = a \times \eta_1 + c \times \eta_2, \tag{3.59}$$

$$CD_{22} = b \times \eta_1 + d \times \eta_2, \tag{3.60}$$

These are then written into the fits header, along with the reference coordinates of $CRPIX1$, $CRPIX2$, $CRVAL1$ and $CRVAL2$ along with the correct format code specifying that a Gnomonic TAN projection had been used in order to complete the astrometic solution for the image.

3.7 Surveys and Data Access

The work presented in this thesis has made significant use of data taken by many wide field surveys in order to photometrically and astrometrically calibrate data, as well as allowing for the efficient surveying of the entirety of a cluster. The vast amount of data generated by these programmes has in turn revolutionised the way in which the data must be stored and accessed. The databases that have been generated have also enabled astronomers to perform a myriad of different cross-correlations between data sets, all the while increasing the available information that can be attributed to each celestial source.

3.7.1 2MASS

The 2MASS was conceived to be the successor to the Two Micron Sky Survey carried out in 1969. Using two dedicated telescopes, one on Mount Hopkins, Arizona for the northern hemisphere and another at Cerro Tololo, Chile for the southern hemisphere it amassed ≈25.4Tbytes of data on over 99.9% of the celestial sphere. Using the J (1.24μm), H (1.66μm) and Ks (2.16μm) photometric bands and 7.8s of accumulated exposure for each on sky source, 10σ detection levels of J=15.8, H=15.1 and Ks=14.3 were reported (Skrutskie et al. 2006). Its photometric and astrometric accuracy have since been exploited and used by other survey programs (Hodgkin et al. 2009) for their calibration efforts. Data access to 2MASS is provided by NASA's Infrared Processing and Analysis Center (IPAC) and Infrared Science Archive (IRSA). Catalogues are also housed and can be queried from the VizieR service provided by the Centre de Données astronomiques de Strasbourg.

3.7.2 Sloan Digital Sky Survey (SDSS, Sloan)

The SDSS (York et al. 2000) has been producing both imaging and spectroscopic data for over 10 years, with the SDSS-III program lasting through to 2014. During this period the 2.5m telescope at Apache Point Observatory, Sunspot, New Mexico with its 120-megapixel camera and pair of optical fibre fed spectrographs has surveyed more than 11,600 square degrees cataloguing over 350 million unique objects. The SDSS Legacy Survey (The completed SDSS-I proposal) alone produced imaging and spectra of over 120,000 quasars. Observing on the AB magnitude system the detection limits of the u, g, r, i and z' filters were reported by the seventh data release as 22.0, 22.2, 22.2, 21.3 and 20.5 respectively. The SDSS data can be accessed via traditional radial, cone and rectangular searches as well as by more advanced SQL searches carried out by the SDSS

Catalog Archive Server (CAS) and Data Archive Server (DAS).

3.7.3 UKIRT Infrared Deep Sky Survey (UKIDSS)

UKIDSS was conceived as part of the next generation of NIR sky surveys considered to be the successors to 2MASS, with UKIDSS offering J, H and K depths some three magnitudes deeper. UKIDSS began its goal of surveying 7500 square degrees of the northern hemisphere from Mauna Kea, Hawaii, (VISTA will survey the southern hemisphere) in May 2005. A large proportion of its survey area was also designed to coincide with that of the optical SDSS program. UKIDSS actually comprises five survey programs (Lawrence et al. 2007); the Large Area Survey (LAS), the Galactic Plane Survey (GPS), the Galactic Clusters Survey (GCS), the Deep Extragalactic Survey (DXS) and the Ultra-deep Extragalactic Survey (UDS). The data contained within this thesis have been taken from the GCS which in addition to the J, H and K filters offers the use of the Z and Y filters (Hewett et al. 2006).

The corresponding survey depths as of the latest data release (Data Release 8; DR8) are as follows; Z=20.4, Y=20.1, J=19.6, H=18.8 and K=18.2. An additional survey in K only is planned for the GCS survey in order to measure proper motions for objects in the clusters and star forming regions of Alpha Per, Coma Berenices, The Hyades, IC 4665, Orion, Perseus OB2, The Pleiades, Praesepe, Scorpius and Taurus-Auriga. The data for each UKIDSS survey is processed by the CASU (Dye et al. 2006; Hodgkin et al. 2009) before being archived and released from the WFCAM Science Archive (WSA;

Hambly et al. 2008) by the Wide Field Astronomy Unit (WFAU) located at the Royal Observatory in Edinburgh. The data in the archive can be accessed from traditional menu driven queries on parameters such as RA and dec but also via the use of free-form SQL commands making use of the relational links set up to the 2MASS and SDSS catalogues amongst others.

Chapter 4

Praesepe

4.1 Introduction

Presented in this chapter are the results of a large and deep optical-NIR multi-epoch survey of the Praesepe open star cluster using data from the UKIDSS DR6 GCS (Baker et al. 2010) with follow up using the DR8 also reported. Multiple colour magnitude diagrams were used to select potential members with proper motions being used to assign levels of membership probability. This chapter describes the data aquisition and analysis with comparisons made against similar studies.

4.2 Cluster Properties

Praesepe lies at a distance of ≈180 pc ($(M-m)_0$ =6.30 ± 0.07, van Leeuwen 2009) with zero reddening and near solar metallicity. Whilst the distance is fairly well constrained, there is a lack of agreement with regards to its age. Allen (1973) placed the value of

Praesepe's age towards the lower end of the scale at 430 Myr and was the standard value for many years. Later work by Vandenberg & Bridges (1984) placed it at a much higher value of 900 Myr. Their value was obtained via the fitting of models describing the main-sequence to the observed colour magnitude diagrams (CMDs). The widest range of age estimates is reported by Tsvetkov (1993) who placed a similar lower limit of 540 Myr but an upper limit of over 1.5 Gyrs. The method of Tsvetkov did not depend on the fitting of the Zero-Age-Main-Sequence but instead relied on models used to calculate the ages of δ Scuti stars that are present within the cluster. Finally, Kharchenko et al. (2005) placed the age in the middle at 795 Myrs after using the Padova grid of post main sequence isochrones from Girardi et al. (2002). This is considered to be closest to the most likely age, as there is some evidence that the Hyades cluster at 625 Myrs shares a common origin with Praesepe (Eggen 1960; Henry et al. 1977). However due to the uncertainty that exists, two ages for the cluster have been adopted throughout this analysis. The first is an age of 500 Myr and the second 1 Gyr. These were chosen as they coincide nicely with ages for which the BT-NextGen and BT-DUSTY models have been calculated.

Praesepe's members all have a common proper motion centred around $\mu_\alpha = -35.81$ mas yr^{-1} and $\mu_\delta = -12.85$ mas yr^{-1}, again from the work by van Leeuwen based on re-reduced Hipparcos data. This distinct proper motion allows relatively easy photometric and astrometric membership surveys to take place. The "high-mass" stellar population (V<13) was identified by Klein Wassink (1927) with "intermediate-mass" (V<17) and "low-mass" M-dwarfs (R>20) being identified by Jones & Cudworth (1983) and Hambly et al. (1995a) respectively. Further work has been carried out by Pinfield et al. (1997, 2003), Adams et al. (2002a), Chappelle et al. (2005) and González-García et al. (2006). However, these surveys have often proved to be contaminated with an excess of field stars, as in the case of Adams et al. or have no proper motion information (Pinfield et al. 1997). The most comprehensive study to date was produced by Kraus & Hillenbrand (2007), who used data from the SDSS, 2MASS, USNOB1.0 (Monet et al. 2003) and finally UCAC2 to find 1010 candidate members of Praesepe, 442 being identified for the first time, down to a spectral type of around M5. The work presented in this chapter is again a return to a search for this "low-mass" population using data made available from the UKIDSS DR6 GCS, 2MASS and SDSS.

4.3 Data Acquisition

To retrieve the data from the WSA a similar SQL query to that of Lodieu et al. (2007b) was devised (See Appendix A for the full queries). The query was adapted to cross match with the SDSS through the use of the newly implemented gcsSourceXDR7PhotoObj table. The Class parameter in each of the five filter bands was set to only select objects that matched with criteria -2 or -1 in value, i.e. those that had been deemed stellar in nature by the pipeline. While this clearly limits the number of sources by requiring the object to be present in all bands, particularly at the faint end (Lodieu et al., 2007a), it does mean a greater level of reliability for the data that have been selected. Alongside the class selection criteria, the query also placed various quality control mechanisms as defined by the use of the post processing error bits flags on the UKIDSS data and the

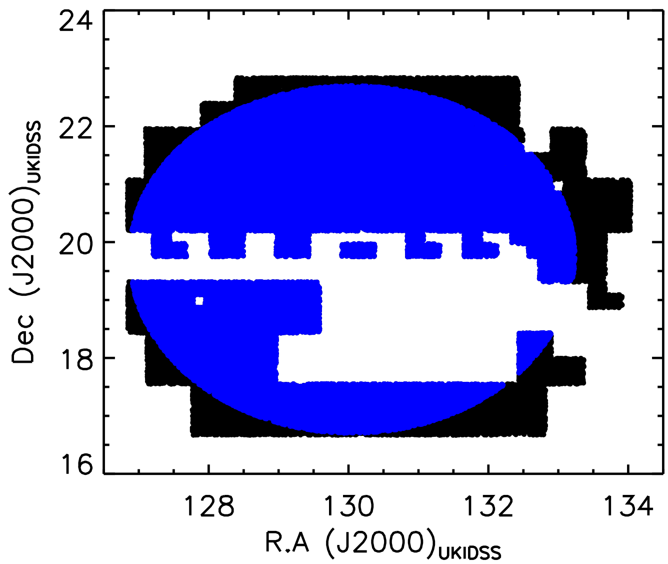

FIGURE 4.1. The full coverage of the Praesepe star cluster available from UKIDSS DR6 with the blue region denoting sources present in the 3 degree radial selection.

flags contained within the SDSS subsection[1].

The SQL query retrieved a total of 79,162 sources from the DR6 archive. When asking for the 2MASS and SDSS cross tables, the UKIDSS source identifier was used in order to merge the two separate queries into a master table, with each source containing any data from UKIDSS, 2MASS and/or SDSS. This match was performed using the TOPCAT program in the STARLINK suite of programs. To try and minimise the contamination due to field stars at the outer edges of the survey area where the cluster is more diffuse, a 3 degree radial cut on the data was applied from the cluster centre. This left 59,779 sources in the UKIDSS DR6 GCS dataset. The UKIDSS DR6 survey failed to fully

[1]The SDSS flag selections were taken from clean photometry section of the SDSS SQL query sample page http://cas.sdss.org/dr6/en/help/docs/realquery.asp Due to the nature of the objects being investigated the constraints were placed only on bands in which the object was likely to be present i.e The i and z' bands.

survey the cluster's extent with only ≈23 square degrees being available in all filters. Restricting this using the 3 degree radial cut limits the area to ≈18 square degrees. The main issue with the UKIDSS GCS DR6 data set is the missing region centred over the cluster's center, Figure 4.1.

The objects found by Adams et al. (2002a), Chappelle et al. (2005), Hambly et al. (1995b), González-García et al. (2006), Kraus & Hillenbrand (2007), Pinfield et al. (1997) and Pinfield et al. (2003) were then matched to this DR6-GCS dataset to select only those whose survey areas overlapped and could be recovered from our data. In total 642 sources were recovered from Adams et al. (who in total report 4,954 objects for their whole survey), 6 from Chappelle et al. (26 in total), 109 from Hambly et al. (515 in total), 0 from González-García et al. (20 in total), 274 from Kraus & Hillenbrand (1,130 in total), and 5 from each of the Pinfield surveys[2]; these can all be seen in Figure 4.2.

The first run of the SQL query contained a cross-correlation between the UKIDSS DR6 GCS dataset with its nearest 2MASS counterpart. This cross-correlation allows a determination of proper motion for the matched objects. Typically over a small area the astrometry provided by 2MASS is good to 50 mas (Skrutskie et al., 2006). As the CASU pipeline performs its astrometric calibration for the WFCAM data based on point sources within the 2MASS catalogues, accurate relative proper motions can be derived by simply taking the difference in 2MASS and WFCAM positions and dividing by the epoch difference (Lodieu et al. 2007b; Jameson et al. 2008). The 2MASS epoch date in the Julian Date format was converted into the Modified Julian Date format used by UKIDSS

[2]The objects retrieved from the two Pinfield surveys are the same 5 objects.

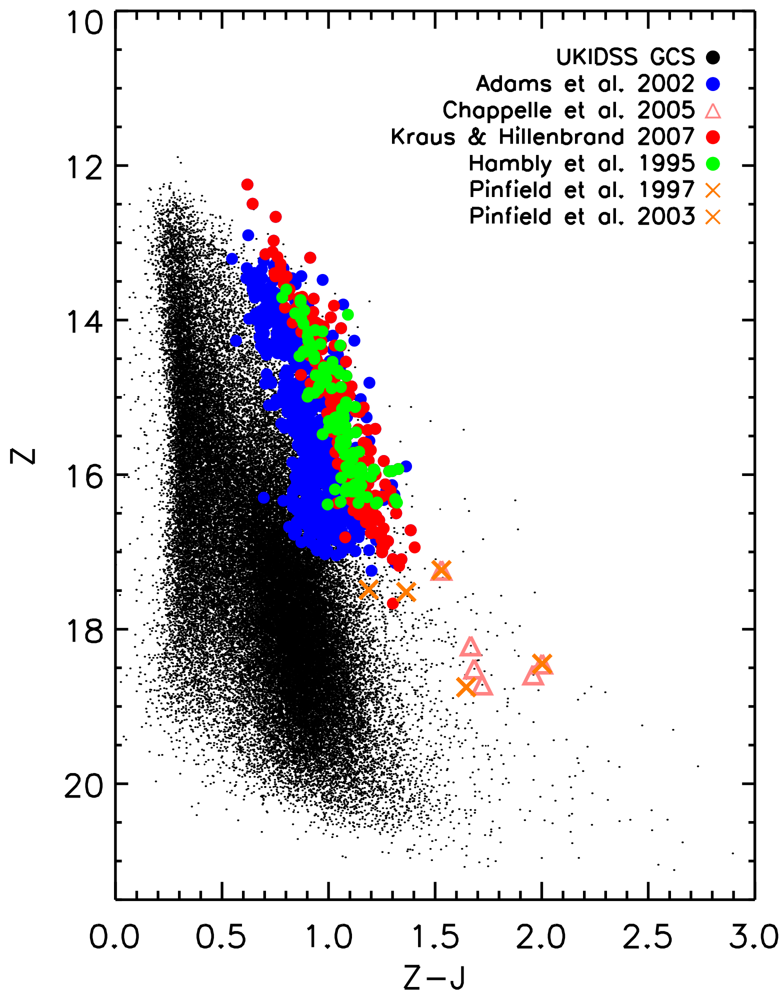

FIGURE 4.2. (Z-J,Z) CMD for the $\approx$ 18 square degrees of the Praesepe cluster selected from the WFCAM Science DR6 Archive with a corresponding 2MASS source within the inner 3 degrees of the cluster centre. Matches to this data set from the surveys of Adams et al. (2002b), Chappelle et al. (2005), Hambly et al. (1995b), Kraus & Hillenbrand (2007), and Pinfield et al. (1997 and 2003) are also shown. The survey of González-García et al. did overlap with this area however for those sources within the region no matches were found, due possibly to the strict selection criteria on the UKIDSS data.

automatically with the resulting proper motion also being converted into mas yr^{-1} by the SQL query when run through the WSA data centre. The accuracy of the astrometry and the average time baseline of around 5 years provides an error of ≈10 mas yr^{-1}. Of the 59,779 sources 34,990 were found to have 2MASS counterparts leaving 24,789 with no 2MASS identifier. Because 2MASS lacks the depth of UKIDSS we only retrieved the brighter of our sample ($K < 16.5$) from this dataset, with the SDSS dataset providing the fainter candidates (The extent of the data set can be seen in Figure 4.2).

Thanks to the implemented gcsSourceXDR7PhotoObj table linking the WFCAM DR6 and SDSS DR7 data sets at the WSA, a cross-correlation between the UKIDSS data set and that of the SDSS was also available for interrogation. SDSS DR7 reported having surveyed 11,000 square degrees in all of its five filters ($ugriz'$) which included the full area of Praesepe (Kraus & Hillenbrand, 2007). Upon inspection of the survey dates it became apparent that only a short amount of time had elapsed between the survey of Praesepe by SDSS and that of UKIDSS (≈2 - 2.5 years on average). The lack of a decent baseline therefore warranted a different approach in order to calculate proper motions and thus cluster membership assignment from that which will be detailed for 2MASS. Again the 59,779 UKIDSS sources were retrieved with 53,562 having an SDSS counterpart and 6,253 being unique to UKIDSS. In total UKIDSS has 2,225 unique sources for which no counterpart has been found in either 2MASS of SDSS (30,998 objects were present in all three surveys).

4.4 Members of Praesepe from 2MASS

This section will describe the processes undertaken to construct the list of candidate cluster members in Praesepe from the UKIDSS colour magnitude diagrams, and where possible proper motion vector point analysis based from the UKIDSS DR6-2MASS cross-correlation. The procedure is as follows:

1. Select only those sources that have a 2MASS identifier associated with their UKIDSS identifier and are within 3 degrees of the defined cluster centre (34,990 objects).

2. To check the proper motion errors fit the reduced data set (CMD and radius selections imposed) with a two dimensional Gaussian, then use the σ of the Gaussian to act as a proxy for the error.

3. Using the theoretical isochrones, select objects that are no more than 0.3 magnitudes to the left, and all of those on the right in both the (Z-J,Z) and (Y-K,Y) CMDs.

4. Analyse the resulting Vector Point Diagram (VPD) for this colour selected data set across a range of magnitude bins and infer from the probability fitting routine a level of cluster membership for each object. Then select out a high probability sample (HPM) with assigned probabilities of p$\geq$0.60.

4.4.1 Calculating Proper Motions

The cross-correlation of UKIDSS with 2MASS provided a value for the matched objects proper motion in $\mu_\alpha \cos_\delta$ and μ_δ. An estimate of the errors based on the time baseline and specifications of 2MASS is $\approx$10 mas yr^{-1}. To confirm this error estimate, the proper motions for those sources that lay within 3 degrees of the cluster centre (which were spread over a region of proper motion space from -150 to 150 mas yr^{-1}) were divided into bins of 20 mas yr^{-1} and the number in each bin totalled. A two dimensional Gaussian was then fitted, enabling a determination of the cluster spread. Objects that were defined as being outside of the 3σ limit were then removed and the fit reapplied. The σ of the Gaussian then provides an estimate for the error in the proper motions (See Lodieu et al. 2007a; Jameson et al. 2008 for further explanation and diagrams) and was found to be of the order of $\approx$12 mas yr^{-1}, instead of the assumed 10 mas yr^{-1}.

4.4.2 Colour Magnitude Diagrams

In order to select candidates from the CMDs the BT-NextGen and BT-DUSTY theoretical isochrones were used with the distance modulus of the cluster added to their photometric values. Due to the temperatures and masses being explored by this survey the objects involved inhabit both the “non-dusty” and “dusty” atmospheric regimes and so the two isochrones needed to be combined. To create a composite isochrone line, the data points from the BT-NextGen isochrone in the relevant band filter were taken to their minimum temperature $\approx$3000 K. This temperature lies just above where dust grains begin to form in the BD atmosphere and the BT-NextGen models become invalid. Combining the BT-DUSTY isochrone models ($T_{eff} < 3000$ K) with the BT-Nextgen models at this point with a simple straight line between the resulting break, the composite isochrone was calculated. This was done for both the 500 Myr and 1 Gyr evolutionary models due to the uncertainty in the age of Praesepe. It was then employed in both the (Z-J,Z) and (Y-K,Y) CMDs with sources laying no more than 0.3 magnitudes to the left in the horizontal direction from the line and those to the right being selected and passed to the proper motion fitting routine. See Figure 4.3 for the VPD and the two CMDs associated with the spatial and colour cut selections. This process selected 7,127 objects out of the possible 34,990. This selection is rather conservative as it aimed to include all the cluster members from the previous surveys, most notably that of Adams et al. (2002a) whose objects appear far bluer than those found by both Kraus & Hillenbrand (2007) and by Hambly et al. (1995b).

4.5 Cluster Distributions and Membership Probability

To calculate the membership probabilities for the UKIDSS DR6-2MASS data sample, two PM distributions were fitted to the cluster. One, a circularly symmetric Gaussian as originally employed by Sanders (1971) and also Francic (1989), and two, an exponential decaying in the direction of the cluster proper motion centre coupled with a perpendicularly oriented Gaussian (Hambly et al. 1995b; Deacon & Hambly 2004). For the fitting process to work the cluster proper motion centre (-35.81,-12.85) is rotated from its original position in proper motion space to lie on the y-axis. The following set of equations

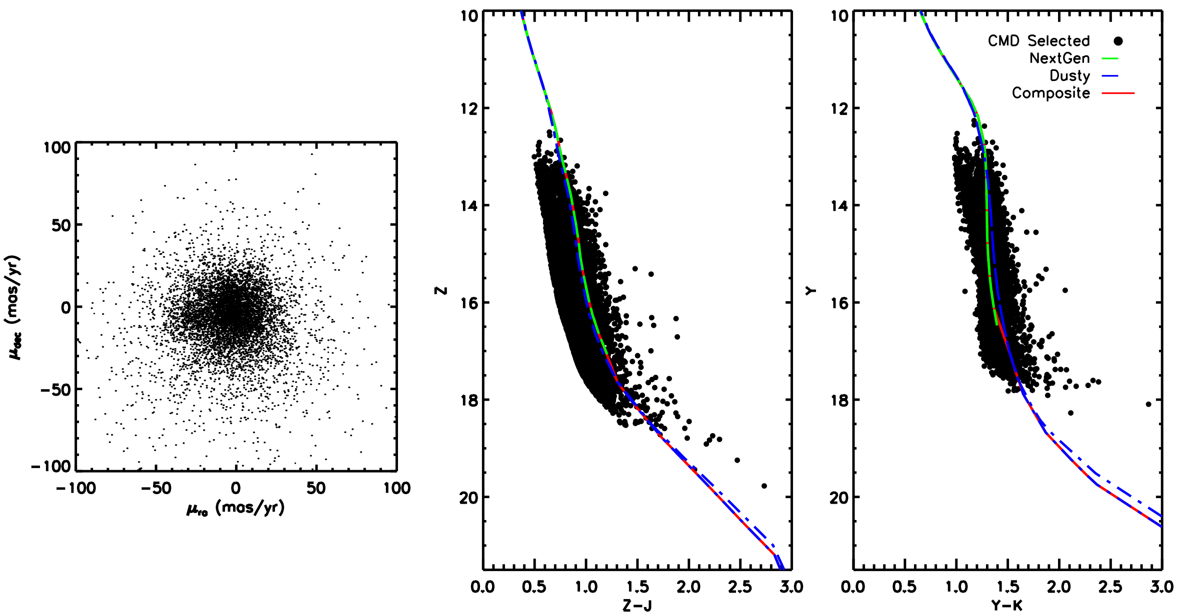

FIGURE 4.3. On the left is the VPD for the sources selected from the spatial and colour cuts in the (Z-J,Z) and (Y-K,Y) colour magnitude diagrams as shown in the middle and on the right respectively. The cluster can be seen as the over-density of objects around -30 and -10 mas yr^{-1} in RA and Dec. The green dashed line is the theoretical isochrone for the BT-NextGen evolutionary model and the blue BT-DUSTY equivalent. Both the 500 Myr and 1 Gyr flavours have been considered due to the uncertainty in the age of Praesepe.

describes the field distribution (Φ_f) the cluster distribution (Φ_c) and the normalisation to the exponential (c_o).

$$\Phi_f = \frac{c_o}{\sqrt{2\pi}\Sigma_x} exp\left(-\frac{(\mu_x - \mu_{xf})^2}{2\Sigma_x^2} - \frac{\mu_y}{\tau}\right). \tag{4.1}$$

$$\Phi_c = \frac{1}{2\pi\sigma^2} exp\left(-\frac{(\mu_x - \mu_{xc})^2 + (\mu_y - \mu_{yc})^2}{2\sigma^2}\right). \tag{4.2}$$

$$c_o = \frac{1}{\tau\left(e^{-\frac{\mu_1}{\tau}} - e^{-\frac{\mu_2}{\tau}}\right)}. \tag{4.3}$$

Where,

$$c_o \int_{\mu_1}^{\mu_2} e^{-\frac{\mu_y}{\tau}} d\mu_y = 1. \tag{4.4}$$

The values of μ_x and μ_y refer to the proper motion attributed to each individual object. The quantity σ is the Gaussian width, whilst μ_{xc} and μ_{yc} are the cluster's mean proper motion. Σ_x is the proper motion dispersion value in x and τ the exponential scale length for the field proper motion distribution in y. μ_{xf} is the field mean proper motion in x and finally μ_1 and μ_2 are the limits for the normalisation to the exponential c_o. For the rotated VPD these were set at 20 and 70 mas yr^{-1} to avoid the mass of stars centred around (0,0).

Combining the field star distribution and the cluster distribution with information about the fraction of stars which are field stars (f) the resulting expression for the total distribution (Φ) is

$$\Phi = f\Phi_f + (1-f)\Phi_c. \tag{4.5}$$

After employing the method of maximum likelihood with Θ representing one of the free parameters,

$$\sum_i \frac{\delta ln\Phi_i}{\delta\Theta} = 0, \tag{4.6}$$

a set of nonlinear equations can be defined as the following.

$$f : \sum_i \frac{\Phi_f - \Phi_c}{\Phi} = 0, \tag{4.7}$$

$$\sigma : \sum_i \frac{\Phi_c}{\Phi}\left(\frac{(\mu_x - \mu_{xc})^2 + (\mu_y - \mu_{yc})^2}{\sigma^2} - 2\right) = 0, \tag{4.8}$$

$$\Sigma_x : \sum_i \frac{\Phi_f}{\Phi}\left(\frac{(\mu_x - \mu_{xf})^2}{\Sigma_x^2} - 1\right) = 0, \tag{4.9}$$

$$\mu_{xf} : \sum_i \frac{\Phi_f}{\Phi}(\mu_x - \mu_{xf}) = 0, \tag{4.10}$$

$$\mu_{xc} : \sum_i \frac{\Phi_c}{\Phi}(\mu_x - \mu_{xc}) = 0, \tag{4.11}$$

$$\mu_{yc} : \sum_i \frac{\Phi_c}{\Phi}(\mu_y - \mu_{yc}) = 0, \tag{4.12}$$

$$\tau : \sum_i \frac{\Phi_f}{\Phi}\left(\frac{\mu_y}{\tau} - 1 - c_o(\mu_1 e^{-\frac{\mu_1}{\tau}} - \mu_2 e^{-\frac{\mu_2}{\tau}})\right) = 0. \tag{4.13}$$

To each of these equations a bi-section algorithm was devised that checked for root bracketing whilst it proceeded to find the root. Once one parameter has been determined, the next parameter is subject to the same process. Finally once τ has been found the process reverts back to its starting point and runs again until all the free parameters have been fixed (showing no further sign of deviation). To start the process a set of initial values is required for the free parameters, these are as in Deacon & Hambly (2004). Once the values are fixed, the membership probabilities for the i^{th} object can be calculated thusly;

$$p_i = \frac{(1-f)\Phi_{ci}}{\Phi_i}. \tag{4.14}$$

The fitted values for each magnitude interval are shown in Table 4.1 with the VPDs and probability histograms in Figure 4.4. Taking the σ value of the Gaussian from Section 4.4.1 and placing it over the cluster's centre of proper motion, 380 objects with a

Table 4.1. Fitted parameter values for the set of magnitude bins analysed by the VPD-Probability Fitting Routine.

Interval	f	σ	μ_{xc}	μ_{yc}	τ	Σ_x	μ_{xf}
12.00 < Z < 14.00	0.75	3.28	3.53	27.73	21.46	18.94	-5.43
14.00 < Z < 16.00	0.71	5.45	4.43	30.65	14.26	18.89	-4.00
16.00 < Z < 18.00	0.89	5.43	-0.27	31.87	14.91	19.54	-1.95

probability assignment were found. Of these, 121 have probabilities that place them in the high membership bracket (p $\geq$ 0.60). In total 145 sources are found to have a p $\geq$ 0.60. The 24 laying outside the sigma selection are still very much consistent with the cluster as can be seen by the small spread of objects in proper motion space in Figure 4.4.

4.6 Members of Praesepe from SDSS

In this section the process for locating any possible candidates/members of the Praesepe cluster from available data within the cross link between UKIDSS and SDSS will be described. The procedure is as follows:

1. Select those objects that are again within the 3 degree radial cut from the cluster centre. These objects are only present in the UKIDSS DR6-SDSS data set. Any corresponding SDSS-2MASS source would have been treated within the previous section.

2. Select the list of candidate objects from 6 CMDs.

3. Extract the FITS files for these objects from the WSA and SDSS Data Access Server.

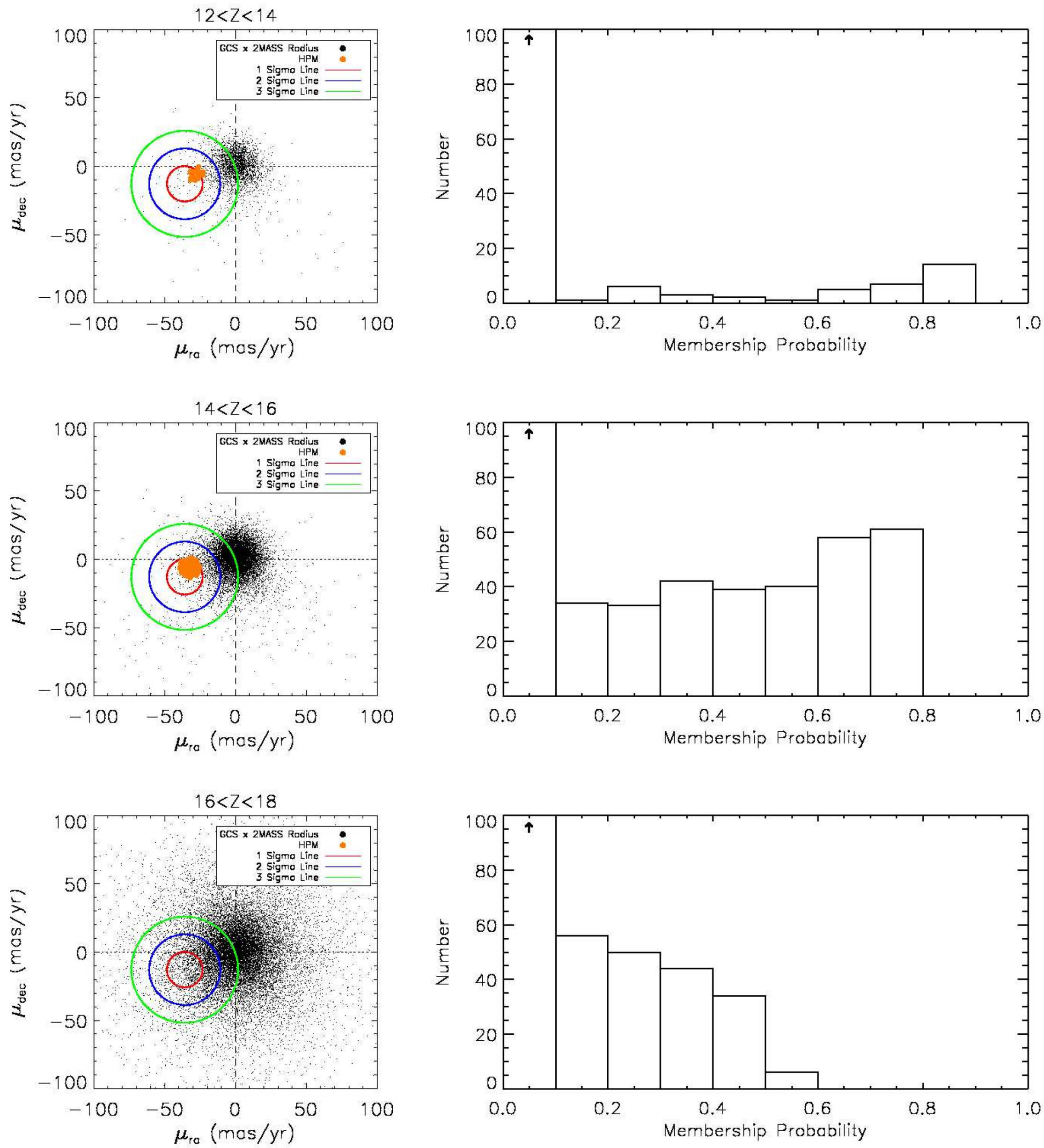

FIGURE 4.4. Proper motion VPDs and the resulting probability histograms for each magnitude interval in the probability fitting of the Praesepe data. In each plot the three coloured lines represent the 1σ, 2σ and 3σ errors obtained from the estimate of proper motion errors by way of the 2D Gaussian fit, they have been shifted to be located over the cluster's proper motion centre. The points in orange show the high probability sample and are in agreement with the direction of motion shown for the Praesepe cluster. The zero motion field stars can clearly be seen to be located around 0,0.

4. Calculate a pixel-pixel transformation between the two images and using the epoch difference calculate a proper motion.

5. Perform a basic probability analysis on the resulting data.

4.6.1 Extracting the Candidates

Performing the same radial cut with objects only present in the UKIDSS DR6-SDSS match (no 2MASS counterpart) led to a selection of 22,564 objects. To extract the candidates from this list, a series of photometric cuts were applied in a range of different CMDs. These can be seen in Figure 4.5. These CMDs made use of a range of different filters and known locations of low-mass stars and BDs as detailed by Hawley et al. (2002). Objects within these predefined regions were selected for further analysis.

4.6.2 Refinement of Proper Motions

The primary problem with the SDSS dataset is the small epoch difference between the two surveys. This subsequently results in larger errors on the proper motion and when coupled with a small number of objects (< 100) means that the analysis as performed for the 2MASS data is not applicable. An alternate approach has therefore been taken in order to assign membership probabilities to these candidates. To begin with, suitable queries were devised to allow for the acquisition of the catalogue and image FITS flat files from each survey's data centre [3]. The candidate objects were then located and a set

[3]For the SDSS data this involved creating a few specific requests as the catalogue data is split amongst a wide range of files. The SDSS DAS has also recently been updated to SDSS DAS Version 2 for use with

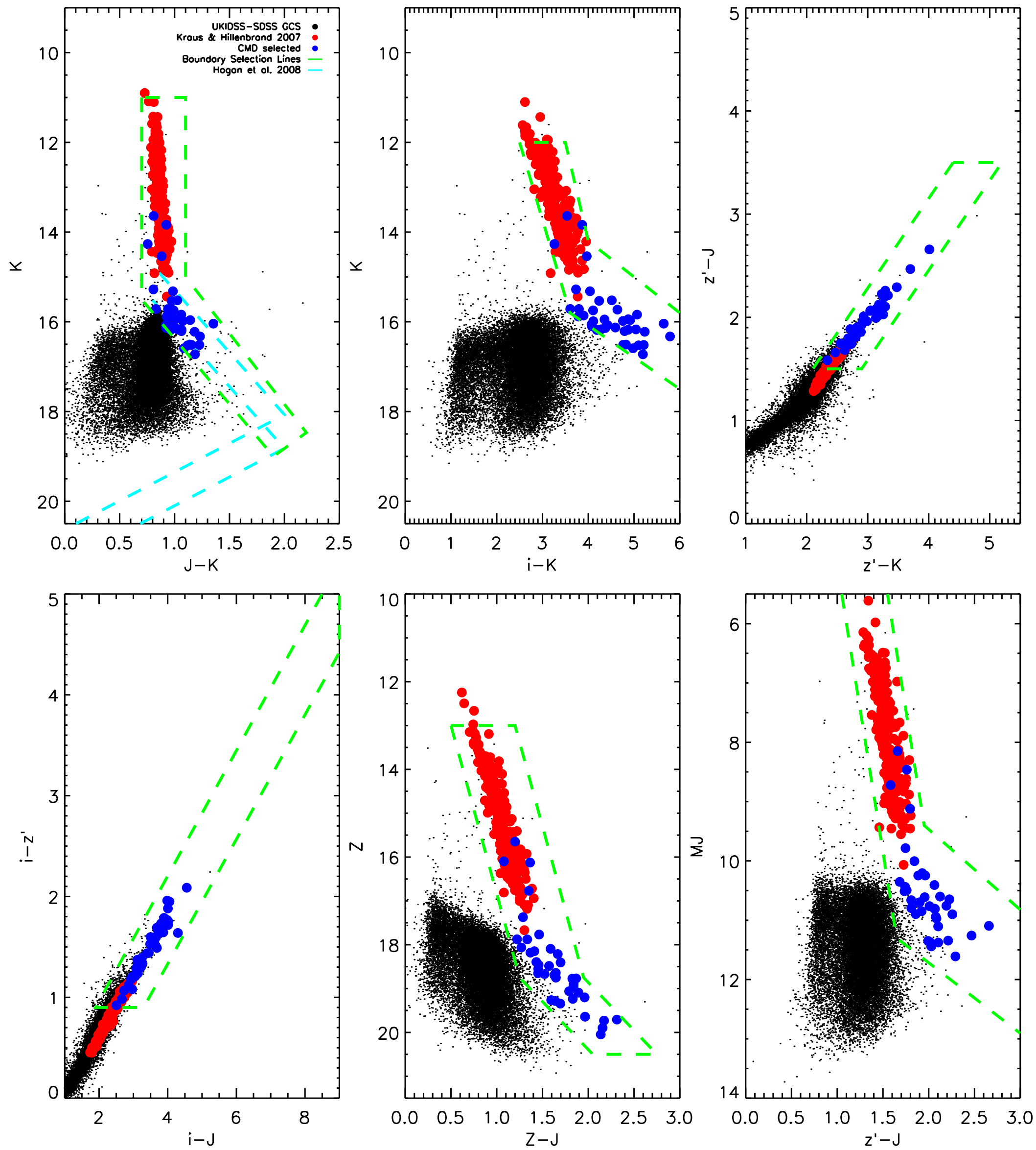

FIGURE 4.5. Colour-magnitude and colour-colour diagrams for SDSS and UKIDSS DR6 photometric bands showing the selection regions (as denoted by the green dashed lines) used to extract the set of 39 candidate objects as shown by the blue circles. The objects of Kraus & Hillenbrand (2007) shown in red have been used alongside information from plots in figure 9 of Hawley et al. (2002) to denote the appropriate approximate regions for the cluster sequence. The Hawley et al. (2002) regions were defined using objects that are fully contracted, given the uncertainty in the age of Praesepe the higher mass sub-stellar objects will according to Burrows et al. (2001) still be undergoing a slight contraction. Additionally the cluster sequence for the Hyades (a cluster of similar age to Praesepe) as found by Hogan et al. (2008) has been corrected to Praesepe's distance and over plotted in the J-K, K plot (blue dashed line) to help trace any possible cluster sequence. The black dots are the UKIDSS DR6-SDSS sources that are not present in the UKIDSS DR6-2MASS population.

of reference objects selected. These reference objects had to be common to both chips (appearing in each epoch), be in the magnitude range $12.0 < Z < 18.0$, have ellipticities less than 0.2 (from UKIDSS catalogue data) and not sit within 5% of the chip border (in pixels) in order to help minimise any radial distortion effects.

The list of reference objects was then used to create a 12 parameter transformation (where too few reference objects were present for the quadratic fit a linear 6 parameter fit was tried instead) that allowed the motion of the candidate object between the two epochs to be calculated. Reference objects that were shown to be moving at a rate greater than 3 times the RMS value of the fit were discarded. The revised reference list was again passed to the fitting routines in order to calculate the correct coefficients that described the motion between the two epochs. This motion was then converted into mas yr^{-1} through the use of equations in Chapter 3.

In order to calculate errors on the proper motions, the magnitudes (m) of all possible objects on the reference flat file images were needed due to the centroiding accuracy of the source extraction routines decreasing as the objects become fainter (less signal-to-noise). To calculate the magnitudes from the WFCAM flat files, which like their SDSS counterparts only return flux information by default the following equation was used;

$$m = -2.5 \times \log flux + zp - ext \times (((air1 + air2)/2) - 1) + 2.5 \times \log exp - apc. \quad (4.15)$$

DR7, users are instructed to read the DR7 release website for more information.

For the $flux$ values used, the appropriate aperture correction value (apc) used was $APCOR3$. The extinction coefficient, ext, along with the airmass values at the start and end of the science exposure ($air1$ and $air2$) can all be found within the FITS header supplied with either the catalogue or image, likewise for the exposure time exp and photometric zero-point (zp) as supplied by the reduction pipeline. For the SDSS data, the magnitude was calculated slightly differently, in this case the process was as follows.

Firstly, the extinction-corrected ratio of the observed count rate to the zero-point count rate was calculated using

$$\frac{f}{f_0} = \left(\frac{counts}{exp}\right) \times 10^{0.4(aa+kk\times airmass)}, \tag{4.16}$$

with aa and kk being the zero-point and extinction coefficients (again found in the relevant FITS file) whilst the $counts$ value is related to the number of photo-electrons measured by the detector via the detector's gain[4]. From this either the conventional Pogson magnitude or SDSS asinh magnitude can be calculated. The SDSS asinh magnitudes (Lupton et al. 1999) replace the logarithmic nature of the Pogson scale with an inverse hyperbolic sine function. For high signal-to-noise detections this shows little difference to the conventional magnitude but for fainter objects the function tends to a definite value with a finite error and as such becomes useful when approaching the detection limits of the survey. To calculate the SDSS magnitudes in terms of the Pogson scale equation 4.17 can be used, whilst for the asinh magnitudes equation 4.18 should be used.

[4]http://www.sdss.org/dr5/algorithms/fluxcal.htmlcounterr

$$m = -2.5 \times \log\left(\frac{f}{f_0}\right). \tag{4.17}$$

$$m = -\left(\frac{2.5}{\ln 10}\right) \times \left(asinh\left(\frac{\frac{f}{f_0}}{2b}\right) + \ln b\right). \tag{4.18}$$

The coefficient b in equation 4.18 is refered to as the softening parameter and for each photometric band[5] takes a different value. As an attempt to minimise the interference caused due to DCR, the proper motions were calculated between the SDSS z' and UKIDSS Z bands, thus the appropriate value for b was 7.4$\times10^{-10}$. After calculating the magnitudes the x and y pixel centroiding errors reported for each object in the catalogue files were then totalled for each bin of width two magnitudes and divided by the number in that bin to give an average centroiding uncertainty value. These values were then added in quadrature with the RMS in that particular direction as found by the 12 parameter quadratic fit.

$$error\_pm = \sqrt{RMS^2 + err^2_{epoch1} + err^2_{epoch2}}. \tag{4.19}$$

The values representing the error found in the x or y direction for both epoch 1 and epoch 2 measurements are in turn calculated from the following;

[5]The table of softening parameters for each photometric band can be found at http://www.sdss.org/dr6/algorithms/fluxcal.htmlcounts2mag.

$$\mu_{\alpha}\_err = \frac{((CD1\_1 \times xerr + yerr \times CD1\_2) \times 3600 \times 1000)}{epoch} masyr^{-1}, \qquad (4.20)$$

$$\mu_{\delta}\_err = \frac{((CD2\_1 \times xerr + yerr \times CD2\_2) \times 3600 \times 1000)}{epoch} masyr^{-1}, \qquad (4.21)$$

where $xerr$ and $yerr$ represent the centroiding errors in the x and y directions as described in the previous paragraph. The errors on the proper motion are likely an overestimation of the astrometric errors as they are based on the RMS from the fitting process rather than an error in the transformed coordinate (Hambly (2008)).

To try and calculate membership probabilities for these objects, an attempt at using control data to determine levels of contamination was undertaken. The cluster circle and two control circles of radius 26" were used. The radius value is the average value taken from the 12 parameter fit information, ignoring any obvious discrepancies (as objects become fainter the centroiding errors become larger). Those that were in the faintest magnitude bin had centroiding errors, a factor ten larger than for the other candidates, and so were discounted from the average. The circles were located at the same distance from (0,0) in proper motion space and as is usual, were split into magnitude bins with the probability being calculated using equation 4.22.

$$P_{membership} = \frac{N_{cluster} - N_{control}}{N_{cluster}}. \qquad (4.22)$$

$P_{membership}$ is the probability assigned for a particular magnitude bin, $N_{cluster}$ the number of field and cluster stars within the cluster circle and $N_{control}$ the number of field stars. Thus $N_{cluster}$-$N_{control}$ should give the number of Praesepe members. One flaw to this method as reported by Casewell et al. (2007) is that this method is dependent on the chosen location of the control circle. A solution to correct this is to use the field star count within the annulus of Figure 4.6 and scale this to the area of the cluster circle to estimate levels of contamination. The resulting probabilities for the control circles and annulus are reported in Table 4.2. Any negative probabilities have been altered to 0.00. The only magnitude bin to contain a positive probability is the bin $19 < Z \leq 20$, for which the control data revealed a probability of 0.5 and 1.0. The annulus method for the same magnitude bin put the probability at 0.58. These membership probabilities should be viewed with caution as the low numbers (i.e. few objects) make the probabilities difficult to fully substantiate. As such, objects in these fainter magnitude bins have not been taken into consideration when constructing the luminosity and mass functions reported in Section 4.7. When the survey of the cluster centre is completed, it is hoped that not only will more low-mass stars/BD candidates be found but that the increase in numbers will also allow for more robust membership probabilities to be assigned.

4.7 Cluster Mass and Luminosity Functions

In order to produce the luminosity function of the cluster the effects of incompleteness on the data must be taken into account. As magnitude increases, the number of objects in a specified magnitude bin of uniform distribution will also increase. Counting the

Table 4.2. Probability of membership against magnitude range for our methods of calculating probabilities of membership using the annulus as well as the two control areas.

Magnitude Range	Probability Annulus	Probability μ_α=0 mas yr^{-1} μ_δ=+37.85 mas yr^{-1}	Probability μ_α=+35.66 mas yr^{-1} μ_δ=-12.70 mas yr^{-1}
15 < Z < 16	0.000	0.000	0.000
16 < Z < 17	0.000	0.000	0.000
17 < Z < 18	0.000	0.000	0.000
18 < Z < 19	0.000	1.000	0.000
19 < Z < 20	0.581	0.500	1.000
20 < Z < 21	0.000	0.000	0.000

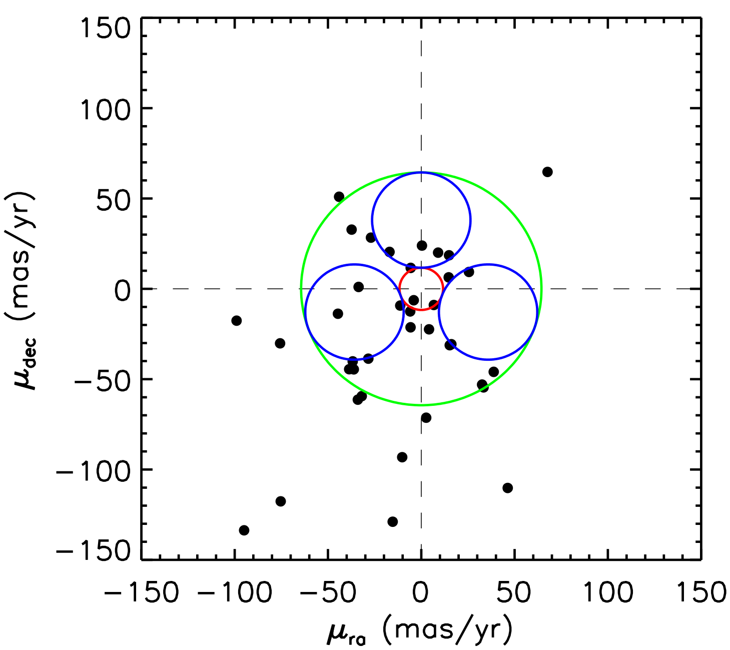

FIGURE 4.6. Proper motion vector diagram for the 39 UKIDSS DR6-SDSS candidate objects selected from the photometric cuts. The cluster location is at $\mu_\alpha = -35.81$ mas yr^{-1} & $\mu_\delta = -12.85$ mas yr^{-1} with the two control circles and the annulus used for the second measure of probability also plotted. None of these objects are included in the luminosity and mass function analysis.

number of stars present and comparing it to this predicted rate of growth will show up any signs of incompleteness (Deacon & Hambly 2004). This is done by taking the logarithm of the number of stars in the magnitude bin and fitting a best fit line to the data up until this "drop off" point. Given Praesepe's galactic lattitude of 32.48° it is placed well within the scale height of the disk and so an estimate for the level of incompleteness can be calculated from the deficit shown to the straight line shown in Figure 4.7. For the purposes of this study the best fit line was fitted between the black points in Figure 4.7 for the UKIDSS DR6-2MASS data set in the Z, J and K filters. The drop off can be clearly seen at the fainter magnitudes with the brighter magnitude drop off likely caused by the bright cut off limit of the surveys.

The cluster luminosity function (Figure 4.8) was calculated by summing the assigned membership probabilities of each object in bins of width one magnitude. Each interval was then multiplied by the incompleteness factor, producing the correction from the dashed blue to solid black lines. In order to avoid distorting the luminosity function this process was applied to the UKIDSS DR6-2MASS population only. The fainter magnitudes and tentative membership probabilities of the UKIDSS DR6-SDSS candidates excluded them, as inappropriately large correction factors would have to be applied. The luminosity function can be seen to have a clear and well defined peak in each of the filters followed by a decrease due to a change in slope of the mass-luminosity relationship (Figure 4.9). The first point in the J-band luminosity function has been artificially raised due to a large incompleteness factor being applied. This point is thus not treated when fitting the mass function. The errors shown are simply Poisson errors.

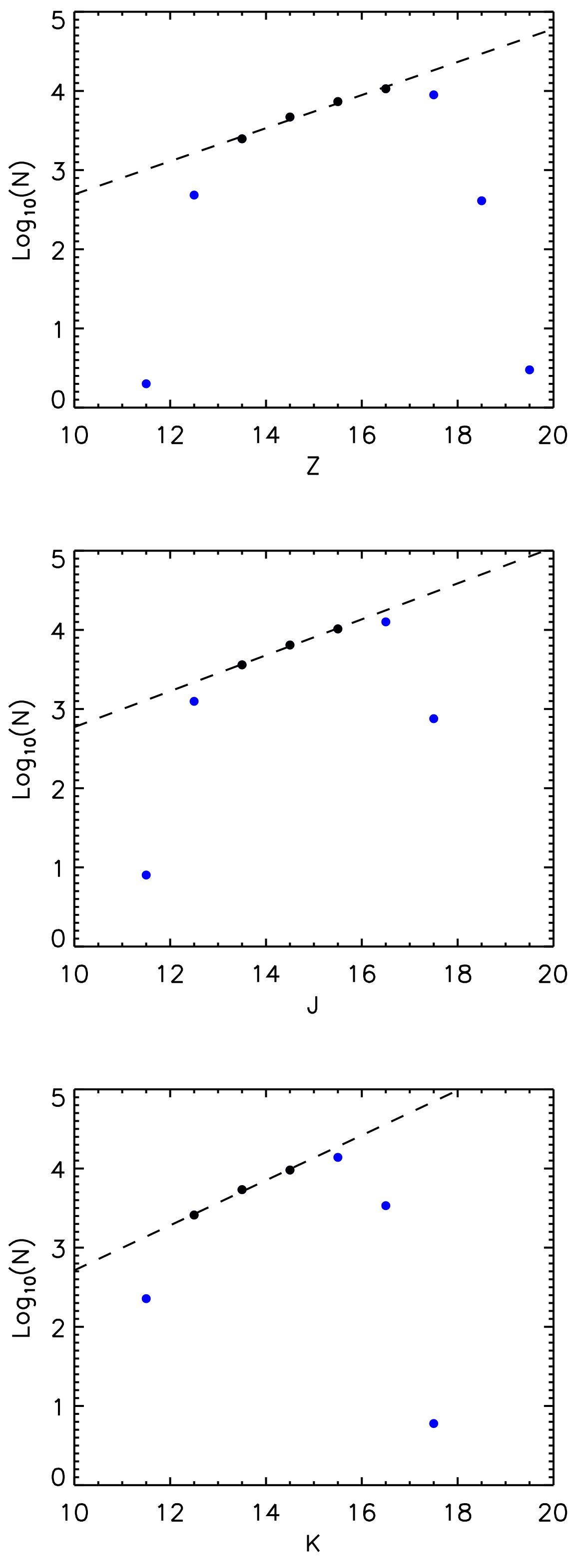

FIGURE 4.7. An estimate of the incompleteness in the 2MASS selected Praesepe data set for the UKIDSS Z, J and K bands respectively. The black dotted line is a least squares fit to the associated black points in figure. There is clearly a drop off at the end of the functions whilst the deficit for the brightest magnitude bins is caused by saturation effects.

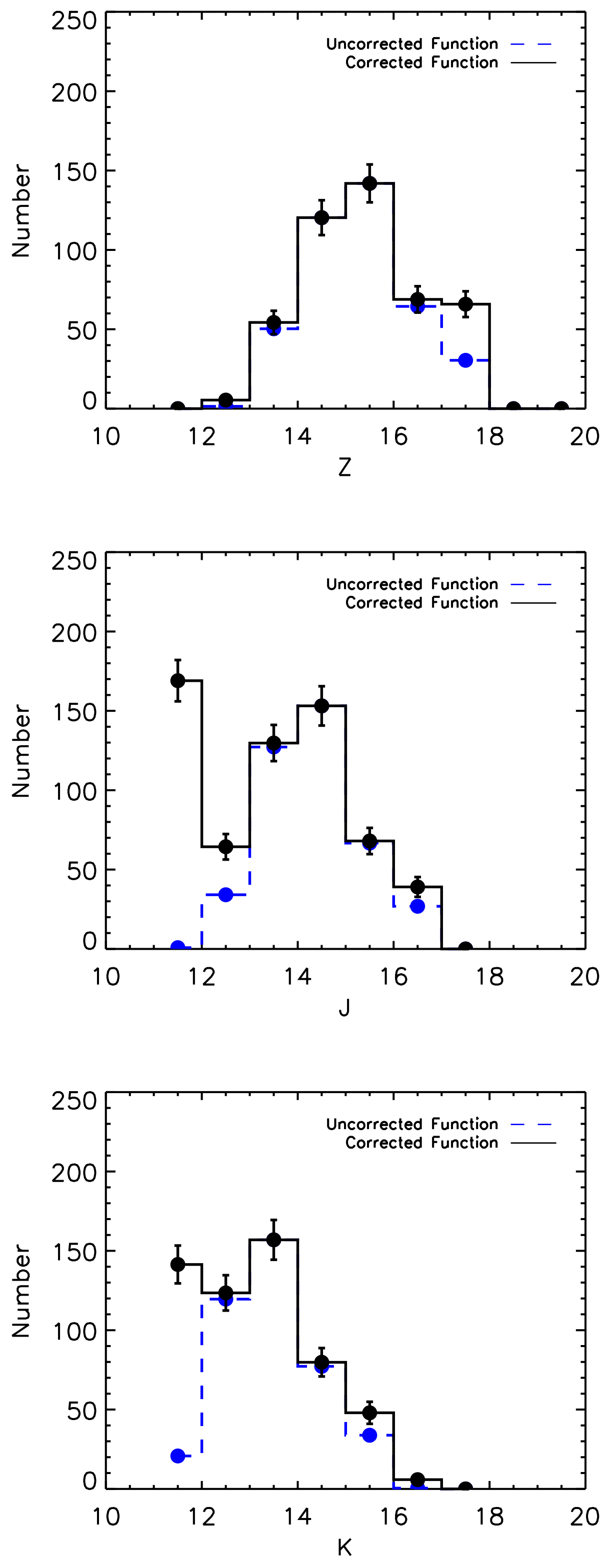

FIGURE 4.8. The Luminosity Functions derived for the Praesepe star cluster in the Z, J and K bands. The distribution rises to a peak before starting to decay due to the change in the slope of the mass-luminosity relationship. The error bars are Poisson errors (N.B These therefore should be Poisson based errors on N).

To convert the cluster luminosity function into a mass function, a mass-luminosity relationship is required (see Figure 4.9). Again, a combined relationship formed from the BT-NextGen and BT-DUSTY models was constructed with cubic spline interpolation used to interpolate between the points. As the age of the Praesepe cluster is not well confined this mass-luminosity relationship has again been constructed based on both the 500 Myr and 1 Gyr model data.

In Figure 4.10, Praesepe's cluster mass function is plotted with a single Scalo type power law between 0.6 and 0.125$M_{\odot}$ for the Z photometric band. The J and K bands have been treated similarly but due to the corrections applied for the incompleteness affecting a wider range of magnitudes a narrower mass range was considered.

The results of this fitting are that α_{500Myr}=1.11 $\pm$ 0.37 and α_{1Gyr}=1.10 $\pm$ 0.37. For the J and K bands the results were α_{500Myr}=1.07, α_{1Gyr}=1.07 and α_{500Myr}=1.09, α_{1Gyr}=1.09 respectively. These values are much lower than the Salpeter IMF (2.35) but the upper limits agree roughly with the values calculated and cited by Kraus & Hillenbrand (2007) of α=1.4 $\pm$ 0.2. The Kraus & Hillenbrand result was derived using a mass-spectral type relationship, however after retrieving 2MASS J band photometry for their objects and constructing the J band luminosity function as done for the UKIDSS DR6-2MASS sample α was found to differ by only 0.1.

A more recent survey of the cluster centre has also just been carried out by Boudreault et al. (2010). The authors identify some 150 candidate members with 6 expected to be BDs. Of these 6 only 3 were within the UKIDSS DR6 survey region, objects 55, 909

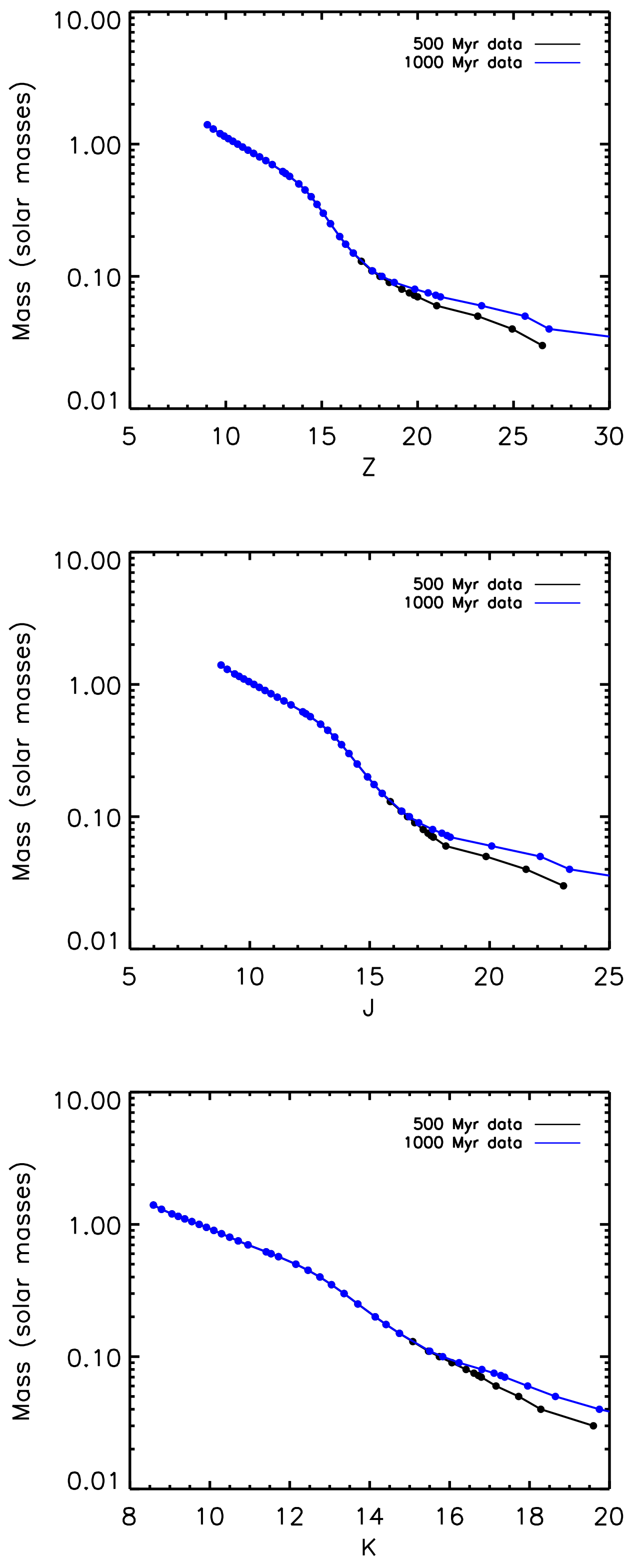

FIGURE 4.9. The mass-luminosity relationship used in this study is based on a composite BT-NextGen and BT-DUSTY line with a cubic spline interpolation. The black points represent the 500 Myr data whilst the blue the 1 Gyr data. The lines only start to deviate appreciably at faint magnitudes, which we do not investigate. Shown here is the mass-luminosity relationship for the Z, J and K bands respectively.

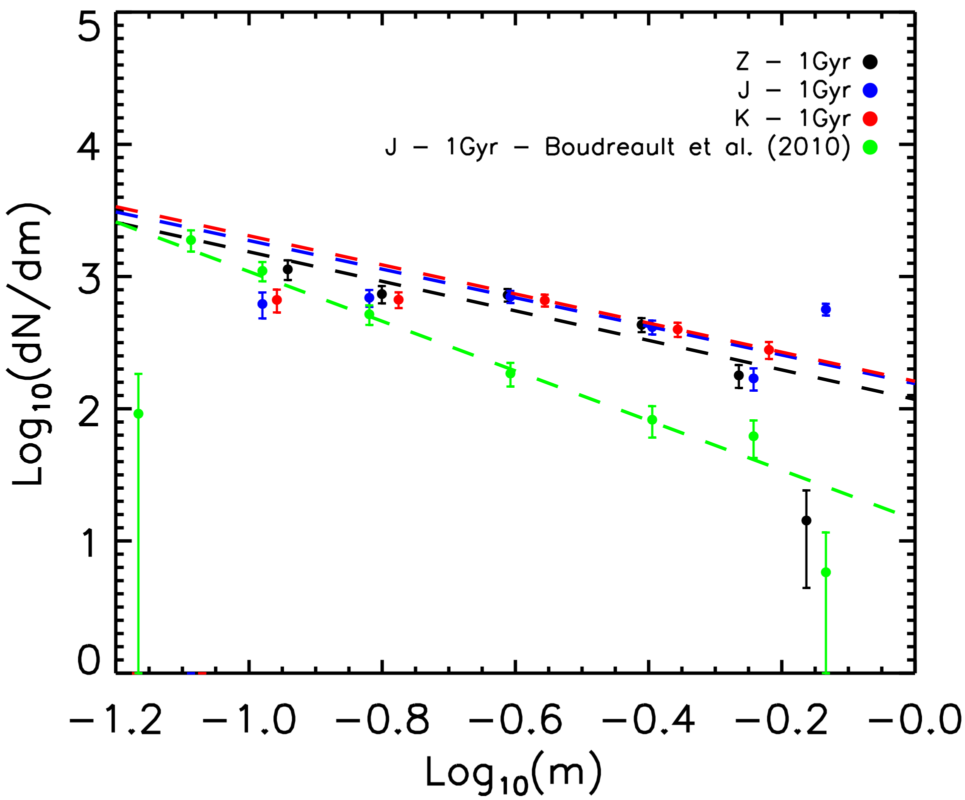

FIGURE 4.10. The derived cluster mass function with the power law fit for the Z photometric band shown in dashed black. The fits for the J and K bands are also shown in blue and red respectively. The green points are taken from Boudreault et al. (2010). The error bars are Poisson errors. For clarity only the 1 Gyr data and fit has been plotted as there is little deviation between that and the 500 Myr fit.

and 910. Objects 55 and 909 are precluded from the search due to their morphological classification in the UKIDSS data. Object 910 is present and photometrically appears to agree with Boudreault et al. ($J = 17.66$, $K = 16.8$). The presence of other photometric bands has however shown this object to be far too blue in the Z-J,J diagram ($Z = 18.33$) for it to be considered as a cluster member by this analysis. The value presented by Boudreault et al. of $\alpha = 1.8 \pm 0.1$ for $\xi(m)$ (the mass function) appears to be much greater than the calculated UKIDSS DR6 value and is more in line with the upper most value presented by Kraus & Hillenbrand.

The Boudreault et al. (2010) survey does not however use proper motion information and restricts its objects to candidates with uniform probability of membership (p=1.0). By making limited photometric cuts and ignoring the distinct motion that separates Praesepe from potential contaminantes and failing to assign any formal membership probability to their candidates their mass function is significantly inflated. Using this as a basis for claiming variation in the IMF is also therefore flawed. Obtaining the J band photometry for the 150 objects and applying the same luminosity-mass relationship used for the UKIDSS DR6 data confirms their result, as an α value of $\alpha = 1.85 \pm 0.15$ is found. This rejects the idea that a different mass-luminosity relationship is the cause of the discrepancy, pointing back to the cluster member selection as the most likely source of error. See Table 4.3 for a summary of the results.

Table 4.3. Mass function results from previous surveys.

Survey	Passband	Mass range	Slope
Baker et al.	Z	0.125 - 0.6 $\mathrm{M}_{\odot}$	1.10 ± 0.37
Baker et al.	J	0.20 - 0.5 $\mathrm{M}_{\odot}$	1.07
Baker et al.	K	0.20 - 0.5 $\mathrm{M}_{\odot}$	1.09
Kraus & Hillenbrand	SED[a]	0.17 - 1 $\mathrm{M}_{\odot}$	1.4 ± 0.2
Boudreault et al.	J	0.10 - 0.7 $\mathrm{M}_{\odot}$	2.3 ± 0.2
Boudreault et al.	J	0.18 - 0.45 $\mathrm{M}_{\odot}$	1.8 ± 0.1

[a] See the appendix of Kraus & Hillenbrand (2007) for a discussion on how the multiple photometric bands coupled with theoretical models were used to derive masses for each spectral type.

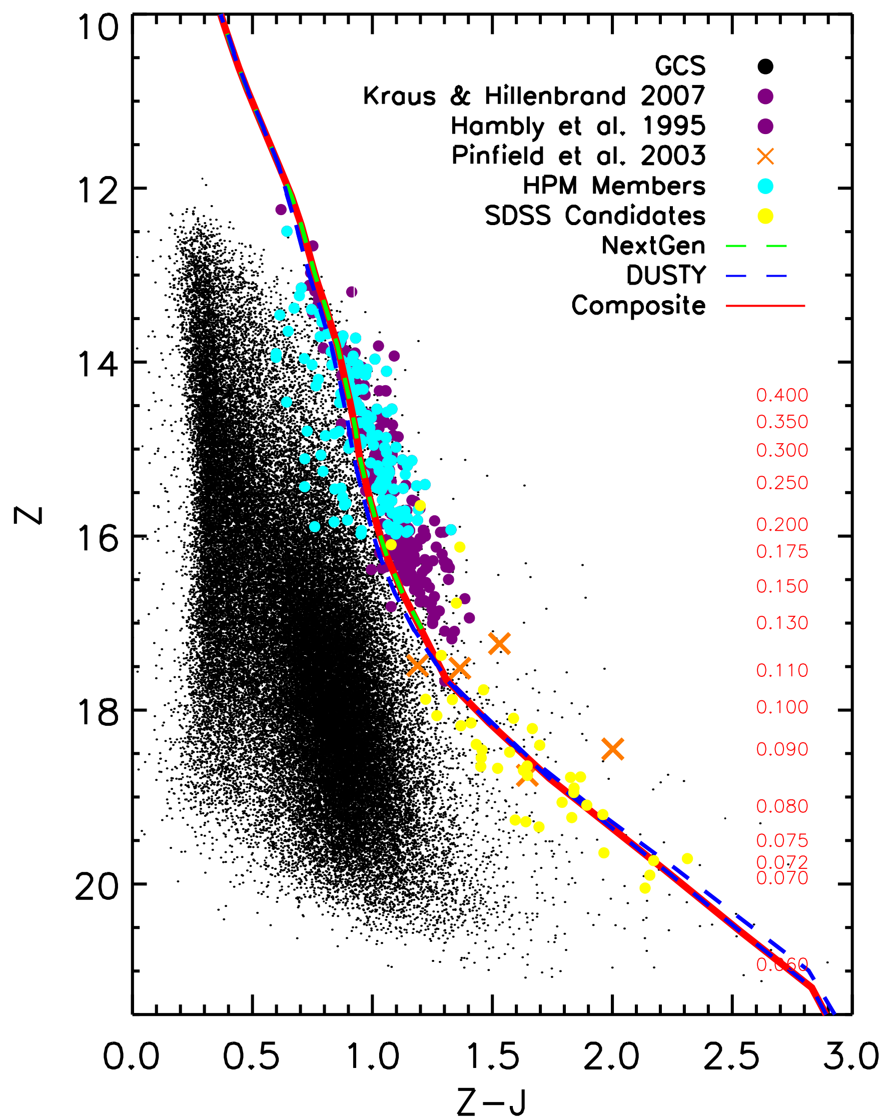

FIGURE 4.11. A Z-J,Z CMD showing the cluster members given by Hambly et al. and Kraus & Hillenbrand alongside the 145 HPM derived from the UKIDSS DR6 work. The BT-NextGen, BT-DUSTY and composite selection lines are also shown as are the masses (in units of solar mass) given by those models for the 500 Myr case. The candidate UKIDSS DR6-SDSS members are also shown to show the limits of the survey. Most of the UKIDSS DR6-SDSS objects were found in this analysis to be non-members.

4.8 UKIDSS DR6 Conclusions

A study of the available UKIDSS DR6 data on the Praesepe star cluster combined with archive data from 2MASS and SDSS surveys for the range of $12 \leq Z < 21$ has found, through a combination of proper motion and colour magnitude selections 145 High Probability Members (HPM; p$\geq$0.6) (see Figure 4.11), of which 14 appear to be new members. The majority of the detected HPM objects have also been found in more than one previous body of work, almost certianly confirming their status as cluster members. These objects all inhabit a fairly bright magnitude region on the cluster sequence as they have been selected from an investigation into the brighter UKIDSS DR6-2MASS data set. The UKIDSS DR6-SDSS data set, whilst allowing for fainter objects to be examined, suffers from a short time base between observations and small number statistics making membership assignments difficult to quantify. An analysis of the cluster luminosity and mass functions has also been carried out, revealing upper limits that agree with the previous result given by Kraus & Hillenbrand (2007) but are in contrast to the values presented in Boudreault et al. (2010). As discussed previously, the lack of membership probability and potential high contamination suffered by Boudreault et al. (2010) due to the exclusion of proper motion information has lead to a potentially highly increased α value. Despite the lower α result presented in this work and that of Kraus & Hillenbrand (2007) a low-mass population of objects is still believed to have once existed within the Praesepe cluster though the dynamical evolution of the cluster over its lifetime has led to a significant population depletion.

4.9 UKIDSS DR8 Follow up

Following the work presented in Baker et al. (2010), the same analysis pipeline has been used on the UKIDSS DR8 data. This data release included for the first time over 90% of the cluster, including a majority of the missing central region. A total of 245 HPM matched to objects found in previous surveys are now reported (Table 4.4) alongside 33 new HPM candidates (Table 4.5). In addition to the increase in "bright" members a total of 6 fainter SDSS candidates are presented with probabilities from the annulus method of 0.88. A further 3 are reported with 0.28, whilst the remaining 45 candidates are rejected. The previous candidate of UGCSJ083955.10+222300.8 is now rejected as the proper motion selection area has changed due to a slight reduction of the size of the Gaussian error. An update to the UKIDSS DR6-2MASS mass function has also been calculated with a slight decrease in the Z, J and K band α values to α_{500Myr}=0.87 $\pm$ 0.33 and α_{1Gyr}=0.88 $\pm$ 0.33, α_{500Myr}=0.87, α_{1Gyr}=0.88 and α_{500Myr}=0.86, α_{1Gyr}=0.86 respectively which despite disagreing with the results of Kraus & Hillenbrand (2007) and Boudreault et al. (2010) are in far greater agreement with the values presented for other clusters (Table 2.1). Including the UKIDSS DR8-SDSS objects (of which there are few) raises the slope back towards $\alpha \sim 0.93$ however it can be argued that such an unreliable point should not be included in the determination of the slope. In addition to re-running the analysis with the same initial query (albeit with the DR8 release) a second less restrictive query to the databases was undertaken that eliminated the requirement of having the object detected in Sloan i. Analgous to the no Z detection of Lodieu et al. (2007b) this was aimed at increasing the sensitivity to cool objects (At least one

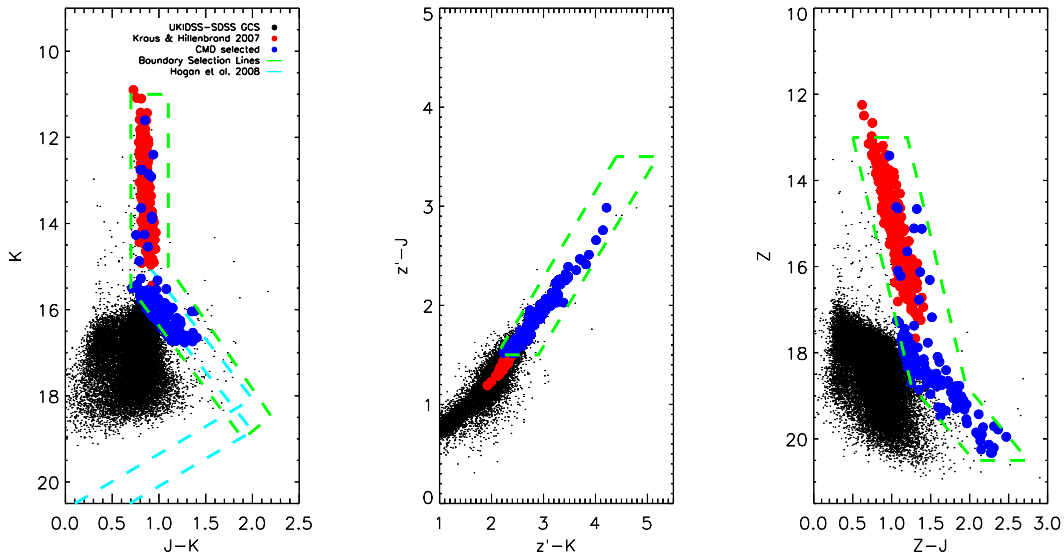

FIGURE 4.12. Colour-magnitude and colour-colour diagrams for the UKIDSS DR8-SDSS z' only population. The previous cuts involving SDSS i have been discounted.

photometric band from SDSS needs to be present in order to calculate proper motions). Asking for non-detections in any of the UKIDSS bands would likely not improve the sensitivity as the bluest of bands, Z, is well matched to that of the Sloan z' band. Keeping the proper motion calculation between z' and Z also helps to minimise any DCR related issues. Colour cuts for the UKIDSS DR8-SDSS z' only objects were carried out as shown in Figure 4.12.

Of the ≈31000 UKIDSS DR8-SDSS z' only detections, 117 were selected for proper motion analysis compared to 39 from the original UKIDSS DR6-SDSS selection. The UKIDSS DR8-SDSS and UKIDSS DR8-SDSS z' only proper motion diagrams as shown in Figure 4.13. Of the 117 selected objects 20 have p≥0.5 and 8 have p≥0.6. These have been folded into the mass function and can be seen contributing to the two lowest mass bins (Figure 4.14 and 4.15), the change between the 500Myr (green) and 1Gyr (blue) mass-luminosity relationships is now evident, whilst for the higher masses the black and red points are indisguisible. A turn over in the mass function appears to be presenting itself but with the SDSS detections relying on one photometric filter at the limit of detection this variation is still uncertain.

Tables 4.4, 4.5 and 4.6 show the members from this analysis that have been matched to previous works, appear to be new and are presented as SDSS candidates respectivley. Shown in bold are the results taken from the z' only population. With a second epoch of K band measurements due as the UKIDSS GCS survey progresses, further constraints can be placed upon the proper motions of these objects. This will become particularly important for restricting the faint SDSS population before assessing which objects are the best candidates for photometric and spectroscopic follow up.

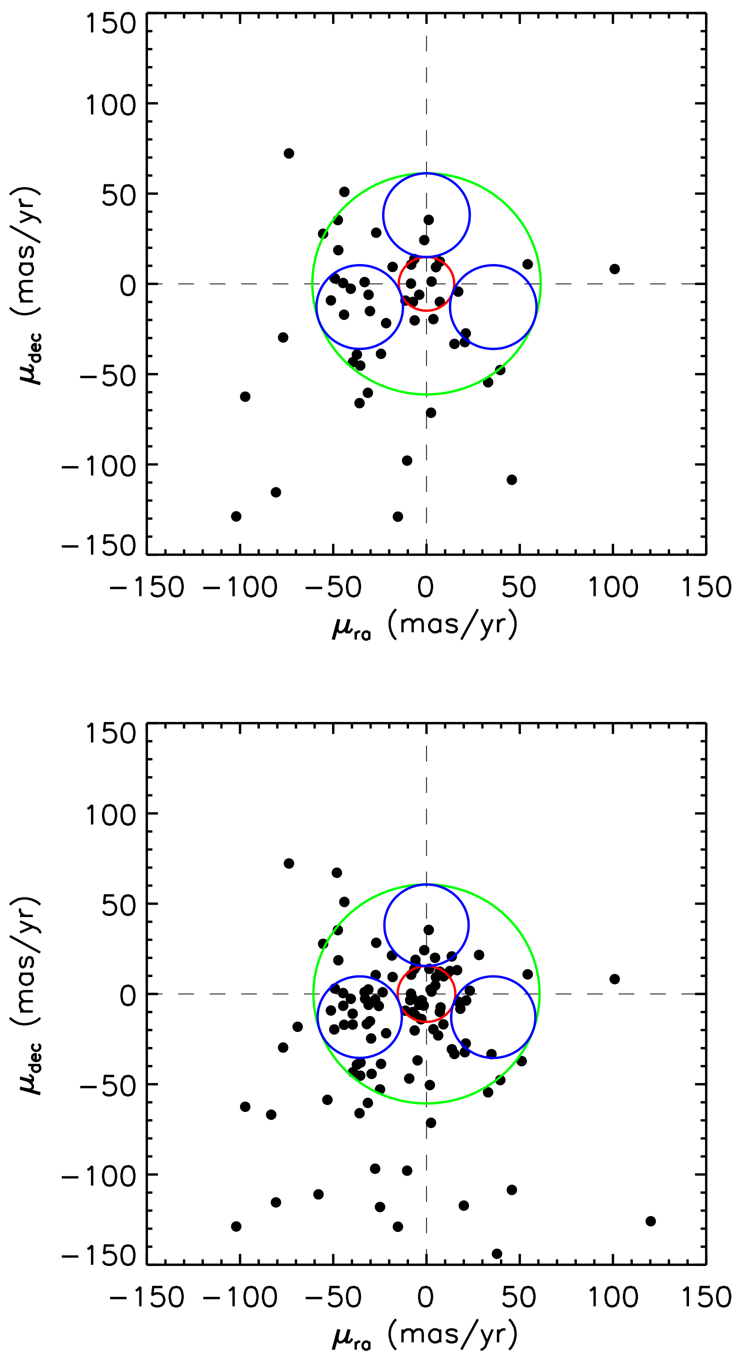

FIGURE 4.13. Proper motion vector diagrams for the UKIDSS DR8-SDSS (top) and UKIDSS DR8-SDSS z' only (bottom) populations.

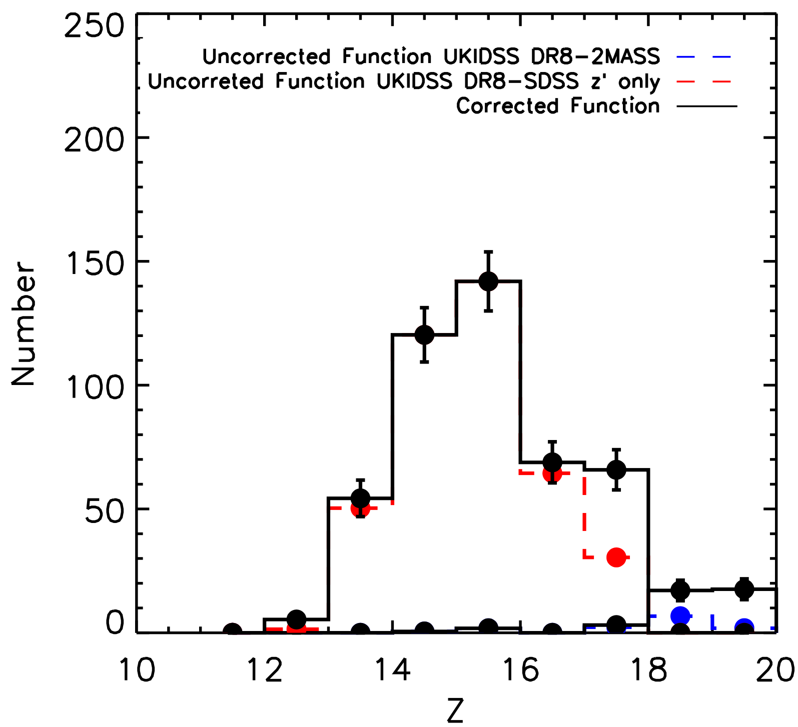

FIGURE 4.14. UKIDSS Z band luminosity function for the UKIDSS DR8-2MASS and UKIDSS DR8-SDSS z' only populations.

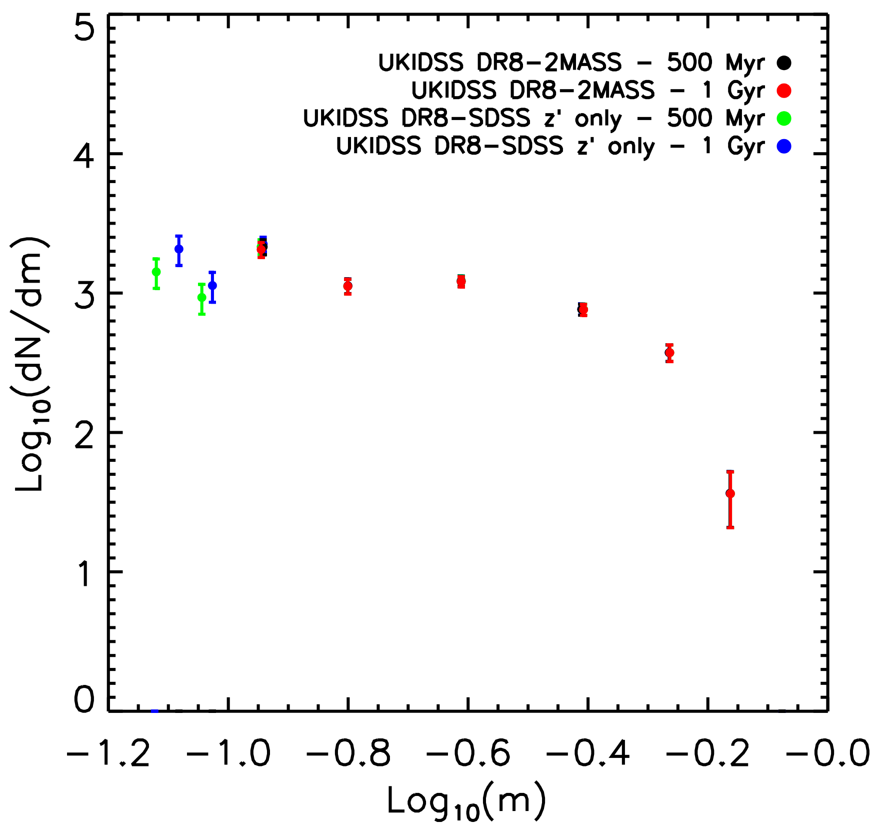

FIGURE 4.15. Mass function for the UKIDSS DR8-2MASS population at 500 Myrs (black) and 1 Gyr (red) with the contributing UKIDSS-SDSS z' only population present for the lowest mass bins (500 Myrs in green and 1 Gyr in blue).

Table 4.4: High Probability Members Matched to Previous Works taken from the UKIDSS DR8-2MASS sample.

ID	Z	Y	J	H	K	μ_α (mas yr^{-1})	μ_δ	Pmem	Previous IDs[a]
UGCSJ083545.87+223042.4	14.70	14.27	13.75	13.18	12.89	-35.9	-11.8	0.70	AD2057; KH561
UGCSJ084207.83+221105.1	14.84	14.39	13.84	13.27	12.99	-35.5	-7.3	0.80	AD3054; HSHJ406; KH691
UGCSJ083722.41+220200.3	14.11	13.61	13.05	12.52	12.21	-34.0	-4.2	0.82	AD2305; KH799
UGCSJ084440.47+214553.7	14.08	13.71	13.20	12.62	12.32	-34.6	-1.3	0.76	AD3337; KH508
UGCSJ084120.88+215453.9	13.96	13.71	13.24	12.64	12.43	-28.5	-10.4	0.80	AD2939
UGCSJ084302.88+214513.6	15.13	14.57	13.97	13.44	13.08	-29.6	-9.6	0.77	AD3161; KH989
UGCSJ083256.66+213829.5	15.82	15.43	14.92	14.36	14.05	-38.2	-6.3	0.74	AD1687
UGCSJ084126.00+213425.2	15.93	15.42	14.82	14.31	13.94	-36.7	-3.8	0.77	AD2951; HSHJ367; KH901
UGCSJ084458.84+213217.1	15.64	15.28	14.76	14.28	13.98	-27.8	-0.6	0.66	AD3361
UGCSJ083454.93+213854.4	15.19	14.75	14.17	13.59	13.28	-34.2	-1.4	0.76	AD1951; KH773
UGCSJ083526.81+213901.7	15.74	15.25	14.65	14.10	13.77	-37.8	-8.8	0.73	AD2021; KH843
UGCSJ083912.55+213557.0	15.90	15.43	14.81	14.24	13.93	-29.2	-7.2	0.79	AD2517; HSHJ250
UGCSJ083413.87+212352.1	15.25	14.75	14.18	13.61	13.31	-27.8	-8.1	0.75	AD1868; KH786
UGCSJ083434.27+212207.2	14.54	14.06	13.46	12.89	12.59	-29.2	-5.2	0.80	AD1915; KH681
UGCSJ083316.62+212020.4	14.08	13.64	13.11	12.54	12.26	-29.8	-9.3	0.78	AD1737; KH677
UGCSJ084143.40+212950.3	15.93	15.25	14.60	14.08	13.70	-31.7	-12.4	0.72	AD3006; HSHJ386; KH1084
UGCSJ084030.70+212333.1	14.94	14.56	14.04	13.47	13.19	-29.1	-9.0	0.77	AD2776; HSHJ318
UGCSJ084048.51+212949.4	13.64	13.43	13.00	12.40	12.24	-26.0	-8.8	0.76	AD2828
UGCSJ082935.64+212047.1	14.79	14.53	14.07	13.45	13.26	-31.2	-4.2	0.81	AD1252
UGCSJ084536.22+211521.1	13.74	13.38	12.87	12.28	12.01	-26.8	-1.4	0.72	AD3427; HSHJ497; JS604; KH450
UGCSJ084457.00+210648.0	15.58	15.11	14.54	13.97	13.67	-28.3	-6.2	0.78	AD3358; KH835
UGCSJ083813.89+210926.1	13.91	13.55	13.07	12.47	12.21	-31.8	-9.9	0.83	HSHJ198; JS216; KH453
UGCSJ083459.25+210837.3	15.42	14.84	14.24	13.69	13.37	-32.9	-1.7	0.78	AD1962; KH961

Continued on next page

Table 4.4– continued from previous page

ID	Z	Y	J	H	K	μ_α	μ_δ	Pmem	Previous IDs[a]
						(mas yr^{-1})			
UGCSJ084123.94+211519.1	15.62	15.24	14.73	14.17	13.90	-28.4	-3.9	0.76	AD2945
UGCSJ084719.06+211102.0	15.58	15.11	14.51	13.95	13.64	-25.2	-6.3	0.65	KH814
UGCSJ084711.92+210748.4	15.72	15.22	14.60	14.07	13.74	-32.4	-12.3	0.72	HSHJ501; KH926
UGCSJ083730.73+210740.2	14.94	14.51	13.99	13.42	13.13	-32.7	-9.7	0.80	KH564
UGCSJ082927.94+210838.2	13.39	13.11	12.65	12.04	11.80	-31.1	-3.6	0.84	AD1240; KH397
UGCSJ084515.55+210335.9	14.41	14.04	13.52	12.96	12.69	-36.0	-1.9	0.75	AD3394; HSHJ496; KH574
UGCSJ084620.04+210032.0	15.80	15.29	14.69	14.14	13.82	-36.7	-6.4	0.78	AD3506; HSHJ499; KH927
UGCSJ084321.75+205510.0	15.07	14.78	14.28	13.74	13.48	-26.7	-4.8	0.72	AD3195
UGCSJ082942.64+205707.2	14.03	13.78	13.28	12.70	12.48	-28.4	-0.3	0.67	AD1263
UGCSJ083629.41+210310.3	14.94	14.54	14.01	13.44	13.16	-31.7	-13.5	0.66	AD2175; HSHJ125; KH614
UGCSJ083715.24+205759.0	14.20	13.90	13.42	12.82	12.59	-27.5	-2.5	0.71	AD2291
UGCSJ083401.54+210039.0	15.77	15.27	14.67	14.11	13.80	-25.4	-5.6	0.66	AD1837; KH871
UGCSJ084114.43+205946.3	15.63	15.17	14.58	14.02	13.71	-30.7	-1.0	0.75	AD2918; HSHJ356; KH838
UGCSJ084859.88+204155.5	15.69	15.12	14.50	13.99	13.62	-39.3	-6.6	0.69	KH965
UGCSJ083918.03+204421.3	13.67	13.36	12.86	12.26	12.05	-31.6	-8.5	0.85	AD2538; JS284; KH419
UGCSJ083922.13+204758.3	15.27	14.78	14.20	13.65	13.32	-32.3	-4.5	0.82	AD2551; HSHJ261; KH828
UGCSJ083232.42+205040.9	14.45	14.06	13.53	12.95	12.70	-26.5	-5.8	0.71	AD1632; JS10; KH528
UGCSJ083110.62+203951.1	15.94	15.52	14.97	14.43	14.13	-37.4	-11.7	0.66	AD1460
UGCSJ084547.77+204246.5	15.10	14.64	14.07	13.53	13.23	-32.5	1.7	0.64	AD3451
UGCSJ083845.67+203943.8	15.44	15.02	14.43	13.90	13.60	-34.5	-4.1	0.81	AD2452; KH812
UGCSJ083834.09+204629.2	15.28	14.84	14.27	13.71	13.40	-36.4	1.5	0.60	AD2420; KH700
UGCSJ083606.29+204059.9	12.97	12.71	12.23	11.64	11.43	-39.4	-5.5	0.64	AD2110; JS109; KH363
UGCSJ083615.51+204109.7	13.15	12.90	12.44	11.83	11.62	-31.7	-4.8	0.85	AD2138; JS117; KH357
UGCSJ083603.23+205015.6	15.67	15.18	14.61	14.08	13.74	-33.6	-5.7	0.83	AD2101; HSHJ96 ; KH841

Continued on next page

Table 4.4– continued from previous page

ID	Z	Y	J	H	K	μ_α (mas yr^{-1})	μ_δ	Pmem	Previous IDs[a]
UGCSJ084114.04+204429.7	13.97	13.53	12.96	12.38	12.12	-26.5	-5.2	0.79	AD2916; JS416; KH707
UGCSJ083711.87+204047.2	14.03	13.72	13.20	12.59	12.35	-27.7	-11.9	0.66	AD2284; JS166; KH477
UGCSJ083406.67+204946.7	15.71	15.26	14.68	14.11	13.80	-29.4	-5.6	0.80	AD1852; KH818
UGCSJ084418.23+204948.4	15.45	14.94	14.32	13.76	13.46	-38.4	-1.7	0.67	AD3300; HSHJ478
UGCSJ083300.38+204310.2	13.72	13.35	12.79	12.23	11.95	-32.0	-3.9	0.84	AD1699; JS19; KH706
UGCSJ083804.60+203935.2	14.95	14.53	13.95	13.38	13.08	-33.0	-10.4	0.78	JS704; KH663
UGCSJ084849.96+202635.9	13.44	13.15	12.66	12.07	11.81	-28.7	-4.3	0.83	KH392
UGCSJ084545.87+202940.9	13.78	13.44	12.92	12.34	12.09	-28.4	-8.8	0.82	AD3447; JS609; KH460
UGCSJ084047.77+202847.8	14.03	13.61	13.09	12.49	12.25	-33.6	-7.9	0.82	AD2825; KH554
UGCSJ084013.75+202608.2	14.28	13.93	13.44	12.85	12.61	-25.8	-10.0	0.63	AD2712
UGCSJ083314.23+203621.1	15.71	15.20	14.57	14.03	13.72	-28.5	-8.4	0.77	AD1731; KH892
UGCSJ083313.45+203301.0	14.33	13.88	13.30	12.72	12.45	-27.7	-12.1	0.65	AD1727; KH678
UGCSJ083308.44+202637.1	13.81	13.35	12.79	12.21	11.93	-32.3	-12.5	0.75	KH634
UGCSJ083807.28+202655.6	13.71	13.37	12.85	12.25	12.03	-32.7	-1.4	0.79	KH437
UGCSJ083808.16+202646.1	13.70	13.35	12.82	12.22	12.01	-30.8	-6.5	0.86	KH418
UGCSJ084611.69+203800.6	14.36	14.04	13.50	12.99	12.71	-32.2	-6.8	0.83	AD3490
UGCSJ083338.36+202852.4	15.31	14.82	14.25	13.71	13.43	-27.1	-10.7	0.67	AD1786; KH724
UGCSJ083952.62+203046.2	14.24	13.84	13.31	12.71	12.46	-30.6	-14.2	0.61	AD2639; JS715; KH591
UGCSJ083943.59+202939.5	14.54	14.14	13.60	13.03	12.75	-25.7	-5.7	0.67	AD2618; JS311; KH629
UGCSJ083912.08+203607.4	14.84	14.38	13.82	13.27	12.96	-39.3	-6.0	0.70	AD2515
UGCSJ083903.93+203402.2	13.98	13.60	13.07	12.50	12.24	-25.8	-7.4	0.77	AD2502; JS266; KH500
UGCSJ082750.59+201436.3	12.50	12.26	11.85	11.32	11.09	-26.0	-0.4	0.65	AD1025; KH300
UGCSJ084111.05+202238.4	13.44	13.12	12.63	12.04	11.81	-25.7	-5.8	0.76	AD2905; JS411; KH416
UGCSJ084137.35+201236.8	15.15	14.66	14.09	13.56	13.27	-30.2	-1.2	0.74	AD2988; HSHJ381; KH667

Continued on next page

Table 4.4– continued from previous page

ID	Z	Y	J	H	K	μ_α	μ_δ	Pmem	Previous IDs[a]
						(mas yr^{-1})			
UGCSJ083641.16+201639.9	15.04	14.60	13.98	13.45	13.14	-30.7	-5.6	0.82	AD2205; KH693
UGCSJ083642.16+201622.9	15.46	14.97	14.37	13.85	13.52	-32.3	-9.9	0.79	AD2208
UGCSJ083403.13+202030.5	14.77	14.34	13.80	13.25	12.97	-26.0	-1.7	0.61	AD1841; KH599
UGCSJ084423.19+201355.6	15.34	14.84	14.28	13.72	13.42	-29.1	-4.8	0.79	AD3312; KH787
UGCSJ083041.51+202426.6	15.55	15.17	14.68	14.10	13.84	-37.2	-9.0	0.75	AD1396
UGCSJ083311.09+201604.1	15.16	14.74	14.17	13.67	13.37	-31.8	-12.6	0.71	AD1719
UGCSJ083942.01+201745.0	14.98	14.50	13.93	13.39	13.11	-31.5	-0.8	0.75	AD2615; KH808
UGCSJ083906.87+202054.2	13.54	13.23	12.75	12.14	11.94	-25.1	-5.5	0.74	AD2508; JS270; KH426
UGCSJ083507.87+202023.1	14.46	14.07	13.55	12.99	12.71	-30.9	-9.5	0.79	AD1978; KH496
UGCSJ083436.75+201155.9	13.71	13.41	12.93	12.32	12.08	-30.4	-6.4	0.86	AD1921; HSHJ58
UGCSJ084151.90+202047.8	13.85	13.51	13.00	12.41	12.18	-29.9	-8.4	0.84	AD3026; JS459; KH470
UGCSJ083855.15+201308.9	14.31	13.90	13.35	12.77	12.50	-32.3	0.1	0.72	AD2478; HSHJ234; JS255; KH606
UGCSJ083825.35+202120.9	15.93	15.45	14.85	14.32	13.99	-31.1	-11.8	0.73	KH903
UGCSJ083539.26+202409.8	14.98	14.48	13.88	13.35	13.04	-31.4	-8.2	0.81	AD2042; KH854
UGCSJ085237.29+200043.2	13.46	13.26	12.84	12.27	12.13	-26.4	-5.0	0.79	AD4003
UGCSJ085056.86+193657.8	14.44	14.05	13.52	12.93	12.67	-30.7	0.6	0.68	KH527
UGCSJ085239.65+192928.5	15.71	15.21	14.64	14.06	13.76	-36.0	1.2	0.63	AD4005; KH893
UGCSJ082757.39+191130.8	15.94	15.55	14.98	14.37	14.12	-36.2	-9.1	0.77	AD1043
UGCSJ083439.68+190812.6	14.61	14.18	13.63	13.05	12.78	-32.7	-4.5	0.82	AD1925; HSHJ60 ; KH596
UGCSJ083430.71+190600.2	14.46	14.08	13.53	12.96	12.73	-38.2	-9.9	0.69	AD1906; HSHJ55 ; JS675; KH513
UGCSJ082848.63+185835.9	15.82	15.26	14.63	14.07	13.72	-31.5	-5.9	0.83	AD1164; KH1025
UGCSJ083150.86+185902.1	15.29	14.85	14.32	13.79	13.47	-29.9	0.6	0.67	AD1549
UGCSJ083218.87+190308.6	14.64	14.21	13.64	13.08	12.78	-33.6	-8.4	0.81	AD1607; HSHJ23 ; KH594
UGCSJ082759.58+185657.8	13.71	13.49	13.06	12.45	12.30	-35.4	-0.3	0.71	AD1047

Continued on next page

Table 4.4– continued from previous page

ID	Z	Y	J	H	K	μ_α (mas yr^{-1})	μ_δ	Pmem	Previous IDs[a]
UGCSJ083544.59+185738.2	15.40	14.93	14.35	13.80	13.50	-29.2	-6.0	0.80	AD2053; HSHJ84 ; KH858
UGCSJ083651.05+190418.5	14.99	14.61	14.09	13.51	13.22	-28.7	-4.4	0.78	AD2231; HSHJ136; KH565
UGCSJ083338.00+185717.5	14.21	13.86	13.31	12.74	12.49	-38.5	-7.4	0.72	AD1785; HSHJ45 ; JS41; KH482
UGCSJ083051.38+185351.5	15.25	14.81	14.22	13.66	13.38	-32.3	0.0	0.72	AD1411; HSHJ8; KH670
UGCSJ083734.95+185607.7	14.47	14.11	13.60	13.09	12.84	-32.2	-6.9	0.83	HSHJ173
UGCSJ083235.23+184409.5	15.94	15.41	14.79	14.24	13.95	-27.6	-6.1	0.76	AD1641; HSHJ24
UGCSJ083207.94+184426.7	14.37	13.97	13.47	12.87	12.59	-26.9	-1.6	0.66	AD1588; KH511
UGCSJ083154.25+184536.1	15.59	15.08	14.51	13.96	13.64	-28.9	-5.9	0.79	AD1555; HSHJ18 ; KH834
UGCSJ083126.88+184056.4	15.41	14.84	14.19	13.64	13.30	-29.9	-6.8	0.81	AD1500; KH1044
UGCSJ083658.63+184952.1	15.19	14.63	14.04	13.51	13.17	-28.2	-7.6	0.77	AD2248; KH923
UGCSJ083808.07+184429.9	15.80	15.28	14.68	14.11	13.82	-27.0	-10.5	0.68	HSHJ196; KH779
UGCSJ083729.39+184135.5	14.89	14.48	13.94	13.38	13.10	-37.7	-7.2	0.75	HSHJ165; KH542
UGCSJ083528.37+184032.9	15.73	15.21	14.63	14.10	13.76	-27.3	-3.6	0.72	AD2022
UGCSJ083506.21+184924.6	14.76	14.33	13.77	13.20	12.92	-38.7	-3.8	0.70	AD1975; HSHJ68 ; JS680; KH644
UGCSJ083540.13+184228.3	14.15	13.72	13.18	12.62	12.33	-34.2	-5.9	0.82	AD2045; HSHJ82 ; JS95; KH636
UGCSJ083058.90+184141.0	13.12	12.82	12.38	11.79	11.59	-38.5	-4.1	0.68	AD1427; KH360
UGCSJ083434.30+184756.4	14.13	13.73	13.19	12.62	12.37	-32.5	-12.6	0.71	AD1917; HSHJ56 ; JS62; KH570
UGCSJ083343.93+184750.7	14.31	13.90	13.40	12.81	12.54	-31.9	-13.7	0.65	AD1797; HSHJ47 ; JS44 KH526
UGCSJ083328.19+184336.2	15.96	15.40	14.81	14.28	13.95	-38.4	-4.3	0.72	AD1763; HSHJ41 ; KH874
UGCSJ083306.43+184141.5	14.28	13.89	13.38	12.84	12.55	-36.5	-13.3	0.61	AD1709; HSHJ32
UGCSJ083142.95+182906.4	15.26	14.81	14.22	13.64	13.36	-26.2	-7.9	0.69	AD1532; HSHJ17 ; KH699
UGCSJ083140.88+182942.9	14.89	14.47	13.90	13.34	13.08	-32.9	-5.7	0.83	AD1526; HSHJ16; KH563
UGCSJ083521.67+182934.1	13.98	13.59	13.11	12.53	12.28	-27.0	-7.6	0.80	AD2011; JS87; KH463
UGCSJ083334.78+183108.9	13.24	12.97	12.54	11.98	11.84	-26.6	-3.3	0.77	AD1776

Continued on next page

Table 4.4– continued from previous page

ID	Z	Y	J	H	K	μ_α (mas yr^{-1})	μ_δ	Pmem	Previous IDs[a]
UGCSJ083014.08+182519.8	14.56	14.15	13.61	13.08	12.78	-35.1	-11.9	0.72	AD1344; HSHJ4; KH559
UGCSJ083453.83+180105.4	15.72	15.23	14.61	14.05	13.73	-32.0	-10.9	0.77	AD1948; HSHJ65; KH817
UGCSJ083547.20+180829.9	14.54	14.12	13.52	12.94	12.67	-30.7	-11.7	0.73	AD2063; HSHJ87 ; KH628
UGCSJ083448.49+175558.7	15.94	15.39	14.78	14.22	13.89	-27.8	-12.2	0.64	AD1939; HSHJ62 ; KH931
UGCSJ083002.92+175702.0	15.79	15.24	14.65	14.07	13.72	-32.0	-12.0	0.73	AD1308; HSHJ2; KH990;
UGCSJ083517.03+173624.3	15.12	14.59	14.00	13.43	13.14	-27.1	-7.7	0.73	AD2000; HSHJ74 ; KH855
UGCSJ083839.13+172948.4	15.98	15.49	14.88	14.33	14.02	-30.6	-10.7	0.76	AD2436; HSHJ217; KH904
UGCSJ084105.75+173227.9	13.91	13.56	13.01	12.41	12.15	-28.9	-13.9	0.66	AD2883
UGCSJ084026.64+172100.2	14.82	14.48	13.98	13.40	13.13	-29.9	-2.9	0.78	AD2760
UGCSJ083855.64+171509.5	14.51	14.12	13.56	12.99	12.70	-27.4	-2.3	0.70	AD2482; KH608
UGCSJ083824.87+165836.0	14.09	13.71	13.16	12.59	12.31	-32.8	-2.0	0.79	AD2396; KH478
UGCSJ083906.50+170100.4	14.58	14.06	13.51	12.96	12.64	-36.2	-7.5	0.79	AD2507
UGCSJ083608.51+165717.5	13.88	13.54	13.05	12.50	12.22	-29.8	-4.0	0.84	AD2114
UGCSJ084312.90+183150.8	14.01	13.64	13.14	12.55	12.29	-36.3	-8.3	0.78	AD3180; HSHJ447; JS525; KH476
UGCSJ084017.05+183629.8	15.28	14.77	14.17	13.63	13.34	-30.7	0.7	0.68	AD2729; HSHJ310; KH771
UGCSJ084031.05+182556.1	14.09	13.71	13.23	12.62	12.39	-28.3	-9.9	0.74	AD2777; HSHJ322; KH525
UGCSJ084748.84+183619.5	14.67	14.18	13.59	13.05	12.73	-27.1	-6.8	0.74	JS761; KH761
UGCSJ084244.59+182800.0	15.62	15.11	14.55	13.99	13.68	-32.1	-3.4	0.81	AD3127; KH836
UGCSJ084618.25+184309.1	15.06	14.62	14.08	13.49	13.22	-34.0	-10.3	0.78	AD3501; JS757; KH719
UGCSJ084536.86+184325.0	15.60	15.09	14.50	13.95	13.64	-26.1	-2.6	0.65	AD3429; KH813
UGCSJ084212.70+184101.0	15.38	14.91	14.38	13.82	13.49	-29.7	-7.4	0.80	AD3061; KH753
UGCSJ084210.27+184600.3	15.68	15.18	14.60	14.02	13.70	-33.4	0.1	0.72	AD3057; KH840
UGCSJ083832.31+184652.8	14.25	13.86	13.35	12.78	12.52	-30.5	-2.5	0.78	AD2413; KH537
UGCSJ084334.60+184513.7	15.23	14.72	14.13	13.56	13.28	-33.0	-10.2	0.79	AD3218; KH768

Continued on next page

Table 4.4– continued from previous page

ID	Z	Y	J	H	K	μ_α (mas yr^{-1})	μ_δ	Pmem	Previous IDs[a]
UGCSJ084312.02+184145.0	15.95	15.44	14.83	14.28	13.97	-39.5	-2.8	0.65	AD3178; KH900
UGCSJ084514.92+184539.9	15.31	14.82	14.21	13.67	13.37	-35.7	-9.9	0.76	AD3392; KH722
UGCSJ084058.43+185046.2	14.97	14.50	13.93	13.39	13.09	-28.4	-2.9	0.75	AD2863; HSHJ343; JS723; KH745
UGCSJ084053.24+184453.9	15.67	15.14	14.53	14.01	13.69	-29.9	-7.4	0.81	AD2840; KH815
UGCSJ083918.88+184836.4	14.59	14.14	13.62	13.06	12.78	-24.7	-7.8	0.61	AD2542; HSHJ260; JS708; KH595
UGCSJ084522.38+190208.2	14.71	14.24	13.64	13.10	12.82	-31.4	-0.6	0.74	AD3403; KH762
UGCSJ084532.16+185752.1	14.73	14.33	13.77	13.20	12.93	-31.2	1.6	0.64	AD3420; KH654
UGCSJ085059.86+190035.5	15.58	15.13	14.51	13.97	13.67	-31.8	-3.1	0.80	AD3836; KH891
UGCSJ084110.74+190153.8	14.71	14.24	13.65	13.11	12.81	-33.7	-7.0	0.82	AD2903; HSHJ353; JS725; KH823
UGCSJ084120.32+185742.9	15.04	14.59	13.99	13.44	13.17	-26.0	-6.7	0.69	AD2936; HSHJ364; KH665
UGCSJ084419.12+185609.9	13.84	13.45	12.92	12.37	12.08	-27.1	-2.0	0.75	AD3301; HSHJ481; JS564; KH622
UGCSJ084427.20+185220.7	15.59	15.10	14.52	13.95	13.64	-25.2	-3.8	0.62	AD3317; KH866
UGCSJ084427.67+185809.5	14.71	14.30	13.73	13.16	12.87	-31.1	-11.9	0.73	AD3318; HSHJ486; JS745; KH687
UGCSJ083930.69+185653.3	15.73	15.26	14.64	14.11	13.80	-30.4	-9.9	0.78	AD2574; HSHJ269; KH778
UGCSJ083945.70+185834.0	14.32	13.94	13.39	12.81	12.56	-36.9	-3.5	0.76	AD2622; HSHJ286; JS315; KH592
UGCSJ084219.21+190214.7	14.24	13.90	13.38	12.81	12.54	-36.5	-8.0	0.78	AD3075; HSHJ417; KH539
UGCSJ084750.50+190910.9	15.30	14.85	14.29	13.73	13.44	-26.6	-6.3	0.72	KH703
UGCSJ084753.82+190753.3	15.36	14.90	14.33	13.76	13.46	-30.2	-3.0	0.79	KH775
UGCSJ084526.62+191412.7	14.97	14.49	13.88	13.34	13.04	-28.7	-9.0	0.76	AD3413; KH807
UGCSJ084052.30+191028.3	13.94	13.53	12.97	12.39	12.12	-28.6	-8.1	0.83	AD2836; HSHJ330; JS391; KH708
UGCSJ084109.49+190920.4	15.99	15.32	14.63	14.11	13.75	-25.0	-7.3	0.63	AD2893; HSHJ351
UGCSJ084559.14+191512.6	14.68	14.25	13.71	13.16	12.88	-36.8	-12.0	0.67	AD3470; KH686
UGCSJ084230.72+190657.7	15.52	15.05	14.50	13.94	13.62	-36.2	-7.4	0.79	AD3094; KH863
UGCSJ083843.91+191738.3	13.69	13.30	12.77	12.22	11.94	-31.5	-2.2	0.82	AD2449; HSHJ224; JS246; KH619

Continued on next page

Table 4.4– continued from previous page

ID	Z	Y	J	H	K	μ_α (mas yr^{-1})	μ_δ	Pmem	Previous IDs[a]
UGCSJ084322.38+191200.7	14.40	14.02	13.49	12.91	12.67	-32.9	1.4	0.66	AD3196; KH549
UGCSJ083722.80+174115.1	14.96	14.49	13.92	13.35	13.07	-30.6	-8.1	0.81	AD2306; KH717
UGCSJ084109.24+173416.9	15.88	15.34	14.74	14.19	13.87	-35.2	-10.0	0.77	AD2892; KH930
UGCSJ084314.65+174230.1	15.56	15.08	14.50	13.96	13.63	-29.9	0.3	0.68	HSHJ449; KH889
UGCSJ083707.20+174748.6	14.31	14.05	13.58	12.95	12.77	-26.1	-9.9	0.65	AD2273
UGCSJ083612.00+175246.6	15.51	15.04	14.44	13.88	13.57	-36.1	-7.8	0.79	AD2127; HSHJ110; KH833
UGCSJ084217.51+175914.7	14.65	14.19	13.66	13.07	12.79	-27.4	-6.1	0.75	AD3069; HSHJ416; KH685
UGCSJ084036.24+175700.3	14.34	13.91	13.39	12.79	12.51	-28.3	-2.8	0.74	AD2795; KH556
UGCSJ084626.29+175044.4	15.51	15.01	14.40	13.85	13.53	-30.4	-2.7	0.78	AD3517; KH861
UGCSJ084600.00+174938.7	15.09	14.58	13.96	13.41	13.12	-30.3	0.4	0.68	AD3472; KH764
UGCSJ083850.82+180052.4	14.73	14.32	13.80	13.24	12.95	-25.0	-7.5	0.63	AD2466; HSHJ230; KH550
UGCSJ084159.88+180436.7	15.21	14.83	14.28	13.72	13.45	-26.4	-5.2	0.71	AD3043
UGCSJ084102.62+181006.6	15.89	15.43	14.81	14.29	13.94	-28.7	-8.8	0.77	AD2875; HSHJ347; KH971
UGCSJ084811.46+181128.0	14.30	13.82	13.20	12.67	12.36	-36.7	-0.1	0.67	KH918
UGCSJ084347.34+180300.1	15.13	14.66	14.07	13.50	13.16	-36.6	0.3	0.66	HSHJ466; KH857
UGCSJ084154.61+181810.0	15.46	14.98	14.36	13.83	13.50	-32.0	-9.7	0.80	AD3034; HSHJ399; KH887
UGCSJ083842.11+182255.4	15.13	14.61	14.01	13.47	13.15	-38.9	-8.6	0.69	AD2444; HSHJ222; KH921
UGCSJ083855.32+182159.4	13.29	13.08	12.65	12.05	11.88	-32.7	-14.8	0.62	AD2480
UGCSJ084019.07+182142.9	14.22	13.88	13.35	12.78	12.50	-30.4	-2.5	0.78	AD2738; HSHJ313; JS351; KH483
UGCSJ083720.46+181418.4	13.79	13.46	12.98	12.38	12.15	-27.3	-4.8	0.81	AD2303; HSHJ156
UGCSJ084422.57+182309.2	14.76	14.33	13.75	13.21	12.92	-29.7	-10.1	0.77	AD3311; HSHJ483; JS744; KH630
UGCSJ084055.87+181446.1	14.63	14.18	13.60	13.04	12.72	-34.9	-9.2	0.79	AD2856; HSHJ341; KH782
UGCSJ084110.49+181607.0	13.62	13.30	12.80	12.21	11.96	-33.8	-4.1	0.83	AD2901; HSHJ355; JS415; KH449
UGCSJ083559.17+181829.6	13.94	13.60	13.12	12.51	12.25	-31.4	1.2	0.69	AD2090; HSHJ94; KH474

Continued on next page

Table 4.4– continued from previous page

ID	Z	Y	J	H	K	μ_α (mas yr^{-1})	μ_δ	Pmem	Previous IDs[a]
UGCSJ083552.87+181850.9	13.96	13.60	13.10	12.48	12.23	-24.9	-11.0	0.66	AD2076; JS686; KH475
UGCSJ083631.48+181854.9	14.92	14.45	13.85	13.32	13.01	-28.7	-1.4	0.72	AD2181; HSHJ127; JS694; KH919
UGCSJ084339.31+182532.0	14.35	13.95	13.41	12.82	12.57	-30.1	-2.5	0.78	AD3230; HSHJ462
UGCSJ084745.09+182123.9	13.48	13.08	12.56	11.98	11.72	-36.0	-7.7	0.79	JS651; KH505
UGCSJ084634.85+191525.9	14.70	14.27	13.72	13.17	12.90	-28.0	-8.2	0.76	AD3534; KH642
UGCSJ084505.88+191757.4	15.40	14.95	14.39	13.83	13.53	-35.4	-3.6	0.79	AD3369; KH755
UGCSJ083954.39+192737.1	15.25	14.78	14.22	13.64	13.34	-29.4	-8.9	0.78	AD2645; HSHJ291; KH770
UGCSJ083953.14+192403.6	14.82	14.40	13.86	13.27	12.99	-30.1	-6.5	0.81	AD2642; KH632
UGCSJ083940.48+191853.9	15.07	14.60	14.01	13.48	13.16	-35.5	-0.7	0.73	AD2607; HSHJ279; KH666
UGCSJ083603.31+192528.7	15.57	15.06	14.49	13.93	13.63	-36.5	-11.7	0.69	AD2103; HSHJ100; KH758
UGCSJ084041.63+193000.7	15.54	14.96	14.37	13.84	13.49	-33.2	-4.1	0.82	AD2806; HSHJ328; KH1046
UGCSJ084106.87+192636.9	14.67	14.22	13.69	13.12	12.86	-27.5	-11.4	0.66	AD2885; KH610
UGCSJ083915.35+191928.3	15.93	15.41	14.83	14.29	14.00	-29.1	-7.8	0.79	AD2527; KH933
UGCSJ083850.70+192454.0	14.01	13.63	13.12	12.59	12.33	-26.4	-7.5	0.70	AD2465; HSHJ228; JS251; KH494
UGCSJ082820.44+192603.9	14.08	13.75	13.28	12.70	12.46	-32.2	-1.9	0.78	AD1099
UGCSJ083841.57+193418.0	15.86	15.37	14.75	14.23	13.91	-36.9	-1.8	0.73	AD2442; HSHJ218; KH872
UGCSJ083803.69+194151.1	14.28	13.90	13.35	12.76	12.52	-36.3	-11.6	0.70	HSHJ192; KH503
UGCSJ083744.93+194028.9	13.68	13.29	12.78	12.23	11.97	-24.3	-3.8	0.68	JS195; KH499
UGCSJ084834.49+195557.4	13.59	13.22	12.71	12.12	11.87	-37.4	-2.8	0.72	KH466
UGCSJ084053.95+200524.3	14.60	14.24	13.73	13.16	12.87	-28.0	-1.7	0.70	AD2845; HSHJ333; KH521
UGCSJ084124.43+200749.5	13.40	13.01	12.48	11.89	11.61	-32.5	-5.8	0.85	AD2947; HSHJ366; JS430; KH523
UGCSJ084125.99+195915.0	14.85	14.39	13.83	13.27	12.96	-35.6	-8.7	0.79	AD2952; HSHJ368; JS729; KH612
UGCSJ084013.08+200328.1	14.07	13.63	13.09	12.52	12.24	-31.1	-2.3	0.79	AD2710; HSHJ303; KH603
UGCSJ084015.18+200513.9	14.62	14.16	13.55	12.99	12.69	-30.3	-7.1	0.81	AD2717; HSHJ305; JS719; KH822

Continued on next page

Table 4.4– continued from previous page

ID	Z	Y	J	H	K	μ_α	μ_δ	Pmem	Previous IDs[a]
						(mas yr^{-1})			
UGCSJ082826.91+200617.1	15.20	14.77	14.19	13.66	13.35	-30.8	-2.5	0.78	AD1121; KH697
UGCSJ083042.56+192230.7	15.73	15.20	14.61	14.07	13.75	-31.4	-4.9	0.82	AD1398; KH868
UGCSJ083310.96+192922.1	14.85	14.31	13.73	13.17	12.89	-34.4	-9.3	0.80	AD1718; HSHJ34 ; KH783
UGCSJ085014.77+184816.5	14.94	14.66	14.16	13.58	13.35	-35.7	-5.9	0.81	AD3758
UGCSJ083707.63+195727.4	15.47	15.00	14.43	13.87	13.56	-32.5	-7.8	0.82	AD2275; KH864
UGCSJ083727.87+195412.6	14.32	13.92	13.38	12.78	12.53	-32.7	-11.3	0.76	AD2328; KH638
UGCSJ083608.58+195725.3	15.13	14.65	14.06	13.49	13.19	-26.1	-9.0	0.67	AD2115; HSHJ102; KH884
UGCSJ084327.57+194940.5	14.66	14.25	13.74	13.17	12.86	-32.0	-6.5	0.83	AD3205; HSHJ455; KH715
UGCSJ084801.26+194939.1	15.38	14.95	14.37	13.79	13.50	-35.2	-6.1	0.81	KH727
UGCSJ084823.55+195011.7	14.64	14.23	13.65	13.07	12.78	-35.9	-4.3	0.79	KH579
UGCSJ084421.21+195611.7	15.06	14.62	14.06	13.52	13.20	-38.4	-5.1	0.73	AD3310; KH826
UGCSJ084034.83+194937.3	14.79	14.49	14.04	13.46	13.19	-29.7	-10.5	0.76	AD2790
UGCSJ084623.86+195804.2	14.36	13.98	13.41	12.86	12.60	-30.6	-5.2	0.82	AD3511; KH627
UGCSJ083519.32+194541.2	15.19	14.73	14.17	13.61	13.33	-35.2	-7.0	0.81	AD2006; HSHJ75 ; KH769
UGCSJ083550.24+195100.1	15.38	14.92	14.33	13.81	13.49	-31.0	0.6	0.69	KH832
UGCSJ083516.93+195453.4	13.93	13.60	13.10	12.53	12.26	-23.9	-6.8	0.68	AD1998; HSHJ72 ; JS84; KH462
UGCSJ084522.32+194940.0	14.34	13.88	13.30	12.79	12.48	-32.1	-6.1	0.83	JS753; KH821
UGCSJ083855.45+195033.3	15.39	14.92	14.35	13.83	13.47	-31.8	-12.4	0.72	AD2481; HSHJ235; KH729
UGCSJ083852.98+195136.4	15.87	15.49	14.93	14.42	14.11	-34.8	-3.2	0.80	AD2471
UGCSJ083333.93+200425.6	14.27	13.89	13.36	12.76	12.52	-26.6	-6.4	0.72	AD1774; HSHJ43 ; KH509
UGCSJ083559.43+200440.5	14.87	14.38	13.81	13.26	12.95	-36.5	-1.0	0.71	AD2091; HSHJ91 ; JS687; KH743
UGCSJ083622.40+200706.9	15.36	14.88	14.32	13.76	13.45	-26.3	-7.9	0.70	AD2155; KH774
UGCSJ083259.56+200714.8	15.87	15.42	14.82	14.27	13.93	-33.9	-12.6	0.70	AD1696; KH896
UGCSJ082849.90+195920.2	13.19	12.82	12.31	11.79	11.43	-36.3	-10.9	0.72	AD1166; KH491

Continued on next page

Table 4.4– continued from previous page

ID	Z	Y	J	H	K	μ_α (mas yr^{-1})	μ_δ	Pmem	Previous IDs[a]
UGCSJ084332.59+195932.9	14.71	14.31	13.75	13.19	12.88	-35.6	-4.5	0.80	AD3211; HSHJ458; KH655
UGCSJ083201.86+195847.1	15.02	14.58	14.00	13.42	13.14	-36.9	-5.1	0.78	AD1571; HSHJ19 ; KH720
UGCSJ083807.98+200350.5	15.33	14.89	14.31	13.78	13.48	-26.3	-1.1	0.61	HSHJ195; KH702
UGCSJ083754.54+200812.2	13.41	13.10	12.62	12.02	11.82	-31.4	-3.5	0.84	HSHJ184; JS206; KH415
UGCSJ085147.06+202720.7	14.36	14.08	13.62	13.03	12.80	-36.4	1.0	0.63	AD3910
UGCSJ083454.42+222050.5	13.45	13.20	12.77	12.17	11.99	-39.7	-7.6	0.61	AD1950

[a] References: AD = Adams et al. (2002b), HSHJ = Hambly et al. (1995b), JS = Jones & Cudworth (1983) and KH = Kraus & Hillenbrand (2007).

Table 4.5: New high probability members taken from the UKIDSS DR8-2MASS sample.

ID	Z	Y	J	H	K	μ_α (mas yr^{-1})	μ_δ	Pmem
UGCSJ083925.46+214721.9	15.46	15.12	14.62	14.06	13.81	-31.1	-8.8	0.80
UGCSJ083301.71+213902.1	13.95	13.75	13.35	12.73	12.58	-24.6	-4.5	0.70
UGCSJ084826.25+213235.7	15.98	15.59	15.02	14.48	14.20	-32.4	-1.6	0.78
UGCSJ083813.61+211329.2	15.05	14.81	14.33	13.72	13.51	-32.5	1.7	0.64
UGCSJ083310.88+210959.8	13.38	13.15	12.71	12.10	11.92	-22.9	-6.5	0.61
UGCSJ083032.17+211015.4	15.26	14.96	14.46	13.84	13.66	-29.4	-7.3	0.80
UGCSJ083956.01+211419.1	15.84	15.49	15.00	14.43	14.18	-25.5	-4.8	0.66
UGCSJ083906.54+205243.8	14.92	14.70	14.24	13.64	13.49	-26.9	-11.6	0.63
UGCSJ083553.75+191055.8	15.11	14.85	14.39	13.79	13.61	-26.2	-6.3	0.70
UGCSJ083115.62+184708.9	15.89	15.58	15.13	14.57	14.35	-31.1	-0.3	0.73
UGCSJ083448.26+181300.2	14.46	14.26	13.82	13.21	13.08	-27.6	-4.5	0.75
UGCSJ083459.25+181805.4	15.43	15.19	14.71	14.10	13.88	-32.9	-1.5	0.77
UGCSJ083509.93+181228.0	14.30	14.11	13.67	13.04	12.91	-25.4	-4.3	0.64
UGCSJ083306.96+174242.1	15.29	14.77	14.16	13.61	13.31	-26.3	-3.6	0.68
UGCSJ083701.06+172005.1	14.80	14.47	13.94	13.41	13.12	-28.1	-7.2	0.77
UGCSJ084709.34+172925.6	15.45	15.11	14.58	14.12	13.87	-33.1	-9.3	0.80
UGCSJ084111.21+171120.9	15.32	15.08	14.63	14.03	13.82	-25.1	-8.4	0.62
UGCSJ084419.37+165615.5	13.64	13.39	12.94	12.31	12.17	-33.4	-3.7	0.83
UGCSJ084316.64+183013.3	15.19	14.87	14.38	13.81	13.56	-29.6	-7.6	0.80
UGCSJ084744.82+182615.7	15.37	14.89	14.38	13.76	13.46	-27.4	-9.0	0.73
UGCSJ083956.77+185009.0	14.68	14.41	14.01	13.45	13.22	-33.3	-2.6	0.80
UGCSJ085036.41+190118.5	13.89	13.73	13.32	12.84	12.71	-37.6	-1.1	0.65
UGCSJ084000.28+185608.4	15.49	15.10	14.60	14.06	13.83	-29.3	-13.5	0.63

Continued on next page

Table 4.5– continued from previous page

ID	Z	Y	J	H	K	μ_α (mas yr^{-1})	μ_δ (mas yr^{-1})	Pmem
UGCSJ084852.59+190246.9	14.38	14.05	13.58	13.02	12.76	-28.8	-8.5	0.77
UGCSJ084925.57+174039.2	14.82	14.59	14.15	13.58	13.42	-28.0	-9.9	0.73
UGCSJ084640.17+180456.3	14.13	13.84	13.35	12.74	12.52	-27.5	-4.9	0.75
UGCSJ083839.93+181218.1	15.29	14.95	14.46	13.92	13.67	-26.2	-4.0	0.68
UGCSJ084843.84+181855.3	13.12	12.97	12.59	12.12	11.97	-25.8	-12.1	0.66
UGCSJ085145.30+184338.5	15.17	14.91	14.46	13.84	13.66	-25.9	-11.0	0.60
UGCSJ084715.19+190842.9	15.22	14.91	14.44	13.79	13.54	-33.6	-12.4	0.71
UGCSJ084825.43+190939.3	15.55	15.10	14.53	13.99	13.71	-38.5	-7.1	0.72
UGCSJ084028.45+200551.2	14.70	14.34	13.82	13.24	12.98	-26.6	-4.1	0.70
UGCSJ083211.79+192232.9	14.59	14.33	13.84	13.21	13.02	-25.7	-4.7	0.67

Table 4.6: UKIDSS DR8-SDSS photometric candidates. Details listed in bold are from the UKIDSS DR8-SDSS z' only selection.

ID	Z	Y	J	H	K	μ_α (mas yr^{-1})	μ_δ	Pmem	Fit Order
UGCSJ083301.71+213534.7	18.65	17.93	17.20	16.61	16.17	17.00	-4.28	0.00	12
UGCSJ084306.24+214134.2	18.40	17.56	16.71	16.16	15.73	-39.45	-43.35	0.00	12
UGCSJ084218.27+212342.1	18.18	17.50	16.81	16.27	15.88	-3.90	-6.05	0.00	12
UGCSJ085052.56+195321.9	19.24	18.34	17.40	16.75	16.22	-6.36	-20.24	0.00	12
UGCSJ084652.65+172017.9	18.67	17.91	17.15	16.62	16.18	20.57	-32.27	0.00	12
UGCSJ083527.36+192043.4	19.54	18.57	17.59	16.99	16.41	-73.76	72.25	0.00	12
UGCSJ083621.08+173544.5	19.01	17.99	17.12	16.52	16.06	-30.32	-15.09	0.88, **0.80**	12
UGCSJ084452.78+171409.8	18.77	17.76	16.90	16.33	15.84	-44.21	-17.09	0.28, **0.54**	12
UGCSJ084045.71+171218.3	19.09	18.17	17.20	16.60	16.17	-33.19	1.00	0.88, **0.80**	12
UGCSJ083732.03+192710.7	18.26	17.51	16.84	16.32	15.90	2.70	1.29	0.00	12
UGCSJ084650.44+214805.4	17.37	16.68	16.08	15.62	15.28	-80.74	-115.45	0.00	12
UGCSJ084926.31+202127.0	18.64	17.76	17.00	16.54	16.08	-76.88	-29.70	0.00	12
UGCSJ083737.24+202902.6	19.71	18.60	17.39	16.64	16.04	-35.91	-66.07	0.00	12
UGCSJ085002.02+201725.9	19.28	18.56	17.64	17.05	16.53	-44.04	50.96	0.00	12
UGCSJ083203.66+202035.8	19.90	18.68	17.74	17.04	16.52	-31.44	-60.36	0.00	12
UGCSJ083748.01+201448.5	18.09	17.25	16.51	15.94	15.53	-35.52	-45.26	0.00	12
UGCSJ083954.96+202955.7	18.90	17.91	17.06	16.44	15.98	33.03	-54.49	0.00	12
UGCSJ083019.80+203418.8	18.95	17.92	17.11	16.59	16.13	-10.39	-97.89	0.00	12
UGCSJ083353.37+182609.4	19.20	18.17	17.24	16.64	16.18	7.16	-9.96	0.00	12
UGCSJ083141.80+183500.4	15.65	15.07	14.45	13.98	13.64	45.77	-108.54	0.00	12
UGCSJ083531.32+201838.9	18.39	17.62	16.96	16.39	15.99	-18.18	9.39	0.00	12
UGCSJ084428.18+182938.5	19.32	18.22	17.39	16.75	16.19	-47.54	35.34	0.00	12
UGCSJ084407.24+181631.2	18.72	17.96	17.18	16.53	16.16	5.07	9.26	0.00	12

Continued on next page

Table 4.6– continued from previous page

ID	Z	Y	J	H	K	μ_α (mas yr^{-1})	μ_δ	Pmem	Fit Order
UGCSJ084826.15+200236.1	19.13	18.17	17.23	16.63	16.12	-31.07	-6.03	0.88, **0.80**	12
UGCSJ083110.12+181252.7	18.15	17.48	16.74	16.20	15.75	39.55	-47.70	0.00	12
UGCSJ084942.75+180123.5	19.30	18.45	17.47	16.88	16.36	-51.25	-9.18	0.88, **0.80**	12
UGCSJ084056.72+180021.7	18.72	17.82	17.00	16.40	15.91	-40.61	-2.73	0.28, **0.54**	12
UGCSJ083955.10+222300.8	19.06	18.11	17.27	16.64	16.21	-11.29	-9.27	0.00	12
UGCSJ084346.46+210829.4	18.46	17.68	17.00	16.45	16.06	-24.40	-38.75	0.00	12
UGCSJ082924.86+211700.3	16.10	15.59	15.02	14.57	14.27	-102.04	-128.79	0.00	12
UGCSJ084138.84+211655.5	17.88	17.29	16.55	16.03	15.72	7.16	12.34	0.00	12
UGCSJ084507.41+210056.5	18.69	17.87	17.06	16.49	16.14	-37.34	-39.20	0.00	12
UGCSJ084449.14+210153.6	18.77	17.79	16.95	16.41	15.94	-1.19	24.24	0.00	12
UGCSJ084204.64+205941.1	16.77	16.09	15.42	14.93	14.54	114.67	-167.13	0.00	12
UGCSJ082839.58+205401.5	18.48	17.69	16.91	16.34	15.95	14.97	-33.25	0.00	12
UGCSJ082945.32+205455.0	19.26	18.48	17.67	17.10	16.51	3.68	-19.54	0.00	12
UGCSJ083900.61+204356.2	20.05	18.76	17.91	17.33	16.72	2.43	-71.38	0.00	12
UGCSJ083920.28+204629.5	19.34	18.49	17.65	16.95	16.51	-7.29	-9.99	0.00	12
UGCSJ083721.24+204306.1	19.73	18.66	17.56	16.84	16.33	54.27	10.85	0.00	12
UGCSJ083054.47+190119.4	16.13	15.47	14.76	14.21	13.84	-15.33	-128.93	0.00	12
UGCSJ083848.58+184305.7	18.92	18.03	17.16	16.54	16.09	-49.17	2.99	0.28, **0.54**	12
UGCSJ084145.67+185609.7	19.89	18.85	17.79	17.11	16.56	100.94	8.22	0.00	12
UGCSJ084054.58+191504.1	19.85	18.59	17.77	17.10	16.63	-44.74	0.48	0.88, **0.80**	12
UGCSJ084946.53+185433.8	18.50	17.77	16.98	16.49	16.08	-55.45	27.76	0.00	12
UGCSJ083953.85+185255.7	19.11	18.09	17.18	16.61	16.10	-21.64	-21.77	0.88, **0.80**	12
UGCSJ083654.60+195415.7	18.75	17.97	17.11	16.53	15.96	-26.98	28.33	0.00	12

Continued on next page

Table 4.6– continued from previous page

ID	Z	Y	J	H	K	μ_α (mas yr^{-1})	μ_δ (mas yr^{-1})	Pmem	Fit Order
UGCSJ083648.03+194902.2	18.21	17.35	16.60	15.97	15.52	-97.21	-62.47	0.00	12
UGCSJ085228.94+191043.1	18.78	17.95	17.20	16.67	16.21	-8.22	10.66	0.00	12
UGCSJ083724.09+164812.9	18.55	17.81	17.10	16.53	16.10	-6.53	13.74	0.00	12
UGCSJ084714.47+194643.7	18.08	17.45	16.80	16.27	15.86	-8.35	0.18	0.00	12
UGCSJ083832.10+195927.8	20.32	18.94	18.04	17.35	16.76	-47.29	18.66	0.00	12
UGCSJ084548.65+200312.5	18.66	17.81	16.93	16.39	15.90	1.20	35.45	0.00	12
UGCSJ084956.27+205300.0	17.85	17.30	16.65	16.09	15.71	21.06	-27.41	0.00	12
UGCSJ082941.96+212106.9	**13.42**	**12.98**	**12.46**	**11.89**	**11.61**	**-57.94**	**-111.02**	**0.00**	**12**
UGCSJ083513.51+220538.8	**18.96**	**18.18**	**17.47**	**16.89**	**16.39**	**21.26**	**-3.66**	**0.00**	**12**
UGCSJ084410.75+211655.7	**17.55**	**17.01**	**16.40**	**15.92**	**15.57**	**7.56**	**-7.45**	**0.00**	**12**
UGCSJ084832.28+214622.4	**17.80**	**17.25**	**16.63**	**16.16**	**15.80**	**1.78**	**-50.48**	**0.00**	**12**
UGCSJ083133.71+203615.4	**18.50**	**17.89**	**17.23**	**16.69**	**16.25**	**-2.71**	**-13.86**	**0.00**	**12**
UGCSJ084022.38+214237.3	**18.40**	**17.81**	**17.10**	**16.57**	**16.14**	**51.02**	**-37.21**	**0.00**	**12**
UGCSJ084419.64+221116.6	**17.77**	**17.23**	**16.63**	**16.09**	**15.77**	**23.22**	**1.80**	**0.00**	**12**
UGCSJ084402.80+222057.6	**18.08**	**17.51**	**16.91**	**16.30**	**15.91**	**9.05**	**-16.82**	**0.00**	**12**
UGCSJ084408.56+211101.3	**17.88**	**17.38**	**16.74**	**16.20**	**15.84**	**4.71**	**4.72**	**0.00**	**12**
UGCSJ084359.06+213546.6	**17.96**	**17.40**	**16.79**	**16.21**	**15.89**	**1.49**	**13.90**	**0.00**	**12**
UGCSJ083408.07+211800.0	**20.21**	**19.31**	**17.90**	**17.23**	**16.54**	**-48.06**	**67.12**	**0.00**	**12**
UGCSJ084251.78+221519.0	**17.70**	**17.16**	**16.58**	**16.07**	**15.73**	**-49.46**	**-19.66**	**0.59**	**12**
UGCSJ083820.61+183023.7	**17.31**	**16.79**	**16.21**	**15.79**	**15.50**	**37.81**	**-143.94**	**0.00**	**12**
UGCSJ085209.03+200622.9	**19.43**	**18.29**	**17.31**	**16.69**	**16.25**	**6.26**	**-22.98**	**0.00**	**12**
UGCSJ083427.98+183656.3	**18.27**	**17.64**	**17.01**	**16.41**	**16.10**	**16.44**	**13.18**	**0.00**	**12**
UGCSJ084015.88+194016.8	**16.22**	**15.70**	**15.10**	**14.56**	**14.26**	**-18.53**	**21.28**	**0.00**	**12**

Continued on next page

Table 4.6– continued from previous page

ID	Z	Y	J	H	K	μ_α (mas yr^{-1})	μ_δ (mas yr^{-1})	Pmem	Fit Order
UGCSJ084542.92+202635.4	**18.31**	**17.70**	**17.03**	**16.49**	**16.10**	**-5.54**	**15.47**	**0.00**	**12**
UGCSJ083127.86+190736.1	**18.46**	**17.75**	**17.05**	**16.48**	**16.13**	**-24.90**	**-52.85**	**0.00**	**12**
UGCSJ083128.54+191209.3	**18.15**	**17.62**	**16.96**	**16.37**	**16.02**	**-23.50**	**0.93**	**0.54**	**12**
UGCSJ084250.23+203719.7	**17.79**	**17.24**	**16.64**	**16.11**	**15.76**	**2.19**	**2.46**	**0.00**	**12**
UGCSJ084929.53+210932.0	**18.24**	**17.65**	**17.04**	**16.45**	**16.11**	**-27.50**	**-3.20**	**0.54**	**12**
UGCSJ084502.13+211239.9	**18.00**	**17.41**	**16.85**	**16.30**	**15.98**	**-3.03**	**-13.98**	**0.00**	**12**
UGCSJ083033.70+200739.7	**17.91**	**17.33**	**16.66**	**16.10**	**15.76**	**18.15**	**-8.20**	**0.00**	**12**
UGCSJ083213.74+202013.4	**17.63**	**17.04**	**16.43**	**15.95**	**15.63**	**-83.29**	**-66.88**	**0.00**	**12**
UGCSJ083644.83+203826.2	**18.71**	**18.07**	**17.45**	**16.84**	**16.43**	**-5.92**	**18.89**	**0.00**	**12**
UGCSJ084510.65+214817.0	**19.78**	**18.38**	**17.42**	**16.69**	**16.03**	**-35.37**	**-37.99**	**0.00**	**12**
UGCSJ085023.27+201317.9	**18.35**	**17.76**	**17.14**	**16.50**	**16.18**	**11.13**	**11.22**	**0.00**	**12**
UGCSJ084039.29+192839.4	**20.33**	**19.11**	**18.06**	**17.34**	**16.65**	**-39.59**	**-10.94**	**0.91**	**12**
UGCSJ084332.00+195915.8	**20.13**	**18.81**	**17.89**	**17.23**	**16.60**	**-5.98**	**-11.87**	**0.00**	**12**
UGCSJ083506.36+191805.8	**15.11**	**14.51**	**13.83**	**13.28**	**12.91**	**120.25**	**-125.89**	**0.00**	**12**
UGCSJ084418.76+202745.4	**18.21**	**17.56**	**16.94**	**16.36**	**16.02**	**28.20**	**21.60**	**0.00**	**12**
UGCSJ084048.29+202410.4	**17.18**	**16.41**	**15.66**	**15.25**	**14.87**	**333.88**	**-213.07**	**0.00**	**12**
UGCSJ084702.09+211352.0	**18.04**	**17.51**	**16.85**	**16.30**	**15.98**	**-9.25**	**-46.87**	**0.00**	**6**
UGCSJ083036.71+194137.4	**19.95**	**18.54**	**17.48**	**16.77**	**16.26**	**-69.09**	**-18.19**	**0.00**	**12**
UGCSJ084247.52+211036.8	**18.16**	**17.58**	**16.94**	**16.44**	**16.03**	**-4.81**	**-36.79**	**0.00**	**12**
UGCSJ084816.73+215050.9	**15.12**	**14.46**	**13.74**	**13.23**	**12.85**	**156.29**	**-325.06**	**0.00**	**12**
UGCSJ082846.48+195744.6	**17.26**	**16.77**	**16.19**	**15.75**	**15.43**	**-27.55**	**-96.81**	**0.00**	**12**
UGCSJ082811.88+200039.7	**20.25**	**19.17**	**18.10**	**17.31**	**16.74**	**-32.01**	**-16.70**	**0.91**	**12**
UGCSJ084619.71+174118.1	**18.64**	**17.82**	**17.02**	**16.53**	**16.09**	**34.86**	**-33.34**	**0.00**	**12**

Continued on next page

Table 4.6– continued from previous page

ID	Z	Y	J	H	K	μ_{α} (mas yr^{-1})	μ_{δ}	Pmem	Fit Order
UGCSJ084946.89+180833.7	**17.45**	**16.91**	**16.28**	**15.85**	**15.51**	**-53.14**	**-58.66**	**0.00**	**12**
UGCSJ083612.51+170842.5	**18.53**	**17.82**	**17.16**	**16.60**	**16.18**	**-32.89**	**-2.69**	**0.54**	**12**
UGCSJ083723.71+171009.9	**18.46**	**17.82**	**17.19**	**16.55**	**16.13**	**-39.57**	**-16.95**	**0.54**	**12**
UGCSJ083912.95+175853.0	**16.31**	**15.54**	**14.82**	**14.29**	**13.90**	**-24.93**	**-118.00**	**0.00**	**12**
UGCSJ084840.59+185438.0	**18.86**	**18.08**	**17.50**	**16.84**	**16.44**	**-25.57**	**-6.67**	**0.54**	**12**
UGCSJ083353.49+174545.8	**17.88**	**17.32**	**16.72**	**16.17**	**15.86**	**-29.72**	**-24.68**	**0.59**	**12**
UGCSJ084244.07+183819.1	**18.32**	**17.64**	**17.03**	**16.43**	**16.10**	**4.57**	**20.02**	**0.00**	**12**
UGCSJ084355.95+185216.8	**17.80**	**17.21**	**16.55**	**16.00**	**15.69**	**-31.19**	**2.48**	**0.59**	**12**
UGCSJ084303.71+191214.8	**14.65**	**14.16**	**13.57**	**13.05**	**12.75**	**54.31**	**-262.66**	**0.00**	**12**
UGCSJ084344.70+183322.5	**14.66**	**13.97**	**13.34**	**12.75**	**12.40**	**20.01**	**-117.24**	**0.00**	**12**
UGCSJ084346.57+184056.8	**17.61**	**17.05**	**16.47**	**15.97**	**15.68**	**13.58**	**-30.63**	**0.00**	**12**
UGCSJ084008.80+184031.4	**18.08**	**17.45**	**16.86**	**16.30**	**15.96**	**-44.66**	**-6.55**	**0.54**	**12**
UGCSJ084006.94+191514.1	**18.73**	**18.01**	**17.28**	**16.77**	**16.29**	**-1.45**	**-6.48**	**0.00**	**12**
UGCSJ082916.37+182749.2	**17.75**	**17.23**	**16.61**	**16.13**	**15.75**	**-27.24**	**10.48**	**0.00**	**12**
UGCSJ085115.44+204044.8	**14.62**	**14.15**	**13.56**	**13.05**	**12.76**	**-104.43**	**-153.35**	**0.00**	**12**
UGCSJ084354.00+172221.8	**18.26**	**17.67**	**17.05**	**16.47**	**16.13**	**-8.75**	**-3.46**	**0.00**	**12**
UGCSJ083636.57+170619.6	**17.62**	**17.06**	**16.43**	**15.92**	**15.54**	**13.54**	**20.78**	**0.00**	**12**
UGCSJ084119.16+173407.6	**18.12**	**17.50**	**16.89**	**16.34**	**16.00**	**-2.66**	**-3.49**	**0.00**	**12**
UGCSJ084420.71+181309.8	**17.74**	**17.21**	**16.60**	**15.97**	**15.73**	**-7.53**	**-2.37**	**0.00**	**12**
UGCSJ084131.98+165226.7	**18.35**	**17.74**	**17.12**	**16.53**	**16.18**	**12.51**	**12.68**	**0.00**	**12**
UGCSJ083556.33+171023.4	**19.48**	**18.76**	**17.85**	**17.33**	**16.72**	**-29.44**	**-44.27**	**0.00**	**12**
UGCSJ083739.70+172854.7	**18.20**	**17.57**	**16.96**	**16.38**	**15.98**	**9.20**	**9.78**	**0.00**	**12**

Chapter 5

Blanco 1

5.1 Introduction

Presented in this chapter are the results of a deep J band imaging program undertaken with WFCAM in 2006 to obtain proper motions for the low mass population presented by Moraux et al. (2007). The candidates are first selected from an examination of their $I-z$, I, $z-J$, z and $I-J$, I colour magnitude sequences before applying a pixel-pixel transformation routine to calculate their proper motions.

5.1.1 Blanco 1

Follow up J band imaging of the cluster ζ Sculptoris, more commonly now known as Blanco 1[1] has been undertaken to provide additional proper motion information in order to aid in the confirmation of cluster members. The cluster itself was first identified in

[1]A determination of proper motion and parallax for ζ Sculptoris have since shown that it is not associated with the cluster, Westerlund et al. (1988).

1949 (Blanco 1949) after an over-density of A0 stars was observed in Kapteyns's area number 140 (Pickering et al. 1923) when compared to regions of similar galactic latitude. Many photometric surveys have since been carried out, for example those of Westerlund (1963), Epstein (1968), Eggen (1970), Eggen (1972) and Perry et al. (1978). In 1985, de Epstein & Epstein published a large photometric survey based upon photographic measurements of about 1500 stars, concluding that about 150 of which belonged to the cluster. Their broad and intermediate band photometry extended the cluster sequence down to magnitudes of $V \simeq 16.6$ and $B \simeq 17.6$ respectively[2]. de Epstein & Epstein (1985) also found the cluster to suffer only a small amount of reddening, E(B-V)=0.013 and based upon estimates of the cluster's volume and mass concluded a stellar space density for Blanco 1 of the order $\simeq 0.8 \mathrm{M}_{\odot}$ / pc^3. Spectroscopic work by Dolidze (1959) showed evidence for Hα emission in 70 stars but the result was not confirmed by the work of Bond (1972).

An extensive period of observations of Blanco 1 began in 1994 starting with Panagi et al. (1994). In analysing low resolution spectra of the Ca II (H,K) lines, medium resolution spectra of the Ca II (H,K), Hα and Ca II (I-R) triplet lines along with high resolution spectra of the Hβ lines for 115 of the de Epstein & Epstein (1985) objects, Panagi et al. (1994) inferred an age for Blanco 1 similar to that of α Per ($\approx$50 Myrs) by measuring the equivalent width of the Li (6708Å) line. In a follow up paper, Panagi & O'dell (1997) used measurements of Hα from the Anglo Australian Telescope's[3] Royal Greenwich Observatory Spectrograph to study the chromospheric activity in 125 stars. The mean

[2] The survey was actually conducted with blue and yellow photographic plates that were subsequently transformed into B and V magnitudes.

[3] Now the Anglo Australian Observatory.

emission strength of Hα had been shown to correlate well with the age of late K and M-dwarfs, with the fraction of Hα emitting stars allowing an age determination[4] of 90 $\pm$ 25 Myrs to be derived. This placed Blanco 1 in an age range much similar to that of the Pleiades cluster at 125 Myrs. It had been suspected that Blanco 1 was also a rather metal rich cluster with Edvardsson et al. (1995) claiming an enrichment about 70% higher than the solar value with [Fe/H]=+0.23. This suggested that Blanco 1 would be a promising candidate for short period exoplanets as suggested by the trend presented in Figure 6 of Santos et al. (2004). High resolution spectroscopy of eight F and G type stars by Ford et al. (2005) showed that on average the metallicity was much lower with [Fe/H]=+0.04. Subsolar abundances for [Ni/Fe], [Si/Fe], [Mg/Fe], and [Ca/Fe] were also reported.

A lot of the interest in Blanco 1 has also followed on from the X-ray observations carried out by Micela et al. (1999). ROSAT High Resolution Imager data revealed a large population of X-ray sources to be present in the cluster. Pillitteri et al. (2003), Pillitteri et al. (2004) and Pillitteri et al. (2005) used corroborating XMM-Newton data to identify candidate members and construct X-ray luminosity distribution functions for the G, K and M type stars, as well as studying X-ray time variability and flaring of some of cluster objects. Cargile et al. (2009) were then successfully able to match 47 X-ray sources that were associated with the cluster to optical counterparts after utilising a standardised $UBVI_c$ survey which combined some 40 years worth of photographic and CCD data[5] taken mostly by the Cesco Observatory in Argentina. This 1.6 x 1.3 square degree survey of Blanco 1 allowed for a high fidelity photometric data set to be coupled

[4] A smaller fraction of stars with Hα emission is indicative of an older age.
[5] The photometric catalogue derived contains 1668 stellar objects.

with the UCAC2 catalogue providing a highly precise proper motion catalogue of members (σ=0.5 mas yr^{-1}). Mermilliod et al. (2008) also used this catalogue to study the membership, binarity and rotation of the F, G and K-type stars within the cluster. Confirming 68 members on the basis of photometry, proper motion and radial velocity with 14 spectroscopic and suspected binaries Mermilliod et al. (2008) place the binary fraction between 20 and 40% which is comparable to that of Lodieu et al. (2007a) who found in the Pleiades a similar binary fraction albeit for a much lower mass range (28-44% over 0.075-0.030$M_\odot$). The survey was still however limited to a magnitude of $V \approx$17, with objects fainter than $V \sim$15 becoming heavily contaminated with unassociated cluster objects. This was highlighted by the authors as the need for obtaining extra information on which to base membership probabilities on e.g proper motions for the faintest stars. It is with this point in mind that a programme was set out to extend the photometric and spectroscopic work of Moraux et al. (2007) to include proper motion determinations. Moraux et al. (2007) performed a deep I and z band survey covering 2.3 square degrees of Blanco 1 and were sensitive down to $\sim$0.03$M_\odot$. The single epoch results concluded that there should be about 30-40 brown dwarfs present and that the radial distribution was indicative that mass segregation had already occured. When combined with the results from Pillitteri et al. (2003) the log-normal Chabrier IMF covering 0.03-3$M_\odot$ also showed a result comparable to the similarly aged northern hemisphere cluster of the Pleiades. In attempting to constrain the cluster members and thus produce a more representative IMF than that presented from photometric cuts alone, differences between the IMFs of the two clusters may become apparent. This can provide indications as to how different environments affect the formation of a cluster and its constituent objects, as well as the role

Table 5.1. Properties of the open cluster Blanco 1.

Cluster Property	Value	References
Ra, Dec (J2000)	00:04:24, -29°56.4'	Lynga & Palous (1987); van Leeuwen (2009)
l, b	14°.1, -79°.3	van Leeuwen (2009)
Age	90±25	Panagi & O'dell (1997)
Distance	207pc, 316pc[a]	van Leeuwen (2009); Moraux et al. (2007)
Metallicity	[Fe/H]=+0.04	Ford et al. (2005)
Mass	≈400-450$M_{\odot}$	Moraux et al. (2007)
Extinction E(B-V)mag	0.013	de Epstein & Epstein (1985)
I_{BD}	19.15	Aigrain et al. (2007)

[a] This was the maximum distance value used in the analysis by Moraux et al. (2007) from the Hipparcos analysis by Robichon et al. (1999).

that dynamical evolution plays in shaping the population of cluster members over time. Table 5.1 lists the properties of the Blanco 1 cluster.

5.2 Data Reduction

The initial Blanco 1 data published in Moraux et al. (2007) was taken with the CFHT12k optical mosaic camera during two separate runs. The first of the runs occurred between 30 September 1999 and 2 October 1999, with the second occurring between 18 and 20 of December 2000. A total of 7 fields were observed covering an area of 2.3 square degrees, in a (mostly) non overlapping pattern. Each separate field covered an area of 28'×42'. The area of sky covered is shown in Figure 5.1. For each filter, I and z, a short observation of 10s was accompanied by two longer 600s exposures. These were then combined to produce an equivalent image containing 1200s worth of exposure. The detection limits of the data were $I{\sim}z{\sim}24$ (Moraux et al. 2007), with the hydrogen burning limit (0.072$M_{\odot}$) occurring at $I{\approx}19.15$. The reduction of the initial data by Moraux et al.

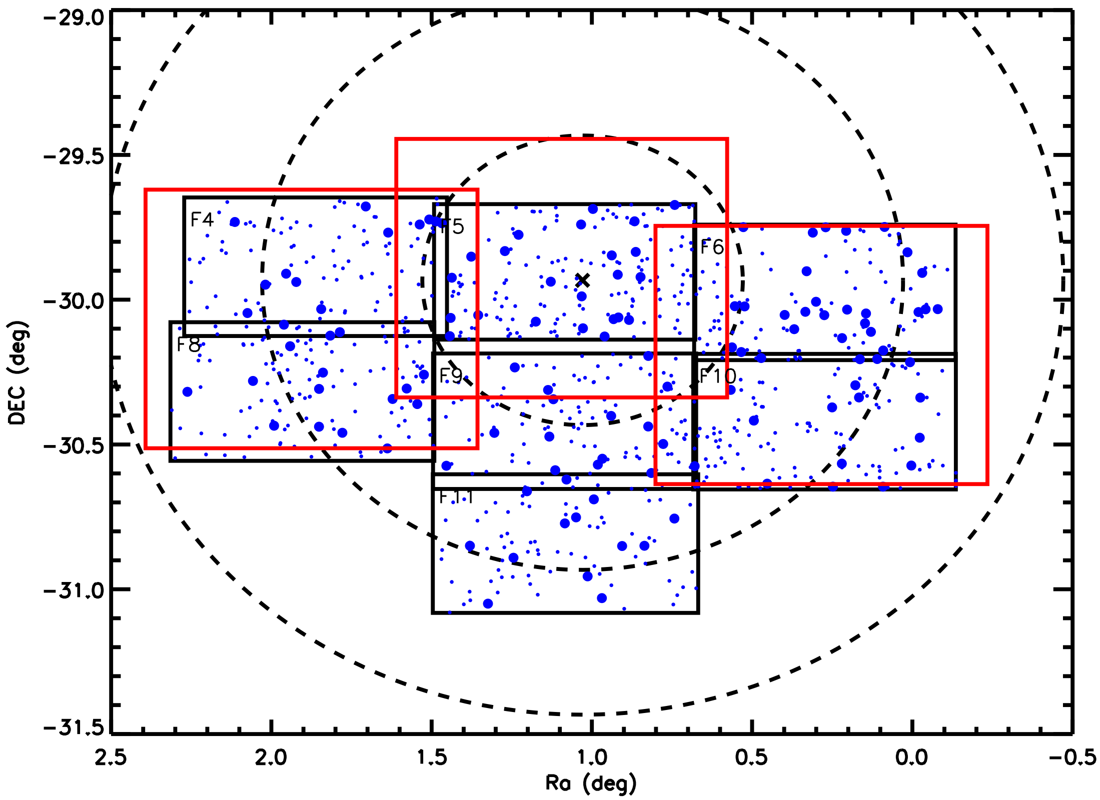

FIGURE 5.1. Outline of the sky coverage of Blanco 1 from the CFHT12k tiles (black) and the WFCAM tiles (red), the low-mass and very-low-mass candidate lists of Moraux et al. (2007) are shown as the small and large blue dots respectively. The black cross indicates the cluster centre, with circles of radius 0.5, 1.0 and 1.5 degrees being shown by the dashed black lines.

(2007) followed the same prescription as described in Moraux et al. (2003). The original raw data have been re-reduced, the process of which is described in Section 5.2.1. In addition to the CFHT12k photometric data, three WFCAM J band tiles were obtained, 2 on the night of 31 October 2006 and 1 on the night of 22 July 2009. Each WFCAM pawprint used exposures of 18s yielding an estimated completeness limit of $J\sim$20.5 and detection limit of $J\approx$22. The WFCAM data were again processed by CASU as described in Chapter 4. The total area covered by the WFCAM fields is smaller than that covered by the CFHT12k data, this is shown by the red lines in Figure 5.1.

5.2.1 CFHT12k data

The original raw 600s I and z data were extracted from the Canadian Astrophysical Data Centre (CADC) archive[6] and were kindly reprocessed by Simon Hodgkin using the optical and imaging pipeline (Irwin & Lewis 2001) that had been used previously in course of a CFHT12k Iz-WFCAM J survey of the Pleaides by Casewell et al. (2007). This required the combining of the two 600s images, attempting where possible, to address the astrometric inaccuracies shown in Figure 3.17 and performing source extraction and subsequent catalogue generation. Sources were identified as having a minimum of 5 interconnected pixels sitting at a significance of 1.5σ above the background, with aperture photometry carried out using a radius of 3.5 pixels. In addition a morphological classification flag was provided with -1 indicating a stellar like profile, 0 noise and +1 non-stellar like sources. For the field-filter-extension/chip combinations of F4-I-10, F4-z-10, F6-I-6, F6-z-6 and F8-I-8 the astrometry needed further correction to that supplied by the CASU pipeline. To do this the telescope's RA and Dec pointing information was first extracted from the FITS extension header associated with the chip, before being used in a wget script that downloaded a circular region of the 2MASS catalogue provided by Vizier using an 8" search radius. From this online catalogue, sources with "AAA" photometry were selected and used as the basis for pattern matching to the source extracted catalogue before a new WCS solution was derived and written to the FITS header as detailed in Chapter 3.

[6]Raw images in the archive are appended with the letter 'o' whilst those that have passed through the ELIXIR pipeline and are designated as calibrated are appended with the letter 'p'. The 10s images of Blanco 1 and the Landolt fields were available in both raw and calibrated forms from CADC, whilst the 600s exposures were only available in raw format.

In order to photometrically calibrate the data two approaches were considered. The first was the approach described in Moraux et al. (2003), whereby the I band zero-point was derived using the Landolt photometric standard fields SA98 and SA113 and the z band zero-point was found using unreddened A0 standard stars (assuming the I and z magnitudes were therefore the same). Simon Hodgkin again kindly constructed source catalogues for the Landolt fields but as with the Blanco 1 data the calibrated CADC data was of poor astrometric quality. To correct this the WCS, of the raw images (which were more astrometrically accurate) were substituted into the FITS headers of the processed data. The central pixels on the chip then provided an approximate RA and Dec from which to obtain a reference 2MASS catalogue for astrometric calibration. After allowing positional matching to take place between the x and y pixel source detections and the standard stars present in the Landolt catalogue few standard stars were identified as being present across all of the chips with a paucity of A0 stars with close to zero colour (B-V < 0.1 and V-I < 0.1) being found. A second method of photometric calibration was then decided upon, one that would allow for a zero point to be calculated for each chip in each filter.

Hodgkin (2010) provided data from a series of observations taken with the 2.2m ESO telescope located at La Silla, Chile as part of the Monitor Project. The Monitor project is a repeating photometric survey of nine clusters within the solar neighbourhood tasked with producing high precision light curves of possible eclipses produced by BD and planetary transits. The survey for transits in the Blanco 1 cluster whilst not covering as large an area as the CFHT12k data does provide a sufficient overlap (see Figure 5.2) to

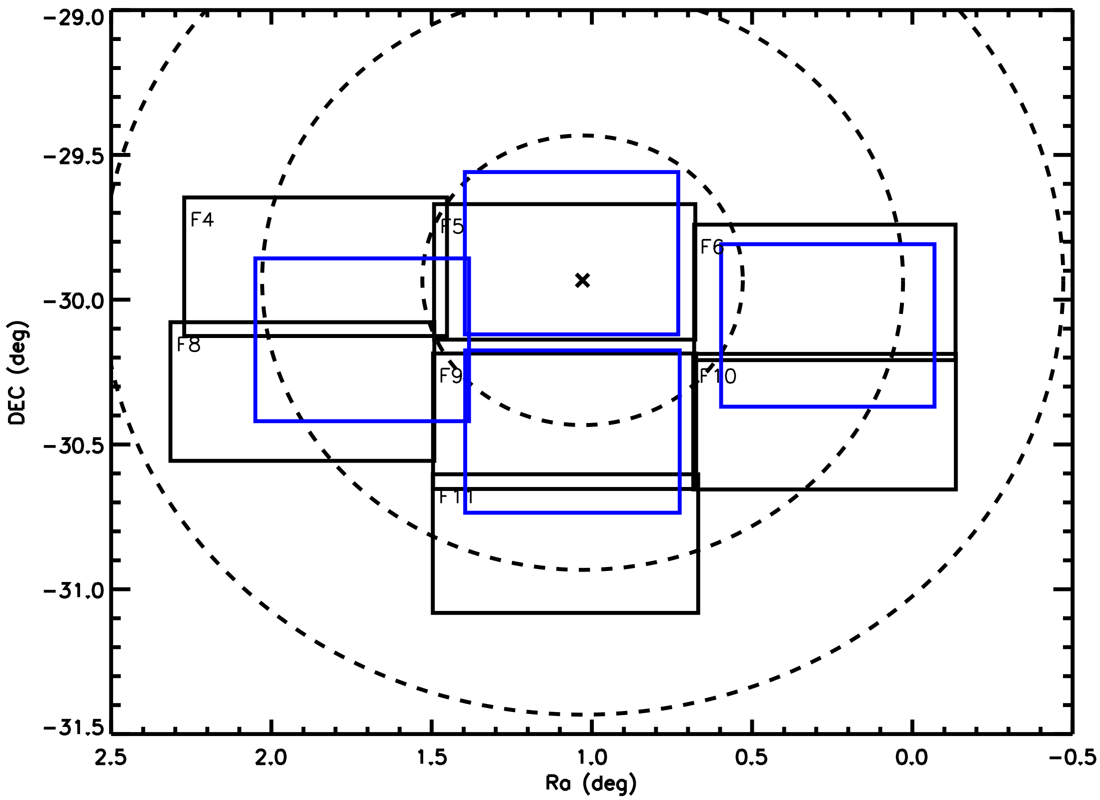

FIGURE 5.2. Outline of the coverage of Blanco 1 offered by the Monitor project data (blue) compared to the coverage given by the CFHT12k fields (black).

allow for a photometric calibration to take place. The repeated I band measurements as well as a number of z band observations also allowed for each filter to be calibrated separately rather than relying on A0 stars.

The magnitudes of the objects detected by the source extraction routines were calculated as follows;

$$m = -2.5 \times \log\left(\frac{Coreflux}{1200s}\right) - apcor + [(airmass - 1) \times extcorr] + colourzp \quad (5.1)$$

where $Coreflux$ is the flux associated with an aperture of 3.5 pixels and $apcor$ is the appropriate aperture correction value located within the catalogue's FITS header. The I band extinction correction ($extcorr$) is taken as 0.04 with the z band extinction given as 0.03 by Bouvier et al. (2008). The zero-point term ($colourzp$) for the I and z band was calculated as described in Chapter 3. To compute approximate errors on the source extracted fluxes the following was used before being folded in to equation 5.1

$$error = \sqrt{\left(\frac{Coreflux}{gain} + \left((\pi \times rcore^2) \times skynoise^2\right)\right)} \tag{5.2}$$

Where $gain$ is the gain level of the CCD, $rcore$ the core pixel radius and $skynoise$ is the pixel noise at sky level given by a robust calculation of the absolute deviation about the median scaled to a Gaussian RMS by multiplying by 1.48[7]. In calculating the zero-point by comparing the uncalibrated instrumental magnitudes against those from the Monitor project the data from each of the 12 CFHT12k CCDs were binned together for each of the two separate runs, e.g. all the objects found on chip 6 taken in the 1999 run were combined to provide one single photometric zero-point for that chip. Values for the calculated zero-points are listed in Table 5.2. As small regions of overlap exist between some of the CFHT12k fields, a test of photometric accuracy was conducted for those objects with duplicate detections. This yielded RMS values of ≈0.035 and ≈0.040 for the z and I filters respectively.

[7] See http://casu.ast.cam.ac.uk/surveys-projects/wfcam/technical/catalogue-generation for more details.

Table 5.2. Zero-points for the CFHT12k I and z 1999 and 2000 observations after being calibrated against Monitor data provided by Simon Hodgkin.

Chip	I zero-point (1999, 2000)	I zero-point error ($\pm$) (1999, 2000)	z zero-point (1999, 2000)	z zero-point error ($\pm$) (1999, 2000)
1	-25.499, -25.413	0.019, 0.067	-24.599, -24.475	0.033, 0.029
2	-25.486, -25.468	0.162, 0.053	-24.624, -24.567	0.016, 0.031
3	-25.460, -25.417	0.025, 0.021	-24.572, -24.519	0.028, 0.016
4	-25.461, -25.455	0.015, 0.041	-24.597, -24.576	0.052, 0.029
5	-25.408, -25.327	0.050, 0.021	-24.597, -24.426	0.047, 0.016
6	-25.350, -25.417	0.076, 0.021	-24.499, -24.519	0.088, 0.016
7	-25.501, -25.417	0.020, 0.021	-24.641, -24.519	0.022, 0.016
8	-25.449, -25.407	0.021, 0.021	-24.584, -24.484	0.016, 0.016
9	-25.514, -25.411	0.017, 0.033	-24.625, -24.570	0.017, 0.012
10	-25.474, -25.371	0.029, 0.033	-24.634, -24.499	0.030, 0.020
11	-25.471, -25.417	0.017, 0.021	-24.668, -24.519	0.021, 0.16
12	-25.498, -25.417	0.022, 0.021	-24.609, -24.519	0.020, 0.016

Following the photometric calibration, the separate I and z catalogues for each CFHT12k CCD chip were merged together. This was done by using a flux limited sample of objects that had been morphologically classified as stellar. This subset was used as an input for pattern matching and linear transformation equation generation between the associated x and y pixel coordinates of the objects. Once a transformation had been established for the "clean" sample it was used to match the full sample together helping to reduce the number of spurious detections between the two images.

5.2.2 Cross-Correlation to the WFCAM data

As can be seen in Figure 5.1 the three WFCAM tiles have a significant amount of overlap. In addition to this, each tile is constructed from four separate slightly overlapping pointings. This means that a large population of objects had multiple detections. These multiple detections suffer from very minor positional changes affecting the effectiveness of cross matching data. To alleviate this problem a number of steps were taken as described below.

1. From the WFCAM source catalogues a reduced set was created consisting solely of sources that were classified as stellar with ellipticities less than 0.2 and J band magnitudes between 15.0 and 19.0.

2. For the full and reduced set of catalogues the first set of pawprints were merged together into one tile.

3. Objects that were separated by less than 1” were then deemed to be the same object.

4. These multiple detections were removed from the combined pawprint, being replaced by just one of the detections.

5. A data flag was used to indicate which objects were multiple sources and contained all of their original unique identification numbers.

6. After repeating the above process for the other pawprints, the three WFCAM tiles now containing single detections were combined.

7. Sources in the overlapping regions between tiles were again selected to be multiple detections if they lay less than 1” from each other.

The CFHT12k data on an individual field by field, chip by chip basis was then pattern matched to the reduced WFCAM data containing single detections. Using the reduced WFCAM data allowed for a more reliable transformation to be established in a much shorter time. Again, after a transformation had been established it was used to transform the full CFHT12k data set onto the WFCAM reference frame before matching began to the non-reduced, single detection WFCAM catalogue. The data set was then expanded by duplicating the CFHT12k object information and associating it with each individual WFCAM detection that had been flagged previously as a duplicate.

The final CFHT12k-WFCAM catalogue was then constructed by requesting that in the merged catalogue, with all its multiple detections, the source be classified as stellar in both the CFHT12k I and z band images as well as the WFCAM J band image. The resulting catalogue contained 9853 sources (8440 of which were unique).

5.3 Results

5.3.1 Colour Cuts

After producing the multi-epoch catalogue, three colour magnitude cuts were made in $I - z$, I, $z - J$, z and $I - J$, I and can be seen in Figure 5.3. In total 76 objects were present between the three bounding box regions (shown in red). The members selected by Casewell et al. (2007) for the similarly aged Pleiades have also been overlaid in Figure 5.3 as the green points. Correcting their magnitudes to each of the distances presented in Table 5.1 and comparing to the clearly observable sequence of Blanco 1 the distance of 207pc found by van Leeuwen (2009) was favoured. This is in contrast with 316pc value used by Moraux et al. (2007).

5.3.2 Calculating Proper Motions and Probabilities

As for the Praesepe data, the CFHT12k-WFCAM data have had their proper motions calculated via the use of a quadratic pixel-pixel transformation routine that uses a set of anonymous stationary sources present between each epoch image. Where a quadratic fit could not be established, a linear fit was attempted instead. The reference objects were selected to have magnitudes $18 \leq \mathrm{mag} < 20$ in I and z, so as to be similar to that of

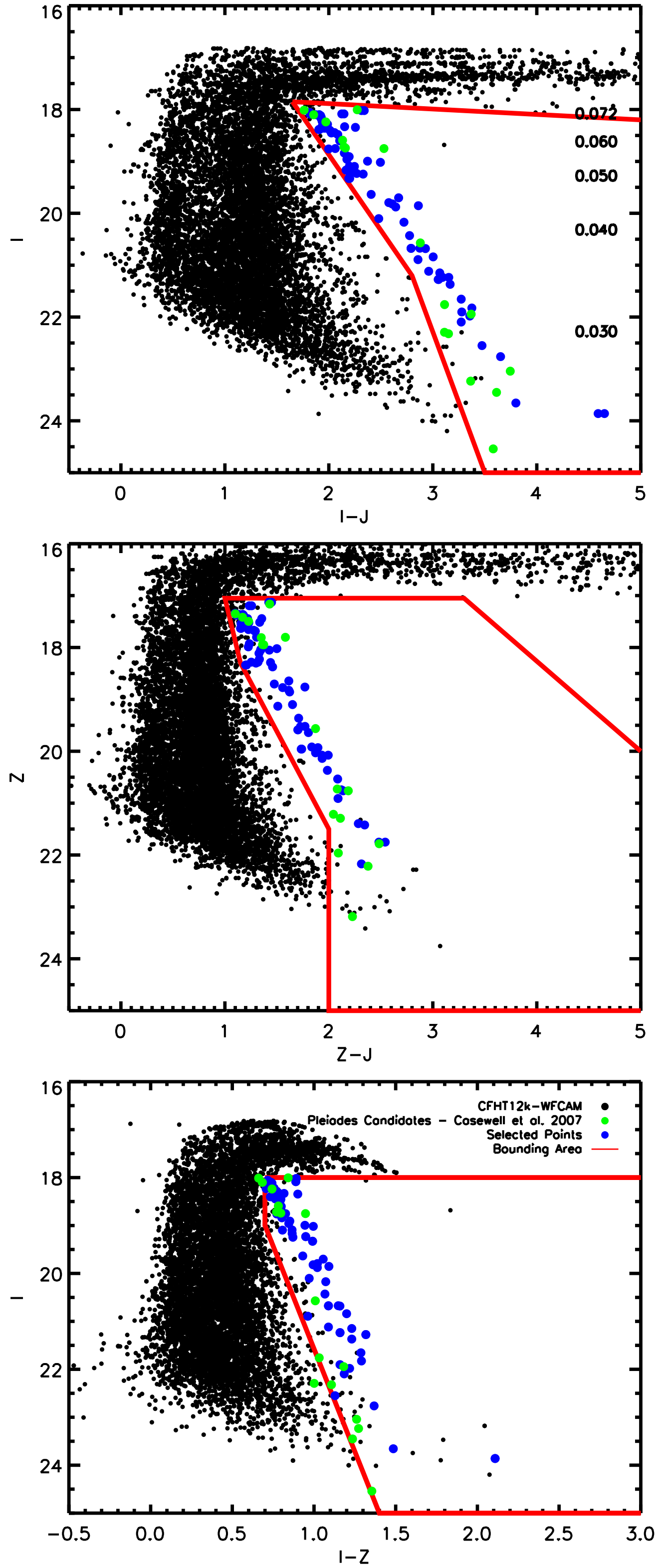

FIGURE 5.3. Colour magnitude selections in $I-J$, I, $z-J$, z and $I-z$, I. The black points are all the stellar CFHT12k-WFCAM sources. Those common to the three selection regions (denoted in red) are shown as the blue points whilst the Pleiades members of Casewell et al. (2007) are shown in green. The Pleiades members were corrected to a distance of 207pc.

the candidates but not so faint as to have poor pixel centroiding. It was also requested that they have an ellipticity of less than 0.2 in the WFCAM J band image and be located at least 20 pixels away from the edges of their respective CCDs. The centroiding errors were produced by running the CASU $imcore$ routine[8] on the CFHT12k images and calculating the average x and y errors in bins of width 1mag, as was done in Chapter 4. Although the survey had been conducted in the far optical and NIR, to help further minimise any effects brought on by DCR the proper motion was calculated between the z and J bands only. Of the 76 objects presented for proper motion analysis 60 were returned. For those CFHT12k sources that had been matched to multiple WFCAM sources the proper motion determination with the most reliable fit was kept. Of the returned 60 sources, 49 were matched to the low mass candidate and very low mass candidate tables of Moraux et al. (2007)[9] with 10 of the spectroscopic targets also being matched. In total Moraux et al. (2007) present ≈830 candidate objects in their data tables. Of these, 445 are found to have a corresponding object from the CFHT12k-WFCAM set within 2”. In all, discounting the area not covered by WFCAM ≈60 objects presented by Moraux et al. (2007) were found not to have any counterpart. This is most likely due to differing source extraction parameters and matching radii employed.

Examining the proper motion VPD (Figure 5.4) it is clear that towards the location of the cluster there is an over-density of objects when compared with regions at a similar distance but on the opposing side of the field star distribution. Unfortunately, the low

[8]The centroiding information for the WFCAM data is a standard feature in the WFCAM catalogues.

[9]It should also be noted that the tables of Moraux et al. (2007) contained duplicate detections of objects. The combined table being matched to the results of the proper motion analysis contains no such duplication.

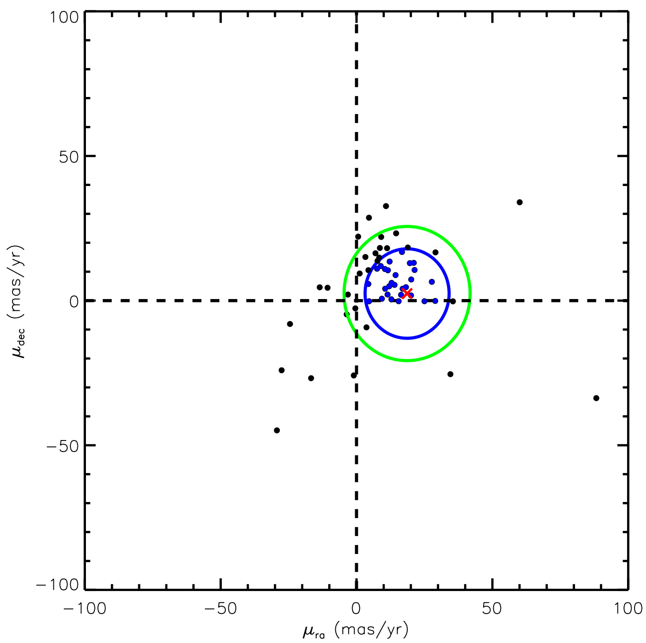

FIGURE 5.4. Proper motion diagram for the Blanco 1 cluster. The proper motion of the cluster is shown by the red cross, whilst the blue and green circles trace out 2 and 3σ circles given the results of fitting a 2D Gaussian to the data and are used to calculate the probability of cluster membership.

number of sources coupled with a proper motion comparable to the average proper motion error means that the two Gaussian approach that was used for the Praesepe 2MASS-UKIDSS data set is not applicable for finding probabilities for the candidate objects. Instead the simpler annulus method was again used. Placing a single 2D Gaussian over the points in proper motion space, rejecting those outside the 2σ boundary and then re-calculating the fit gave a Gaussian width of $\sigma \sim 7.73$ mas yr^{-1}. The binning of the objects in 5 mas yr^{-1} bins resulted in a peak of the Gaussian being placed at $\mu_\alpha = 9.21$ and $\mu_\delta = 6.94$ mas yr^{-1}. This is somewhat different to the cluster motion presented by van Leeuwen (2009) and that present in the analysis of Mermilliod et al. (2008). A circle of radius 2σ was placed over the cluster's proper motion centre as defined by van Leeuwen (2009) with a larger circle of radius 3σ used to create an annulus with which to estimate levels of contamination. For each bin of width 1 magnitude covered by the CFHT12k-WFCAM data set, the number of objects inside the cluster circle was compared to that obtained within the annulus scaled to the same area as the cluster. Using equation 4.22 the membership probabilities were then calculated. These are shown in Table 5.3 whilst Table 5.4 shows the probabilities calculated for each of the candidate members identified by Moraux et al. (2007) that were retrieved in this analysis. Objects shown in bold in the table are those which have been identified as candidate members by this analysis but for which there was no corresponding source in the lists of Moraux et al. (2007).

Table 5.3. Table of probabilities determined from a comparison between the number of objects present within 2σ of the cluster's proper motion centre and those in an annulus located at a distance between 2 and 3σ away.

Magnitude range	Number in Cluster	Number in Annulus	Membership Probability
$15.00 \leq J < 16.00$	0	1	0.00
$16.00 \leq J < 17.00$	17	8	0.84
$17.00 \leq J < 18.00$	6	3	0.83
$18.00 \leq J < 19.00$	4	3	0.75

Table 5.4: Candidate objects presented by Moraux et al. (2007) that were within the cluster area shown in Figure 5.4. Objects also present for which no match was found to the lists of Moraux et al. (2007) as shown in bold.

CFHT-BL	RA	Dec	I	z	J	μ_α mas yr^{-1}	μ_δ	Spectra (Y/N)	Pmem
53	00:02:16	-30:18:41	19.70	18.65	17.03	8.92	1.96	N	0.83
89	23:59:54	-30:20:18	21.98	20.76	18.62	25.00	-0.21	N	0.75
93	00:04:58	-30:14:02	22.10	20.91	18.82	10.53	4.11	N	0.75
526	00:03:32	-30:04:11	18.06	17.34	16.24	16.95	4.10	N	0.84
527	00:02:13	-30:01:19	18.12	17.37	16.20	12.19	13.51	N	0.84
528	00:03:30	-29:59:54	18.09	17.38	16.27	20.04	1.79	N	0.84
532	00:00:07	-30:30:42	18.10	17.36	16.23	7.56	11.02	N	0.84
534	00:00:26	-30:18:19	18.11	17.40	16.21	16.40	2.00	N	0.84
547[a]	00:01:29	-30:06:07	18.23	17.52	16.29	14.37	8.82	Y	1.00
563	00:00:49	-30:02:03	18.48	17.69	16.40	21.07	13.06	N	0.84
567[a]	00:00:40	-30:20:15	18.45	17.65	16.43	12.91	6.13	Y	1.00
571	00:07:51	-30:05:10	18.40	17.67	16.39	28.97	-0.12	N	0.84
580[a]	00:00:43	-30:17:44	18.60	17.80	16.50	11.56	10.49	Y	1.00
595	00:06:11	-30:21:37	18.75	17.93	16.69	16.73	16.81	N	0.84
600[a,b]	00:01:49	-30:38:06	19.00	18.05	16.62	10.44	10.92	Y	1.00
608[a,b]	00:03:24	-29:55:17	19.02	18.02	16.52	11.42	2.10	Y	1.00
609[a]	00:07:09	-30:06:43	18.91	18.06	16.71	21.37	10.59	Y	1.00
621	00:00:36	-30:19:16	19.17	18.30	17.00	27.72	6.50	N	0.83
663	00:03:40	-30:03:41	20.43	19.36	17.65	12.04	4.96	N	0.83
670	23:59:53	-29:54:27	20.68	19.52	17.75	15.51	-0.20	N	0.83
696	00:05:46	-30:03:45	21.24	20.08	18.14	19.63	12.95	N	0.75
705	00:06:49	-29:40:42	20.67	19.53	17.80	18.20	4.63	N	0.83

Continued on next page

Table 5.4– continued from previous page

CFHT-BL	RA	Dec	I	z	J	μ_α	μ_δ	Spectra	Pmem
						mas yr^{-1}		(Y/N)	
719	00:05:05	-29:49:56	20.89	19.93	18.04	12.83	0.45	N	0.75
CW1	**23:59:53**	**-30:13:34**	**19.10**	**18.29**	**16.85**	**4.36**	**5.74**	**N/A**	**0.84**
CW2	**00:06:12**	**-30:00:57**	**18.38**	**17.63**	**16.48**	**9.33**	**0.65**	**N/A**	**0.84**
CW3	**00:07:51**	**-30:05:10**	**18.45**	**17.68**	**16.39**	**4.63**	**-0.22**	**N/A**	**0.84**
CW4	**00:03:26**	**-29:51:07**	**19.79**	**18.77**	**17.22**	**14.00**	**5.43**	**N/A**	**0.83**

[a] As these objects also had spectra consistent with membership their probability was adjusted to equal that of a cluster member. [b] These objects had later spectral types and lower temperatures than their I-magnitudes suggested, coupled with estimates of a low surface gravity, Moraux et al. (2007) believed these to be binary systems. The objects highlighted in bold are those for which a match to the candidates of Moraux et al. (2007) was not found, they have been identified as CFHT-WFCAM candidates (CW).

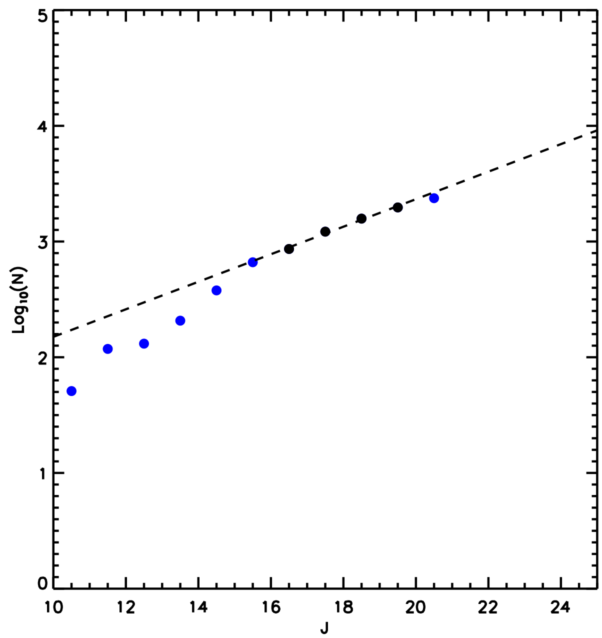

FIGURE 5.5. The measure of incompleteness as found from the CFHT12k-WFCAM stellar source population as a function of J magnitude. The black dotted line is a least squares fit to the associated black points in the figure.

5.4 Mass Spectrum

As in Chapter 4 an incompleteness corrected luminosity function has been produced with the numbers weighted by the probabilities of membership found using the annulus method (Figure 5.6). The incompleteness correction can be seen in Figure 5.5. Objects identified as CFHT-BL-547, 567, 580, 600, 608 and 609 have had spectra taken with the FORS2 spectrograph on the VLT and were identified by Moraux et al. (2007) as members. Accordingly their membership probabilities have been adjusted to 1.0. The luminosity function was produced for the WFCAM J band as the smaller uncertainty on the photometry allowed for a more robust transformation from luminosity to mass to be carried out. The errors are again Poissonian with no corrections made for binarity, though for completeness at least 2 of the objects identified by Moraux et al. (2007) and found here are believed to be binaries (CFHT-BL-600 and CFHT-BL-608). Examining the cluster sequence at least 6 of the objects present themselves as further binary candidates (10%) with estimates as high as 40% achievable with a suitably defined single star sequence. In recent communication, Estelle Moraux has indicated that spectra for the remaining Moraux et al. (2007) candidates has been acquired. Matching the resulting single and binary stars to the sequence shown here will provide a clearer indication of the binary fraction and show if it is in agreement with not only the higher mass result from Mermilliod et al. (2008) but also that of the low-mass Pleiades sequence (Lodieu et al. 2007b). A combined 100 Myr J band mass-luminosity relationship was constructed from the BT-NextGen and BT-DUSTY atmospheric models and scaled to distances of 316pc (distance modulus 7.5) and 207pc (distance modulus 6.57) the results for the former are shown in black in Figure 5.7 whilst the blue points show the latter. Ignoring the relative shift in the x direction a similar trend to that observed in the Moraux et al. (2007) mass function (red) is seen, with a decline in the slope occurring between the bins of 0.125$M_{\odot}$ and 0.06$M_{\odot}$ before rising again to that of the lowest bin at 0.04$M_{\odot}$, for the black points. The lowest mass bin for a distance of 207pc corresponds to 0.03$M_{\odot}$. The mass spectrum appears to be flat or slightly falling overall, but with so few points and large error bars is not statistically significant. It was inappropriate therefore to calculate an α value.

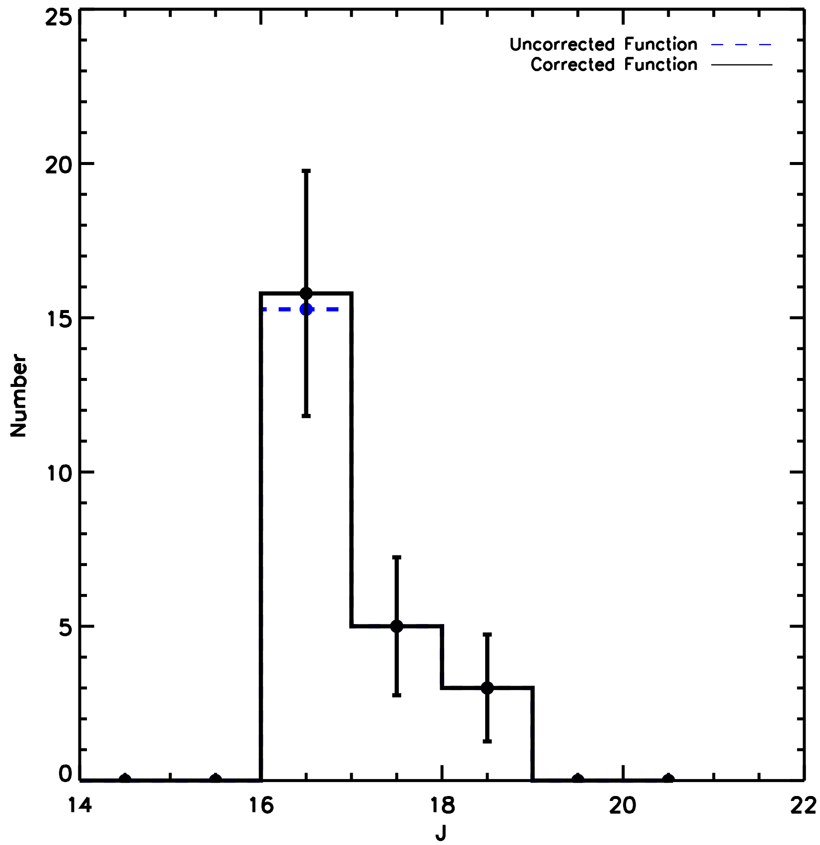

FIGURE 5.6. A J band incompleteness corrected luminosity function produced from the p≥0.6 sample of photometric and proper motion selected objects in Blanco 1. The error bars shown are Poissonian.

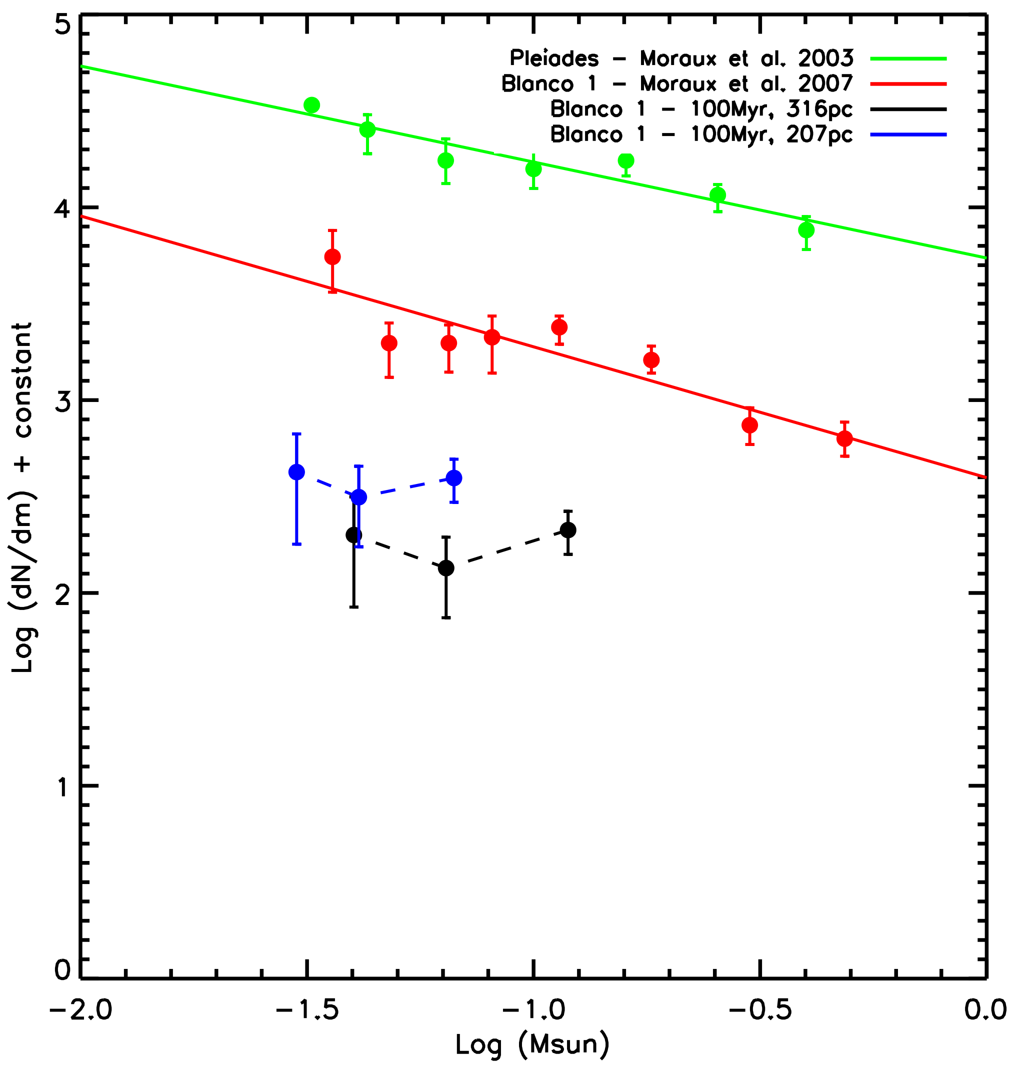

FIGURE 5.7. The Blanco 1 mass function shown in black for a distance of 316pc and blue for the revised 207pc distance from this analysis. The Blanco 1 system mass function of Moraux et al. (2007) is shown in red, whilst the northern Pleiades cluster from Moraux et al. (2003) is shown in green.

5.5 Conclusion

Incorporating proper motion information with a set of photometrically selected targets, 27 cluster members have been identified (23 of which are also identified by Moraux et al. 2007). Of these 27, 6 also have spectroscopic data that are indicative of cluster membership. The masses of these 6 objects from the mass-luminosity relationship range from $\sim$0.075 to $\sim$0.059$M_\odot$. This is given a revised cluster distance of 207pc, a distance that matches well with a suitably corrected Pleiades sequence and is in contrast to the distance of Robichon et al. (1999). With the three WFCAM tiles failing to cover the entire area surveyed by the CFHT12k data, these results have not yet been folded into that of Moraux et al. (2007) or combined with the results of the search for F, G and K-dwarf members by Mermilliod et al. (2008). Doing so would provide an extensive IMF covering a much wider range of masses than covered previously. Ratios of the numbers of objects within discrete mass bins such as 0.02-0.075$M_\odot$, 0.075-0.2$M_\odot$ and 0.2-0.7$M_\odot$ (the *"brown dwarf"*, *"very low-mass star"* and *"stellar"* populations as defined by Boudreault 2008) to each other can be used to test for variations within the IMF due to age and environment. Using the results of Moraux et al. (2007), Boudreault (2008) showed a strong agreement between the Blanco 1 and Pleiades clusters both in terms of age and metallicity (Blanco 1 is slightly more metal rich that the Pleiades). The result is however based upon an IMF constructed out of single epoch data at a distance that is much larger than current estimates would suggest. Data from the VISTA VIKING survey (which aims to cover the whole of the Blanco 1 cluster) will provide deeper multi-band photometry, as well as a far greater baseline between observations to be used in carry-ing out a proper motion analysis looking for cluster members. Combined with follow up spectroscopic data which will allow us to place constraints on the binary fraction, a more constrained IMF can then be derived. This can then be properly compared to clusters such as the Pleiades in order to test for the environmental tolerance of the IMF, as well as providing further observational constraints to compare with the results of BD formation simulations.

Chapter 6

ULAS 0822+0730

6.1 Introduction

The UKIDSS LAS survey aims to survey some 4000 square degrees of the northern hemisphere that has already been covered by the optical SDSS. Some 3 magnitudes deeper therefore allowing a survey volume about 10 times greater than 2MASS (Jameson 2006) and the first to employ the Y band it has the potential to identify (new) objects with unusual features near 1μm. Objects with red $Y - J$ colours are common-place and so a search through the UKIDSS DR3 archive for objects with significantly blue $Y - J$ colours, i.e. colours that were less than the combined Y, J errors, or colours less than the Rayleigh Jeans colours of very hot stars was conducted to search for any unidentified population. Just two objects were found that matched the criteria laid out, ULAS0822+0730 and another object identified as the soft X-ray source from the ROSAT All Sky Survey RXJ0515.6+0105, more commonly known as GG Leo.

6.2 Polars

GG Leo was discovered using the X-ray telescope component of the ROSAT all sky survey with Burwitz et al. (1998) finding that RXJ1015.6+0904 was the X-ray detection of a AM Herculis binary (a polar). AM Herculis type systems are so named after the variable star AM Her which has been shown to show a 3 magnitude variation in its light curve, it too was found as optical counterpart to an X-ray source, that of 3U 1809+50 by Berg & Duthie (1977). Its similarities to the X-ray binaries of Sco X-1 and Cyg X-2 lead Crampton & Cowley (1977) to obtain a spectrum revealing an orbital period of 3.09h with Tapia (1977) finding linearly and circularly polarised light variations for the system. The polarised light is indicative of a strong magnetic field being present, one that could be produced by an unseen white dwarf companion. Ingham et al. (1976) argue for this case by suggesting that the cyclotron emission seen in a series of white dwarf observations is the source of the polarisation. The polarised radiation (cyclotron radiation) is created due to the interaction between non-relativistic charged particles and a magnetic field. The interaction event itself causes a deflection in the path of the particle which in turn causes it to generate its own magnetic field resulting in a feed-back loop occurring. The overall result of this is that the particle becomes confined to orbiting along the magnetic field line, an effect that is often described as being “frozen in”. By forcing the particle flow along the field lines, the accretion of the gas onto the primary does not come from a disk but from the material flowing towards the poles (case b in the bottom panel of Figure 6.3). The fundamental frequency with which the cyclotron emission occurs for a given cyclotron velocity ν_c is given below,

$$\nu_c = \frac{\omega_c}{2\pi} = \frac{eB}{2\pi mc} = 2.8 \times 10^{14} B_8 \text{Hz}, \tag{6.1}$$

where B is the magnetic field strength in gauss, e the charge on the electron, m the electron's mass and c the speed of light. The results of Tapia (1977) suggested that the AM Her system did indeed possess a strong magnetic field ($\sim 2 \times 10^8$G), one that could only come from the white dwarf primary. By preferentially looking for circular polarisation variation seen in AM Her many other objects were soon discovered, becoming known as Polars. Warner (1995) notes that this definition has since been expanded upon to stipulate that Polars are only those systems in which the primary is phase-locked, rotating synchronously with its orbital motion, whilst the Intermediate-Polars are a class where the rotation is seen to be asynchronous after the discovery of the system DQ Her. For the Intermediate Polars the weaker magnetic field can allow for the partial formation of a disk which is then truncated by the white dwarf's magnetic field.

6.3 WHT Spectra

Spectra of ULAS0822+0730 were obtained on the 13 October 2008 with the WHT's ISIS spectrograph during a period of service time. The red and blue arms of the spectrograph were employed simultaneously using a slit of 1" and the R300B and R158R gratings to allow for a usable wavelength coverage of $\sim$3000Å - 11000Å . Flat field and CuNe+CuAr Arc lamp calibration frames were also taken. The G2V standard star SP0813+077 was also observed within an airmass of $\sim$0.2 to enable a flux calibration to be achieved. The spectra were reduced as described in Chapter 3. The combined red and blue arm spectrum is shown in Figure 6.1 with regions of excessive noise between the transition of blue to red spectra having been cut. The spectral region near to that of the UKIDSS Y band shows a clear and distinct hump peaking at ∼0.99μm. This is interpreted as strong evidence for a cyclotron harmonic being produced as material from the secondary is funnelled along the magnetic field lines towards the unseen white dwarf primary. Given the reported Y band magnitude in the UKIDSS discovery image ($Y = 16.02$), the flux of the harmonic is somewhat lower than expected, indicating that the system had possibly been caught in transition from its accreting state into one of quiescence. Another bump in the spectrum is clearly visable peaking at ∼0.66μm. The ratio of the two peaks suggests these two bumps are the 2^{nd} and 3^{rd} cyclotron harmonics. A NIR spectrum obtained at Nasa's Infrared Telescope Facility (IRTF) by Matt Burleigh (Figure 6.2) following that of the optical spectra however showed no evidence of a cyclotron hump. It is beleived the Polar had entered into a low-state with little to no accretion occuring. The lower than expected cyclotron emission in the combined WHT ISIS sprectra in Figure 6.1 has allowed the secondary star to show some of its atmospheric features. In comparing it to catalogues of spectral sequences (Kirkpatrick et al. 1991) it's suggested that it is best matched by a late K-type star, possibly of subclass 5-7. Spectral features for late K-dwarfs have been overlaid upon the combined red and blue spectrum.

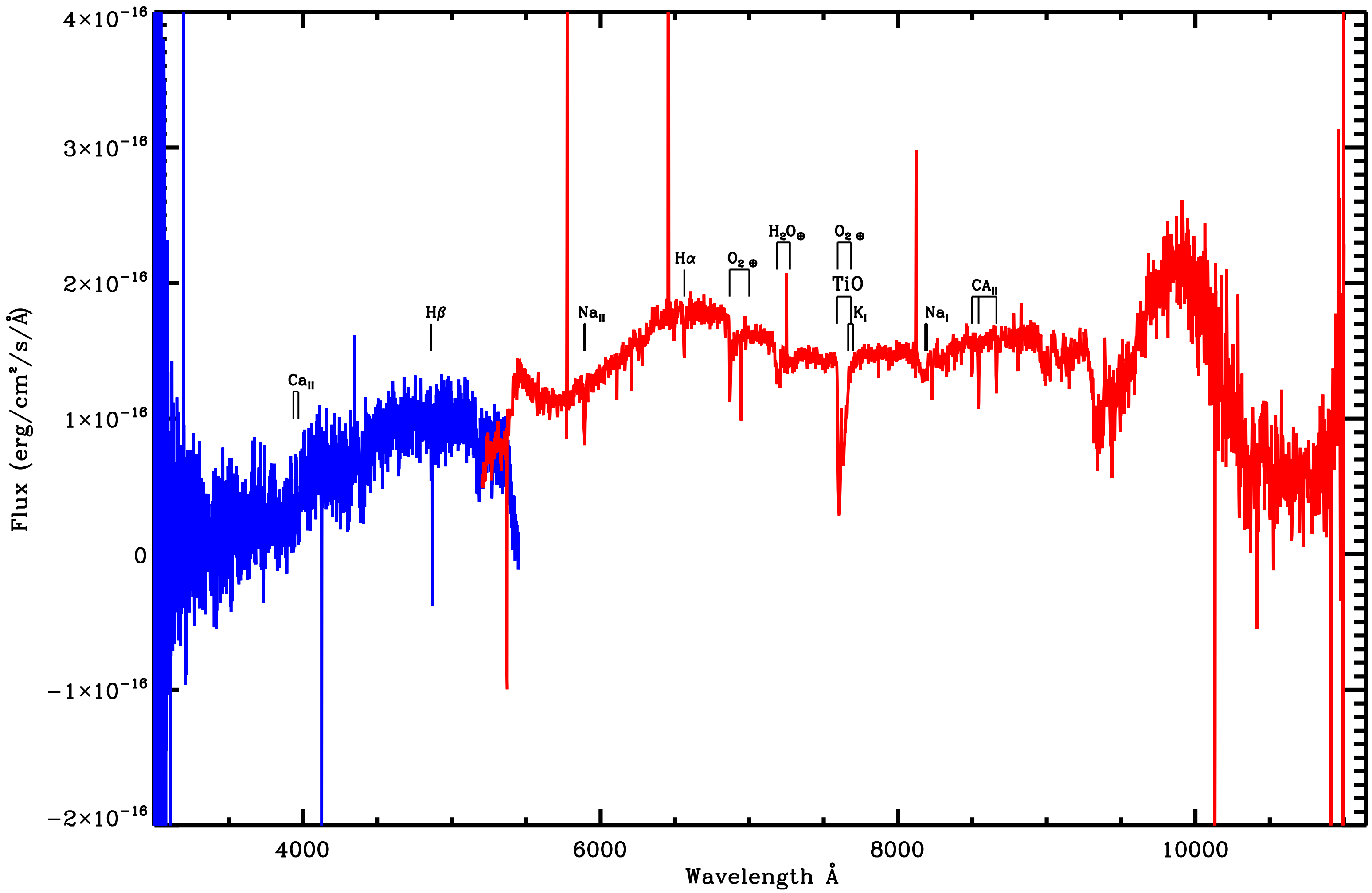

FIGURE 6.1. Spectra of ULAS0822+0730 taken by the Blue and Red arms of the ISIS spectrograph on the WHT. Some observed (Hα, CAII) and typical features (NaI,II, TiO and KI of Mid to Late K-dwarfs from Kirkpatrick et al. (1991) have been overlaid along with telluric absorption bands of O_2 and H_2O.

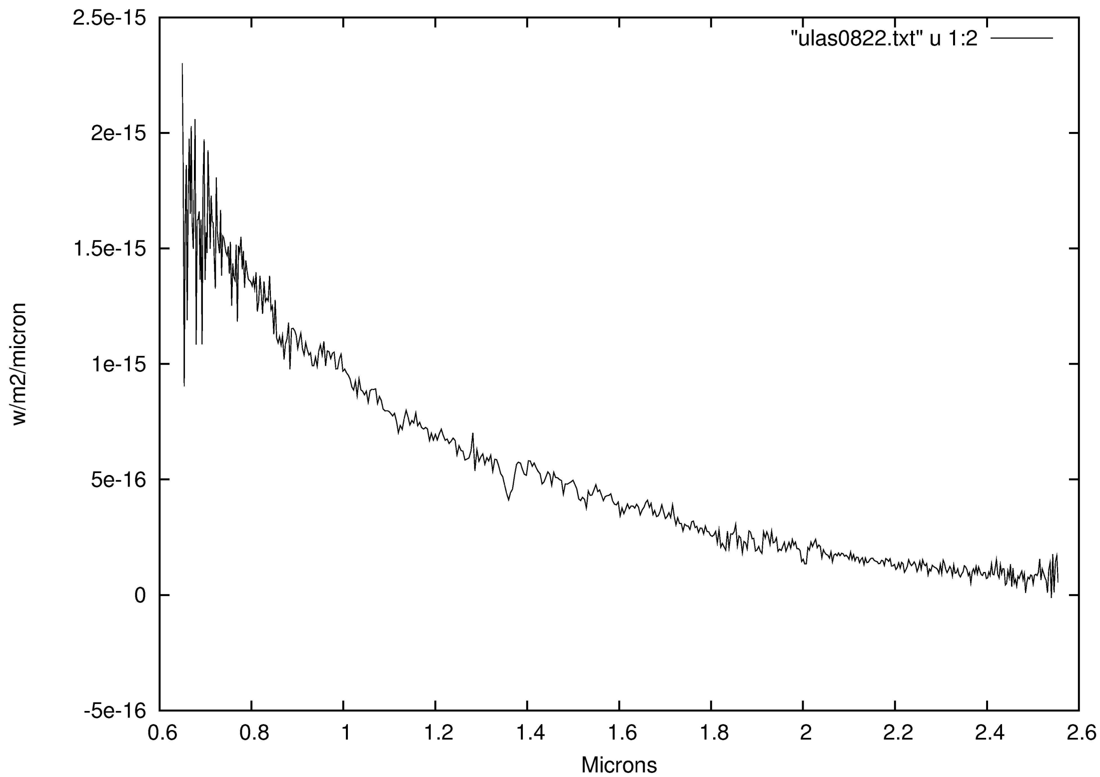

FIGURE 6.2. Spectra of ULAS0822+0730 taken by Matt Burleigh whilst observing at the IRFT on Hawaii. There is no evidence for a cyclotron harmonic at 1.98μm, indicating that by the time of this observation the Polar had entered a low-state.

6.3.1 Assumed system properties

If it assumed that the secondary is indeed a late K-type star with a typical mass and radius of $0.7\mathrm{M}_{\odot}$ and $0.7\mathrm{R}_{\odot}$ and that the white dwarf is also fairly typical ($\sim$$0.65\mathrm{M}_{\odot}$, $0.01\mathrm{R}_{\odot}$) then the period for such as system (P_{orb}) would be ≈6.75h. This can be found from a consideration of the Roche lobe geometry. For binary systems the shapes of the Roche lobe equipotential gravitational surfaces depend upon the mass ratio (q) and the binary orbital period (or binary separation, a). For an accreting system the more massive secondary must fill its Roche lobe with gas traversing the Lagrangian L1 point

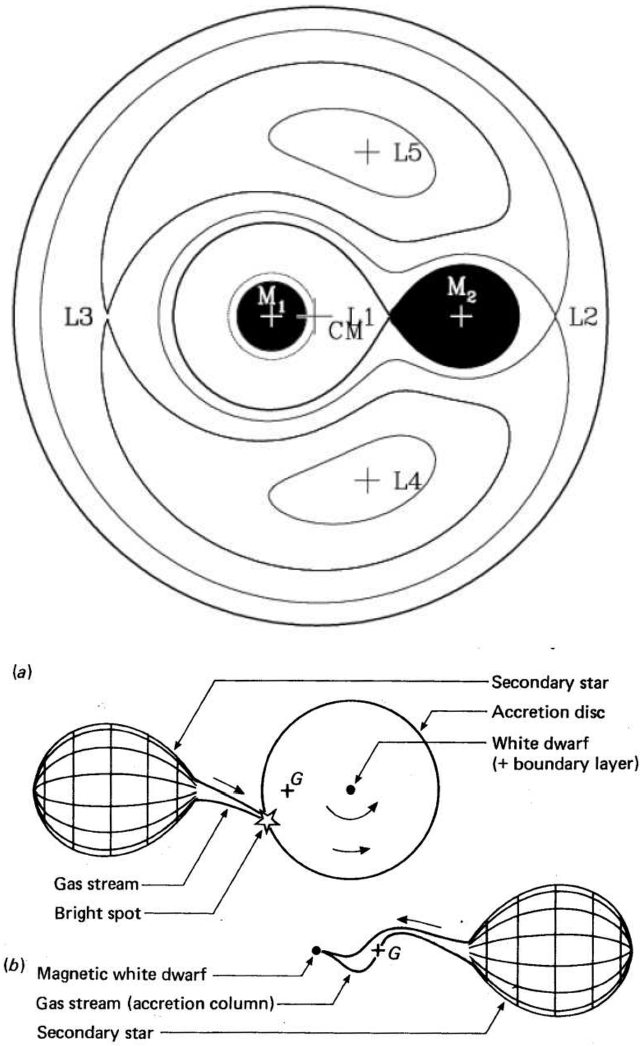

FIGURE 6.3. Top: Figure showing the Roche Lobe gravitational equipotentials. The secondary star is filling its Roche Lobe with material passing through the L1 point. Bottom: Figure showing accretion occuring with a disk (a) or without a disk (b), as is the case for a Polar.

(Figure 6.3). With Roche lobe overflow taking place and the systems tidally locked with the spin period equal to the orbital period, Kepler's law can be invoked in order to determine the period,

$$P_{orb}{}^2 = \frac{4\pi^2 a^3}{G(M_1 + M_2)} \tag{6.2}$$

Taking the approximation derived by Paczyński (1971) for binaries with a mass fraction of $0.1 \gtrsim q \gtrsim 0.8$, the radius of the secondary star given Roche lobe overflow and the binary separation was shown to be,

$$\frac{R_2}{a} = 0.462 \left(\frac{M_2}{M_1 + M_2}\right)^{1/3}. \tag{6.3}$$

Used in conjunction with equation 6.2, a can be eliminated to show that the binary period becomes solely a function of the secondary's density. Using the approximation of Eggleton (1983) which is valid for a wider range of q and accurate to $\pm 1\%$ as oppposed to $\pm 2\%$ for the Paczyński approximation (Warner 1995), the relationship for the mean density of the secondary given a period in hours is,

$$\bar{\rho_2} = 107 \times {P_{orb}}^2(h)\ \mathrm{gcm}^{-3}. \tag{6.4}$$

With the assumed system properties of $0.7\mathrm{M}_\odot$ and $0.75\mathrm{R}_\odot$ for the K-type secondary an average density of $\approx$2.34 g cm^{-3} is found which yielded a system period of P_{orb}~6.75 hours. If confirmed this would make this system one of the longest known period Polars (Golovin et al. 2008). From binary evolution calculations a relationship between the mass transfer from the secondary and the orbital period given that magnetic braking is occurring as the angular momentum loss mechanism gives an accretion rate of $\sim 10^{-9}\mathrm{M}_\odot$ yr^{-1} (Verbunt & Zwaan 1981; Rappaport et al. 1983; Howell et al. 2001). The upshot of which for a Polar means that this mass transfer rate from the secondary through the L1 point is exactly equal to the accretion rate onto the primary white dwarf as the magnetic field traps the gas preventing the formation of a disk. From the calculations of Rappaport et al. (1983) the mass transfer rate from the secondary above the period gap given magnetic braking is occurring is,

$$\dot{M}(2) = 2.0 \times 10^{-11} P_{orb}^{3.2 \pm 0.2}(h) \mathrm{M}_{\odot}\, yr^{-1} (P_{orb} > 2.7h), \tag{6.5}$$

where $\dot{M}(2)$ is the mass transfer rate from the secondary and P_{orb} is given in hours. Given a system period of ∼6.75 hours this equates to a mass transfer rate of $\sim 9 \times 10^{-9}$ $\mathrm{M}_{\odot}$ yr^{-1}. The rate of mass transfer in the system is not however a constant and in fact varies as the Polar changes from high to low states. This change in state occurs when starspots on the secondary enter the base of the accretion stream lowering the temperature of the gas as the balance between the magnetic pressure and gas pressure changes thus preventing its escape through the L1 point, effectively reducing or shutting off the flow of gas to the primary. Taking the mass transfer rate as $\sim 9 \times 10^{-9}$ $\mathrm{M}_{\odot}$ yr^{-1} an estimate of the potential energy liberated during the accretion of the gas onto the white dwarf is given by

$$L_{acc} = \frac{G M_{wd} \dot{M}}{R_{wd}} \tag{6.6}$$

and results in $\sim 7 \times 10^{34}$erg s^{-1}.

The shock temperature (in Kelvin) of this accretion in an optically thin case is given by Kuijpers & Pringle (1984) as

$$T_s = 3.7 \times 10^8 M_1 R_9^{-1}, \tag{6.7}$$

where M_1 is the mass of the white dwarf in stellar mass units and R_9 the white dwarf radius in units of 10^9cm. This equates to temperatures of $\sim$14.4 keV for the gas as it strikes the white dwarf photosphere. In the high accretion states this shock is likely to be buried in the white dwarf atmosphere as shown in Figure 6.4. In this case the energy of the shock is thermalised and radiated away over some proportion of the white dwarf polar cap in so called soft X-rays and UV.

The observed cyclotron harmonics seen in Figure 6.1 at $\sim$0.99μm and $\sim$0.66μm relate to the 2^{nd} and 3^{rd} harmonics respectively, with the fundamental expected to therefore occur in the NIR around 1.98μm. Re-writing equation 6.1 in terms of wavelength (λ) gives

$$\lambda = \frac{2\pi mc}{neB}, \tag{6.8}$$

with the additional harmonic number factor, n. Using the second harmonic (n=2), the local estimate of the magnetic field was found to be $\sim$54MG. As a check upon this value the critical surface magnetic field of the white dwarf can also be calculated using the

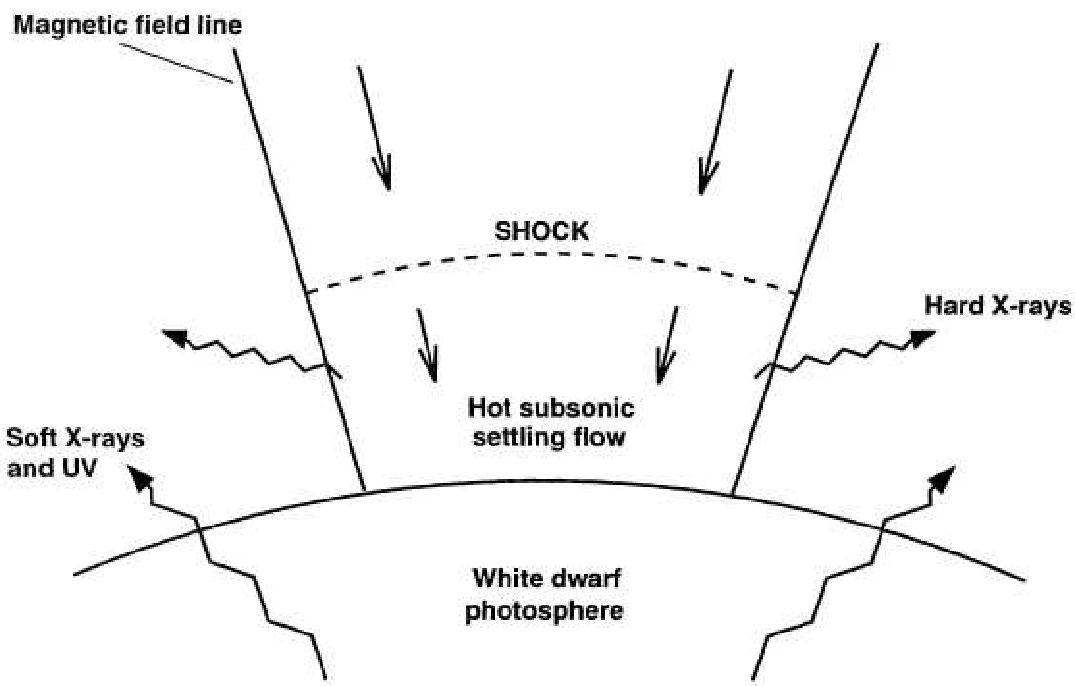

FIGURE 6.4. Picture of an accretion column onto a magnetic white dwarf. Figure from King (1995).

locking condition. For the system to be a Polar the magnetic fields of the primary and secondary must be acting in such a way as to counteract the spin-up torque generated by the accretion of matter onto the primary (due to angular momentum transfer) locking the system into its synchronous period. This is expressed as in King & Wynn (1999) as,

$$\frac{\mu_1\mu_2}{a^3} > \frac{2\pi\dot{m}b^2}{P_{orb}}. \tag{6.9}$$

Where μ_1 and μ_2 are the magnetic moments of the primary and secondary, a is the binary separation, $\dot{m}$ the accretion rate and b the distance from the primary to the L1 point. Using equation 6.2 this simply becomes

$$\mu_1\mu_2 > \dot{m}\left[G\left(m_1+m_2\right)\right]^{5/3}\left(\frac{P_{orb}}{2\pi}\right)^{7/3}\left(\frac{b}{a}\right)^2. \tag{6.10}$$

Utilising King & Wynn (1999) this can be reduced further from

$$\mu_1\mu_2 > 7.59 \times 10^{69}\left(\frac{b}{a}\right)^2 \tag{6.11}$$

for an accretion rate of 9×10^{-9} $\mathrm{M_\odot}$ yr^{-1} to

$$\mu_1\mu_2 > 1.97 \times 10^{69} \tag{6.12}$$

where

$$\left(\frac{b}{a}\right) = 0.500 - 0.277 \log\left(\frac{m_1}{m_2}\right). \tag{6.13}$$

Warner (1995) gives an expression for the secondary's magnetic moment as

$$\mu_2 = 1.0 \times 10^{33} B_3(2) R_{10}^3(2), \tag{6.14}$$

which finally yields $\mu_1 > 1.97 \times 10^{36}$ G cm^3 and thus $B_1 > 5.9 \times 10^9$G. Initially this seems at odds to the field strength derived from the cyclotron harmonics however, that field strength was calculated using the IR and so probes a different part of the white dwarf atmosphere and hence local field. With the field proportional to R^{-3}, a field of $\sim$54MG would be reached in less than 5 white dwarf radii. All the derived properties agree with typical cataclysmic variable properties. The final assumption that can be made is that of the distance to the system. Taking a typical K5 absolute R band magnitude of +6.3 and adding a small $\sim$0.4 mag contribution due to cyclotron emission from the system and comparing that with the SDSS r band photometry of 18.00[1] gives a distance of $\sim$2600pc. A similar calculation using a typical U band value (+9.53; +9.13 with cyclotron contribution) and SDSS u (+20.57) yields a distance of $\sim$1950pc. Distances with which optical, UV and X-ray instruments should easily be able to detect and monitor such a source as it is accreting, the SWIFT satellite's X-ray telescope with its detector

[1] It is believed that the SDSS image was captured during a low state period due to the faint z' detection of 17.59

Table 6.1. Observed, assumed and calculated properties of ULAS0822+0730.

Parameter	Value	Note
RA	08:22:58.96	
dec	+07:30:20.13	
u	20.57	Suspected low state SDSS magnitudes.
g	18.71	
r	18.00	
i	17.76	
z'	17.59	
Y	16.02	Suspected high state UKIDSS magnitudes.
J	16.66	
H	16.21	
K	16.09	
Secondary type	Mid-Late K-dwarf (~K5)	Assumed typical; ~0.7$\mathrm{M_\odot}$ and ~0.75$\mathrm{R_\odot}$.
Primary type	White dwarf	Assumed typical; ~0.65$\mathrm{M_\odot}$ and ~0.01$\mathrm{R_\odot}$.
Orbital Period	6.75h	
$\dot{M}$	$\sim9\times10^{-9}\mathrm{M_\odot}$ yr^{-1}	
L_{acc}	$\sim7\times10^{34}$erg s^{-1}	
B	54 MG	
Distance	~1950-2500pc	From K-type magnitude.

area of 2.4cm×2.4cm would detect on average ~280 counts over a 1ks observation, given an average 1keV photon being produced from an accretion rate of 7×10^{34} erg s^{-1} at a distance of 2500pc. Table 6.1 lists the assumed properties of the system derived above.

6.4 IAC-80 Light Curves

To ascertain if the system was showing any variability photometric light curves utilising the IAC-80 telescope were obtained on 16 March 2009 and 16 April 2009. Lacking the use of a Y band filter a z' filter was instead used as this would again be close to the region of cyclotron emission and thus would have been sensitive to any variation. The raw

600s exposure images were reduced (bias, flat fields) and astrometrically calibrated as described in Chapter 3. Aperture photometry was then used on the target and 3 comparison stars to check for variability via differential photometry. The process of differential photometry was carried out with apertures with a semi-major axis of 12 pixels, using automated scripts working with the STARLINK $kappa$, $figaro$ and $autophotom$ routines. The fluxes from ULAS0822+0730 and the comparisons were then summed in various combinations and normalised to produce the differential photometry plots in Figure 6.5. As well as having the target normalised to the the three comparison stars, each comparison star was checked against the other two to make sure they were not varying. The amplitude of the variations ($\sim\pm5\%$) and the calibrated photometric value of $\sim$17.6 in z' are in agreement with the reported SDSS magnitude for a period of suspected quiesence.

6.5 SWIFT measurements

On the 16 October 2009 a proposal was accepted for the SWIFT satellite to look at ULAS0822+0730 as a target of opportunity with both its X-ray telescope (XRT) and UV-Optical telescope (UVOT). A archival search of the ROSAT All Sky Survey had found that ULAS0822+0730 had not been detected nor was it in an area for which the XMM Slew Survey would have had coverage. In total 4 separate 1ks observations of the source were requested with the XRT in order to balance sensitivity and the risk of a null result with the timing requirements needed to best ensure that a bright phase of accretion during the orbit would be spotted. The $uwv2$ filter was also selected for the UVOT in order to detect emission as close as possible to the expected hot white dwarf peak. As

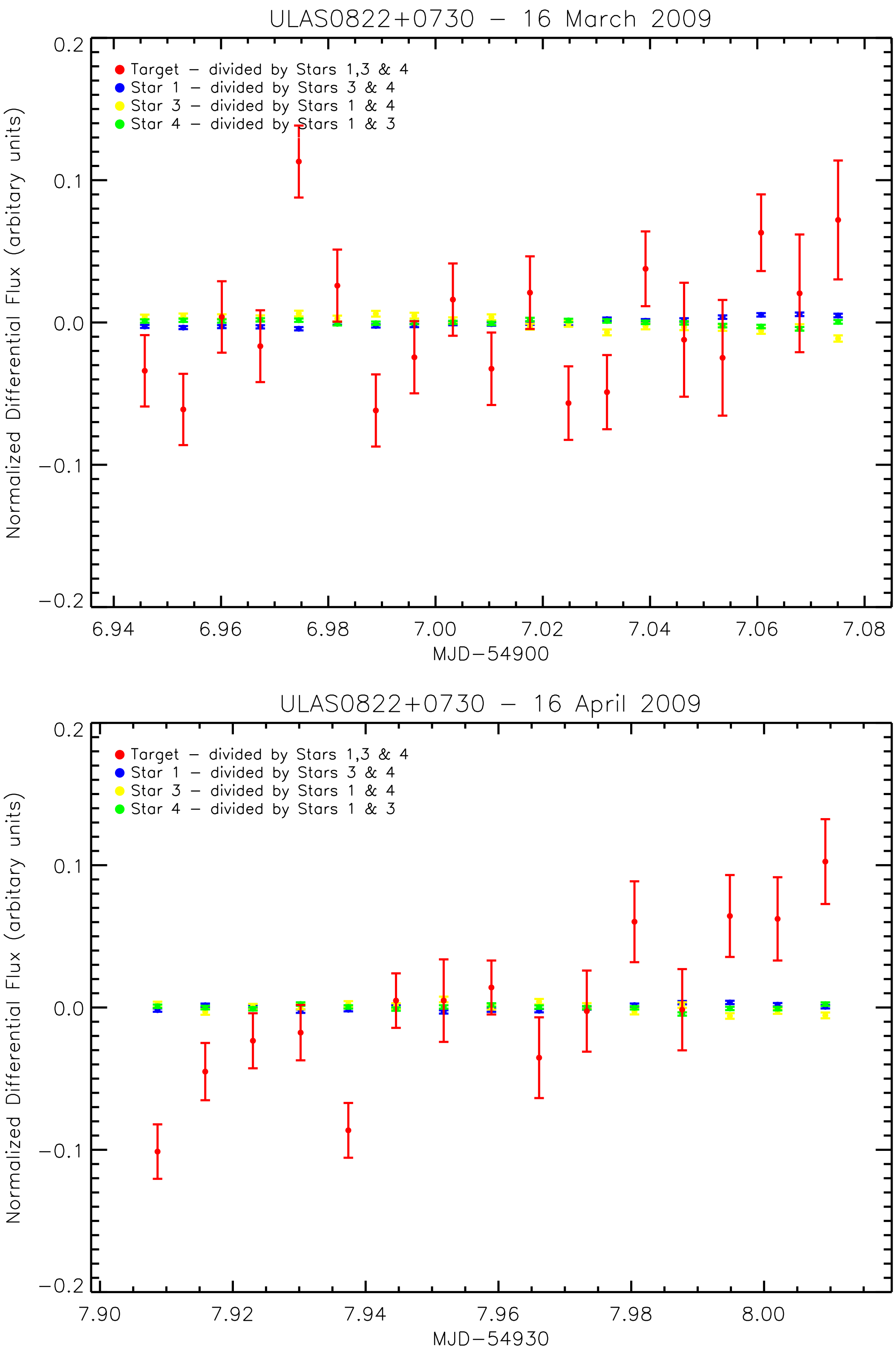

FIGURE 6.5. Short term light curves of ULAS0822+0730 covering a period ∼2.5 hours taken by the IAC-80 telescope on La Palma. Small (∼±5%) variations of ULAS0822+0730 can be seen in relation to the non-varying comparison stars. The typical magnitude of ULAS0822+0730 is ∼17.6 which is in agreement with the reported SDSS magnitudes and about a magnitude fainter than that expected given the UKIDSS photometry.

can be seen in Figures 6.6 however there was no detected X-ray or UV emission from the system indicating again that we had observed it in a low state.

6.6 UKIRT Long Term Light Curve

As the need for an X-ray light curve is paramount for understanding the accretion processes in these systems a joint long term monitoring project was set-up between UKIRT and SWIFT. With the kind aid of Andy Adamson, observers at UKIRT agreed to take a Y band image of ULAS0822+0730 every night starting from 21 March 2010. A photometric estimation script was then run each night to see if the Y band magnitude was altering from the low-state $\sim$17.0 back towards the 16.02 of the UKIRT discovery image. Should such a change occur then a reversal of the usual roles between UKIRT and SWIFT would occur as the SWIFT telescope would be triggered to look at ULAS0822+0730 with its XRT. Removing nights of bad weather the Figure 6.7 shows the results of the monitoring campaign.

Using the same comparison stars as for the IAC-80 light curves it is clear that the magnitude-time and differential photometry plots (top and bottom respectively) of Figure 6.7 show no signs of variation, this indicates that the Polar spends periods of at least 2 months in the low state. The campaign ceased on 24 May 2010 as ULAS0822+0730 began to move back behind the Sun.

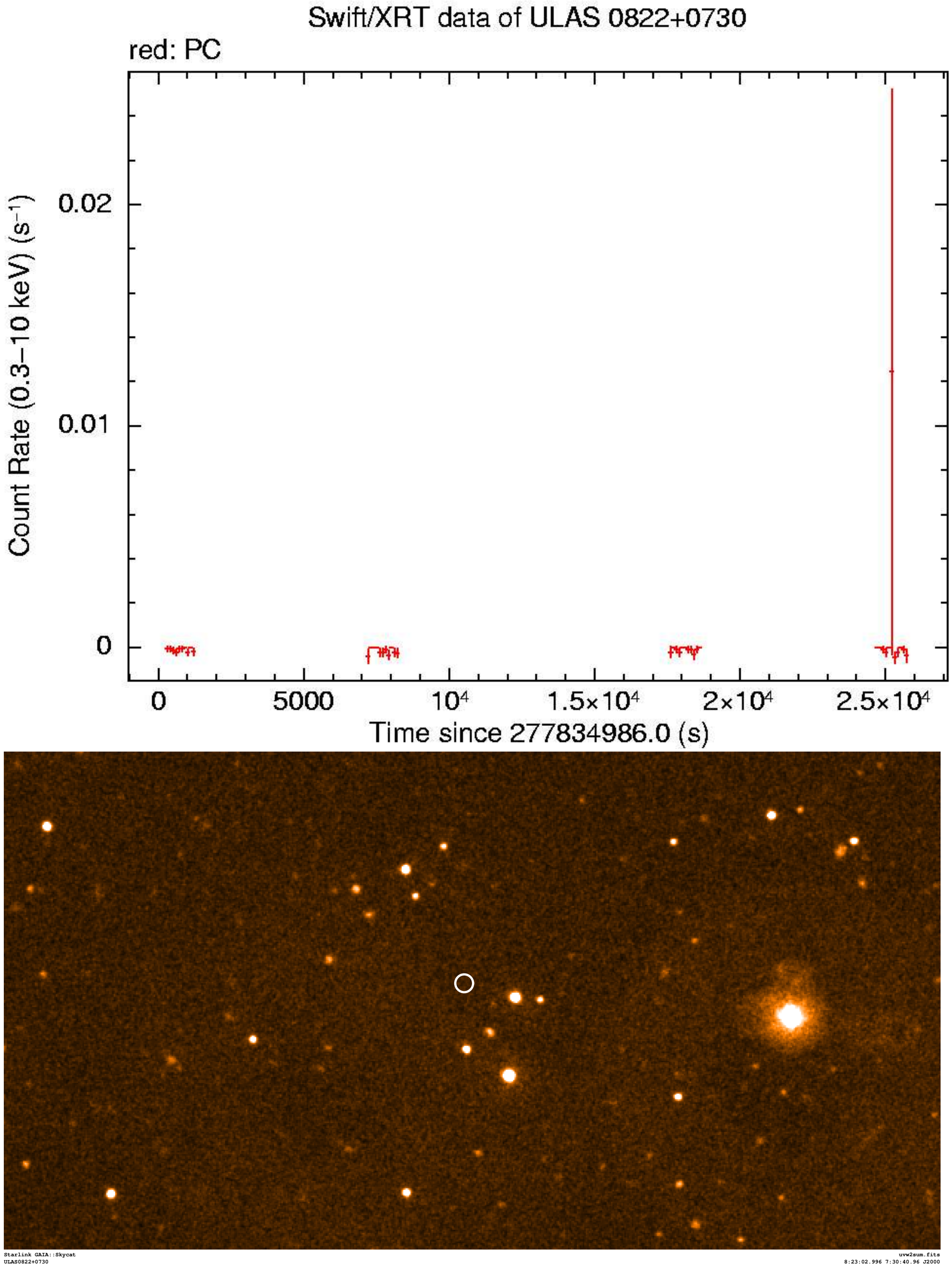

FIGURE 6.6. Top: Results from the SWIFT XRT monitoring of ULAS0822+0730 showing zero X-ray emission detected from the system. Bottom: Results from the concurent UVOT measurement showing a null detection of the Polar in the UV. The position of ULAS0822+0730 is shown by the white circle.

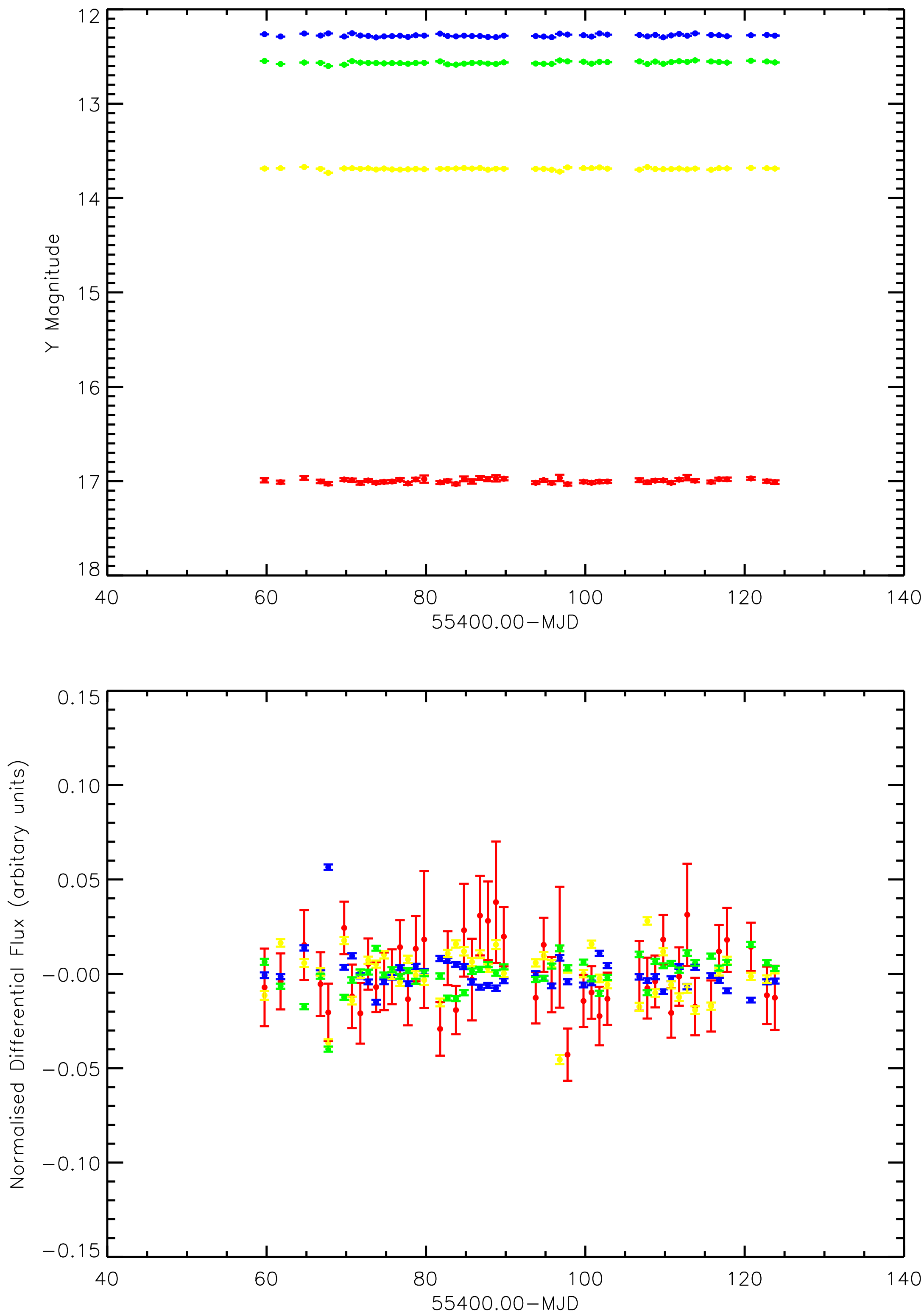

FIGURE 6.7. Top: Long term (∼2 months) monitoring of ULAS0822+0730 with the UKIRT Y band filter. The magnitude of the object is constant at ∼17.0, 1 mag fainter than its UKIDSS discovery image. The same comparison stars have been used as for the differential photometry in Section 6.4. Bottom: Normalised differential photometry plot for the same time period, again emphasising a clear lack of variation. Bad weather nights have been removed.

6.7 A sister system: V1309 Ori

Despite the failure to capture ULAS0822+0730 back in a high accretion state the need to do so may become very important as with assumed system properties from Section 6.3.1 it could represent a sister system to that of V1309 Ori. The eclipsing polar of V1309 Ori is an outlier in the traditional paradigm as with an orbital period of $\sim$8 hours it is longer than any previously known polar by a factor of 2 (Schwarz et al. 2005). A magnetic field of $\sim$61MG and an M0 secondary all at a distance of $\sim$500pc (Shafter et al. 1995; Reinsch et al. 2006) make the system very much like ULAS0822+0730 if the assumed system properties are confirmed. Finding another long period system such as V1309 Ori will enable far more constraints to be placed upon the theories that govern the evolution of such systems, providing clues as to how the synchronisation process between the magnetic fields alters and controls the flow of material in the binary.

6.8 Conclusions

ULAS0822+0730 appears to be a Polar, based upon the cyclotron humps observed within its spectrum. If so, it will be the first Polar with a K-type companion. The optical/NIR spectrum is clearly not that of an M star with there being no obvious TiO bands. One contre indication to this conclusion is the lack of expected emission lines though these could be swamped by the stronger optical continum of the K star. Clearly the Y band monitoring campaign needs to be restarted in order to try and catch ULAS0822+0730 in a high state. Observations by SWIFT could then be made of its X-ray and UV output. If observations are made over a sufficiently long period with either ground based optical or SWIFT X-ray measurements a measure of the orbital period should be possible based upon the light curves generated. This additional data would then allow for a more complete and robust description of this system, hopefully aiding the confirmation of its Polar status.

Chapter 7

Conclusions and Future Work

This chapter reviews the work presented in this thesis. Chapter 2 discussed brown dwarfs, from the theories governing their formation and the observational history of their discovery, through to our current understanding of the spectral sequence and models used to describe their atmospheres. Chapter 3 provided a description of the instruments used to gather the data within this thesis as well as the processes involved in its reduction. Photometry, spectroscopic data reduction, astrometry and proper motion calculations were discussed. The remaining three chapters discuss the work that has been performed over the course of this PhD. Each chapter is reviewed below along with suggestions for future work.

7.1 Chapter 4 - Praesepe

This chapter described a study of the Praesepe open star cluster (Baker et al. 2010). The survey used a combination of UKIDSS GCS data cross correlated with data taken by the 2MASS and SDSS surveys. Candidates were divided into two separate populations. The bright population consisting of the UKIDSS-2MASS detections and the fainter population consisting of the UKIDSS-SDSS objects. Candidate cluster members were then selected from each set via the use of multiple colour magnitude diagrams utilising theoretical isochrones and previous observations as an aid in locating the cluster sequence. Proper motion information for the UKIDSS-2MASS candidates allowed for membership probabilities to be calculated via the fitting of separate field and cluster star distributions. For the UKIDSS-SDSS population the proper motions were calculated with quadratic (and linear) pixel-to-pixel transformation routines between the SDSS z' and UKIDSS Z band images. Control regions were then used to estimate the probability of membership for these objects. 278 UKIDSS-2MASS objects were found to be high probability members (p$\geq$0.6), 33 of which are new. 6 UKIDSS-SDSS candidate members have also been identified as high probability members satisfying a requirement of SDSS i and z' detection, with the mass of the current lowest member estimated to be $\sim$0.071$\mathrm{M}_{\odot}$ using the 500Myr isochrone. If the i band detection requirement is relaxed the number of members increases to 8 and futher increases to 20 given probability selection of p$\geq$0.5. A revised mass spectrum for the cluster gives $\alpha \sim 0.87 \pm 0.33$ a value that is substantially lower than that of $\alpha = 1.8$ given by Boudreault et al. (2010) and at the lower end of the Kraus & Hillenbrand (2007) value of $\alpha = 1.4 \pm 0.2$. The value is however far more consistent with that seen for other clusters of $\approx$0.6.

7.1.1 Future Work

For the fainter UKIDSS-SDSS candidates whose memberships were calculated by comparison to a control region spectroscopic follow up will be needed to confirm their spectral type and thus membership status. Given an age of 500Myrs the lowest mass candidates would be approaching $\sim$65$\mathrm{M_J}$.

The spectroscopic follow up may also reveal differences in metallicity between some of the targets. Work on identifying metallicity tracers in the NIR has been carried out by Rojas-Ayala & Lloyd (2010). If differing metallicities are found over the extent of the cluster then further evidence would be presented that the cluster had recently undergone a collision. The observed mass function would then be a combination of mass functions from two separate epochs of star formation and would provide a useful result with which to compare to cluster merger simulations. Information from the spectral type can be further used to enable determination of parameters such as log g via the BD evolution models. Having constrained properties such as log g, age and distance will be useful in identifying any objects that could be used as benchmarks (Pinfield et al. 2006) to test against the predictions of the atmospheric models.

Second epoch K band data that is expected as part of the original UKIDSS GCS proposal will also enable a greater baseline between SDSS/2MASS and UKIDSS observations to be established. This increased baseline will enable a refinement to the proper motion selection by increasing the cluster's apparent displacement and reducing errrors. Subsequent refinement of the cluster sequence will enable better identification of the single and equal mass binary tracks which occur 0.75 mag above the single star sequence ($Z-K$, K should be usefull for this). Using theoretical BD models artificial binaries of masses M, M+0.1M, M+0.2M all the way to M+M, where M is the mass of the BD can then be constructed. These tracks can be used to identify the higher companion mass binary systems, separating them from those of the single BDs (and those with companions of very low mass). From the relative fractions a constraint on the binary fraction of the cluster can be deduced and factored into the mass function. These results in turn can also be used in testing and refining the evaporation models which preferentially eject the single BD population from the cluster.

7.2 Chapter 5 - Blanco 1

This chapter presented work on the southern hemisphere cluster Blanco 1. The survey combined optical CFHT12k I and z band data along with WFCAM J NIR data that made for a cluster sequence that was much more identifiable in colour magnitude plots than that provided by I and z alone. The source extracted objects were cross correlated with the detections in the other images via the use of pattern matching code. Subsequent colour magnitude cuts and proper motion calculations between the CFHT12k z and UKIDSS J band images gave 71 candidates of which 60 were unique individual sources. Using control regions to estimate cluster membership probabilities 27 cluster members were identified, 6 of which had spectra from Moraux et al. (2007) that was also indicative of cluster membership.

7.2.1 Future Work

The WFCAM J band survey did not survey the entirety of Blanco 1, this will be addressed in the future as a stripe of the more sensitive VISTA VIKING survey will cover the cluster. VISTA VIKING will not only provide an increase in the baseline that can be used for proper motion confirmation of members but will also provide a larger area and an increase in sensitivity compared with previous studies. This will enable a determination of the cluster's full on sky extent. With L-type BD masses as low as $\sim$25-30$\mathrm{M_J}$ detectable in multiple filters, better constraints on the single and binary star sequences should enable a refinement to the low-mass binary fraction. Whilst the clusters in the northern hemisphere generally appear older than those found in the south, Blanco 1 with its lithium age of 90Myrs appears to be at a similar stage in its evolution to that of the well studied Pleiades cluster. Although further away and with a lower density of objects, Blanco 1 could be considered to be a southern analogue of the Pleiades. By reliably extending the cluster sequence to the low mass L-type BDs it should be possible to construct statistically comparable mass functions for the two clusters, changes in which may reveal the effect (if any) that the environment has on the underlying form of the IMF. Spectroscopy will also be needed to confirm the spectral types of the cluster members. This will provide a key challange to current instruments due to the distance of the cluster and the faintness of the targets. If a significant signal-to-noise can be achieved then radial velocity information could also be used as a further membership discriminator (Mermilliod et al. 2008).

7.3 Chapter 6 - ULAS0822+0730

This chapter discussed the observations of the suspected Polar of ULAS0822+0730. Discovered by its unusual Y band photometry, ULAS0822+0730 has been shown in follow up images to have changed by at least 1 magnitude. Spectroscopic follow up using the WHT ISIS showed features resembling cyclotron emission humps at 0.66μm and 0.99μm as well as an underlying K star spectrum. Attributing these humps to the 3^{rd} and 2^{nd} harmonics respectively a magnetic field strength a few white dwarf radii away from the primary was calculated to be $\sim$ 54MG. Using standard prescriptions for binary systems an orbital period of $P_{orb} \sim 6.75$h was calculated. This would make ULAS0822+0730 the second longest period known system and the only such system with a K-type secondary. Follow up observations with the IAC-80 telescope, SWIFT and UKIRT all provided null results with the system in quiescence. With so few systems of this type known (only V1309 Ori shows a longer period) it is of vital importance that this system be studied to confirm if it is indeed a Polar.

7.3.1 Future Work

Attempts are being made to resume the UKIRT Y band monitoring campaign in conjunction with placing an alert trigger on the SWIFT telescope. Should the system re-enter a period of accretion the NIR, X-ray and UV data taken by these telescopes would then provide a wealth of information to help determine more precise system properties via monitoring the flux and modulations of the light curves, e.g. the orbital period from Y

band photometry (Burleigh et al. 2006). High resoultion optical spectroscopy can also be used to better constrain the spectral type of the secondary and to create Doppler tomograms. The Doppler tomograms can be used to study the gas flow from the secondary donor thereby revealing the geometry of the accretion stream (Marsh 2001; Staude et al. 2001; Richards 2007). However these future studies are dependent upon the system once again going through a period of outburst.The confirmation of two Polar systems with long periods would then suggest that V1309 Ori is not an outlier within the current paradigm but that a population of similar systems may exist (although rare). Further theoretical work would then be needed to see how these systems can form, particularly in the case where the secondary is that of a K-star. With 1 known and 1 suspected Polar contained within the DR2 release of UKIDSS this equates to a density of 1 per 141 deg^2 given a combined full filter set area of 282 deg^2 (Warren et al., 2007). Naively this would imply that many tens of systems would be found within the LAS, but as shown by the repeated attempts to re-image the system obtaining a detection during outburst is a substantial roadblock to further discoveries.

Appendix A

Below are the two SQL queries that were submitted to the WSA in order to download the UKIDSS DR8-2MASS and UKIDSS DR8-SDSS population of objects. The UKIDSS DR8-SDSS z' only population was obtained with the removal of the lines highlighted in bold.

A.1 UKIDSS DR8-2MASS

```
SELECT
g.sourceID as u_id,
T2.pts_key as t_id,
T2.designation t_designation,

g.ra as u_ra,
g.dec as u_dec,

T2.ra as t_ra,
T2.dec as t_dec,

m.mjdObs as u_mjd,
(T2.jdate-2400000.5) as t_mjd, /* Conversion from JD into MJD */

g.zaperMag3 as u_z,
g.zaperMag3Err as u_zerr,
g.yaperMag3 as u_y,
g.yaperMag3Err as u_yerr,
g.japerMag3 as u_j,
g.japerMag3Err as u_jerr,
g.haperMag3 as u_h,
g.haperMag3Err as u_herr,
g.k_1aperMag3 as u_k,
g.k_1aperMag3Err as u_kerr,
```

```
T2.j_m as t_j,
T2.h_m as t_h,
T2.k_m as t_k,

(T2.distanceMins * 60) as ut_separation,

/* Proper motion calculations */
3.6e6*COS(RADIANS(g.dec))*(g.ra-T2.ra)/((m.mjdObs-(T2.jdate-2400000.5))/365.25)
AS ut_pmra,
3.6e6*(g.dec-T2.dec)/((m.mjdObs-(T2.jdate-2400000.5))/365.25) AS ut_pmdec,

g.framesetid as framesetid,
f.multiframeid as multiframeid,
m.filename as filename,
m.catname as catname,
f.extNum as extnum

FROM
gcsMergeLog AS ml,
Multiframe AS m,
gcsFrameSets as f,

(
SELECT mass.designation, mass.pts_key, mass.ra, mass.dec, x.slaveObjID,
x.masterObjID, x.distanceMins, mass.jdate, mass.j_m, mass.h_m, mass.k_m

FROM gcsSourceXtwomass_psc AS x, TWOMASS..twomass_psc as mass

WHERE x.slaveObjID = mass.pts_key AND mass.j_m > 9 AND mass.h_m > 8.5 AND
mass.k_m > 8 AND
distanceMins IN(
SELECT MIN(distanceMins) FROM gcsSourceXtwomass_psc WHERE
masterObjID = x.masterObjID AND distanceMins < 1.0 / 60
)
)
AS T2 RIGHT OUTER JOIN gcsSource AS g on g.sourceID=T2.masterObjID
WHERE
/* Sample selection predicates:
Praesepe RA=120-135 deg  dec=15-25 deg
*/
g.ra BETWEEN 120.0 AND 135.0
AND g.dec BETWEEN 15.0 AND 25.0 and
(zXi BETWEEN -1.0 AND +1.0 OR zXi < -0.9e9)
AND yXi BETWEEN -1.0 AND +1.0
```

```
AND jXi BETWEEN -1.0 AND +1.0
AND hXi BETWEEN -1.0 AND +1.0
AND k_1Xi BETWEEN -1.0 AND +1.0
AND (zEta BETWEEN -1.0 AND +1.0 OR zEta < -0.9e9)
AND yEta BETWEEN -1.0 AND +1.0
AND jEta BETWEEN -1.0 AND +1.0
AND hEta BETWEEN -1.0 AND +1.0
AND k_1Eta BETWEEN -1.0 AND +1.0
AND (zClass BETWEEN -2 AND -1 OR zClass < -9999)
AND yClass BETWEEN -2 AND -1
AND jClass BETWEEN -2 AND -1
AND hClass BETWEEN -2 AND -1
AND k_1Class BETWEEN -2 AND -1
AND (priOrSec = 0 OR priOrSec = g.frameSetID)
AND g.frameSetID = ml.frameSetID

AND ml.zmfID = m.multiframeID

AND g.zppErrBits < 16
AND g.yppErrBits < 16
AND g.jppErrBits < 16
AND g.hppErrBits < 16
AND g.k_1ppErrBits < 16
AND g.framesetID=f.framesetID
AND f.multiframeID=m.multiframeID
```

A.2 UKIDSS DR8-SDSS

```
SELECT
g.sourceID as u_id,
T2.slaveObjID as s_id,

g.ra AS u_ra,
g.dec AS u_dec,

T2.ra AS s_ra,
T2.dec AS s_dec,

m.mjdObs AS u_mjd,
```

```
T2. mjd_z AS s_mjd,

g.zaperMag3 as u_z,
g.zaperMag3Err as u_zerr,
g.yaperMag3 as u_y,
g.yaperMag3Err as u_yerr,
g.japerMag3 as u_j,
g.japerMag3Err as u_jerr,
g.haperMag3 as u_h,
g.haperMag3Err as u_herr,
g.k_1aperMag3 as u_k,
g.k_1aperMag3Err as u_kerr,

T2.psfMag_u as s_u,
T2.psfMagErr_u as s_uerr,
T2.psfMag_g as s_g,
T2.psfMagErr_g as s_gerr,
T2.psfMag_r as s_r,
T2.psfMagErr_r as s_rerr,
T2.psfMag_i as s_i,
T2.psfMagErr_i as s_ierr,
T2.psfMag_z as s_z,
T2.psfMagErr_z as s_zerr,

(T2.distanceMins * 60) as us_separation,

3.6e6*COS(RADIANS(g.dec))*(g.ra-T2.ra)/((m.mjdObs-T2.mjd_z)/365.25) AS us_pmra,
3.6e6*(g.dec-T2.dec)/((m.mjdObs-T2.mjd_z)/365.25) AS us_pmdec,

g.framesetid as framesetid,
f.multiframeid as multiframeid,
m.filename as filename,
m.catname as catname,
f.extNum as extnum,
T2.run as run,
T2.rerun as rerun,
T2.camcol as camcol,
T2.field as field,
T2.rowc_z as xpix,
T2.colc_z as ypix,
T2.segmentID as segmentID,
T2.stripe as stripe,
T2.chunkID as chunkID,
T2.startmu as startmu
```

FROM
gcsMergeLog AS ml,
Multiframe AS m,
gcsFrameSets as f,

(
SELECT sdss.ra, sdss.dec, x.slaveObjID, x.masterObjID, x.distanceMins,
sdss.psfMag_u, sdss.psfMagErr_u, sdss.psfMag_g, sdss.psfMagErr_g, sdss.psfMag_r, sdss.psfMagErr_r,
sdss.psfMag_i, sdss.psfMagErr_i, sdss.psfMag_z, sdss.psfMagErr_z, f.mjd_z, sdss.run,
sdss.rerun,
sdss.camcol, sdss.field, sdss.rowc_z, sdss.colc_z,sg.segmentID, sg.stripe, c.chunkID, c.startmu
FROM gcsSourceXDR7PhotoObj as x, BestDR7..PhotoObj as sdss,
BestDR7..Field as f, BestDR7..Segment as sg, BestDR7..Chunk as c
WHERE sdss.type = 6 AND x.slaveObjID = sdss.objID AND f.fieldID = sdss.fieldID
AND f.segmentID = sg.segmentID AND sg.chunkID = c.chunkID

/* Detected in BINNED 1 */
AND ((flags_i 0x10000000) != 0)
AND ((flags_z 0x10000000) != 0)

/* Not EDGE, NOPROFILE, PEAKCENTER, NOTCHECKED
PSF_FLUX_INTERP, SATURATED, or BAD_COUNTS_ERROR */
AND ((flags_i 0x8100000c00a4) = 0)
AND ((flags_z 0x8100000c00a4) = 0)

/* Not DEBLEND_NOPEAK or small PSF error */
AND (((flags_i 0x400000000000) = 0) or (psfmagerr_i <= 0.2))
AND (((flags_z 0x400000000000) = 0) or (psfmagerr_z <= 0.2))

/* Not INTERP_CENTER or not COSMIC_RAY */
AND (((flags_i 0x100000000000) = 0) or (flags_i 0x1000) = 0)
AND (((flags_z 0x100000000000) = 0) or (flags_z 0x1000) = 0)

AND distanceMins IN (
SELECT MIN(distanceMins) FROM gcsSourceXDR7PhotoObj WHERE
masterObjID = x.masterObjID AND distanceMins < 1.0 / 60
)
)

AS T2 RIGHT OUTER JOIN gcsSource AS g on g.sourceID=T2.masterObjID
WHERE
/* Sample selection predicates:
Praesepe RA=120-150 deg dec=15-25 deg
*/
g.ra BETWEEN 120.0 AND 135.0

```
AND g.dec BETWEEN 15.0 AND 25.0 and
(zXi BETWEEN -1.0 AND +1.0 OR zXi < -0.9e9)
AND yXi BETWEEN -1.0 AND +1.0
AND jXi BETWEEN -1.0 AND +1.0
AND hXi BETWEEN -1.0 AND +1.0
AND k_1Xi BETWEEN -1.0 AND +1.0
AND (zEta BETWEEN -1.0 AND +1.0 OR zEta < -0.9e9)
AND yEta BETWEEN -1.0 AND +1.0
AND jEta BETWEEN -1.0 AND +1.0
AND hEta BETWEEN -1.0 AND +1.0
AND k_1Eta BETWEEN -1.0 AND +1.0
AND (zClass BETWEEN -2 AND -1 OR zClass < -9999)
AND yClass BETWEEN -2 AND -1
AND jClass BETWEEN -2 AND -1
AND hClass BETWEEN -2 AND -1
AND k_1Class BETWEEN -2 AND -1
AND (priOrSec = 0 OR priOrSec = g.frameSetID)
AND g.frameSetID = ml.frameSetID

AND ml.zmfID = m.multiframeID

AND g.zppErrBits < 16
AND g.yppErrBits < 16
AND g.jppErrBits < 16
AND g.hppErrBits < 16
AND g.k_1ppErrBits < 16
AND g.framesetID=f.framesetID
AND f.multiframeID=m.multiframeID
```

Bibliography

Ackerman A. S., Marley M. S., 2001, ApJ, 556, 872

Adams F. C., Fatuzzo M., 1996, ApJ, 464, 256

Adams F. C., Myers P. C., 2001, ApJ, 553, 744

Adams J. D., Stauffer J. R., Skrutskie M. F., Monet D. G., Portegies Zwart S. F., Janes K. A., Beichman C. A., 2002a, AJ, 124, 1570

Adams T., Davies M. B., Jameson R. F., Scally A., 2002b, MNRAS, 333, 547

Aigrain S., Hodgkin S., Irwin J., Hebb L., Irwin M., Favata F., Moraux E., Pont F., 2007, MNRAS, 375, 29

Allard F., 2010, Stellar Model Atmospheres: From Very Low Mass Stars to Brown Dwarfs (talk)

Allard F., Hauschildt P. H., Alexander D. R., Tamanai A., Schweitzer A., 2001, ApJ, 556, 357

Allen C. W., 1973, Astrophysical quantities, Allen, C. W., ed.

Auman Jr. J., 1967, ApJS, 14, 171

Baker D. E. A., Jameson R. F., Casewell S. L., Deacon N., Lodieu N., Hambly N., 2010, MNRAS, 408, 2457

Baraffe I., Chabrier G., Allard F., Hauschildt P. H., 1998, A&A, 337, 403

—, 2002, A&A, 382, 563

Baraffe I., Chabrier G., Barman T. S., Allard F., Hauschildt P. H., 2003, A&A, 402, 701

Barrado y Navascués D., Bouvier J., Stauffer J. R., Lodieu N., McCaughrean M. J., 2002, A&A, 395, 813

Barrado y Navascués D., Stauffer J. R., Bouvier J., Jayawardhana R., Cuillandre J., 2004, ApJ, 610, 1064

Basri G., 1998, in Astronomical Society of the Pacific Conference Series, Vol. 134, Brown Dwarfs and Extrasolar Planets, R. Rebolo, E. L. Martin, & M. R. Zapatero Osorio, ed., pp. 394–+

—, 2000, ARA&A, 38, 485

Basri G., Marcy G. W., Graham J. R., 1996, ApJ, 458, 600

Bastian N., Covey K. R., Meyer M. R., 2010, Annual Review of Astronomy and Astrophysics, 48, 339

Bate M. R., Bonnell I. A., Bromm V., 2003, MNRAS, 339, 577

Becklin E. E., Zuckerman B., 1988, Nature, 336, 656

Beichman C. A., 1987, ARA&A, 25, 521

Béjar V. J. S., Martín E. L., Zapatero Osorio M. R., Rebolo R., Barrado y Navascués D., Bailer-Jones C. A. L., Mundt R., Baraffe I., Chabrier C., Allard F., 2001, ApJ, 556, 830

Berg R. A., Duthie J. G., 1977, ApJ, 211, 859

Bertin E., Arnouts S., 1996, A&AS, 117, 393

Bertin G., Lodato G., 1999, A&A, 350, 694

Bethe H. A., 1939, Physical Review, 55, 434

Blanco V. M., 1949, PASP, 61, 183

Boeshaar P. C., 1976, PhD thesis, Ohio State Univ., Columbus.

Bond H. E., 1972, PASP, 84, 583

Bonnell I. A., Bate M. R., Clarke C. J., Pringle J. E., 2001a, MNRAS, 323, 785

Bonnell I. A., Clarke C. J., Bate M. R., Pringle J. E., 2001b, MNRAS, 324, 573

Boudreault S., 2008, PhD thesis, Ruperto-Carola University of Heidelberg

Boudreault S., Bailer-Jones C. A. L., Goldman B., Henning T., Caballero J. A., 2010, A&A, 510, A27+

Bouvier J., Kendall T., Meeus G., Testi L., Moraux E., Stauffer J. R., James D., Cuillandre J., Irwin J., McCaughrean M. J., Baraffe I., Bertin E., 2008, A&A, 481, 661

Bouvier J., Stauffer J. R., Martin E. L., Barrado y Navascues D., Wallace B., Bejar V. J. S., 1998, A&A, 336, 490

Boyd D. F. A., Whitworth A. P., 2005, A&A, 430, 1059

Briceño C., Luhman K. L., Hartmann L., Stauffer J. R., Kirkpatrick J. D., 2002, ApJ, 580, 317

Burgasser A. J., 2001, PhD thesis, Department of Physics, California Institute of Technology

Burgasser A. J., Geballe T. R., Golimowski D. A., Leggett S. K., Kirkpatrick J. D., Knapp G. R., Fan X., 2003, in IAU Symposium, Vol. 211, Brown Dwarfs, E. Martín, ed., pp. 377–+

Burgasser A. J., Geballe T. R., Leggett S. K., Kirkpatrick J. D., Golimowski D. A., 2006, ApJ, 637, 1067

Burgasser A. J., Kirkpatrick J. D., Brown M. E., Reid I. N., Burrows A., Liebert J., Matthews K., Gizis J. E., Dahn C. C., Monet D. G., Cutri R. M., Skrutskie M. F., 2002a, ApJ, 564, 421

Burgasser A. J., Kirkpatrick J. D., Lowrance P. J., 2005, AJ, 129, 2849

Burgasser A. J., Marley M. S., Ackerman A. S., Saumon D., Lodders K., Dahn C. C., Harris H. C., Kirkpatrick J. D., 2002b, ApJ, 571, L151

Burgasser A. J., McElwain M. W., Kirkpatrick J. D., Cruz K. L., Tinney C. G., Reid I. N., 2004, AJ, 127, 2856

Burgasser A. J., Reid I. N., Siegler N., Close L., Allen P., Lowrance P., Gizis J., 2007, Protostars and Planets V, 427

Burleigh M. R., Marsh T. R., Gänsicke B. T., Goad M. R., Dhillon V. S., Littlefair S. P., Wells M., Bannister N. P., Hurkett C. P., Martindale A., Dobbie P. D., Casewell S. L., Baker D. E. A., Duke J., Farihi J., Irwin M. J., Hewett P. C., Roche P., Lewis F., 2006, MNRAS, 373, 1416

Burningham B., Leggett S. K., Lucas P. W., Pinfield D. J., Smart R. L., Day-Jones A. C., Jones H. R. A., Murray D., Nickson E., Tamura M., Zhang Z., Lodieu N., Tinney C. G., Zapatero Osorio M. R., 2010a, MNRAS, 404, 1952

Burningham B., Pinfield D. J., Leggett S. K., Tinney C. G., Liu M. C., Homeier D., West A. A., Day-Jones A., Huelamo N., Dupuy T. J., Zhang Z., Murray D. N., Lodieu N., Barrado Y Navascués D., Folkes S., Galvez-Ortiz M. C., Jones H. R. A., Lucas P. W., Calderon M. M., Tamura M., 2009, MNRAS, 395, 1237

Burningham B., Pinfield D. J., Lucas P. W., Leggett S. K., Deacon N. R., Tamura M., Tinney C. G., Lodieu N., Zhang Z. H., Huelamo N., Jones H. R. A., Murray D. N., Mortlock D. J., Patel M., Barrado Y Navascués D., Zapatero Osorio M. R., Ishii M., Kuzuhara M., Smart R. L., 2010b, MNRAS, 406, 1885

Burrows A., Hubbard W. B., Lunine J. I., Liebert J., 2001, Rev. Mod. Phys., 73, 719

Burrows A., Liebert J., 1993, Reviews of Modern Physics, 65, 301

Burrows A., Marley M. S., Sharp C. M., 2000, ApJ, 531, 438

Burrows A., Sudarsky D., Hubeny I., 2006, ApJ, 640, 1063

Burwitz V., Reinsch K., Schwope A. D., Hakala P. J., Beuermann K., Rousseau T., Thomas H., Gänsicke B. T., Piirola V., Vilhu O., 1998, A&A, 331, 262

Caballero J. A., Béjar V. J. S., Rebolo R., Eislöffel J., Zapatero Osorio M. R., Mundt R., Barrado Y Navascués D., Bihain G., Bailer-Jones C. A. L., Forveille T., Martín E. L., 2007, A&A, 470, 903

Calabretta M. R., Greisen E. W., 2002, A&A, 395, 1077

Cargile P. A., James D. J., Platais I., 2009, AJ, 137, 3230

Casali M., Adamson A., Alves de Oliveira C., Almaini O., Burch K., Chuter T., Elliot J., Folger M., Foucaud S., Hambly N., Hastie M., Henry D., Hirst P., Irwin M., Ives D., Lawrence A., Laidlaw K., Lee D., Lewis J., Lunney D., McLay S., Montgomery D., Pickup A., Read M., Rees N., Robson I., Sekiguchi K., Vick A., Warren S., Woodward B., 2007, A&A, 467, 777

Casewell S. L., Dobbie P. D., Hodgkin S. T., Moraux E., Jameson R. F., Hambly N. C., Irwin J., Lodieu N., 2007, MNRAS, 378, 1131

Chabrier G., 2003, PASP, 115, 763

Chabrier G., Baraffe I., 2000, ARA&A, 38, 337

Chabrier G., Baraffe I., Allard F., Hauschildt P., 2000, ApJ, 542, 464

Chappelle R. J., Pinfield D. J., Steele I. A., Dobbie P. D., Magazzù A., 2005, MNRAS, 361, 1323

Chapra S. C., Canale R. P., 2005, Numerical Methods for Engineers, Fifth Edition

Chiu K., Fan X., Leggett S. K., Golimowski D. A., Zheng W., Geballe T. R., Schneider D. P., Brinkmann J., 2006, AJ, 131, 2722

Cossins P., 2010, PhD thesis, University of Leicester, private communication

Crampton D., Cowley A. P., 1977, PASP, 89, 374

Cuillandre J., Starr B., Isani S., McDonald J. S., Luppino G., 2001, in Astronomical Society of the Pacific Conference Series, Vol. 232, The New Era of Wide Field Astronomy, R. Clowes, A. Adamson, & G. Bromage, ed., pp. 398–+

Dalton G. B., Caldwell M., Ward A. K., Whalley M. S., Woodhouse G., Edeson R. L., Clark P., Beard S. M., Gallie A. M., Todd S. P., Strachan J. M. D., Bezawada N. N., Sutherland W. J., Emerson J. P., 2006, in Society of Photo-Optical Instrumentation Engineers (SPIE) Conference Series, Vol. 6269, Society of Photo-Optical Instrumentation Engineers (SPIE) Conference Series

Danielson R. E., 1966, ApJ, 143, 949

D'Antona F., 1995, in The Bottom of the Main Sequence - and Beyond, C. G. Tinney, ed., pp. 13–+

de Epstein A. E. A., Epstein I., 1985, AJ, 90, 1211

de La Fuente Marcos R., de La Fuente Marcos C., 2000, Ap&SS, 271, 127

Deacon N. R., Hambly N. C., 2004, A&A, 416, 125

Dick K. A., Fink U., 1977, J. Quant. Spec. Radiat. Transf., 18, 433

Dobbie P. D., Kenyon F., Jameson R. F., Hodgkin S. T., Pinfield D. J., Osborne S. L., 2002, MNRAS, 335, 687

Dolidze V. M., 1959, Astron. Circ. USSR, 200, 9

Dye S., Warren S. J., Hambly N. C., Cross N. J. G., Hodgkin S. T., Irwin M. J., Lawrence A., Adamson A. J., Almaini O., Edge A. C., Hirst P., Jameson R. F., Lucas P. W., van Breukelen C., Bryant J., Casali M., Collins R. S., Dalton G. B., Davies J. I., Davis C. J., Emerson J. P., Evans D. W., Foucaud S., Gonzales-Solares E. A., Hewett P. C., Kendall T. R., Kerr T. H., Leggett S. K., Lodieu N., Loveday J., Lewis J. R., Mann R. G., McMahon R. G., Mortlock D. J., Nakajima Y., Pinfield D. J., Rawlings M. G., Read M. A., Riello M., Sekiguchi K., Smith A. J., Sutorius E. T. W., Varricatt W., Walton N. A., Weatherley S. J., 2006, MNRAS, 372, 1227

Edvardsson B., Pettersson B., Kharrazi M., Westerlund B., 1995, A&A, 293, 75

Eggen O. J., 1960, MNRAS, 120, 540

—, 1970, ApJ, 161, 159

—, 1972, ApJ, 173, 63

Eggleton P. P., 1983, ApJ, 268, 368

Elmegreen B. G., 1999, ApJ, 522, 915

—, 2000, ApJ, 530, 277

Epstein I., 1968, AJ, 73, 556

Evans D. W., Irwin M., 1995, MNRAS, 277, 820

Fink U., Larson H. P., 1979, ApJ, 233, 1021

Ford A., Jeffries R. D., Smalley B., 2005, MNRAS, 364, 272

Forrest W. J., Shure M., Skrutskie M. F., 1988, ApJ, 330, L119

Francic S. P., 1989, AJ, 98, 888

Fukugita M., Ichikawa T., Gunn J. E., Doi M., Shimasaku K., Schneider D. P., 1996, AJ, 111, 1748

Geballe T. R., Knapp G. R., Leggett S. K., Fan X., Golimowski D. A., Anderson S., Brinkmann J., Csabai I., Gunn J. E., Hawley S. L., Hennessy G., Henry T. J., Hill G. J., Hindsley R. B., Ivezić Ž., Lupton R. H., McDaniel A., Munn J. A., Narayanan V. K., Peng E., Pier J. R., Rockosi C. M., Schneider D. P., Smith J. A., Strauss M. A., Tsvetanov Z. I., Uomoto A., York D. G., Zheng W., 2002, ApJ, 564, 466

Girardi L., Bertelli G., Bressan A., Chiosi C., Groenewegen M. A. T., Marigo P., Salasnich B., Weiss A., 2002, A&A, 391, 195

Gizis J. E., Reid I. N., Knapp G. R., Liebert J., Kirkpatrick J. D., Koerner D. W., Burgasser A. J., 2003, AJ, 125, 3302

Goldman B., Cushing M. C., Marley M. S., Artigau É., Baliyan K. S., Béjar V. J. S., Caballero J. A., Chanover N., Connelley M., Doyon R., Forveille T., Ganesh S., Gelino C. R., Hammel H. B., Holtzman J., Joshi S., Joshi U. C., Leggett S. K., Liu M. C., Martín E. L., Mohan V., Nadeau D., Sagar R., Stephens D., 2008, A&A, 487, 277

Golovin A., Malygin M., Pavlenko E., 2008, ArXiv e-prints

González-García B. M., Zapatero Osorio M. R., Béjar V. J. S., Bihain G., Barrado Y Navascués D., Caballero J. A., Morales-Calderón M., 2006, A&A, 460, 799

Goodwin S. P., Whitworth A. P., Ward-Thompson D., 2004a, A&A, 414, 633

—, 2004b, A&A, 423, 169

Greene T., 2001, American Scientist, 89,4

Grether D., Lineweaver C. H., 2006, ApJ, 640, 1051

Gunn J. E., Carr M., Rockosi C., Sekiguchi M., Berry K., Elms B., de Haas E., Ivezić Ž., Knapp G., Lupton R., Pauls G., Simcoe R., Hirsch R., Sanford D., Wang S., York D., Harris F., Annis J., Bartozek L., Boroski W., Bakken J., Haldeman M., Kent S., Holm S., Holmgren D., Petravick D., Prosapio A., Rechenmacher R., Doi M., Fukugita M., Shimasaku K., Okada N., Hull C., Siegmund W., Mannery E., Blouke M., Heidtman D., Schneider D., Lucinio R., Brinkman J., 1998, AJ, 116, 3040

Hambly N. C., 2008. private communication

Hambly N. C., Collins R. S., Cross N. J. G., Mann R. G., Read M. A., Sutorius E. T. W., Bond I., Bryant J., Emerson J. P., Lawrence A., Rimoldini L., Stewart J. M., Williams P. M., Adamson A., Hirst P., Dye S., Warren S. J., 2008, MNRAS, 384, 637

Hambly N. C., Davenhall A. C., Irwin M. J., MacGillivray H. T., 2001, MNRAS, 326, 1315

Hambly N. C., Steele I. A., Hawkins M. R. S., Jameson R. F., 1995a, MNRAS, 273, 505

—, 1995b, A&AS, 109, 29

Hawley S. L., Covey K. R., Knapp G. R., Golimowski D. A., Fan X., Anderson S. F., Gunn J. E., Harris H. C., Ivezić Ž., Long G. M., Lupton R. H., McGehee P. M., Narayanan V., Peng E., Schlegel D., Schneider D. P., Spahn E. Y., Strauss M. A., Szkody P., Tsvetanov Z., Walkowicz L. M., Brinkmann J., Harvanek M., Hennessy G. S., Kleinman S. J., Krzesinski J., Long D., Neilsen E. H., Newman P. R., Nitta A., Snedden S. A., York D. G., 2002, AJ, 123, 3409

Hawley S. L., Gizis J. E., Reid I. N., 1996, AJ, 112, 2799

Hayashi C., 1961, PASJ, 13, 450

Hayashi C., Nakano T., 1963, Progress of Theoretical Physics, 30, 460

Helling C., Dehn M., Woitke P., Hauschildt P. H., 2008, ApJ, 675, L105

Henry R. C., Anderson R., Hesser J. E., 1977, ApJ, 214, 742

Hester J. J., Scowen P. A., Sankrit R., Lauer T. R., Ajhar E. A., Baum W. A., Code A., Currie D. G., Danielson G. E., Ewald S. P., Faber S. M., Grillmair C. J., Groth E. J., Holtzman J. A., Hunter D. A., Kristian J., Light R. M., Lynds C. R., Monet D. G., O'Neil Jr. E. J., Shaya E. J., Seidelmann K. P., Westphal J. A., 1996, AJ, 111, 2349

Hewett P. C., Warren S. J., Leggett S. K., Hodgkin S. T., 2006, MNRAS, 367, 454

Hodgkin S. T., 2010. private communication

Hodgkin S. T., Irwin M. J., Hewett P. C., Warren S. J., 2009, MNRAS, 394, 675

Hogan E., Jameson R. F., Casewell S. L., Osbourne S. L., Hambly N. C., 2008, MNRAS, 388, 495

Holland K., Jameson R. F., Hodgkin S., Davies M. B., Pinfield D., 2000, MNRAS, 319, 956

Howell S. B., Nelson L. A., Rappaport S., 2001, ApJ, 550, 897

Hoyle F., 1953, ApJ, 118, 513

Ingham W. H., Brecher K., Wasserman I., 1976, ApJ, 207, 518

Irwin M., Lewis J., 2001, New A Rev., 45, 105

Jameson R. F., 2006

Jameson R. F., Casewell S. L., Bannister N. P., Lodieu N., Keresztes K., Dobbie P. D., Hodgkin S. T., 2008, MNRAS, 384, 1399

Jameson R. F., Dobbie P. D., Hodgkin S. T., Pinfield D. J., 2002, MNRAS, 335, 853

Jeffries R. D., 2000, in Astronomical Society of the Pacific Conference Series, Vol. 198, Stellar Clusters and Associations: Convection, Rotation, and Dynamos, R. Pallavicini, G. Micela, & S. Sciortino, ed., pp. 245–+

Joergens V., 2006, A&A, 448, 655

Johnson H. L., Morgan W. W., 1953, ApJ, 117, 313

Jones B. F., Cudworth K., 1983, AJ, 88, 215

Kafatos M. C., Harrington R. S., Maran S. P., 1986, Astrophysics of brown dwarfs. Proceedings of the Second George Mason Fall Workshop in Astrophysics, held at Fairfax, Va., USA, 14 - 15 October 1985., Kafatos, M. C., Harrington, R. S., & Maran, S. P., ed.

Kharchenko N. V., Piskunov A. E., Röser S., Schilbach E., Scholz R., 2005, A&A, 438, 1163

King A. R., 1995, in Astronomical Society of the Pacific Conference Series, Vol. 85, Magnetic Cataclysmic Variables, D. A. H. Buckley & B. Warner, ed., pp. 21–+

King A. R., Wynn G. A., 1999, MNRAS, 310, 203

Kirkpatrick J. D., 2005, ARA&A, 43, 195

Kirkpatrick J. D., Allard F., Bida T., Zuckerman B., Becklin E. E., Chabrier G., Baraffe I., 1999a, ApJ, 519, 834

Kirkpatrick J. D., Henry T. J., McCarthy Jr. D. W., 1991, ApJS, 77, 417

Kirkpatrick J. D., Kelly D. M., Rieke G. H., Liebert J., Allard F., Wehrse R., 1993, ApJ, 402, 643

Kirkpatrick J. D., Reid I. N., Liebert J., Cutri R. M., Nelson B., Beichman C. A., Dahn C. C., Monet D. G., Gizis J. E., Skrutskie M. F., 1999b, ApJ, 519, 802

Klein Wassink W. J., 1927, Publications of the Kapteyn Astronomical Laboratory Groningen, 41, 1

Kraus A. L., Hillenbrand L. A., 2007, AJ, 134, 2340

Kraus A. L., White R. J., Hillenbrand L. A., 2005, ApJ, 633, 452

Krotov R., Wang D., Z. S. N., 1980, ApJ, 240, 940

Kroupa P., 2001, MNRAS, 322, 231

—, 2002, Science, 295, 82

Kroupa P., Tout C. A., Gilmore G., 1993, MNRAS, 262, 545

Kuijpers J., Pringle J. E., 1984, Physica Scripta Volume T, 7, 120

Kumar S. S., 1963, ApJ, 137, 1121

Lada C. J., 2010, Royal Society of London Philosophical Transactions Series A, 368, 713

Landolt A. U., 1992, AJ, 104, 340

—, 2009, AJ, 137, 4186

Larson R. B., 1992, MNRAS, 256, 641

Lawrence A., Warren S. J., Almaini O., Edge A. C., Hambly N. C., Jameson R. F., Lucas P., Casali M., Adamson A., Dye S., Emerson J. P., Foucaud S., Hewett P., Hirst P., Hodgkin S. T., Irwin M. J., Lodieu N., McMahon R. G., Simpson C., Smail I., Mortlock D., Folger M., 2007, MNRAS, 379, 1599

Leggett S. K., Geballe T. R., Fan X., Schneider D. P., Gunn J. E., Lupton R. H., Knapp G. R., Strauss M. A., McDaniel A., Golimowski D. A., Henry T. J., Peng E., Tsvetanov Z. I., Uomoto A., Zheng W., Hill G. J., Ramsey L. W., Anderson S. F., Annis J. A., Bahcall N. A., Brinkmann J., Chen B., Csabai I., Fukugita M., Hennessy G. S., Hindsley R. B., Ivezić Ž., Lamb D. Q., Munn J. A., Pier J. R., Schlegel D. J., Smith J. A., Stoughton C., Thakar A. R., York D. G., 2000, ApJ, 536, L35

Leggett S. K., Saumon D., Burningham B., Cushing M. C., Marley M. S., Pinfield D. J., 2010, ApJ, 720, 252

Lenzuni P., Chernoff D. F., Salpeter E. E., 1991, ApJS, 76, 759

Liu M. C., Leggett S. K., Golimowski D. A., Chiu K., Fan X., Geballe T. R., Schneider D. P., Brinkmann J., 2006, ApJ, 647, 1393

Lodieu N., 2004, PhD thesis, Astrophysikalisches Institut Potsdam

Lodieu N., Dobbie P. D., Deacon N. R., Hodgkin S. T., Hambly N. C., Jameson R. F., 2007a, MNRAS, 380, 712

Lodieu N., Hambly N. C., Jameson R. F., Hodgkin S. T., 2008, MNRAS, 383, 1385

Lodieu N., Hambly N. C., Jameson R. F., Hodgkin S. T., Carraro G., Kendall T. R., 2007b, MNRAS, 374, 372

Lodieu N., Zapatero Osorio M. R., Rebolo R., Martín E. L., Hambly N. C., 2009, A&A, 505, 1115

Low C., Lynden-Bell D., 1976, MNRAS, 176, 367

Lucas P. W., Tinney C. G., Burningham B., Leggett S. K., Pinfield D. J., Smart R., Jones H. R. A., Marocco F., Barber R. J., Yurchenko S. N., Tennyson J., Ishii M., Tamura M., Day-Jones A. C., Adamson A., Allard F., Homeier D., 2010, MNRAS, L124+

Luhman K. L., 2004, ApJ, 617, 1216

—, 2006, ApJ, 645, 676

Luhman K. L., Adame L., D'Alessio P., Calvet N., McLeod K. K., Bohac C. J., Forrest W. J., Hartmann L., Sargent B., Watson D. M., 2007a, ApJ, 666, 1219

Luhman K. L., Joergens V., Lada C., Muzerolle J., Pascucci I., White R., 2007b, Protostars and Planets V, 443

Lupton R. H., Gunn J. E., Szalay A. S., 1999, AJ, 118, 1406

Lynga G., Palous J., 1987, A&A, 188, 35

Magnier E. A., Cuillandre J., 2004, PASP, 116, 449

Marcy G. W., Butler R. P., 2000, PASP, 112, 137

Marley M. S., Saumon D., Guillot T., Freedman R. S., Hubbard W. B., Burrows A., Lunine J. I., 1996, Science, 272, 1919

Marley M. S., Seager S., Saumon D., Lodders K., Ackerman A. S., Freedman R. S., Fan X., 2002, ApJ, 568, 335

Marsh T. R., 2001, in Lecture Notes in Physics, Berlin Springer Verlag, Vol. 573, Astrotomography, Indirect Imaging Methods in Observational Astronomy, H. M. J. Boffin, D. Steeghs, & J. Cuypers, ed., pp. 1–+

Martín E. L., Barrado y Navascués D., Baraffe I., Bouy H., Dahm S., 2003, ApJ, 594, 525

Martín E. L., Delfosse X., Basri G., Goldman B., Forveille T., Zapatero Osorio M. R., 1999, AJ, 118, 2466

Martin E. L., Zapatero Osorio M. R., Rebolo R., 1998, in Astronomical Society of the Pacific Conference Series, Vol. 134, Brown Dwarfs and Extrasolar Planets, R. Rebolo, E. L. Martin, & M. R. Zapatero Osorio, ed., pp. 507–+

Matthews K., Nakajima T., Kulkarni S. R., Oppenheimer B. R., 1996, AJ, 112, 1678

Mayor M., Pepe F., Queloz D., Bouchy F., Rupprecht G., Lo Curto G., Avila G., Benz W., Bertaux J., Bonfils X., Dall T., Dekker H., Delabre B., Eckert W., Fleury M., Gilliotte A., Gojak D., Guzman J. C., Kohler D., Lizon J., Longinotti A., Lovis C., Megevand D., Pasquini L., Reyes J., Sivan J., Sosnowska D., Soto R., Udry S., van Kesteren A., Weber L., Weilenmann U., 2003, The Messenger, 114, 20

McCarthy Jr. D. W., Probst R. G., Low F. J., 1985, ApJ, 290, L9

McLean I. S., McGovern M. R., Burgasser A. J., Kirkpatrick J. D., Prato L., Kim S. S., 2003, ApJ, 596, 561

Mermilliod J., Platais I., James D. J., Grenon M., Cargile P. A., 2008, A&A, 485, 95

Micela G., Sciortino S., Favata F., Pallavicini R., Pye J., 1999, A&A, 344, 83

Miller G. E., Scalo J. M., 1978, PASP, 90, 506

—, 1979, ApJS, 41, 513

Monet D. G., Levine S. E., Canzian B., Ables H. D., Bird A. R., Dahn C. C., Guetter H. H., Harris H. C., Henden A. A., Leggett S. K., Levison H. F., Luginbuhl C. B., Martini J., Monet A. K. B., Munn J. A., Pier J. R., Rhodes A. R., Riepe B., Sell S., Stone R. C., Vrba F. J., Walker R. L., Westerhout G., Brucato R. J., Reid I. N., Schoening W., Hartley M., Read M. A., Tritton S. B., 2003, AJ, 125, 984

Moraux E., Bouvier J., Stauffer J. R., Barrado y Navascués D., Cuillandre J., 2007, A&A, 471, 499

Moraux E., Bouvier J., Stauffer J. R., Cuillandre J., 2003, A&A, 400, 891

Morgan W. W., Keenan P. C., Kellman E., 1943, An atlas of stellar spectra, with an outline of spectral classification, Morgan, W. W., Keenan, P. C., & Kellman, E., ed.

Nakajima T., Oppenheimer B. R., Kulkarni S. R., Golimowski D. A., Matthews K., Durrance S. T., 1995, Nature, 378, 463

Nelson L. A., Rappaport S., Chiang E., 1993, ApJ, 413, 364

Oppenheimer B. R., Kulkarni S. R., Matthews K., Nakajima T., 1995, Science, 270, 1478

Oppenheimer B. R., Kulkarni S. R., Matthews K., van Kerkwijk M. H., 1998, ApJ, 502, 932

Paczyński B., 1971, ARA&A, 9, 183

Padoan P., Nordlund Å., 2002, ApJ, 576, 870

Panagi P. M., O'dell M. A., 1997, A&AS, 121, 213

Panagi P. M., O'dell M. A., Collier Cameron A., Robinson R. D., 1994, A&A, 292, 439

Pavlenko Y. V., Rebolo R., Martin E. L., Garcia Lopez R. J., 1995, A&A, 303, 807

Perry C. L., Walter D. K., Crawford D. L., 1978, PASP, 90, 81

Phillips J. G., Davis S. P., Lindgren B., Balfour W. J., 1987, ApJS, 65, 721

Pickering E. C., Kapteyn J. C., van Rhijn P. J., 1923, Annals of Harvard College Observatory, 102, 276

Pillitteri I., Micela G., Reale F., Sciortino S., 2005, A&A, 430, 155

Pillitteri I., Micela G., Sciortino S., Damiani F., Harnden Jr. F. R., 2004, A&A, 421, 175

Pillitteri I., Micela G., Sciortino S., Favata F., 2003, A&A, 399, 919

Pinfield D. J., Burningham B., Tamura M., Leggett S. K., Lodieu N., Lucas P. W., Mortlock D. J., Warren S. J., Homeier D., Ishii M., Deacon N. R., McMahon R. G., Hewett P. C., Osori M. R. Z., Martin E. L., Jones H. R. A., Venemans B. P., Day-Jones A. C., Dobbie P. D., Folkes S. L., Dye S., Allard F., Baraffe I., Barrado Y Navascués D., Casewell S. L., Chiu K., Chabrier G., Clarke F., Hodgkin S. T., Magazzù A., McCaughrean M. J., Nakajima T., Pavlenko Y., Tinney C. G., 2008, MNRAS, 390, 304

Pinfield D. J., Dobbie P. D., Jameson R. F., Steele I. A., Jones H. R. A., Katsiyannis A. C., 2003, MNRAS, 342, 1241

Pinfield D. J., Hodgkin S. T., Jameson R. F., Cossburn M. R., von Hippel T., 1997, MNRAS, 287, 180

Pinfield D. J., Jameson R. F., Hodgkin S. T., 1998, MNRAS, 299, 955

Pinfield D. J., Jones H. R. A., Lucas P. W., Kendall T. R., Folkes S. L., Day-Jones A. C., Chappelle R. J., Steele I. A., 2006, MNRAS, 368, 1281

Probst R. G., 1983, ApJS, 53, 335

Rappaport S., Verbunt F., Joss P. C., 1983, ApJ, 275, 713

Rebolo R., Martin E. L., Basri G., Marcy G. W., Zapatero-Osorio M. R., 1996, ApJ, 469, L53+

Rebolo R., Martin E. L., Magazzu A., 1992, ApJ, 389, L83

Rees M. J., 1976, MNRAS, 176, 483

Reid I. N., Burgasser A. J., Cruz K. L., Kirkpatrick J. D., Gizis J. E., 2001, AJ, 121, 1710

Reid I. N., Kirkpatrick J. D., Liebert J., Gizis J. E., Dahn C. C., Monet D. G., 2002, AJ, 124, 519

Reinsch K., Kim Y., Beuermann K., 2006, A&A, 457, 1043

Reipurth B., 2000, AJ, 120, 3177

Reipurth B., Clarke C., 2001, AJ, 122, 432

Richards M. T., 2007, in IAU Symposium, Vol. 240, IAU Symposium, W. I. Hartkopf, E. F. Guinan, & P. Harmanec, ed., pp. 160–169

Rieke G. H., 2007, ARA&A, 45, 77

Robichon N., Arenou F., Mermilliod J., Turon C., 1999, A&A, 345, 471

Rojas-Ayala B., Lloyd J. P., 2010, in Astronomical Society of the Pacific Conference Series, Vol. 430, Pathways Towards Habitable Planets, V. Coudé Du Foresto, D. M. Gelino, & I. Ribas, ed., pp. 528–+

Ruiz M. T., Leggett S. K., Allard F., 1997, ApJ, 491, L107+

Salpeter E. E., 1955, ApJ, 121, 161

Sanders W. L., 1971, A&A, 14, 226

Santos N. C., Israelian G., Mayor M., 2004, A&A, 415, 1153

Saumon D., Marley M. S., 2008, ApJ, 689, 1327

Saumon D., Marley M. S., Lodders K., Freedman R. S., 2003, in IAU Symposium, Vol. 211, Brown Dwarfs, E. Martín, ed., pp. 345–+

Scalo J. M., 1986, Fund. Cosmic Phys., 11, 1

Schilbach E., Kharchenko N. V., Piskunov A. E., Röser S., Scholz R., 2006, A&A, 456, 523

Schwarz R., Reinsch K., Beuermann K., Burwitz V., 2005, A&A, 442, 271

Shafter A. W., Reinsch K., Beuermann K., Misselt K. A., Buckley D. A. H., Burwitz V., Schwope A. D., 1995, ApJ, 443, 319

Sirianni M., Nota A., De Marchi G., Leitherer C., Clampin M., 2002, ApJ, 579, 275

Skrutskie M. F., Cutri R. M., Stiening R., Weinberg M. D., Schneider S., Carpenter J. M., Beichman C., Capps R., Chester T., Elias J., Huchra J., Liebert J., Lonsdale C., Monet D. G., Price S., Seitzer P., Jarrett T., Kirkpatrick J. D., Gizis J. E., Howard E., Evans T., Fowler J., Fullmer L., Hurt R., Light R., Kopan E. L., Marsh K. A., McCallon H. L., Tam R., Van Dyk S., Wheelock S., 2006, AJ, 131, 1163

Stamatellos D., Hubber D. A., Whitworth A. P., 2007, MNRAS, 382, L30

Stamatellos D., Whitworth A. P., 2009, MNRAS, 392, 413

Staude A., Schwope A. D., Schwarz R., 2001, A&A, 374, 588

Stauffer J. R., Schultz G., Kirkpatrick J. D., 1998, ApJ, 499, L199+

Stuik R., Bruls J. H. M. J., Rutten R. J., 1997, A&A, 322, 911

Tapia S., 1977, ApJ, 212, L125

Tarter J., 1975, PhD thesis, Univ. Calif., Berkeley.

Tej A., Sahu K. C., Chandrasekhar T., Ashok N. M., 2002, ApJ, 578, 523

Testi L., D'Antona F., Ghinassi F., Licandro J., Magazzù A., Maiolino R., Mannucci F., Marconi A., Nagar N., Natta A., Oliva E., 2001, ApJ, 552, L147

Tinney C. G., ed., 1995, The Bottom of the Main Sequence - and Beyond

Tsuji T., 2001, in Ultracool Dwarfs: New Spectral Types L and T, H. R. A. Jones & I. A. Steele, ed., pp. 9–+

Tsuji T., Nakajima T., Yanagisawa K., 2004, ApJ, 607, 511

Tsuji T., Ohnaka K., Aoki W., 1999, ApJ, 520, L119

Tsuji T., Ohnaka K., Aoki W., Nakajima T., 1996, A&A, 308, L29

Tsvetkov T. G., 1993, Ap&SS, 203, 247

Valdes F. G., Campusano L. E., Velasquez J. D., Stetson P. B., 1995, PASP, 107, 1119

van Leeuwen F., 2009, A&A, 497, 209

Vandenberg D. A., Bridges T. J., 1984, ApJ, 278, 679

Verbunt F., Zwaan C., 1981, A&A, 100, L7

Walch S., Burkert A., Whitworth A., Naab T., Gritschneder M., 2009, MNRAS, 400, 13

Walch S., Naab T., Whitworth A., Burkert A., Gritschneder M., 2010, MNRAS, 402, 2253

Warner B., 1995, Cambridge Astrophysics Series, 28

Warren S. J., Hambly N. C., Dye S., Almaini O., Cross N. J. G., Edge A. C., Foucaud S., Hewett P. C., Hodgkin S. T., Irwin M. J., Jameson R. F., Lawrence A., Lucas P. W., Adamson A. J., Bandyopadhyay R. M., Bryant J., Collins R. S., Davis C. J., Dunlop J. S., Emerson J. P., Evans D. W., Gonzales-Solares E. A., Hirst P., Jarvis M. J., Kendall T. R., Kerr T. H., Leggett S. K., Lewis J. R., Mann R. G., McLure R. J., McMahon R. G., Mortlock D. J., Rawlings M. G., Read M. A., Riello M., Simpson C., Smith D. J. B., Sutorius E. T. W., Targett T. A., Varricatt W. P., 2007, MNRAS, 375, 213

Watkins S. J., Bhattal A. S., Boffin H. M. J., Francis N., Whitworth A. P., 1998, MNRAS, 300, 1214

Westerlund B. E., 1963, MNRAS, 127, 83

Westerlund B. E., Lundgren K., Pettersson B., Garnier R., Breysacher J., 1988, A&AS, 76, 101

Whitworth A., Bate M. R., Nordlund Å., Reipurth B., Zinnecker H., 2007, Protostars and Planets V, 459

Whitworth A. P., Zinnecker H., 2004, A&A, 427, 299

Wiese W. L., Smith M. W., Glennon B. M., 1966, Atomic transition probabilities. Vol.: Hydrogen through Neon. A critical data compilation, Wiese, W. L., Smith, M. W., & Glennon, B. M., ed.

York D. G., Adelman J., Anderson Jr. J. E., Anderson S. F., Annis J., Bahcall N. A., Bakken J. A., Barkhouser R., Bastian S., Berman E., Boroski W. N., Bracker S., Briegel C., Briggs J. W., Brinkmann J., Brunner R., Burles S., Carey L., Carr M. A., Castander F. J., Chen B., Colestock P. L., Connolly A. J., Crocker J. H., Csabai I., Czarapata P. C., Davis J. E., Doi M., Dombeck T., Eisenstein D., Ellman N., Elms B. R., Evans M. L., Fan X., Federwitz G. R., Fiscelli L., Friedman S., Frieman J. A., Fukugita M., Gillespie B., Gunn J. E., Gurbani V. K., de Haas E., Haldeman M., Harris F. H., Hayes J., Heckman T. M., Hennessy G. S., Hindsley R. B., Holm S., Holmgren D. J., Huang C., Hull C., Husby D., Ichikawa S., Ichikawa T., Ivezić Ž., Kent S., Kim R. S. J., Kinney E., Klaene M., Kleinman A. N., Kleinman S., Knapp G. R., Korienek J., Kron R. G., Kunszt P. Z., Lamb D. Q., Lee B., Leger R. F., Limmongkol S., Lindenmeyer C., Long D. C., Loomis C., Loveday J., Lucinio R., Lupton R. H., MacKinnon B., Mannery E. J., Mantsch P. M., Margon B., McGehee P., McKay T. A., Meiksin A., Merelli A., Monet D. G., Munn J. A., Narayanan V. K., Nash T., Neilsen E., Neswold R., Newberg H. J., Nichol R. C., Nicinski T., Nonino M., Okada N., Okamura S., Ostriker J. P., Owen R., Pauls A. G., Peoples J., Peterson R. L., Petravick D., Pier J. R., Pope A., Pordes R., Prosapio A., Rechenmacher R., Quinn T. R., Richards G. T., Richmond M. W., Rivetta C. H., Rockosi C. M., Ruthmansdorfer K., Sandford D., Schlegel D. J., Schneider D. P., Sekiguchi M., Sergey G., Shimasaku K., Siegmund W. A., Smee S., Smith J. A., Snedden S., Stone R., Stoughton C., Strauss M. A., Stubbs C., SubbaRao M., Szalay A. S., Szapudi I., Szokoly G. P., Thakar A. R., Tremonti C., Tucker D. L., Uomoto A., Vanden Berk D., Vogeley M. S., Waddell P., Wang S., Watanabe M., Weinberg D. H., Yanny B., Yasuda N., 2000, AJ, 120, 1579